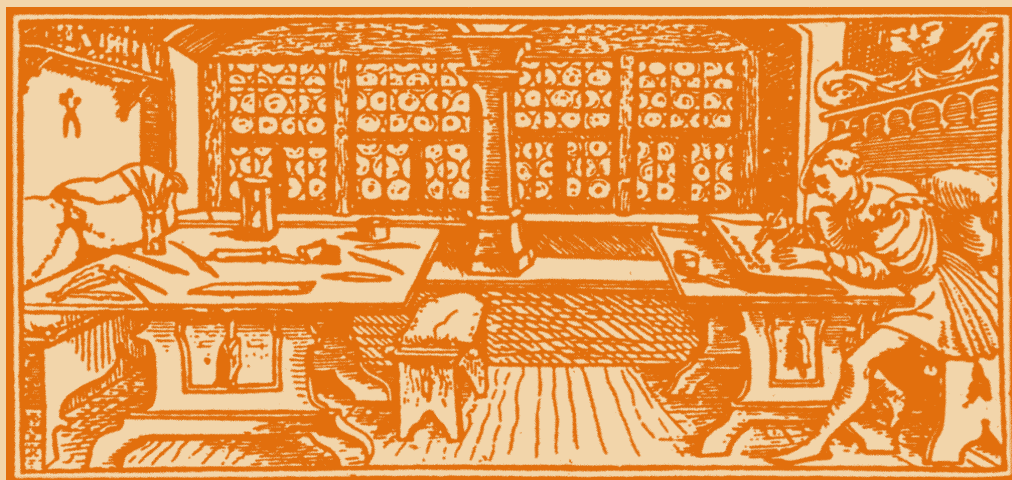


STUDIA

UNIVERSITATIS
BABEȘ-BOLYAI

C h e m i a

C L U J - N A P O C A 2 0 0 3



STUDIA UNIVERSITATIS BABEȘ-BOLYAI CHEMIA 1

EDITORIAL OFFICE: Republicii no. 24, 3400 Cluj-Napoca ♦ Phone 0264-40.53.52

SUMAR - CONTENTS - SOMMAIRE - INHALT

M. V. DIUDEA, B. PÂRV, O. URSU, Hex Tori from Square Tori.....	3
M. V. DIUDEA, O. URSU, B. PÂRV, Hex Tubes from Square Tubes	11
M. V. DIUDEA, I. SILAGHI-DUMITRESCU, Small Fullerenoids.....	21
M. V. DIUDEA, The "Zig-Zag" Cylinder Rule	31
G. KATONA, M. V. DIUDEA, Correlating Ability of Cluj Type Indices	41
A. PATRUT, A. NICOARA, D. MARGINEAN, Current Aspects of the Poly-oxometalate / Metal Oxide-Based Clusters. I. General Aspects.....	77
A. PATRUT, A. NICOARA, D. MARGINEAN, Current Aspects of the Poly-oxometalate / Metal Oxide-Based Clusters. II. Special Aspects.....	85
G. SZABO, J. ZSAKO, I. BALDEA, CS. BOLLA, Kinetic Study on Hydrolysis Reaction of Dioximes	93
G. SZABO, J. ZSAKO, CS. BOLLA, Temperature Dependences of the Dioximes Hydrolysis Reaction Rate.....	99
E. SZABO, G. SZABO, CS. BOLLA, Influence of Iodate Ion Concentration on Oscillations in the Briggs-Rauscher Reaction.....	103

M. SOCOL, I. BALDEA, Flow Graphs in Chemical Kinetics (I).....	109
GABRIELA-CRISTINA BUCSA, CLAUDIA-GEMMA MURESAN, I. BALDEA, Kinetics and Mechanism of O-Xylene Oxidation by Ce(IV) in Aqueous Acidic Medium.....	125
IOVANCA HAIDUC, SIMONA COBZAC, AURORA MOCANU, M. C. BACIU, Sample Handling. Chromatographic Analysis of Trifluralin from Environmental Sample. I. Water Sample	137
ANCA PETER, VIRGINIA DANCIU, VERONICA COSOVEANU, Cathodic Electro- deposition of Titanium Dioxide Films	143
MICHAELA PONTA, T. FRENTIU, C. McCORMICK, A. BELA, CECILIA ROMAN, E. CORDOS, An Investigation into the Cu, Pb and Zn Pollution of the Somes and Lapus Rivers of Baia-Mare Area, Romania	151
MARIA JITARU, RAMONA IACOB, MARIA POPA, Voltamperometric Methods for the Cooper Ions Determination	161
AURORA BATINAS, AL. POP, CAMELIA GHERMAN, S. AGACHI, The Deter- mination of the Kinetic Parameters to Sulfur Dioxide Chemosorption in Ammonia Sulfite	169
R. SILAGHI-DUMITRESCU, F.D.IRIMIE, C.PAIZS, CORNELIA MAJDIK, MONICA TOSA, PAULA MOLDOVAN, ANGELA SAS, L. TAMAS, Horseradish Peroxidase-Catalyzed Oxidation of Some Benzyl-Type Alcohols	177
ADINA GHIRISAN, AL.POP, V. MICLAUS, Sedimentation. Koagulation. Flocculation. I. Sedimentationsanalyse einer geflockten kaolinsuspension	183
S. DRAGAN, MIHAELA DRAGAN, The Solubility of Drugs in Supercritical CO ₂ and the Effect of Entrainers	191
MARIA TOMOAI-COTISEL, J. ZSAKO, AURORA MOCANU, M. SALAJAN, C. RACZ, SIMONA BRAN, E. CHIFU, Adsorption Kinetics of Dibucaine and Tetracaine at the Benzene/Water Interface Studied by Pendant Drop Method	201
ELISABETA VERESS, V. LITEANU, I. O. MARIAN, ANDREEA OLTEAN, Pho- toelectrochemical Phenomena on Semiconductor Redox Glass Electrodes	219
L. KEKEDY-NAGY, T. FRENTIU, ANA-MARIA RUSU, MICHAELA PONTA, E.A. CORDOS, Flame Atomic Emission Determination of Strontium in Flotation Tailings Using the Methane-Air Flame as Excitation Source.....	225

HEX TORI FROM SQUARE TORI

MIRCEA V. DIUDEA^{a*}, BAZIL PARV^b and OLEG URSU^c

^a Faculty of Chemistry and Chemical Engineering

^b Department of Computer Science, Faculty of Mathematics
Babes-Bolyai University, 3400 Cluj, Romania

^c Department of Chemistry, Cleveland State University
2121 Euclid Avenue, Cleveland OHIO 44115 USA

ABSTRACT. Hex and other tiled tori can be derived from square tori. This way of building toroidal fullerenes is a versatile one, enabling various tilings: rhomboidal C₄, polyhex C₆, C₄C₈, azulenic C₅C₇ as well as twisted lattices. The stability of polyhex toroids is discussed in terms of molecular mechanics energy.

INTRODUCTION

Among the carbon allotropes, the only orientable closed surface entirely coverable by a bezenoid lattice is the torus. The polyhedral (combinatorial) torus obeys the Euler theorem:¹

$$N - E + F = 2 - 2g \quad (1)$$

(*N*, *E*, *F*, *g* being respectively the number of vertices, edges, faces, and genus – for the torus *g* = 1). Formula is useful for checking the consistency of an assumed structure.

"Circle crops" structures were first observed by Liu *et al.*² and then by other groups.³⁻⁵ Martel *et al.*⁵ argued that the observed rings were coils rather than perfect tori, but these structures have continued to attract a multitude of theoretical studies, dealing with construction, mathematical and physical properties of graphitic tori.⁶⁻¹⁴

This paper describes a novel way of generating polyhex tori, starting from quadrilateral tori. Several cutting procedures and transformations of the square toroidal nets are proposed in the view of obtaining chemically significant lattices. The stability of polyhex tori, the main toroidal objects herein generated, is discussed in terms of the MM+ energy.

SQUARE TORI GENERATION

Covering a torus by hexagons is achieved mainly by the well-known graphite zone-folding.¹¹⁻¹⁶ The method finds an equivalent planar parallelogram, tiled by a polyhex lattice. The graphite sheet is folded to form a tube and finally

the two ends of the tube are glued in order to form a torus. A torus $T_{p,q,t}$ thus obtained is completely defined by four integers, reducible to three parameters:^{14,16} p and q count the hexagons stacked in a $p \times q$ -parallelogram and t is the twisting parameter, *i.e.*, the number of hexagons offset before final pasting.

An alternative to the parallelogram procedure is the AME (*i.e.*, adjacency matrix eigenvectors).¹⁷⁻²⁰ Our construction starts from a square net embedded on the toroidal surface.²¹⁻²⁴ A c -fold cycle, circumscript to a tube section of radius r , is circulating along the toroidal circle, of radius $R > r$ (Figure 1). Its subsequent n images, equally spaced and joined with edges, point by point, form a polyhedral torus tiled by a square pattern. The position of each of the n images of the circulant around the large circle is characterized by angle θ while angle φ locates the c points of the circulant around the small circle. In all, $c \times n$ points are generated.

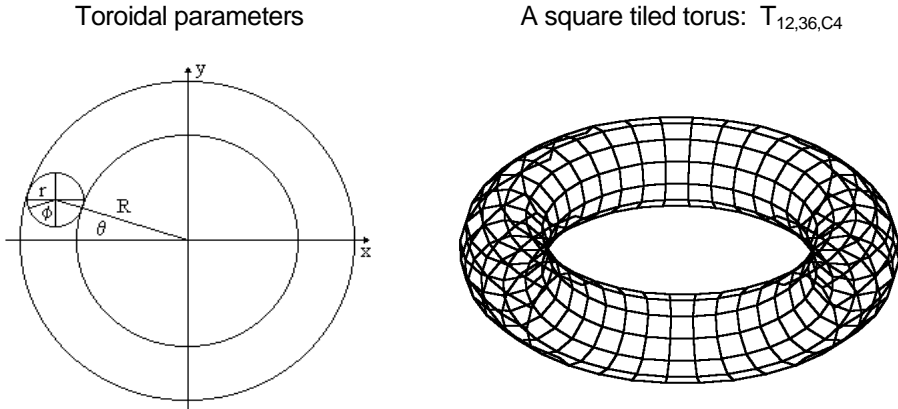


Figure 1. Construction of a toroidal surface.

The parameters are calculated by the following formulas:

$$P(x, y, z): \quad (2)$$

$$x = \cos(\theta)(R + r \cos \varphi)$$

$$y = \sin(\theta)(R + r \cos \varphi)$$

$$z = r \sin \varphi$$

$$\theta_i = \frac{2\pi}{n} i \quad ; \quad i = 0, \dots, n-1$$

$$\varphi_j = \frac{2\pi}{c} j \quad ; \quad j = 0, \dots, c-1$$

The problem is *how to transform a square net* covering the toroidal surface into patterns of chemical interest. At this stage, the genuine length of r and R is not a matter.

The square lattice generated as described above is a torus, $C_4[c,n]$ completely defined by two integers: c –dimension of the tube and n –dimension of the torus (*i.e.*, the combinatorial dimensions of the square toroidal net). The subscript in C_4 specifies the size of the polygonal tiling pattern.

In case of single-wall tori, the square net consists of $c \times n$ vertices, $c \times n$ squares and $4 \times c \times n / 2$ edges, 4 being the vertex degree of the net (which is a regular graph). The above relations come out as a consequence of Euler's formula.

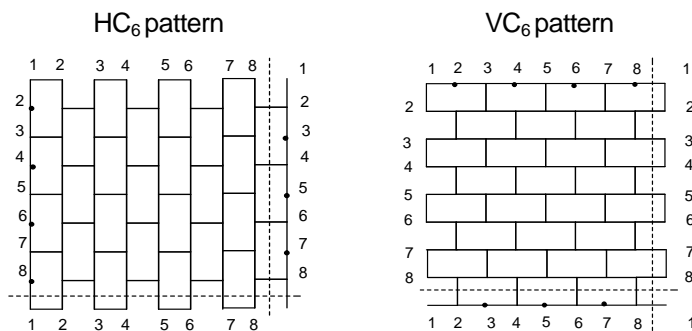
HEX TORI FROM SQUARE TORI

A cutting operation consists of deleting appropriate edges in a square lattice in order to produce some larger polygonal faces. By deleting each second *horizontal* edge and alternating edges and cuts in each second row it results in a standard HC_6 pattern (Figure 2 (a), top).

After optimizing by a molecular mechanics program, a phenacenic pattern appears on the torus (Figure 2 (a), bottom).

A *vertical action* of the above algorithm leads to a standard VC_6 pattern (Figure 2, (b)). It means that, after optimization, an acenic pattern is obtained (Figure 2 (b), bottom).

Note that each hexagon consumes exactly two squares in the square-like lattice. By construction, the number of hexagons in the HC_6 pattern is half the number of squares on dimension c of the torus $HC_6[c,n]$ while in the $VC_6[c,n]$ torus the reduced number of hexagons appears on dimension n . Recall that, the above cutting procedure leaves unchanged the number of vertices in the original square torus. The name of a polyhex torus, thus generated, has to remind the *type of cutting* (H or V), as well as the *size of cycles* occurring in a given pattern. Figures 3 illustrates two isomeic objects originated in $C_4[12,24]$. Within this pattern no twisted, chiral polyhex tori are discussed.



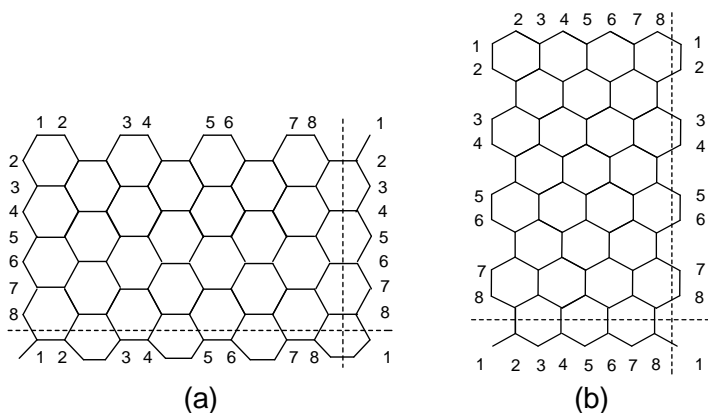


Figure 2. Standard C_6 patterns and their optimized forms.

$HC_6[12,36]$ (side)
 $h=5.90$

$HC_6[12,36]$ (top) $N=432$
 $d=2.90$; $D=23.91$

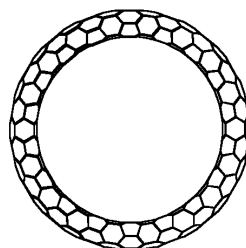
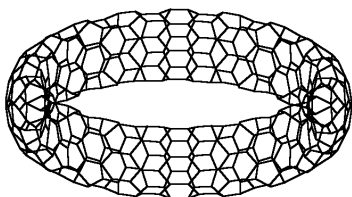


Figure 3a. Polyhex tori $HC_6[c,n]$: height h , tube diameter d and torus diameter D , respectively (in Angstroms)

$VC_6[12,72]$ (side)
 $h=11.44$

$VC_6[12,72]$ (top) $N=864$
 $d=3.51$; $D=27.52$

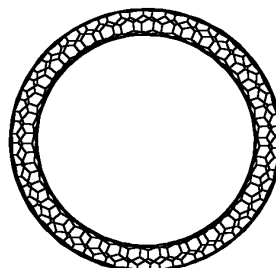
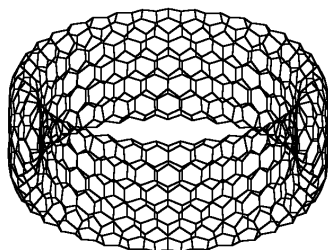


Figure 3b. Polyhex tori $VC_6[c,n]$: height h , tube diameter d and torus diameter D , respectively (in Angstroms)

MOLECULAR MECHANICS CALCULATIONS

Our TORUS software package enabled us to generate huge tori, up to 20,000 atoms, which could be optimised by a molecular mechanics procedure.

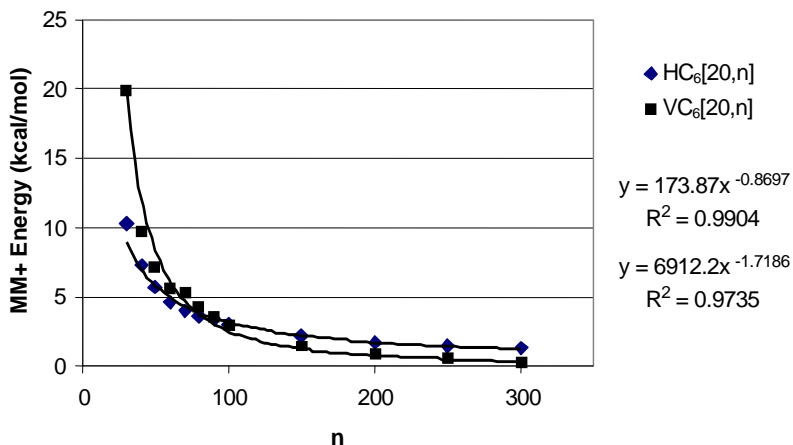


Figure 4. Plot of MM+ energy per atom vs the n -dimension

The MM+ energy per atom decreases as n (*i.e.*, the central hollow) increases, by a power function (Figure 4). The tori of V-series are more stable than those of H-series.

Note that the MM+ energy for C₆₀ is about 4.454 kcal/mol, value reached in HC₆[20, n] series at more than 120 atoms while in VC₆[20, n] series around 160 atoms. However, in toroids with thousand atoms, the MM+ energy lowers very much, as shown in Table 1.

Table 1.
MM+ energy per atom (kcal/mol) in tori of series [20, n]

n	MM+ for H-series		MM+ for V-series	
	Tori	Tubes	Tori	Tubes
20	17.7158	1.0427	36.3829	-0.7782
30	10.3547	1.0313	19.9559	-0.8227
40	7.2618	1.0256	9.7139	-0.8450
50	5.6703	1.0222	7.1764	-0.8584
60	4.6234	1.0212	5.5514	-0.8673
70	4.0344	1.0183	5.3005	-0.8737
80	3.6848	1.0148	4.2428	-0.8785
90	3.3578	1.0181	3.4806	-0.8822
100	3.0931	1.0172	2.9123	-0.8850
150	2.1789	1.0135	1.4550	-0.8941
200	1.7113	1.0149	0.8847	-0.8986
250	1.4706	1.0120	0.6008	-0.9010
300	1.3348	1.0111	0.2310	-0.9029

The energy of the corresponding open tubes is even less, for V-tubes (Table 1) approaching to the graphite sheet value (about (-) 1.85 kcal/mol).

Strain energy (per atom) is here defined as the difference between the energy of a torus minus the energy of the corresponding open tube. Strain energy was found proportional to the diameters ratio:

$$S = \frac{d}{D} \quad (3)$$

where d and D are given in number of hexes. Thus, the two series: H and V show different strain energy laws:

$$d_{HC_6[20,n]} = \frac{c}{2\pi}; \quad D_{HC_6[20,n]} = \frac{n}{\pi}; \quad S_{HC_6[20,n]} = \frac{c}{2n} \quad (4)$$

$$d_{VC_6[20,n]} = \frac{c}{\pi}; \quad D_{VC_6[20,n]} = \frac{n}{2\pi}; \quad S_{VC_6[20,n]} = \frac{2c}{n} \quad (5)$$

Despite this difference, the same trend appeared: the strain energy decreases by enlarging the torus central hollow (*i.e.*, by decreasing the d/D ratio). The excellent correlating equations given in Figure 5 support the strain energy as a function of d/D ratio.

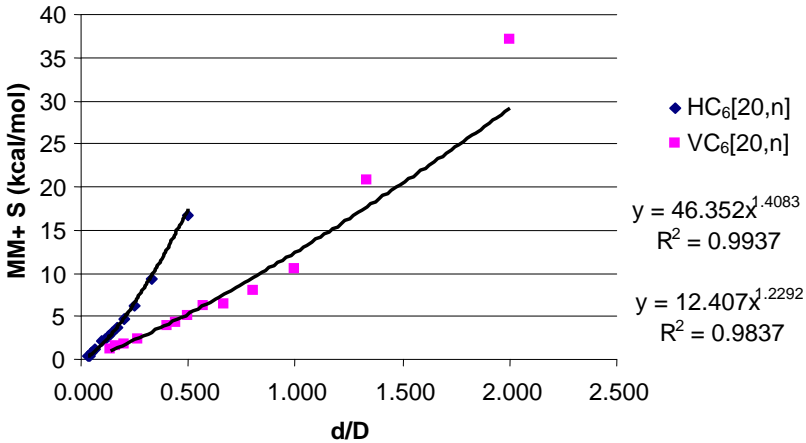


Figure 5. Plot of strain energy S vs the d/D ratio

The d/D dependency of the strain energy is in disaccord with that reported by Han²⁵ which found it to be a of $1/D^2$ (for a given tube dimension). The author reported the following features of polyhex toroids, as D increases:

- (i) a buckling tube (for $10\text{nm} < D < 20\text{ nm}$), with oscillating energy minima and migrating buckle position;
- (ii) an elliptic cross section tube (for medium D valued, *e.g.*, $D > 20\text{ nm}$, in case of torus (8,8)), as a transition state, and
- (iii) a perfect circular tube and an energetically stable torus (for higher D values).

In our approach, the same stages were observed. H-series approaches the circular cross-section shape at $HC_6[20,500]$ while in the V-series at $VC_6[20,1000]$, a normal result keeping in mind that the V-torus is twice thicker than the corresponding H-torus. Note that our tori are next huge objects ($20 \times 1000 = 20,000$ atoms) after the largest 30,000 atoms reported by Han, in his NAS report.²⁵

Figure 6 illustrates some different shapes of polyhex tori. Observe the "elongated" cross-section²⁶ in case of V-tori.

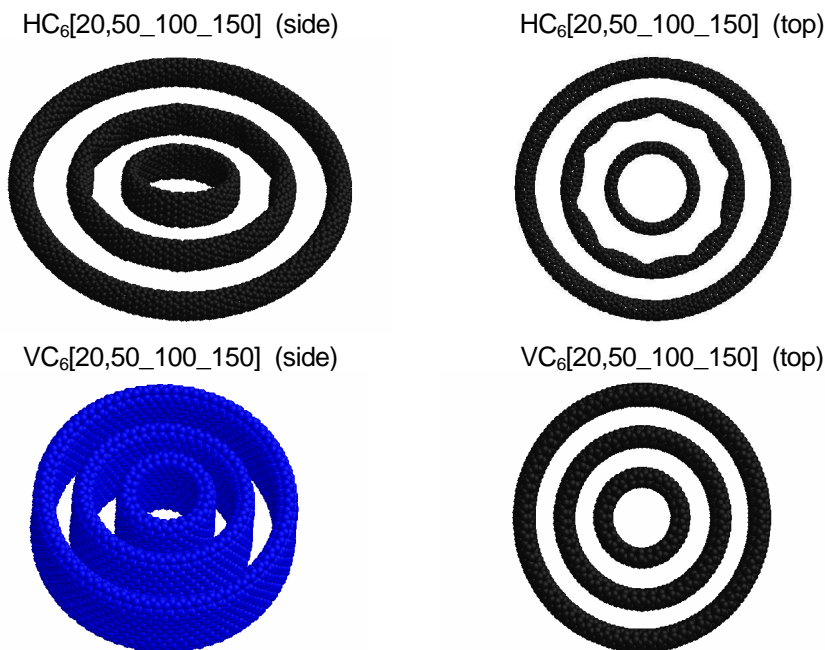


Figure 6. A collection of polyhex tori.

MM+ calculations have been performed on the HiperChem software package.²⁷

CONCLUSIONS

Generation of hex tori from square tori is a third major route, along with the graphite zone - folding and adjacency matrix eigenvectors methods. Our method is far more versatile, enabling various polygonal coverings.²⁸⁻³⁰

A d/D dependency of the strain energy obtained by us is in disaccord with the previously reported $1/D^2$ dependency. Very large polyhex toroids approach to the MM+ energy of graphite.

ACKNOWLEDGEMENT. This paper was supported by the Romanian CNCSIS GRANT 2003.

REFERENCES

1. L. Euler, *Comment. Acad. Sci. I. Petropolitanae*, **1736**, 8, 128-140.
2. J. Liu, H. Dai, J. H. Hafner, D. T. Colbert, R. E. Smalley, S. J. Tans, and C. Dekker, *Nature*, **1997**, 385, 780-781.
3. M. Ahlskog, E. Seynaeve, R. J. M. Vullers, C. Van Haesendonck, A. Fonseca, K. Hernadi, and J.B. Nagy, *Chem. Phys. Lett.*, **1999**, 300, 202-206.
4. R. Martel, H. R. Shea, and Ph. Avouris, *Nature*, **1999**, 398, 299-299.
5. R. Martel, H. R. Shea, and Ph. Avouris, *J. Phys. Chem., B*, **1999**, 103, 7551-7556.
6. D. Babić, D. J. Klein, and T. G. Schmalz, *J. Mol. Graphics Modell.*, **2001**, 19, 222-231.
7. A. Ceulemans, L. F. Chibotaru, and P. W. Fowler, *Phys. Rev. Lett.*, **1998**, 80, 1861-1864.
8. J. K. Johnson, B. N. Davidson, M. R. Pederson, and J. Q. Broughton, *Phys. Rev., B*, **1994**, 50, 17575-17582.
9. V. Meunier, Ph. Lambin, and A. A. Lucas, *Phys. Rev., B*, **1998**, 57, 14886-14890.
10. M. F. Lin and D. S. Chuu, *Phys. Rev., B*, **1998**, 57, 6731-6737.
11. E. C. Kirby, *Croat. Chem. Acta*, **1993**, 66, 13-26
12. E. C. Kirby, R. B. Mallion, and P. Pollak, *J. Chem. Soc. Faraday Trans.*, **1993**, 89, 1945-1953.
13. A. Ceulemans, L. F. Chibotaru, S. A. Bovin, and P. W. Fowler, *J. Chem. Phys.*, **2000**, 112, 4271-4278.
14. D. Marušić and T. Pisanski, *Croat. Chem. Acta*, **2000**, 73, 969-981.
15. D.J. Klein, *J. Chem. Inf. Comput. Sci.*, **1994**, 34, 453-459.
16. E. C. Kirby and P. Pollak, *J. Chem. Inf. Comput. Sci.*, **1998**, 38, 66-70.
17. T. Pisanski and J. Shawe-Taylor, *J. Chem. Inf. Comput. Sci.*, **2000**, 40, 567-571.
18. A. Graovac, D. Plavšić, M. Kaufman, T. Pisanski, and E. C. Kirby, *J. Chem. Phys.*, **2000**, 113, 1925-1931.
19. A. Graovac, M. Kaufman, T. Pisanski, E. C. Kirby, and D. Plavšić, *J. Chem. Phys.*, **2000**, 113, 1-7.
20. I.Laszlo, A. Rassat, P. W. Fowler, and A. Graovac, *Chem. Phys. Lett.*, **2001**, 342, 369-374.
21. M. V. Diudea and A. Graovac, *Commun. Math. Comput. Chem. (MATCH)*, **2001**, 44, 93-102.
22. M. V. Diudea, I. Silaghi-Dumitrescu, and B. Parv, *Commun. Math. Comput. Chem. (MATCH)*, **2001**, 44, 117-133.
23. M. V. Diudea and E. C. Kirby, *Fullerene Sci. Technol.*, **2001**, 9, 445-465.
24. M. V. Diudea, *Bull. Chem. Soc. Japan*, **2002**, 75, 487-492.
25. J. Han, *Chem. Phys. Lett.*, **1998**, 282, 187-191.
26. S. Itoh and S. Ihara, *Phys. Rev., B*, **1993**, 48, 8323-8328.
27. HyperChem [TM], release 4.5 for SGI, © 1991-1995, HyperCube, Inc.
28. M. V. Diudea, *Fullerenes, Nanotubes, Carbon Nanostruct.*, **2002**, 10, 273-292.
29. M. V. Diudea, *Phys. Chem., Chem. Phys.*, **2002**, 4, 4740-4746.
30. M. V. Diudea, B. Parv and E. C. Kirby, *Commun. Math. Comput. Chem. (MATCH)*, **2003**, 47, 53-70.

HEX TUBES FROM SQUARE TUBES

MIRCEA V. DIUDEA^{a*}, OLEG URSU^b and BAZIL PARV^c

^a Faculty of Chemistry and Chemical Engineering, Babes-Bolyai University, 3400 Cluj, Romania

^b Department of Chemistry, Cleveland State University 2121 Euclid Avenue, Cleveland, OHIO 44115 USA

^c Department of Computer Science, Faculty of Mathematics, Babes-Bolyai University, 3400 Cluj, Romania

ABSTRACT. Single wall nanotubes, covered by hexes can be generated from square tiled lattices, embedded on the cylinder. This route enables the "in silico" synthesis of a variety of tubes: crenelated (*i.e.*, armchair, or acenic), zig-zag (or phenacennic), as well as twisted (*i.e.*, chiral) objects. The energetic stability and topological characterization of such pure carbon lattices is discussed.

INTRODUCTION

Novel forms of carbon allotropes, besides ancient graphite and diamond, have been designed and obtained by condensing the vaporised graphite.¹ Finite molecular cages have been synthesised, characterised, functionalized or inserted into some supramolecular compounds.²⁻⁶ Besides the well known near-spherical fullerenes, cylinders, capped tubules and tori have aroused both theoretical and experimental interest.⁷⁻²³ Multi elemental large cages have also been studied.²⁴

This paper describes a novel way of generating single-walled nanotubes SWNTs, starting from square tiled cylinders. Several cutting procedures and transformations of the square nets are proposed in the view of obtaining chemically significant lattices. The stability of SWNTs, as given by the MM+ energy calculations, is discussed.

SQUARE AND HEX NET GENERATION

Covering a cylindrical surface by hexagons (and other polygons) is mainly achieved by the graphite zone-folding procedure, as follows.^{25,26}

A SWNT is generated by rolling up a graphite sheet (despite the metal nanoparticle catalyzed tube synthesis suggests a different way). The structural characteristics (diameter and helicity) are uniquely characterized by the roll-up vector $Ch = na + mb$ with a and b being the graphite net vectors and n, m

integers. The translation vector T follows the tube axis and is orthogonal to Ch . The rolled up area, delimited by T and Ch (Figure 1) corresponds to the repeat unit of an (n,m) chiral tube, (3,2) in this example. The limiting, achiral cases, $(n,0)$ zigzag or phenacenic, and (n,n) armchair or acenic, are drawn with dashed lines in Figure 1.

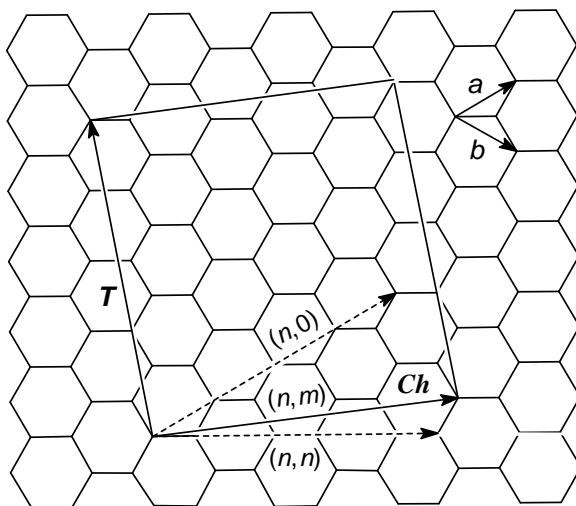


Figure 1. A graphite sheet with its net vectors a and b and the roll-up vector $Ch = na + mb$ and the translation vector T , along the tube axis and normal to Ch . The chiral (n,m) tube is actually a (3,2) tube. The achiral cases: $(n,0)$ zigzag and (n,n) armchair are indicated by dashed lines.

In our procedure, a cylindrical surface is covered by squares by moving a cross section c -fold polygon along the cylinder generator Figure 2,a). Next, bonds are alternatively removed in order to change the squares into hexagons. If the deleted edges laid *horizontally* (i.e., parallel to the cylinder generator) a standard HC_6 (i.e., a phenacenic) pattern results (Figure 2,b). If *vertical* edges are cut off, a standard VC_6 (i.e., an acenic) pattern is obtained (Figure 2,c). Several cutting procedures have been developed in this respect.¹⁹⁻²³

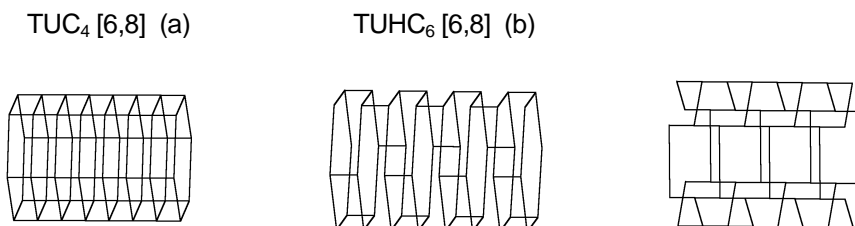


Figure 2. A square cylindrical net (a) and its derived HC_6 (b) and VC_6 (c) patterns.

After optimising by a molecular mechanics program, the polyhex nanotubes look like in Figure 3. The phenacenic (*i.e.*, HC_6 patterned) tube ends in "zig-zag" while the tips of the acenic (*i.e.*, VC_6 patterned) one are "crenelated" (or "armchair").

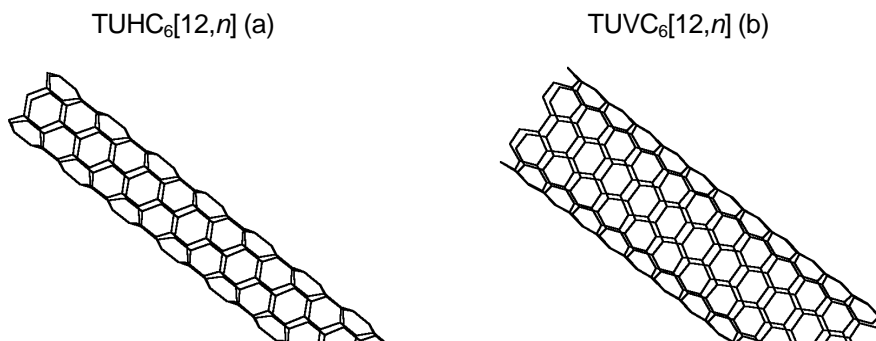


Figure 3. A phenacenic (*i.e.*, zigzag – (a)) and an acenic (*i.e.*, armchair) tube.

Note that, by cutting some edges within a torus, a spanning tube can be obtained. The name of a tube, *e.g.*, $TUHC_6[12,n]$, is derived from that of the original torus. The two first letters come from "tube", the third one specifies the type of cut edges, further letters and numbers denote the type of tiling. In brackets, the (combinatorial) dimensions of the net are given: c -fold cross-section polygon and n -slices of the cylinder. The number of points (*i.e.*, atoms) in the structure is $N = c \cdot n$.

Let's now switch the connections, in a horizontal row of squares, one edge to the right (or to the left – Figure 4, a). Next, cut horizontal (Figure 4, b) or vertical (Figure 4, c) edges in an alternating manner (see above). Twisted nets are thus obtained. Note that the number of switched rows must be even for a pure polyhex net.

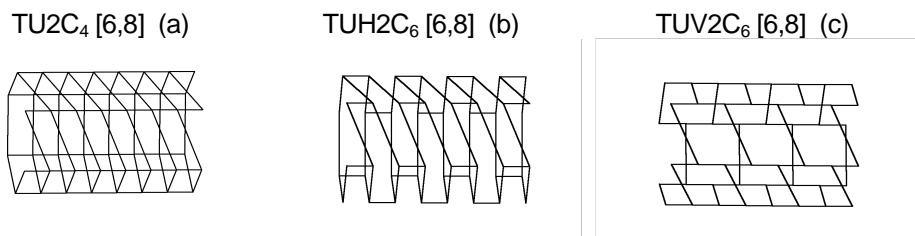


Figure 4. Cylindrical twisted nets, covered by: squares (a), H-hexes (b) and V-hexes (c)

After optimization, the polyhex tubular net is a chiral one (see below). The name of the twisted tubes is formed by adding, after the letter of cut type, the number of twisted rows t , *e.g.*, $TUVtC_6 [c,n]$.

A CHIRAL TUBE FAMILY: $TU\alpha C_6$ [12,60].

In the following, a family of twisted nanotubes is presented. First, their topology is given: number of hexes h , number of zig-zag's zz , and number of crenels cr . Also given are the length L and tube diameter d (in Angstroms - see Figures 5 and Table 1).

$TUVC_6$ [12,60]
 $L = 71.54$; $d = 8.04$; $h = 12$; $zz = 0$; $cr = 6$
 $TUHC_6$ [12,60]
 $L = 124.07$; $d = 4.71$; $h = 6$; $zz = 6$

$TUV2C_6$ [12,60]
 $L = 70.53$; $d = 8.04$; $h = 12$; $zz = 2$; $cr = 5$
 $TUH2C_6$ [12,60]
 $L = 120.93$; $d = 4.75$; $h = 7$; $zz = 7$

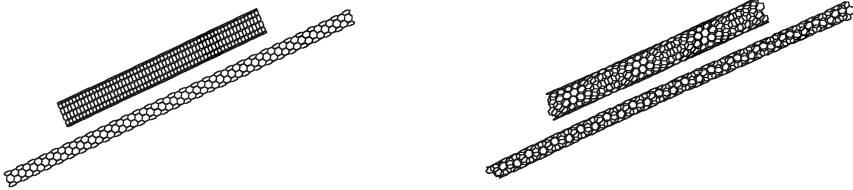


Figure 5. a.

$TUV4C_6$ [12,60]
 $L = 69.04$; $d = 8.18$; $h = 12$; $zz = 4$; $cr = 4$
 $TUH4C_6$ [12,60]
 $L = 110.20$; $d = 5.39$; $h = 8$; $zz = 8$

$TUV6C_6$ [12,60]
 $L = 67.97$; $d = 8.23$; $h = 12$; $zz = 6$; $cr = 3$
 $TUH6C_6$ [12,60]
 $L = 95.76$; $d = 6.14$; $h = 9$; $zz = 9$

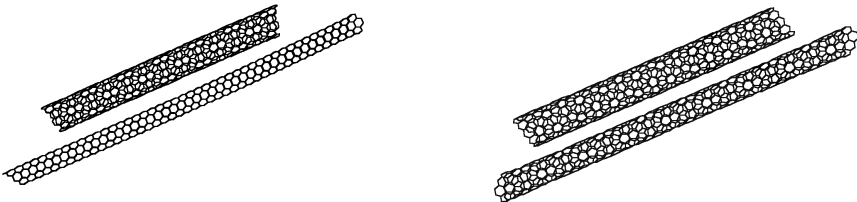


Figure 5. b.

$TUV8C_6$ [12,60]
 $L = 66.57$; $d = 8.57$; $h = 12$; $zz = 8$; $cr = 2$
 $TUH8C_6$ [12,60]
 $L = 81.92$; $d = 7.09$; $h = 10$; $zz = 10$

$TUV10C_6$ [12,60]
 $L = 63.68$; $d = 8.88$; $h = 12$; $zz = 10$; $cr = 1$
 $TUH10C_6$ [12,60]
 $L = 70.25$; $d = 8.13$; $h = 11$; $zz = 11$

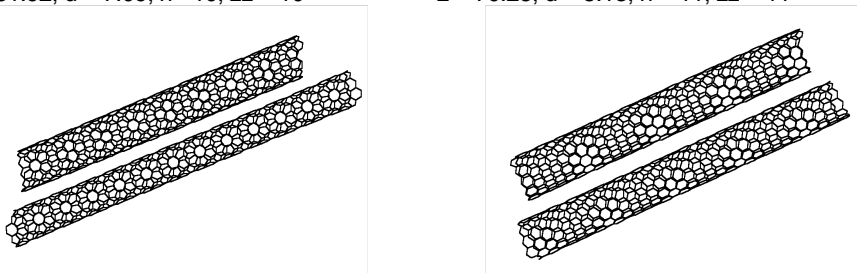


Figure 5. c.

HEX TUBES FROM SQUARE TUBES

TUV12C₆[12,60]
 L = 61.65; d = 9.26; h = 12; zz = 12; cr = 0
 TUH12C₆[12,60]
 L = 61.65; d = 9.26; h = 12; zz = 12

TUHC₆[24,30]
 L = 61.65; d = 9.26; h = 12; zz = 12

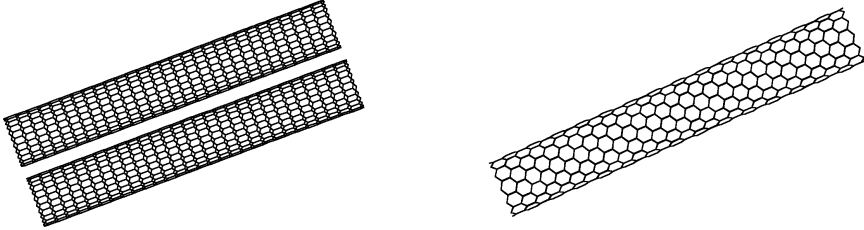


Figure 5. d.

At $t = c$, TUH t C₆ [c, n] switches the class of size (*i.e.*, becomes twice thick and half long), while TUV t C₆ [c, n] switches the class of cutting (becoming a H-cut tube).

Encoding the type of tessellation can be achieved by means of the ring spiral code.^{27,28} It was first proposed for coding and constructing spherical fullerenes. Diudea²⁹ proposed recently a modification, useful in tubular structures. In a periodic tubular net, the spiral code brings information on size and sequence of faces and embedding the actual net on the parent all-C₄ [c, n]. The spiral code for the polyhex tubes is given in Table 1. Also included in this table are the net parameters (for calculating, by the spiral code formulas, the number of hexes in the cross-section of twisted tubes - in general non-integer numbers, as exemplified in Table 2) as well as the number of zig-zags and crenels, as twisting feature data.

Table 1.

Formulas for the spiral code, net parameters and the number of zig-zags (crenels).

Tube	Spiral code	Net parameters	zz, {cr}
TUHC ₆ [c, n]	$[6_{c/2}]_{(n-1)}$	c, n	$c/2$
TUH t C ₆ [c, n]	$[(6_{c/2})_t]_{(n-1)/t}$	$c' = c/(1-t/2c)$ $n' = n(1-t/2c)$	$(c+t)/2$
TUV t C ₆ [c, n]	$[(6_c)_t]_{\{[n-(2+z)]+cz\}/2t}$	c, n $2c, n/2$	$t, \{(c-t)/2\}$
TUVC ₆ [c, n]	$[6_c]_{\{[n-(2+z)]+cz\}/2}$	c, n	$\{c/2\}$

$$z = \text{mod}(n, 2)$$

Table 2

Parameters of the TUH(V) t C ₆ [12,60] family						
No	t	c'	n'	Cut type	zz	k
[12,60]						
TUH t						
1	0	12	60	H	6	0
2	2	13.091	55	H	7	0
3	4	14.400	50	H	8	0

No	t [12,60]	c'	n'	Cut type	zz	k
4	6	16.000	45	H	9	0
5	8	18.000	40	H	10	0
6	10	20.571	35	H	11	0
7	12	24	30	H	12	0
TUV t						
8	0	12	60	V	0	6
9	2	12	60	V	2	5
10	4	12	60	V	4	4
11	6	12	60	V	6	3
12	8	12	60	V	8	2
13	10	12	60	V	10	1
14	12	24	30	H	12	0

MOLECULAR MECHANICS CALCULATIONS

Our TORUS software package enables generation of huge tubes, up to 20,000 atoms, which could be optimised by a molecular mechanics procedure (see Figures 5).

The energy calculated by MM+ force field (by HyperChem software package)³⁰ decreases as twisting t increases (Table 3). This energy (per atom) is plotted against t , with a rather good correlation (Figure 6).

Table 3

MM+ Energy E (Kcal·mol⁻¹) and Wiener index W in tubes TUH(V) t C₆[12,60]

t	MM+ E TUH t C ₆	W	MM+ E TUV t C ₆	W
0	3697.395	10416420	604.008	6009408
2	3384.387	9277724	585.336	5995628
4	2656.301	8314604	535.643	5953396
6	1814.103	7468448	458.833	5883634
8	1093.638	6724178	361.800	5789712
10	546.411	6083308	253.726	5677120
12	141.162	5553216	141.165	5553216

Compared with the MM+ energy of C₆₀ (about 4.454 kcal/mol – per atom value), it appears that the structure of twisted tubes (of the discussed family) quickly stabilise, as t increases, a fact confirmed by experimental data.²⁵

Note that both series TUH t C₆ and TUV t C₆ converge to one and the same structure: TUHC₆[24,30], which is a non-chiral nanotube, identical with the totally twisted tubes TUH12C₆[12,60] and TUH(V)12C₆[12,60] (see Tables 2 and 3). This identity holds (at least) for tubes having $n = pc$; $p = 1, 2, \dots$. The MM+ energy can be predicted, with good accuracy, from the topological distance count, also known as the Wiener index^{31,32} (see Table 3 and Figures 7 and 8).

HEX TUBES FROM SQUARE TUBES

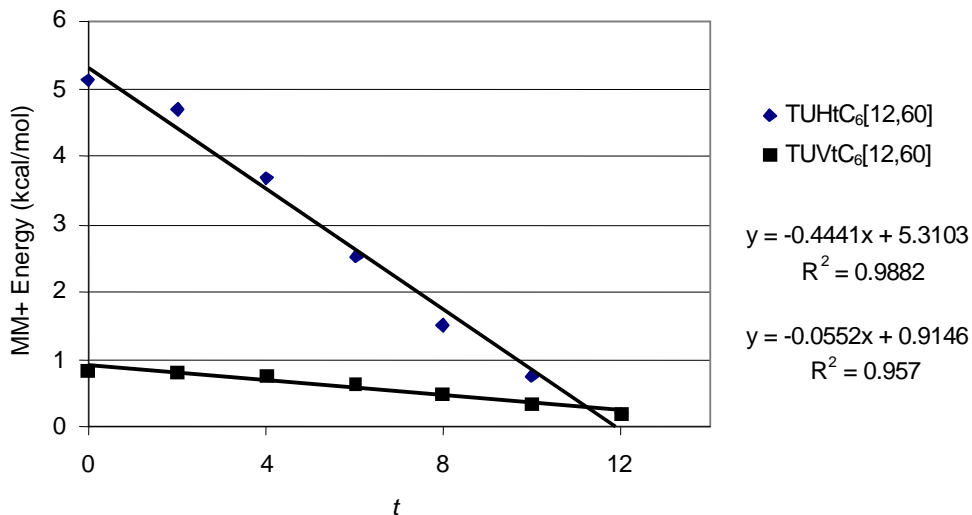


Figure 6. MM⁺ energy per atom vs twisting t in polyhex tubes

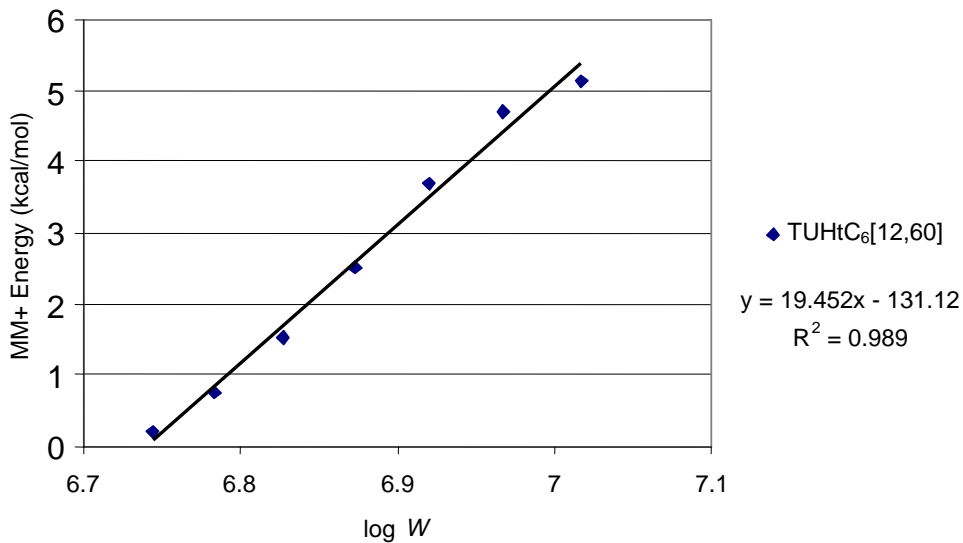


Figure 7. MM⁺ energy per atom vs $\log W$ in TUHtC₆[12,60] series

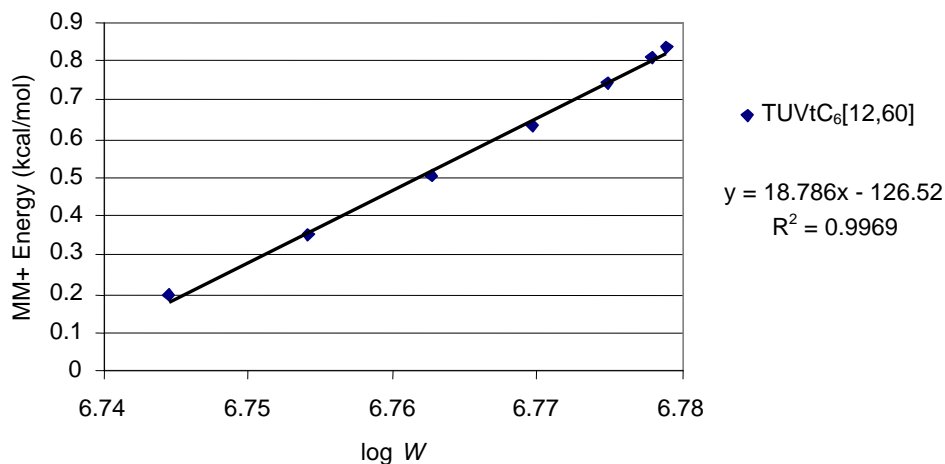


Figure 8. MM⁺ energy per atom vs log W in TUVtC₆[12,60] series

CONCLUSIONS

Generation of hex tubes from square tubes, proved to be a simple and versatile method. Topology and energetic stability of a family of chiral/twisted nanotubes was investigated.

By twisting, major changes in the tube topology occur: the tube becomes chiral and, at $t = c$, TUHtC₆ [c,η] switches the class of size, while TUVtC₆ [c,η] switches the class of cutting (becoming a H-cut tube).

Twisting induces a relaxation of the total MM⁺ energy of the polyhex tubular net.

MM⁺ energy can be predicted by a topological descriptor, such as the Wiener index, counting all the topological distances in a given graph. Analytical formulas for calculating this parameter were given elsewhere.^{33,34}

Acknowledgement. This paper was supported by the Romanian CNCSIS GRANT 2003.

REFERENCES

1. H. Kroto, *Fuller. Sci. Technol.*, **1994**, 2, 333-342.
2. H. Kroto, J. R. Heath, S. C. O'Brian, R. F. Curl, and R. E. Smalley, *Nature* (London), **1985**, 318, 162-163.

3. W. Kraetschmer, L. D. Lamb, K. Fostiropoulos and D. R. Huffman, *Nature* (London), **1990**, *347*, 354-358.
4. W. Qian and Y. Rubin, *Angew. Chem. Int. Ed.*, **2000**, *39*, 3133-3137.
5. K. Lee, Ch. H. Lee, H. Song, J. T. Park, H. Y. Chang and M.-G. Choi, *Angew. Chem. Int. Ed.*, **2000**, *39*, 1801-1804.
6. T. F. Fässler, R. Hoffmann, S. Hoffmann and M. Würle, *Angew. Chem. Int. Ed.*, **2000**, *39*, 2091-2094.
7. J. Liu, H. Dai, J. H. Hafner, D. T. Colbert, R. E. Smalley, S. J. Tans and C. Dekker, *Nature*, **1997**, *385*, 780-781.
8. M. Ahlskog, E. Seynaeve, R. J. M. Vullers, C. Van Haesendonck, A. Fonseca, K. Hernadi and J.B. Nagy, *Chem. Phys. Lett.*, **1999**, *300*, 202-206.
9. R. Martel, H. R. Shea and Ph. Avouris, *Nature*, **1999**, *398*, 299-299.
10. R. Martel, H. R. Shea and Ph. Avouris, *J. Phys. Chem., B*, **1999**, *103*, 7551-7556.
11. D. Babić, D. J. Klein and T. G. Schmalz, *J. Mol. Graphics Modell.*, **2001**, *19*, 222-231.
12. A. Ceulemans, L. F. Chibotaru and P. W. Fowler, *Phys. Rev. Lett.*, **1998**, *80*, 1861-1864.
13. J. K. Johnson, B. N. Davidson, M. R. Pederson and J. Q. Broughton, *Phys. Rev., B*, **1994**, *50*, 17575-17582.
14. E. C. Kirby, *Croat. Chem. Acta*, **1993**, *66*, 13-26
15. E. C. Kirby, R. B. Mallion and P. Pollak, *J. Chem. Soc. Faraday Trans.*, **1993**, *89*, 1945-1953.
16. A. Ceulemans, L. F. Chibotaru, S. A. Bovin and P. W. Fowler, *J. Chem. Phys.*, **2000**, *112*, 4271-4278.
17. D. Marušić and T. Pisanski, *Croat. Chem. Acta*, **2000**, *73*, 969-981.
18. E. C. Kirby and P. Pollak, *J. Chem. Inf. Comput. Sci.*, **1998**, *38*, 66-70.
19. M. V. Diudea and A. Graovac, *Commun. Math. Comput. Chem. (MATCH)*, **2001**, *44*, 93-102.
20. M. V. Diudea, I. Silaghi-Dumitrescu and B. Parv, *Commun. Math. Comput. Chem. (MATCH)*, **2001**, *44*, 117-133.
21. M. V. Diudea and E. C. Kirby, *Fullerene Sci. Technol.*, **2001**, *9*, 445-465.
22. M. V. Diudea, *Bull. Chem. Soc. Japan*, **2002**, *75*, 487-492.
23. M. V. Diudea, *Fullerenes, Nanotubes, Carbon Nanostruct.*, **2002**, *10*, 273-292.
24. A. Müller, P. Kögerler and Ch. Kuhlmann, *Chem. Commun.*, **1999**, 1347-1358.
25. T. W. Odom, J.-L. Huang, Ph. Kim and Ch. M. Lieber, *J. Phys. Chem. B.*, **2000**, *104*, 2794-2809.
26. A. L. Ivanovskii, *Russ. Chem. Rev.*, **1999**, *68*, 103-118.
27. D. E. Manolopoulos, J. C. May and S. E. Down, *Chem. Phys. Lett.*, **1991**, *181*, 105-111.
28. G. Brinkmann, P. W. Fowler and M. Yoshida, *Commun. Math. Comput. Chem. (MATCH)*, **1998**, *38*, 7-17.
29. M. V. Diudea, *Phys. Chem., Chem. Phys.*, **2002**, *4*, 4740-4746.

30. HyperChem [TM], release 4.5 for SGI, © 1991-1995, HyperCube, Inc.
31. H. Wiener, *J. Am. Chem. Soc.*, **1947**, *69*, 17-20.
32. M.V. Diudea; I. Gutman; L. Jäntschi, *Molecular Topology*, Nova Science, Huntington, New York, 2001.
33. P. E. John and M. V. Diudea, *Croat. Chem.Acta*, **2003** (submitted).
34. M. V. Diudea, M. Stefu, B. Parv and P. E. John, *Croat. Chem. Acta*, **2003** (submitted).

SMALL FULLEROIDS

MIRCEA V. DIUDEA^a and IOAN SILAGHI-DUMITRESCU^b

^{a, b} Faculty of Chemistry and Chemical Engineering
Babes-Bolyai University, 3400 Cluj, Romania
diudea@chem.ubbcluj.ro; isi@chem.ubbcluj.ro

ABSTRACT. Novel small fullerooids were "in silico" synthesized by enlarging some Archimedean well-known polyhedra. The energetic stability and topological characterization of such pure carbon cages is discussed.

INTRODUCTION

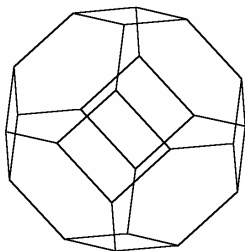
A fullerene is an all-carbon molecule in which the atoms are arranged on a pseudospherical framework made up entirely of pentagons and hexagons. "Nonclassical" extensions to include rings of other sizes have been considered^{1,2} and may be competitive in energy with the classical fullerenes.

The initial fascinating appeal, coming from their beautiful symmetry³⁻⁵ shifted later to real chemistry.⁶⁻⁸ Carbon allotropes with finite molecular cage structures have been functionalized or inserted in supramolecular assemblies.⁹⁻¹¹ Besides the well known near-spherical fullerenes, cylinders, capped tubules and tori have aroused both theoretical and experimental interest.¹²⁻²⁰ Multi elemental large cages have also been studied.²¹

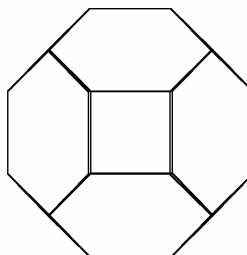
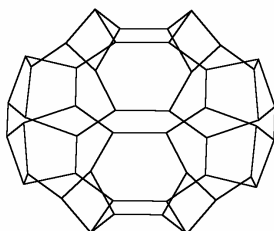
EXTENDED ARCHIMEDEAN CAGES

In addition to the earlier five Platonic polyhedra: the tetrahedron (T_d), cube (O_h), octahedron (O_h), dodecahedron (I_h), and icosahedron (I_h), other 13 elegant objects, resulting mainly by a truncation operation, are due to Archimede.²² Two of them attracted our attention: the truncated octahedron (O_h) and truncated cuboctahedron (O_h), (OT4 and COT4, respectively) in connection with some successful synthesis of phenylenes, organic compound having alternating sequence: C_4, C_6 .^{23,24}

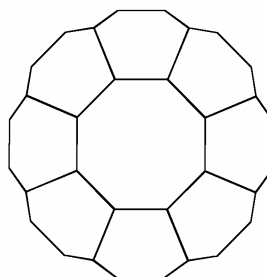
Our goal was the building of some cubic cages (*i.e.*, trivalent cages), originating in (or related to) the above two Archimedean objects, keeping in mind that the smallest cage obeying the "12 pentagon" definition of fullerenes is just the dodecahedron. Semiempirical AM1 calculations, performed by the HyperChem²⁵ software package, were aimed to give information on the energetic stability of such all-carbon cages, possibly appearing in the synthesis of fullerenes. By enlarging the polar ring from 4 up to 8, families of cages are generated. In the following we illustrate the cages and give semiempirical and spectral (see below) data in tables for each family.

OT4; (D_{4h}); $N = 24$ (side)

OT4 (top)

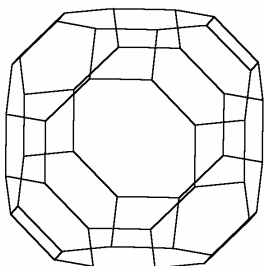
OT8; (D_{8h}); $N = 48$ 

OT8; (top)

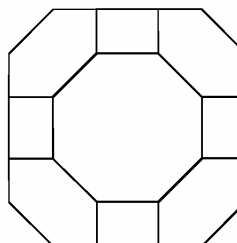


Cage	N	Sym.	AM1 HF/atom	AM1 GAP	Spectral Data				
					$\lambda_{N/2}$	$\lambda_{N/2+1}$	GAP	Shell	
1	OT5	30	D_{5h}	33.044	6.4437	0.4772	-0.4142	0.8914	PC
2	OT6	36	D_{6h}	35.068	6.5199	0.4142	-0.4142	0.8284	PC
3	OT7	42	D_{7h}	45.213	2.5661	0.3922	-0.4142	0.8064	PC
4	OT8	48	D_{8h}	47.584	-	0.4142	-0.4142	0.8284	PC

PC = properly closed shell

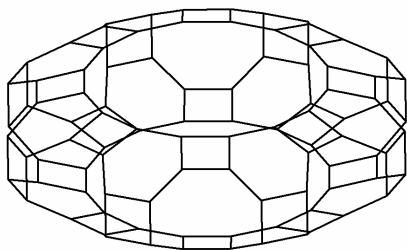
COT4; (C_{4h}); $N = 48$ (side)

COT4 (top)

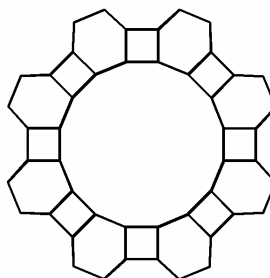


SMALL FULLEROIDS

COT8; (C_{8h}); $N = 96$ (side)



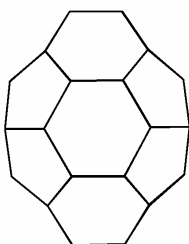
COT8 (top)



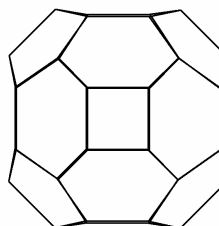
	Cage	N	Sym.	AM1 HF/atom	AM1 GAP	Spectral Data			
						$\lambda_{N/2}$	$\lambda_{N/2+1}$	GAP	Shell
1	COT5	60	C_{5h}	29.275	1.6354	0	0	0	OP
2	COT6	72	C_{6h}	28.907	5.6600	0	0	0	M
3	COT7	84	C_{7h}	30.934	5.4804	0	0	0	OP

OP = open shell; M = metallic shell

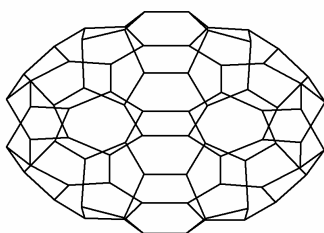
A554; (C_{4h}); $N = 40$ (side)



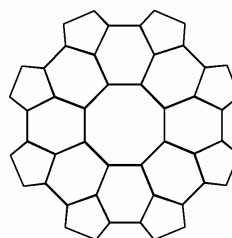
A554 (top)



A558; (C_{2v}); $N = 80$ (side)

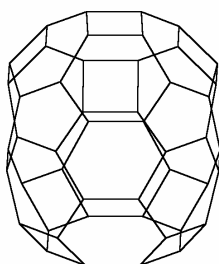


A558 (top)

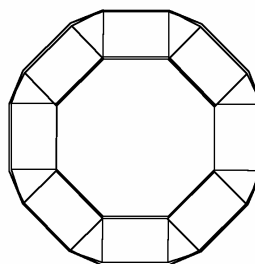
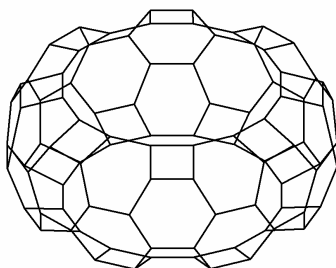


	Cage	N	Sym.	AM1 HF/atom	AM1 GAP	Spectral Data			
						$\lambda_{N/2}$	$\lambda_{N/2+1}$	GAP	Shell
1	A555	50	C_s	20.425	4.8581	0.4142	0.3111	0.1031	PSC
2	A556	60	C_{2h}	20.379	5.5507	0.4142	0.3111	0.1031	PSC
3	A557	70	C_1	24.076	6.0451	0.4142	0.3111	0.1031	PSC
4	A558	80	C_{2v}	30.134	6.6226	0.4142	0.3111	0.1031	PSC

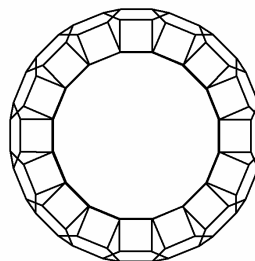
PSC = pseudoclosed shell

COTX4; (S_8); $N = 48$ (side)

COTX4 (top)

COTX8; (S_{16}); $N = 96$ (side)

COTX8 (top)



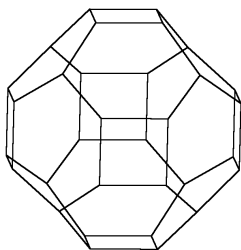
This family is derived from COT by a twist-1 coupling.

	Cage	N	Sym.	AM1 HF/atom	AM1 GAP	Spectral Data			
						$\lambda_{N/2}$	$\lambda_{N/2+1}$	GAP	Shell
1	COTX5	60	S_{10}	24.591	4.9335	0	0	0	OP
2	COTX6	72	S_{12}	24.891	4.6341	0	0	0	OP
3	COTX7	84	S_{14}	26.000	4.3729	0	0	0	OP

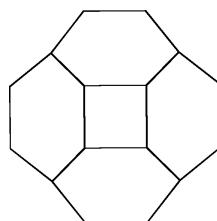
OP = open shell

SMALL FULLEROIDS

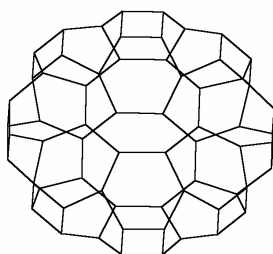
AA4; (D_{4h}) $N = 32$ (side)



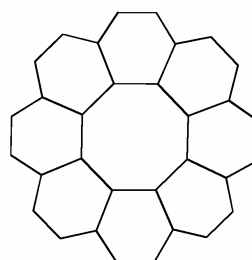
AA4 (top)



AA8; (D_{8h}); $N = 64$ (side)



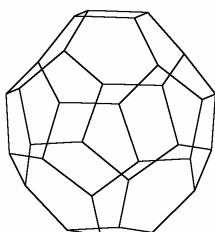
AA8 (top)



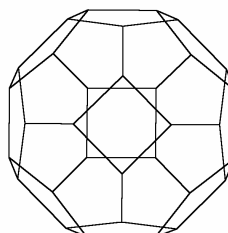
Cage	N	Sym.	AM1 HF/atom	AM1 GAP	Spectral Data			Shell	
					$\lambda_{N/2}$	$\lambda_{N/2+1}$	GAP		
9	AA5	40	D_{5h}	30.202	3.3198	0.2056	0	0.2056	PC
10	AA6	48	C_i	30.949	5.2355	0	0	0	OP
11	AA7	56	D_{7h}	39.484	1.8858	-0.0612	-0.0612	0	OP
12	AA8	64	D_{8h}	43.246	5.8994	0	0	0	M

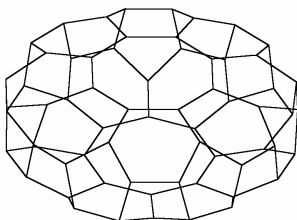
PC = properly closed shell; OP= open shell; M = metallic shell

AAX4; $N = 32$ (side)

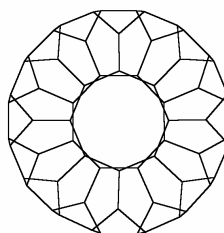


AAX4 (top)



AAX8; (D_8); $N = 64$ (side)

AAX8 (top)

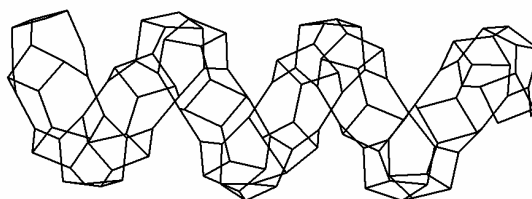


Note that this family is obtained by a twist -1 coupling performed on the above AA family.

Cage	N	Sym.	AM1 HF/atom	AM1 GAP	Spectral Data				
					$\lambda_{N/2}$	$\lambda_{N/2+1}$	GAP	Shell	
1	AAX5	40	C_1	24.311	2.1470	0.4865	0.1133	0.3732	PSC
2	AAX6	48	D_6	25.789	6.1145	0.4142	0.2007	0.2135	PSC
3	AAX7	56	D_{7d}	31.374	6.6641	0.4856	0.1851	0.3005	PSC
4	AAX8	64	D_8	38.821	6.9308	0.4444	0.1559	0.2885	PSC

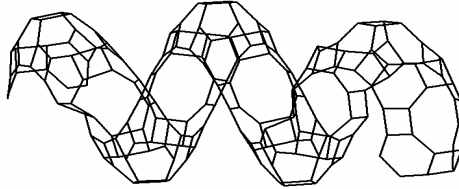
PSC = pseudo closed shell

In cages with larger polar rings, the strain is so high that a cross-section cutting results in more stable spiral objects (see the two spirals, corresponding to the OT and COT families). This tendency appears by examination of the semiempirical data: an increase in the heat of formation, in going to larger polar rings, is observed. Spiral structures have been reported by the group of Volhardt.^{23,24}

OT11spiral, $N = 132$;

SMALL FULLEROIDS

COT16 spiral; $N = 192$



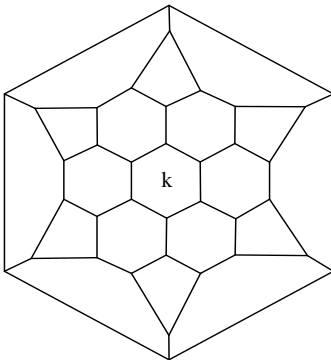
SCHLEGEL PROJECTION OF RELATED ARCHIMEDEAN CAGES

A graph is said to be embedded in a surface S when it is drawn on S so that no two edges intersect.²⁶ A graph is planar if it is embeddable in the plane (or in the sphere). Any spherical polyhedron obeys the Euler theorem:²⁷

$$V - E + F = 2 \quad (1)$$

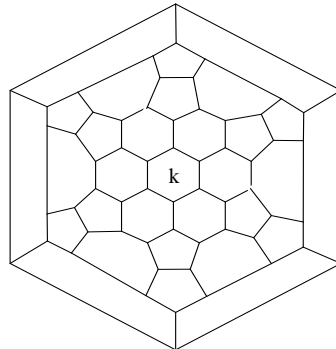
The graph associated to a polyhedron, consisting of its vertices V , edges E and faces F , is a planar map, and clearly satisfies relation (1). Thus, a polyhedron can be drawn on the plane as a Schlegel projection. We use this representation in the case of our extended Archimedean polyhedra, as illustrated below. In the top of each Schlegel diagram, the point group symmetry and spiral code^{28,29} are given. The spiral sequence starts from the polar ring (of size k) and finishes to the opposite pole.

$OTk; (D_{kh})$
 $k 6_k (4 6)_k k$



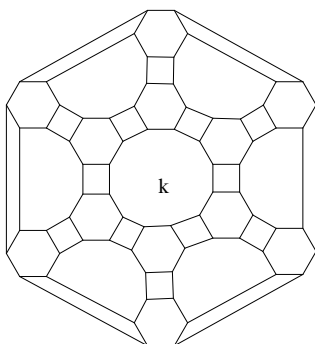
$COTk; (C_{kh})$

$A55k; k = 5; 6$ (fullerene)
 $k 6_k (5 6)_k (5 6)_k k$

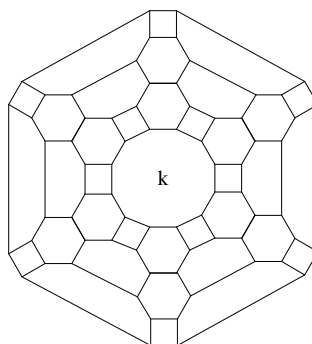


$COTXk; (S_{2k})$

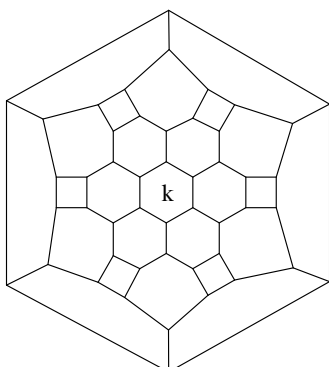
$2k(4\ 6)_k(4\ 8)_k(4\ 6)_k2k$



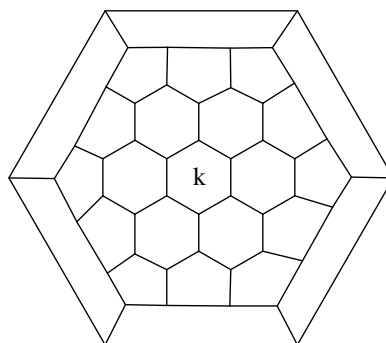
$2k(4\ 6)_k(6\ 6)_k(4\ 6)_k2k$



$AAk; (D_{kh})$
 $k6_k(4\ 6)_k6_kk$



$AAXk; k = 5; 6$ (fullerene); (D_k)
 $k6_k5_{2k}6_kk$



DISCUSSION

The semiempirical data indicate an increase in the heat of formation in going to larger polar rings. The cross-section cut performed on such cages leads to spiral objects. Spiral structures have already been synthesized in phenylenes.

The topology of polyhedral cages herein designed could be rationalised by the spiral code.^{28,29} the polar ring size k is the generalizing parameter.

Some of the proposed polyhedra belong to the classical fullerenes: $A55k; k = 5; 6$ ($A555, N = 50, HF = 20.425$ kcal/mol; $A556, N = 60, HF = 20.379$ kcal/mol) and $AAXk; k = 5; 6$ ($AAX5, N = 40, HF = 24.311$ kcal/mol; $AAX6, N = 50, HF = 25.789$ kcal/mol). Their AM1 HF is, however, far from that of C_{60} , of 16.208 kcal/mol.

The HOMO-LUMO gap is a measure of the kinetical stability; a value around 6 eV would be satisfactory. This desiderate is approached by the $k = 6$ members of the studied objects. In the spectral theory,³⁰ the type of the band gap is used to classify the π -electronic shell of the molecules: properly closed shells are expected for the isolable fullerenes, such as C_{60} .

From the above data, it appears that none of the extended Archimedean cages can be considered candidates to the real fullerene status.

CONCLUSIONS

Two of the Archimedean polyhedra: the truncated octahedron (O_h) and truncated cuboctahedron (O_h), have been extended in view of finding information on the thermodynamic and kinetic stability of the derived polyhedra (some of them having alternating sequence: C_4 , C_6 , as in phenylenes). Related polyhedral cages have also been designed. The conclusion of this study is the following: even the modelled cages hardly compete the already synthesized C_{60} molecule, but they can be useful in understanding the possibility of synthesis of some non-classical fullerenes and/or related structures.

Acknowledgement. This paper was supported by a Romanian CNCSIS Grant, 2003.

REFERENCES

1. Y. D. Gao and W. C. Herndon, *J. Amer. Chem. Soc.* **1993**, *115*, 8459-8460.
2. P. W. Fowler, T. Heine, D. E. Manolopoulos, D. Mitchell, G. Orlandini, R. Schmidt, G. Seiferth and F. Zerbetto, *J. Phys. Chem.* **1996**, *100*, 6984-6991.
3. H. Kroto, *Fuller. Sci. Technol.* **1994**, *2*, 333-342.
4. R. B. King, *Croat. Chem. Acta*, **2000**, *73*, 993-1015.
5. H. Hosoya and Y. Tsukano, *Fuller. Sci. Technol.*, **1994**, *2*, 381-393.
6. H. Zorc, Lj. P. Tolić, S. Martinović and D. Srzić, *Fuller. Sci. Technol.*, **1994**, *2*, 471-480.
7. F. Diedrich and C. Thilgen, *Science*, **1996**, *271*, 317-323.
8. I. S. Neretin, K. A. Lyssenko, M. Yu. Antipin, Yu. L. Slovokhotov, O. V. Boltalina, P. A. Troshin, A. Yu. Lukonin, L. N. Sidorov and R. Taylor, *Angew. Chem. Int. Ed.*, **2000**, *39*, 3273-3276.
9. W. Qian and Y. Rubin, *Angew. Chem. Int. Ed.*, **2000**, *39*, 3133-3137.
10. K. Lee, Ch. H. Lee, H. Song, J. T. Park, H. Y. Chang and M.-G. Choi, *Angew. Chem. Int. Ed.*, **2000**, *39*, 1801-1804.
11. T. F. Fässler, R. Hoffmann, S. Hoffmann and M. Würle, *Angew. Chem. Int. Ed.*, **2000**, *39*, 2091-2094.

12. J. Liu, H. Dai, J. H. Hafner, D. T. Colbert, R. E. Smalley, S. J. Tans and C. Dekker, *Nature*, **1997**, *385*, 780-781.
13. M. Ahlskog, E. Seynaeve, R. J. M. Vullers, C. Van Haesendonck, A. Fonseca, K. Hernadi and J.B. Nagy, *Chem. Phys. Lett.*, **1999**, *300*, 202-206.
14. R. Martel, H. R. Shea and Ph. Avouris, *Nature*, **1999**, *398*, 299-299.
15. R. Martel, H. R. Shea and Ph. Avouris, *J. Phys. Chem., B*, **1999**, *103*, 7551-7556.
16. M. V. Diudea and A. Graovac, *Commun. Math. Comput. Chem. (MATCH)*, **2001**, *44*, 93-102.
17. M. V. Diudea, I. Silaghi-Dumitrescu and B. Parv, *Commun. Math. Comput. Chem. (MATCH)*, **2001**, *44*, 117-133.
18. M. V. Diudea and E. C. Kirby, *Fullerene Sci. Technol.*, **2001**, *9*, 445-465.
19. M. V. Diudea, *Bull. Chem. Soc. Japan*, **2002**, *75*, 487-492.
20. M. V. Diudea, *Fullerenes, Nanotubes, Carbon Nanostruct.*, **2002**, *10*, 273-292.
21. A. Müller, P. Kögerler and Ch. Kuhlmann, *Chem. Commun.*, **1999**, 1347-1358.
22. La Vaissière, P. W. Fowler and M. Deza, *J. Chem. Inf. Comput. Sci.* **2001**, *41*, 376-386.
23. S. Han, A. D. Bond, R. L. Disch, D. Holmes, J. M. Schulman, S. J. Teat, K. P.C. Vollhardt and G. D. Whitener, *Angew. Chem.*, **2002**, *36*, 3357-3361.
24. S. Han, D. R. Anderson, A. D. Bond, H. V. Chu, R. L. Disch, D. Holmes, J. M. Schulman, S. J. Teat, K. P.C. Vollhardt and G. D. Whitener, *Angew. Chem.*, **2002**, *36*, 3361-3364.
25. HyperChemTM, Release 4.5 for SGI, © 1991-1995, HyperCube, Inc
26. F. Harary, *Graph Theory*, Addison-Wesley, Reading, MA, **1969**, p. 102.
27. L. Euler, *Comment. Acad. Sci. I. Petropolitanae*, **1736**, *8*, 128-140
28. P. W. Fowler and K. M. Rogers, *J. Chem. Inf. Comput. Sci.*, **2001**, *41*, 108-111.
29. G. Brinkmann and P. W. Fowler, *J. Chem. Inf. Comput. Sci.* **1998**, *38*, 463-468.
30. P. W. Fowler and T. Pisanski, *J. Chem. Soc., Faraday Trans.*, **1994**, *90*, 2865-2871.

THE "ZIG-ZAG" CYLINDER RULE

MIRCEA V. DIUDEA^a

^a Faculty of Chemistry and Chemical Engineering
Babes-Bolyai University, 3400 Cluj, Romania

ABSTRACT. Spectral data revealed some cluster properties of tubulenes. The "zig-zag" cylinder rule on the π -electronic structure states that properly closed shell exists in two complementary series of fullerenes derived from the $13k$ cluster, $k = 4m; 4m+2$, $m = 1, 2, \dots$, by adding a $3kn$, $n = 1, 2, \dots$, nanotube distancer between the two zig-zag ended caps. Semiempirical calculations support this finding.

INTRODUCTION

A fullerene is, according to a classical definition, an all-carbon molecule consisting entirely of pentagons (exactly 12) and hexagons ($N/2-10$).¹ Besides the well known near-spherical fullerenes, open ended nanotubes, capped tubules and tori have aroused both theoretical and experimental interest.²⁻¹⁰ Non-classical fullerene extensions to include rings of other sizes have been considered.^{11,12} Multi elemental large cages have also been studied.¹³

In simple π -only Hückel theory, the energy of the i^{th} molecular orbital $E_i = \alpha + \lambda_i \beta$ is calculated on the ground of the adjacency matrix associated to the molecular hydrogen depleted graph. Systematic studies on this matrix and their eigenvalue spectra (*i.e.*, the decreasing sequence of eigenvalues λ_i), provided some magic number rules for the stability of molecules, such as the oldest Hückel¹⁴ $4n+2$ rule for aromatic rings and the more recent $60 + 6m$ ($m \neq 1$) *leapfrog* rule¹⁵ for the properly closed fullerenes (see also ref. 16).

The π -electronic shells of neutral fullerenes are classified, function of their eigenvalue spectra, as:¹⁷ (i) *properly closed*, PC, when $\lambda_{N/2} > 0 \geq \lambda_{N/2+1}$; (ii) *pseudo-closed*, PSC, in case $\lambda_{N/2} > \lambda_{N/2+1} > 0$; (iii) *meta-closed*, MC, with $0 \geq \lambda_{N/2} > \lambda_{N/2+1}$ and (iv) *open*, OP, when the $N/2^{\text{th}}$ (HOMO) and $N/2+1^{\text{th}}$ (LUMO) molecular orbitals are degenerate, $\lambda_{N/2} = \lambda_{N/2+1}$. The bandgap is taken as the absolute value of the difference $E_{\text{HOMO}} - E_{\text{LUMO}}$. The most frequent case is that of the pseudo-closed shell, since the number of positive eigenvalues is, in general, larger than that of the negative ones, $n_+ \geq n_-$.¹⁸

The other rule predicting closed-shell fullerenes is the *cylinder rule*.^{19,20} Fullerenes with k -fold cylindrical symmetry, of general formula $C_{N,k-V[2k,\eta]-[6]}$, have a closed shell at each nuclearity $N = 2k(7 + 3m)$, $m = 0, 1, 2, \dots$, ($k = 4$ to 7 in this paper). These cages have a non-degenerate non-bonding orbital (NBO) LUMO separated by a gap from HOMO; in this case $n_+ = 1 + n_-$. Exceptions exist, e.g., the first term of series $k = 6$, $C_{72,6-V[2k,1]-[6]}$, has LUMO triply degenerate, and the first term of series $k = 7$, $C_{84,7-V[2k,1]-[6]}$, has its NBO not the LUMO (actually is $\lambda_{N/2+3}$).

The cylinder rule, better called the "armchair" cylinder rule, can equivalently be written, in distancing tube dimension, as: $n = 1 + 3m$.

Recall that, our notations for nanotubes $TUVC_6[c,\eta]$ and $TUHC_6[c,\eta]$ correspond to the "armchair" ($c/2, c/2$) and "zig-zag" ($c/2, 0$), respectively.

This paper describes a further investigation of fullerenes with the aim of finding some novel rules of their electronic stability.

TUBULENES BY "ZIG-ZAG" NANOTUBE DISTANCER

A spherical fullerene, say C_{60} (I_h), can provide a cap suitable for joining an armchair nanotube (i.e., a $TUVC_6$); the cap, having a k -fold polar ring, will be denoted by $C_{N,k-V[2k,0]}$ with N being the number of atoms in the parent fullerene. In a fullerene cluster the polar ring can vary, in our work most often $k = 4, 5, 6, 7$ (with the main term at $k = 5$). The cap $C_{N,k-V[2k,0]}$ can be used in generating a cluster of tubulenes by using a TUV distancer. The procedure is illustrated in Figure 1. This is the cluster $C_{N,k-V[2k,\eta]-[6]}$, obeying the armchair cylinder rule (initially defined for $k = 5; 6$).¹⁹

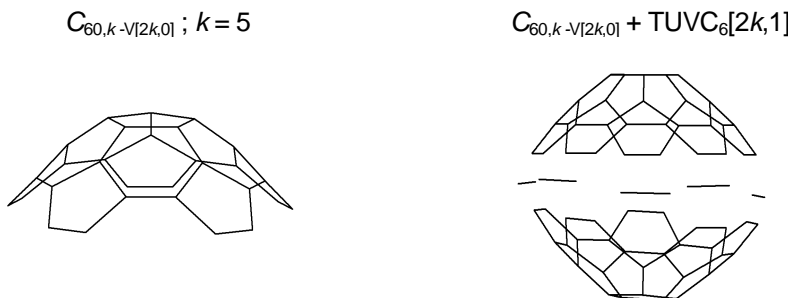


Figure 1. "Armchair" tubulene construction

THE "ZIG-ZAG" CYLINDER RULE

$$C_{72,k-V[2k,0]} + \text{TUVC}_6[2k,3]; k = 6$$

$$C_{18k}$$

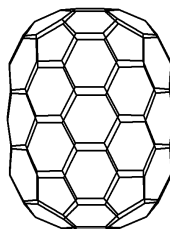
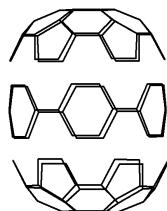
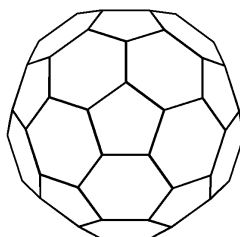
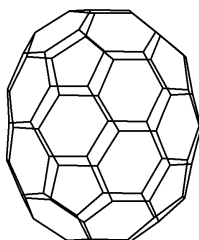


Figure 1. (continued)

The first term of the sub-cluster $C_{60,5-V[10,1H6]}$ is just the isolated fullerene C_{70} (see below). Its topology is given as the spiral code.^{21,22} We amended this code by specifications for the mode of inserting the new polygon, either by an edge (*e*) or by an angle (*a*).

$$C_{60,5-V[10,1H6]} = C_{70}$$

$$C_{70}; (\text{top})$$



$$k, 6k, (a5, e6)k, (e6, e6)k, (a5, e6)k, k$$

$$k = 4; 5; 6; 7$$

$$\text{Cluster } C_{14k}, k = 4; 5; 6; 7$$

$$N = 14k; 56; 70; 84; 98$$

A different cap, denoted $C_{N,k-H[2k,0]}$, is that favoring the coupling with a zig-zag nanotube (*i.e.*, TUHC_6).²⁰ Figure 2 gives such an example.

$$2(C_{60,5-H[10,0]}) + \text{TUHC}_6[10,2]$$

$$C_{60,5-H[10,3H7.6.7]}$$

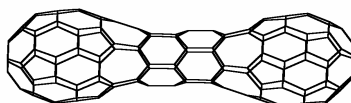
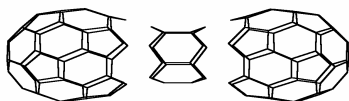
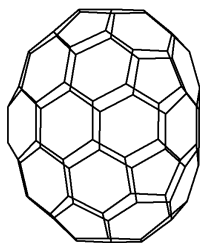


Figure 2. "Zig-zag" tubulene construction

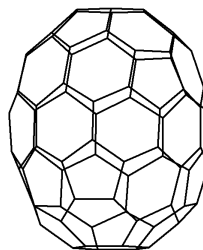
A tubulene $C_{N,k-V[2k6]-[6]}$ can be viewed as originating in the coalescence product of two spherical fullerenes, namely the $C_{N,k-H[2k,1]-[7]}$, from which it results by a series of Stone-Wales^{23,24} edge flipping. Similar coalescence reactions between spherical cages and nanotubes have been considered.²⁵

Resuming to the nomenclature, the *C* letter (*i.e.*, cage) is followed by the number of atoms N of the parent fullerene, having a k -fold polar ring, the cap being attached to a $V/H[c,n]$ tube (with a cross-section of c atoms, and n atom rows distancing the two caps; $n = 0$ for the cap, only). The numbers in the last brackets denote the tiling polygons in the region between the two caps.

A quite different cap $C_{N,k-H[c,0]}$ is provided by the isolated fullerene C_{78} , the two of its IP (*i.e.*, isolated pentagon) isomers being given below.

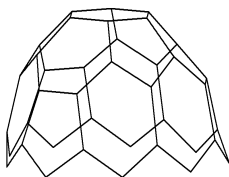
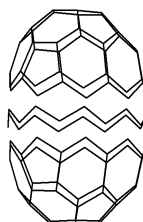
 $C_{78a}; C_S$ 

$$k, (5, 6)k/2, (a6, a6, e5)k/2, (a6)k, \\ (e5, a6, a6)k/2, (6, 5)k/2, k \\ k = 6$$

 $C_{78c}; C_1$ Cluster C_{13k} , $k = 4; 6; 8; 10$

$$N = 13k, \quad 52; \quad 78; \quad 104; \quad 130$$

The formal building of the related tubulenes is illustrated in Figure 3.

 $C_{78,k-H[3k,0]}; k = 6$  $C_{78,k-H[3k,0]} + \text{TUHC}_6[3k,1]$  $C_{78,k-H[3k,0]} + \text{TUHC}_6[3k,2]$ $C_{78,k-H[3k,2]-[6]} = C_{19k}; k = 6$

THE "ZIG-ZAG" CYLINDER RULE



Figure 3. "Zig-zag" tubulenes derived from C_{78}

SPECTRAL PROPERTIES OF THE NOVEL CLUSTER

The zig-zag tubulenes derived from the cluster C_{13k} form a properly closed shell tubulene cluster with the general formula $C_{13k, k+H[3k, n]-[6]}$ and the following construction $N = 13k + 3kn; k = 4m + 2z; m = 1, 2, \dots; z = 0, 1; n = 1, 2, \dots$. It shows the same bandgap for a given z value at each positive n . The last parameter is just the n -dimension of the distancing tube and it discriminates between the twin odd and even sub-clusters (see Figures 4 and 5).

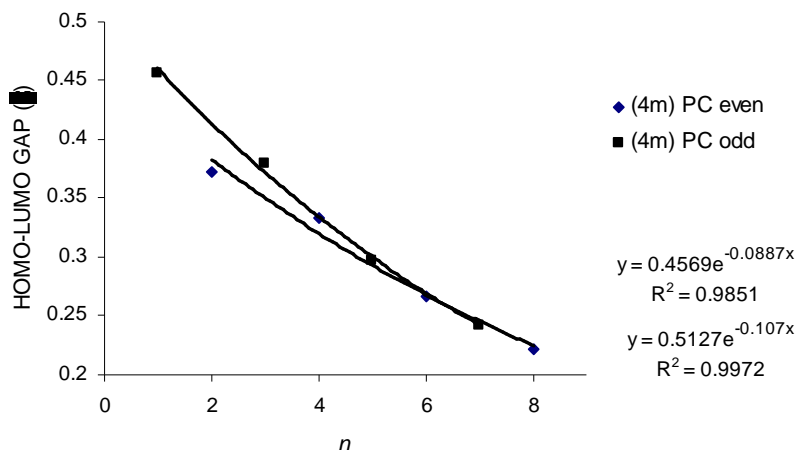


Figure 4. The plot of the spectral gap vs. n , in the series $k = 4m$

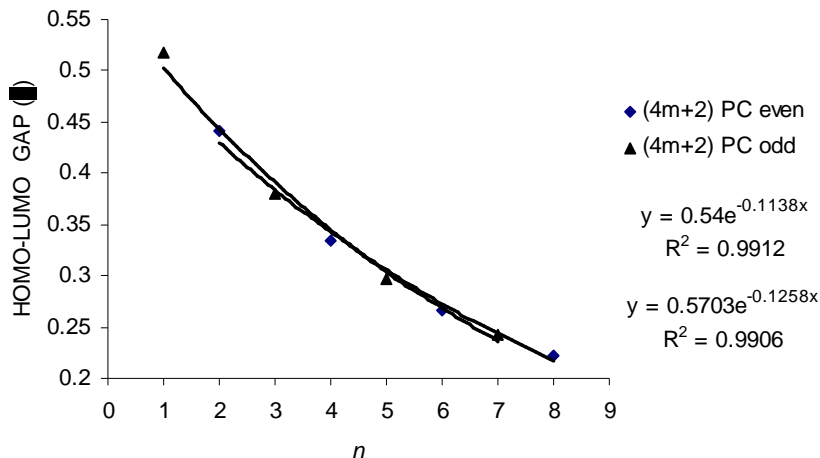


Figure 5. The plot of the spectral gap vs. n , in the series $k = 4m+2$

In the opposite to the 1st (armchair) cylinder rule, the terms for $n = 0$ do not (properly) belong to the new cluster. In the series $k = 4m$, LUMO is an NBO (not encountered at higher n -values) while in the series $k = 4m+2$, the gaps are different for different m -values. The identity of the gaps appears only at $n > 0$. Figure 6 gives the repeating units of the twin sub-clusters, in the so-called geodesic projection.

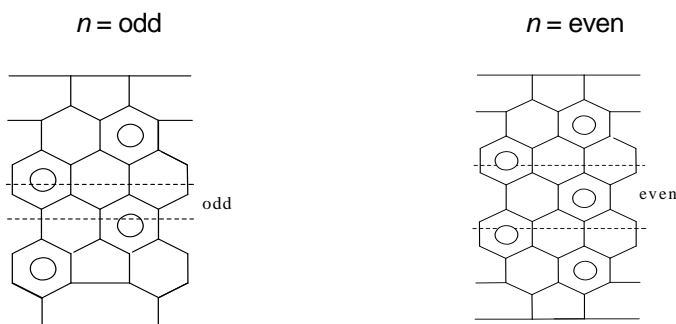


Figure 6. Geodesic projection of the repeating units of the twin sub-clusters with the general formula $C_{13k,k-H[3k,\eta]-[6]}$

The novel cluster $C_{13k,k-H[3k,\eta]-[6]}$, of properly closed shell fullerenes, having $N = 13k + 3kn$; $n = 1, 2, \dots$ and equal number of positive and negative eigenvalues $n_+ = n_-$, we call *the zig-zag cylinder rule*, to specify the type of the tube distancing the two caps. This cluster does not superimpose over the

leapfrog^{15,18,19} (properly closed-shell) fullerenes with the exception of the cages having $k = 6$. The spectral data are supported by semiempirical calculations (see Table 1).

In going from one sub-cluster to the other, complementary (twisted) series of pseudo-closed shell tubulenes appear. Figure 7 shows the plots of PSC and PC series corresponding to $k = 6$ (viewed as single odd&even series). Clearly, the gap is deeper for the PC series, suggesting a higher kinetic stability of the corresponding tubulenes. Note that the term $n = 0$ in PSC is just the $C_{78}C_1$; C_1 (see above).

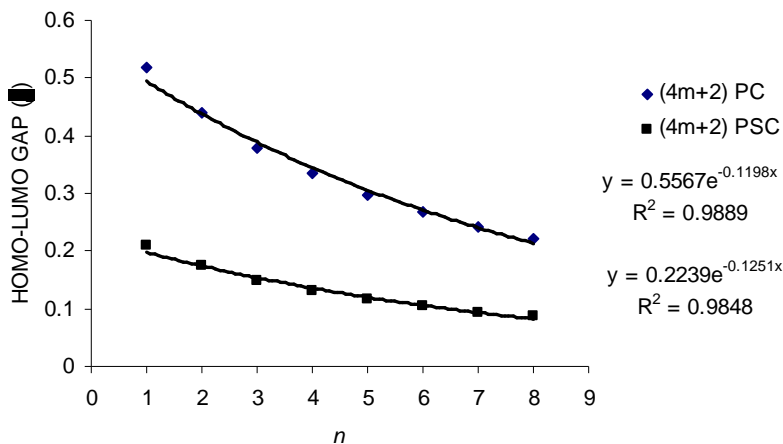


Figure 7. Comparison between the PSC and PC series corresponding to $k = 6$

In the case of objects with formula $C_{N,k-H[2k,n]-[7,6,7]}$ (see Figure 2) the open shell appears, starting with the first row of hexes ($n = 2$) distancing the two caps. The two frontier orbitals degenerate within the positive domain of eigenvalue for $k = 4$, while for higher k they are located either in the positive or negative domain (as in some tetrahedral fullerenes, with $N \geq 628$).¹⁸ The most important exception is $C_{72,6-H[12,2]-[7,6,7]}$ ($N = 156$), with a meta-closed shell. The "accidental" gap is, however, very thin (-0.026439; -0.028345). This is the only case of MC shell reported in spherical fullerenes (more exactly, fullerenes of genus zero).¹⁸

SEMIEMPIRICAL CALCULATIONS

The semiempirical calculations were calculated with the PM3 Hamiltonian (by HyperChem software package).²⁶ Data are given in Table 1.

Fowler²⁷ has found that geometric instability appears in fullerenes at a "small" gap of ca. 5 eV, in semiempirical calculation, or 0.4 $|\beta|$ in simple Hückel calculation. At least the first terms, and particularly in the series $k = 4m+2$

(Table 1, entries 4-6 and 10-12), show favorable bandgap and relatively low heat of formation (per atom). Compare these data with those for C_{60} : HF = 13.512; PM3 Gap = 6.594 and find that we are in the same domain. Besides the isolated C_{78} (entry 4), some other tubulenes can be candidates to the status of real molecules. A cage having a 10-fold face could appear strange but it just obeys the Hückel $4m+2$ aromatic rule.

Table 1.

Data for the tubulenes $C_{13k,k-H[3k,n]-[6]}$

	Cage k, n	N	Sym.	PM3	PM3	Spectral Data			Shell
				HF/at. (kcal/mol)	GAP (eV)	$\lambda_{N/2}$	$\lambda_{N/2+1}$	GAP ($ \beta $ units)	
1	4; 0	52	D_{2h}	21.585	5.533	0.2564	0	0.2564	PC
2	4; 1	64	S_4	19.271	5.783	0.3789	-0.0774	0.4563	PC
3	4; 2	76	D_{2h}	18.162	5.469	0.3260	-0.0470	0.3731	PC
4	6; 0	78	C_s	12.294	6.083	0.5157	-0.1176	0.6333	PC
5	6; 1	96	D_{3d}	11.015	5.564	0.4329	-0.0844	0.5173	PC
6	6; 2	114	C_s	10.381	5.195	0.3688	-0.0721	0.4409	PC
7	8; 0	104	C_{4h}	11.453	5.730	0.2564	0	0.2564	PC
8	8; 1	128	D_{4d}	10.158	5.497	0.3789	-0.0774	0.4563	PC
9	8; 2	152	C_{4h}	9.390	5.112	0.3260	-0.0470	0.3731	PC
10	10; 0	130	C_{5h}	12.518	5.998	0.4579	-0.0874	0.5453	PC
11	10; 1	160	D_{5d}	11.875	5.512	0.4329	-0.0844	0.5173	PC
12	10; 2	190	C_{5h}	10.715	5.115	0.3688	-0.0721	0.4409	PC

CONCLUSIONS

The zig-zag cylinder rule, first reported in this paper, presents a cluster with the general formula $C_{13k,k-H[3k,n]-[6]}$, of properly closed shell tubulenes, having $N = 13k + 3kn$; $n = 1, 2, \dots$. The number n is just the number of atom rows in the tube distancing the two caps. It shows the same bandgap for either odd or even k value at each positive n . The semiempirical calculations support the idea of relatively stable molecules, possible appearing in the soot of the vaporized graphite.

Acknowledgement. This paper was supported by the Romanian CNCSIS GRANT 2003.

REFERENCES

1. H. Kroto, *Fuller. Sci. Technol.*, **1994**, 2, 333-342.
2. J. Liu, H. Dai, J. H. Hafner, D. T. Colbert, R. E. Smalley, S. J. Tans and C. Dekker, *Nature*, **1997**, 385, 780-781.
3. R. Martel, H. R. Shea and Ph. Avouris, *J. Phys. Chem., B*, **1999**, 103, 7551-7556.
4. D. Babić, D. J. Klein and T. G. Schmalz, *J. Mol. Graphics Modell.*, **2001**, 19, 222-231.
5. A. Ceulemans, L. F. Chibotaru and P. W. Fowler, *Phys. Rev. Lett.*, **1998**, 80, 1861-1864.
6. E. C. Kirby, R. B. Mallion and P. Pollak, *J. Chem. Soc., Faraday Trans.*, **1993**, 89, 1945-1953.
7. A. Ceulemans, L. F. Chibotaru, S. A. Bovin and P. W. Fowler, *J. Chem Phys.*, **2000**, 112, 4271-4278.
8. E. C. Kirby and P. Pollak, *J. Chem. Inf. Comput. Sci.*, **1998**, 38, 66-70.
9. M. V. Diudea, I. Silaghi-Dumitrescu and B. Parv, *Commun. Math. Comput. Chem. (MATCH)*, **2001**, 44, 117-133.
10. M. V. Diudea, *Fullerenes, Nanotubes, Carbon Nanostruct.*, **2002**, 10, 273, 292.
11. Y. D. Gao and W. C. Herndon, *J. Amer. Chem. Soc.*, **1993**, 115, 8459.
12. P. W. Fowler, T. Heine, D. E. Manolopoulos, D. Mitchell, G. Orlandini, R. Schmidt, G. Seiferth and F. Zerbetto, *J. Phys. Chem.*, **1996**, 100, 6984.
13. Müller, P. Kögerler and Ch. Kuhlmann, *J. Chem. Soc., Chem. Commun.*, **1999**, 1347-1358.
14. E. Hückel, *Z. Phys.*, **1931**, 70, 204.
15. P. W. Fowler and J. I. Steer, *J. Chem. Soc., Chem. Commun.*, **1987**, 1403.
16. M. V. Diudea, P. E. John, A. Graovac and T. Pisanski, *Croat. Chem. Acta*, (in press).
17. P. W. Fowler and T. Pisanski, *J. Chem. Soc., Faraday Trans.*, **1994**, 90, 2865
18. P. W. Fowler, *J. Chem. Soc., Faraday Trans.*, **1997**, 93, 1-3.
19. P. W. Fowler, *J. Chem. Soc., Faraday Trans.*, **1990**, 86, 2073-2077.
20. M. V. Diudea, *Int. J. Nanostruct.*, **2003** (submitted)
21. D. E. Manolopoulos, J. C. May and S. E. Down, *Chem. Phys. Lett.*, **1991**, 181, 105-111.
22. G. Brinkmann, P. W. Fowler and M. Yoshida, *MATCH - Commun. Math. Comput. Chem.*, **1998**, 38, 7-17.
23. A. J. Stone and D. J. Wales, *Chem. Phys. Lett.*, **1986**, 128, 501-503.

24. M. V. Diudea, Cs. L. Nagy, O. Ursu and S. T. Balaban, *Fullerenes, Nanotubes Carbon Nanostruct.*, **2003**, (submitted).
25. Y. Zhao, R. E. Smalley, and B. I. Yakobson, *Phys. Rev. B*, 2002, 66, 195409.
26. HyperChemTM, Release 4.5 for SGI, © 1991-1995, HyperCube, Inc. Y.
27. P. W. Fowler and J. P. B. Sandall, *J. Chem. Soc., Perkin Trans.2*, **1994**, 1917-1921.

CORRELATING ABILITY OF CLUJ TYPE INDICES

GABRIEL KATONA^a and MIRCEA V. DIUDEA^b

^{a,b} Faculty of Chemistry and Chemical Engineering
Babes-Bolyai University, 3400 Cluj, Romania

ABSTRACT. This paper reviews the most important results in using Cluj type indices in correlating tests on several sets of organic compounds (alkanes, cycloalkanes, dipeptide ACE inhibitors, substituted 3-(phthalimidoalkyl)-pyrazolin-5-ones, aromatase inhibitors, nitrogen-containing compounds and poly-chlorinated bipheniles).

INTRODUCTION

QSPRs/QSARs (Quantitative Structure-Property Relationships/ Quantitative Structure-Activity Relationships) link in a quantitative manner the physico-chemical or biological properties of chemicals with their molecular structure.¹

Some molecular properties (*i.e.*, those of which numerical value vary with changes in the molecular structure) such as the normal boiling point, critical parameters, viscosity, solubility, retention chromatographic index, are often used for characterizing chemicals in databases. However, a certain property is not always available in tables or other reference sources. It is just the case of newly synthesized compounds. As a consequence, methods of evaluating physico-chemical properties from the structural features of organic molecules become very important.

In this work several correlating results, both QSPRs and QSARs, by using Cluj type topological indices are reported, with the aim to demonstrate the capability of our indices to model the molecular properties or activities of organic compounds.

Cluj indices are calculated on the ground of the Cluj matrices²⁻⁹.

Cluj type indices

The graph-theoretical descriptors CJ and CF represent the theoretical ground for counting the fragmental property indices. They are vertex sets defined by:

$$CJ_{i,j,p} = \{v \mid v \in V(G); di(G)_{v,i} < di(G)_{v,j}; \text{ and } \exists w \in W_{v,i}, V(w) \cap V(p) = \{i\}\} \quad (1)$$

$$CF_{i,j,p} = \{v \mid v \in V(G); di(G_p)_{v,i} < di(G_p)_{v,j}; G_p = G - p \quad (2)$$

In the above relations, $G_p = G - p$ is the spanning subgraph, resulted by deleting the path p joining the vertices i and j (except its endpoints), $dl(G)$ and $dl(G_p)$ denote the topological distances measured in G and G_p , respectively.

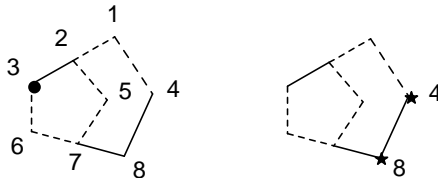
The sets $CJ_{i,j,p}$ and $CF_{i,j,p}$ represent subgraphs (connected or not) in G , referred to the endpoint i and related to j and path p .

In defining *Cluj indices*, the *path* p plays the central role in selecting the subgraphs (eqs 1 and 2), particularly in cycle-containing graphs, where more than one path could join the pair (i,j) . In such graphs, more than one subgraph (*i.e.*, fragment), referred to i , can be counted. By this reason, the non-diagonal entries $[UM]_{ij}$ in Cluj matrices are defined as the *maximum cardinality* of the sets supplied by eq 1 or 2

$$[UM]_{ij} = \max_p |V_{i,j,p}| \tag{3}$$

where $V_{i,j,p}$ is either $CJ_{i,j,p}$ or $CF_{i,j,p}$ and consists of vertices, v , lying *closer* to the vertex i than to the vertex j . When $p \in Dl(G)$, (*i.e.*, the set of all topological distances, or geodesics in G) then $M = CJD_i$ (Cluj-Distance) or CFD_i (Cluj-Fragmental-Distance). When $p \in De(G)$, (*i.e.*, the set of all topological detours, or the longest distances in G) $M = CJDe$ (Cluj-Detour) or $CFDe$ (Cluj-Fragmental-Detour). The diagonal entries are zero. The Cluj matrices are square arrays, of dimension $N \times N$, usually *unsymmetric* (excepting some symmetric regular graphs).

Figure 1 illustrates the construction of **CJDe** matrix.



Cluj Detour Sets $CJDe_{i,j,p}$; pair (3, 4):

$(3, 4) [3, 6, 7, 5, 2, 1, 4] \{3\} (4, 3) [4, 1, 2, 5, 7, 6, 3] \{4, 8\}$

Cluj-Detour Matrix **UC JDe**

0	1	1	1	1	1	2	1	8
2	0	2	2	2	2	2	3	15
2	1	0	1	1	1	1	1	8
1	1	2	0	2	2	1	1	10
1	1	1	1	0	1	1	1	7
1	1	1	1	1	0	1	2	8
3	2	2	2	2	2	0	2	15
1	2	1	1	1	1	1	0	8
11	9	10	9	10	10	9	11	79

$$IP2(CJDe) = 56$$

$$IE2(CJDe) = 15$$

Figure 1. Construction of Cluj Detour matrix, UCJDe

The unsymmetric matrices can be symmetrized, e.g., by the Hadamard product with their transposes

$$\mathbf{SM}_p = \mathbf{UM} \bullet (\mathbf{UM})^T \quad (4)$$

$$\mathbf{SM}_e = \mathbf{SM}_p \bullet \mathbf{A} \quad (5)$$

The symbol \bullet indicates the Hadamard (pairwise) matrix product (i.e., $[\mathbf{M}_a \bullet \mathbf{M}_b]_{ij} = [\mathbf{M}_a]_{ij} [\mathbf{M}_b]_{ij}$). In eq 5, the Hadamard product between the path-defined matrix \mathbf{SM}_p and the adjacency matrix \mathbf{A} (i.e., the matrix having the non-diagonal entries unity for two adjacent vertices and zero otherwise) provides the corresponding edge-defined matrix, \mathbf{SM}_e , which is a weighted adjacency matrix. For the symmetric matrices, the letter \mathbf{S} is usually missing.

In trees, \mathbf{CJD}_i , \mathbf{CJD}_e , \mathbf{CFD}_i and \mathbf{CFD}_e , are identical, due to the uniqueness of the path joining a pair of vertices (i, j).

The above matrices allow the calculation of indices by relations given for the fragmental property indices⁹.

Model Description

Let (i, j) be a pair of vertices and Fr_{ij} any fragment referred to i and related to j .

Dense Topological Model

Let v be a vertex in the fragment Fr_{ij} . The property descriptor applies to the vertex property p_v and topological distance $d_{Tv,j}$. The fragmental *property descriptor* PD , resulting by the vertex descriptor superposition, gives the interaction of all the points belonging to the fragment Fr_{ij} with the point j :

$$PD(Fr_{i,j}) = \Psi_{v \in Fr_{i,j}} (\Omega(d_{Tv,j}, p_v)) \quad (6)$$

The j point can be conceived as an *internal probe atom* with no chemical identity.

Rare Topological Model

Within this model, the property descriptor applies to the fragmental property and topological distance d_{Tij} . The fragmental property descriptor models the interaction of the whole fragment Fr_{ij} with the point j and looks the global property being *concentrated* in the vertex i :

$$PD(Fr_{i,j}) = \Omega(d_{Tij}, \Psi_{v \in Fr_{i,j}}(p_v)) \quad (7)$$

Dense Geometric Model

The fragmental property descriptor is the vector sum of the vertex descriptor vectors. It applies the property descriptor to the vertex property p_v and the Euclidean distance $d_{E v,j}$ in providing a *point of equivalent (fragmental) property* located at the Euclidean distance $d_{E CP,j}$ (with $d_{E CP,j}$ being the *distance*

of property). The vector of the fragmental property has the orientation of this distance vector. The model simulates the interactions in non-uniform fields (gravitational, electrostatic, etc):

$$PD(Fr_{i,j}) = \left\| \sum_{v \in Fr_{i,j}} \vec{\Omega}(d_{E v,j}, p_v) \right\|; \vec{\Omega} = \Omega \frac{\vec{d}_{E v,j}}{d_{E v,j}}; P(Fr_{i,j}) = \Psi(p_v);$$

$$d_{E CP,j} = \Omega_p^{-1}(DG(Fr_{i,j}), P(Fr_{i,j})), \quad (8)$$

where $d_{E CP,j}$ is the distance that satisfies: $\Omega(d_{E CP,j}, P(Fr_{i,j})) = PD(Fr_{i,j})$

Rare Geometric Model

The scalar fragmental descriptor applies the property descriptor to the center of fragment property and Euclidean distance between this center and the vertex j .

The model simulates the interactions in uniform fields (uniform gravitational, electrostatic, etc.):

$$PD(Fr_{i,j}) = \Omega(d_{E CP,j}, \Psi(p_v));$$

$$CP(x_{CP,j}, y_{CP,j}, z_{CP,j}); x_{CP,j} = \frac{\sum_{v \in Fr_{i,j}} x_v \cdot p_v}{\sum_{v \in Fr_{i,j}} p_v} \quad (9)$$

$$y_{CP,j} = \frac{\sum_{v \in Fr_{i,j}} y_v \cdot p_v}{\sum_{v \in Fr_{i,j}} p_v}; z_{CP,j} = \frac{\sum_{v \in Fr_{i,j}} z_v \cdot p_v}{\sum_{v \in Fr_{i,j}} p_v}$$

Fragmental Property Matrices

The fragmental property matrices are non-symmetric square matrices of order N (i.e., the number of non-hydrogen atoms in the molecule). The non-diagonal entries in such matrices are fragmental properties corresponding to any pair of vertices (i,j) by a chosen model.

In case of Cluj criteria, the fragmentation can supply more than one maximal fragment for the pair (i,j) . In such cases, the matrix entry is the arithmetic mean of the individual values.

Thus, if $i, j \in V(G)$, $i \neq j$ and $P_{ij} = \{p_{i,j}^1, p_{i,j}^2, \dots, p_{i,j}^k\}$ paths joining i and j , then cf. *CJ* or *CF* definition, the fragments $Fr_{i,j}^1, Fr_{i,j}^2, \dots, Fr_{i,j}^k$ are generated. Let m be the number of maximal fragments among all the k fragments, $1 \leq m \leq k$, and let $\sigma_1, \dots, \sigma_m$ be the index for the maximal fragments.

By applying any of the above models, for all m maximal fragments we obtain m values, e.g.:

$$PD(Fr_{i,j}^{\sigma_1}), PD(Fr_{i,j}^{\sigma_2}), \dots, PD(Fr_{i,j}^{\sigma_m})$$

and consequently, the matrix entry associated to the pair (i,j) is the mean value:

$$PD_{i,j} = \frac{\sum_{t=1}^m PD(Fr_{i,j}^{\sigma_t})}{m} \quad (10)$$

Fragmental Property Indices

Fragmental property indices are calculated at any fragmental property matrices above discussed, by applying four types of index operators: P_- , P_2 , E_- , E_2 according to the relations:

$$\begin{aligned} P_-(M) &= \frac{1}{2} \sum \sum [\mathbf{M}]_{i,j}; & P_2(M) &= \frac{1}{2} \sum \sum [\mathbf{M}]_{i,j} [\mathbf{M}]_{j,i}; \\ E_-(M) &= \frac{1}{2} \sum \sum [\mathbf{M}]_{i,j} [\mathbf{A}]_{i,j}; & E_2(M) &= \frac{1}{2} \sum \sum [\mathbf{M}]_{i,j} [\mathbf{M}]_{j,i} [\mathbf{A}]_{i,j} \end{aligned} \quad (11)$$

where \mathbf{M} is any property matrix, symmetric or unsymmetric.

Symbolism of the Fragmental Property Matrices and Indices

The name of *fragmental property matrices* is of the general form:

$$\mathbf{ABcDdEffffG} \quad (12)$$

where:

$\mathbf{A} \in \{\mathbf{D}, \mathbf{R}\}$; \mathbf{D} = Dense; \mathbf{R} = Rare;

$\mathbf{B} \in \{\mathbf{T}, \mathbf{G}\}$; \mathbf{T} = Topological; \mathbf{G} = Geometric;

$\mathbf{c} \in \{\mathbf{f}, \mathbf{j}, \mathbf{s}\}$; \mathbf{f} = CF-type; \mathbf{j} = CJ-type; \mathbf{s} = Sz-type;

$\mathbf{Dd} \in \{\mathbf{Di}, \mathbf{De}\}$; \mathbf{Di} = Distance; \mathbf{De} = Detour;

$\mathbf{E} \in \Phi$ (i.e., $\mathbf{E} \in \{\mathbf{M}, \mathbf{E}, \mathbf{C}, \mathbf{P}\}$)

where \mathbf{M} = mass; \mathbf{E} = electronegativity; \mathbf{C} = cardinality;

\mathbf{P} = other atomic property - implicitly, *partial charge*; explicitly, a property given by manual input);

$\mathbf{ffff} \in \Omega$ (i.e., $\mathbf{ffff} \in \{_p, _1/p, _d, _1/d, _p.d, _p/d, _p/d^2, p^2/d^2\}$)

$\mathbf{G} \in \Psi$ (i.e., $\mathbf{G} \in \{\mathbf{S}, \mathbf{P}, \mathbf{A}, \mathbf{G}, \mathbf{H}\}$ with the known meaning (see above).

The name of *fragmental property indices* is of the general form:

$$\mathbf{ABcDdEffffGii} \quad (13)$$

where: $\mathbf{ii} \in \{P_-, P_2, E_-, E_2\}$ with the known meaning (eq 24).

If an operator, such as $f(x)=1/x$ (inverse operator) or $f(x)=\ln(x)$, is applied the indices are labeled as follows:

$$\ln \mathbf{ABcDdEffffGii} := \ln(\mathbf{ABcDdEffffGii});$$

$$1/\mathbf{ABcDdEffffGii} := \frac{1}{\mathbf{ABcDdEffffGii}} \quad (14)$$

For example, index $\ln DGfDeM_p_SP_$ is the logarithm of index $DGfDeM_p_SP_$ computed on the property matrix $DGfDeM_p_S$. The model used is dense, geometric, on fragment of type *CF*, with the cutting path being detour. The chosen property is the mass, the descriptor for property is even the property (mass) and the sum operator counts the vertex descriptors.

The fragmental indices were calculated by the aid of **Cluj3Cmd** 16-bit windows computer programs.

CORRELATING STUDIES

A mathematical model for correlating some biological activities or physical properties with molecular structures can be built up by using *multy linear regression MLR*.

MLR, for n observations and m independent variables is represented by equation

$$Y_i = b_0 + \sum_j^m b_{ij} X_{ij} \quad (15)$$

The regression coefficients b_{ij} can be determined by the least-squares method. Eq (28) can be used for estimating a chosen property in any other sets of chemical structures.

To avoid the chance correlations, it is recommended that the number of descriptors submitted to regression be less than 60 % of the number of observations in the training set.¹⁰

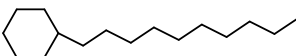
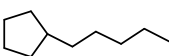
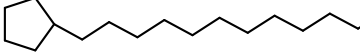
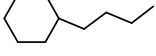
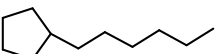
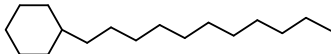
Physico-chemical properties

Cycloalkanes

A set of 25 cycloalkanes⁴ (Table 1) was chosen for testing the correlating ability of some Cluj type indices with viscosity (as $\log \eta$)¹⁴⁻¹⁵ (Table 1). Topological indices and several properties are presented in ref 4, while the statistics of multilinear regression (MLR) appear in Table 2.

Table 1.

Structural formula for some cycloalkanes.

No.	Structural formula	No.	Structural formula
1		14	
2		15	
3		16	

CORRELATING ABILITY OF CLUJ TYPE INDICES

Table 1. (continued)

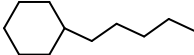
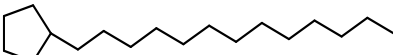
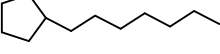
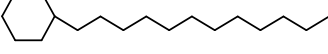
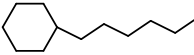
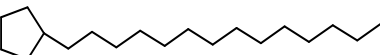
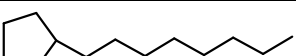
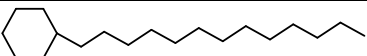
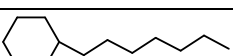
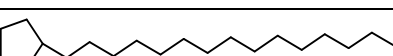
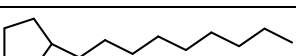
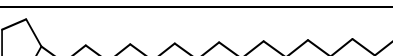
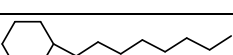

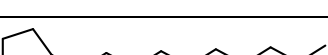
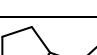
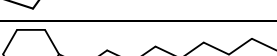
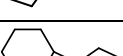
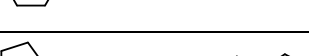
No.	Structural formula	No.	Structural formula
4		17	
5		18	
6		19	
7		20	
8		21	
9		22	
10		23	
11		24	
12		25	
13			

Table 2.

MLR data: $Y = a + \sum_i b_i X_i$; $Y =$ viscosity of structures in Table 1.

No.	X_i	b_i	a	r	s	$cv(\%)$	F
1	CJD_p	0.0001	0.1489	0.8760	0.1721	34.746	75.897
2	CJD_e	0.0008	0.0387	0.9213	0.1389	28.020	129.074
3	$CJ\Delta_p$	0.0001	0.1872	0.8530	0.1864	37.598	61.459
4	$CJ\Delta_e$	0.0008	0.1178	0.8887	0.1638	33.037	86.392
5	$\ln CJD_p$	0.3018	-1.7589	0.9944	0.0377	7.600	2044.310
6	$\ln CJD_e$	0.3905	-1.8722	0.9922	0.0446	9.002	1450.474
7	$\ln CJ\Delta_p$	0.2619	-1.3651	0.9920	0.0451	9.094	1420.770
8	$\ln CJ\Delta_e$	0.3172	-1.3142	0.9887	0.0536	10.824	996.154
9	$\ln CJD_p$	0.2684	-1.5958	0.9969	0.0292	5.879	1137.362
	CJD_p	0.0002					
	$CJ\Delta_p$	-0.0002					
10	$\ln CJ\Delta_p$	0.2169	-1.1728	0.9970	0.0289	5.833	1162.764
	CJD_p	0.0003					
	$CJ\Delta_p$	-0.0003					

The logarithm of the values of both Wiener and Cluj-type indices led to good correlation coefficients (over 0.99, already in single variable regression) and coefficients of variance less than 10 %.

A cross-validation procedure (leave one out – loo) indicated a good predicting ability of our indices:

$\ln CJD_p$ (entry 5 –Table 3), $r_{(loo)} = 0.9933$; $s = 0.0414$; $v\% = 8.349$;

$\ln CJD_p \& CJD_p \& C\Delta_p$ (entry 9), $r_{(loo)} = 0.9957$; $s = 0.0330$; $v\% = 6.661$;

$\ln C\Delta_p \& CJD_p \& C\Delta_p$ (entry 10), $r_{(loo)} = 0.9957$; $s = 0.0329$; $v\% = 6.638$.

N-containing compounds

A set of 90 N-containing compounds (Table 3) of industrial importance was taken from the paper.²³ The tested property was the normal boiling point, B.P. The authors modeled this property by using four categories of molecular descriptors: topological, geometric, electronic and charged-partial surface area descriptors (CPSA).^{24,25}

The nitrogen-containing compounds were problematic in modeling a diverse set of organic chemicals, so that the authors excluded such compounds from their initial model.

The best found MLR model involved ten descriptors (1. dipole moment; 2. partial negative surface area; 3. relative negative charge; 4. relative negative charged surface area; 5. number of aromatic bonds; 6. path 2 molecular connectivity index; 7. cluster 3 valence connectivity index; 8. sum of all path weights from heteroatoms; 9. surface area of donatable hydrogens and 10. charge of donatable hydrogens) and showed the following statistics: $n = 90$ compounds; $R = 0.990$; $s = 10.7$ K. The largest pairwise R value of descriptors was 0.83. The modeling was performed by the ADAPT system.²⁶

Our aim was to verify the quality of our property descriptors exactly in the same conditions as given in ref.²³ Thus, we extracted from the initial set of 104 N-containing compounds the same subset of 90 structures.

Molecular geometries and partial charges were calculated by the semiempirical AM1 method. The set of 19350 descriptors were reduced to 16383 after the monivariate regression.¹⁹ Our procedure for finding the optimal subset of descriptors led to a subset of 72 descriptors.

The best scores in ten variate regression for the set of 90 compounds of Table 3 are listed in Table 4.

The best model was:

$$\begin{aligned} BP_{\text{calc}} = & 225.441 - 59.627 \cdot \ln DTsDiP_p/d2SE2 + 316.627 \cdot RTsDiPp2/d2AE_ \\ & 1.124 \cdot DGfDePp2/d2PP_ - 1729.562 \cdot 1/DTsDiE_p \cdot d_HE2 - \\ & 0.010 \cdot 1/DTsDePp2/d2SP2 - 49.623 \cdot 1/DGsDeP_p \cdot d_HE_ + \\ & 8.846 \cdot \ln DGjDiPp2/d2GP_ - 4.698 \cdot 1/RGjDeP_p \cdot d_GP_ - \\ & 12.188 \cdot \ln DGjDeP_p/d_HP_ + 33.597 \cdot DGjDeE_p_SE2 \end{aligned}$$

$$R = 0.98543; s = 13.149; n = 90 \quad (16)$$

Table 3.**Nitrogen-Containing Compounds and Their Boiling Points.**

No.	Compound	BP	No.	Compound	BP
1.	2-ethylpyridine	422.2	46.	n-tetradecylamine	564.5
2.	2-ethylpiperidine	416.2	47.	acridine	619.2
3.	1-ethylpiperidine	404.2	48.	tri-n-butylamine	487.2
4.	2,2-dimethyl-1,3-diaminomethane	426.2	49.	n-dodecylamine	532.4
5.	N,N-dimethyl-1,3-diaminomethane	418.2	50.	diamylamine	476.1
6.	3,3-dimethylpiperidine	410.2	51.	tripropylamine	429.7
7.	p-fluorobenzylamine	456.2	52.	n-nonylamine	475.4
8.	cianogene	252	53.	quinoline	510.8
9.	m-bromoaniline	524.2	54.	acetoneitrile	354.8
10.	o-bromoaniline	502.2	55.	isoquinoline	516.4
11.	N-ethylbutylamine	381.2	56.	n-octylamine	452.8
12.	triethylamine	362	57.	indole	526.1
13.	N,N-diethylamin $\frac{3}{4}$	337.2	58.	n-heptylamine	430.1
14.	o-nitrotoluene	498.2	59.	p-nitrotoluene	511.7
15.	nitrocyclopentane	453.2	60.	benzotrile	464.1
16.	N-alylaniline	492.2	61.	3-nitrobenzotrifluoride	475.9
17.	ethylamine	289.7	62.	di-n-propilamine	382
18.	p-nitrophenole	552.2	63.	nitrohexane	436.8
19.	cyclopentylamine	380.2	64.	phenilhidrazine	516.7
20.	2-methylbutylamine	368.7	65.	methylamine	266.8
21.	N-methylbutylamine	364.2	66.	3-methylpyridine	417.3
22.	benzylamine	457.7	67.	aniline	457.2
23.	p-methoxyaniline	514.7	68.	p-chloroaniline	503.7
24.	m-methoxyaniline	524.2	69.	m-chloroaniline	501.7
25.	o-methoxyaniline	498.2	70.	n-pentylamine	377.6
26.	t-pentylamine	350.2	71.	isobutylamine	340.9
27.	dimethylamine	280	72.	diethylamine	328.6
28.	1-(2-aminoethyl)-piperidine	459.2	73.	tert-butylamine	317.5
29.	1-(2-aminoethyl)-piperidine	493.2	74.	n-butylamine	350.6
30.	9-methyl carbazole	616.8	75.	Pirolidine	359.7
31.	carbazole	627.8	76.	nitromethane	374.4
32.	4-methylaniline	473.6	77.	isobutyronitrile	376.8
33.	3-methylaniline	476.5	78.	n-butyronitrile	390.8
34.	2-methylaniline	473.5	79.	cis-crotonitrile	380.6
35.	2-propylamine	304.9	80.	trimethylamine	276
36.	1-naphtylamine	573.8	81.	2-nitropropane	393.4
37.	nitroethane	387	82.	1-nitropropane	404.3
38.	piperidine	376.4	83.	propionitrile	370.5
39.	4-methylpyridine	418.5	84.	acrylonitrile	350.5
40.	2-methylpyridine	402.5	85.	N-methylhexylamine	414.2
41.	pyridine	388.4	86.	n-heptylamine	428.2
42.	pyrole	402.9	87.	N-t-butyl-i-propylamine	371.2
43.	2-butylamine	335.9	88.	2-aminoheptane	416.2
44.	triethylamine	516.2	89.	malononitrile	491.5
45.	ethylenimine	329	90.	hydrogen cyanide	298.8

Table 4.

The Best Multivariate Regressions for the 90 Structures of Table 14.

	X ₁	X ₂	X ₃	X ₄	X ₅	X ₆	X ₇	X ₈	X ₉	X ₁₀	R
1	7	4959									0.9446
3	5	4959									0.9487
5	5	4959	10990	9671							0.9628
6	5	4959	10990	7206							0.9671
8	5	4959	10990	9671	3320	6422					0.9761
9	5	4959	10990	9671	3528	6422					0.9766
11	5	4959	10990	9671	3528	6422	16148	6895			0.9798
12	5	4959	10990	9671	3528	6422	6895	15789			0.9800
14	5	4959	10990	9671	3528	6422	16158	16225	15060	15789	0.9843
12	6	6895	4	16275	963	841	163	13920	1	4727	0.9854

The plot corresponding to eq 16 is given in Figure 1.

Our result is slightly lower ($s = 13.149$ K) than that reported in ref.² ($s = 10.7$ K). It is possible to further improve the model by mining the whole descriptor pool not only within the limits of a heuristic procedure. Another possibility is to use different training subset selection and outlier elimination. Such procedures will be reported in a future paper.

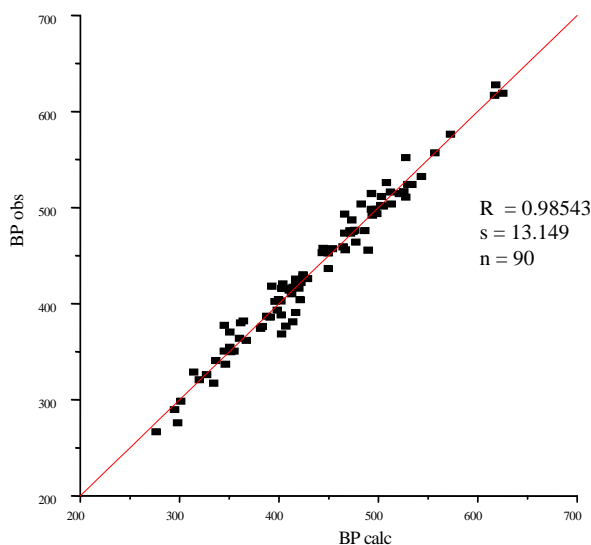


Figure 1. The plot of calculated vs observed normal boiling points (the set of Table 4).

Polychlorinated Biphenils

Polychlorinated biphenils, PCBs, have been synthesized and used as dielectric fluids in electrotechnics, fire retardents, plasticizers or pesticides.³⁹⁻⁴¹ The occurrence of PCBs in the environment⁴² is detrimental for the reproduction⁴³ of several animal species and is hazardous to humans.⁴⁴

By these reasons, PCBs were monitored in the environment⁴⁵ and their biological activity was modeled.⁴⁶⁻⁴⁸

In the present work the *vapor pressure* of PCBs (as logVP), taken from the Rouvray's report⁴⁶) at 25 °C (VP25) and 100 °C (VP100), respectively are modeled by using *FPIF*. The property is important in connection with PCBs spread and toxicity. Table 5 lists the VP25 values and the corresponding TIs (showing the best scores in mono and bivariate regression).

Table 5.
Polychlorinated Biphenils PCBs, logVP25, logVP100 and *FPIF* Descriptors

PCBs	logVP	logVP	lnDGfD	lnDGjD	1/RGjD	1/RTjDi	1/DGjDi	1/RTjDi
	25 (°C)	100 (°C)	eP_p/ d2HP2 (1) ^a	eP_p/ d2HP2 (2)	eCp2/ d2GE_ (3)	C_p* d_HP2 (13325)	E_p/ d_GP2 (13060)	M_p* d_AP2 (14595)
1 Biphenyl	0.0043	-	5.6402	5.6449	0.1846	0.0179	0.0123	0.0011
2 2-Chloro-	0.1847	2.4553	5.8422	5.8669	0.1856	0.0104	0.0078	0.0006
3 3-Chloro-	-0.1409	-	6.0050	6.0077	0.1876	0.0103	0.0068	0.0005
4 4-Chloro-	-0.757	-	6.1627	6.1660	0.1883	0.0088	0.0059	0.0005
5 2,2'-Dichloro-	-0.8729	-	6.0255	6.0105	0.1865	0.0066	0.0056	0.0003
6 3,3'-Dichloro-	-1.5889	1.3257	6.3264	6.3291	0.1908	0.0059	0.0041	0.0003
7 4,4'-Dichloro-	-2.58	1.0667	6.6288	6.6313	0.1924	0.0044	0.0030	0.0002
8 2,5'-Dichloro-	-1.1107	1.679	6.1390	6.1595	0.1889	0.0063	0.0042	0.0003
9 2,3,4-Trichloro-	-1.8601	1.0366	6.3540	6.3721	0.1924	0.0038	0.0030	0.0002
10 2,4,6-Trichloro-	-1.9066	1.4201	6.4185	6.4252	0.1903	0.0042	0.0029	0.0003
11 2,2',5,5'-Tetrachloro-	-2.3036	0.9128	6.5843	6.5947	0.1934	0.0027	0.0020	0.0001
12 2,2',4,5,5'-Pentachloro-	-2.9547	0.3892	6.9262	6.9279	0.1976	0.0018	0.0013	0.0001
13 2,2',4,4',6,6'-Hexachloro-	-2.762	0.4518	7.0418	7.0554	0.1963	0.0014	0.0010	0.0001
14 2,2',3,3',5,5',6,6'-Octachloro-	-4.5391	-	7.7351	7.7474	0.2018	0.0010	0.0007	0.0001
15 2,2',3,3',4,4',5,5',6,6'-Decachloro-	-7.2757	-2.9914	8.9277	8.9613	0.2127	0.0005	0.0004	0.0001
			<i>mono</i>	<i>mono</i>	<i>mono</i>	<i>bi</i>	<i>bi</i>	<i>bi</i>
						lnDGfD	lnDGfD	lnDGfD
						eP_p/ d2HP2	eP_p/ d2HP2	eP_p/ d2HP2
	<i>n</i> = 15					(1)	(1)	(1)
	<i>r</i>		-0.9869	-0.9863	-0.9852	0.9889	0.9890	0.9881
	<i>s</i>		0.323	0.330	0.343	0.314	0.315	0.320
	<i>F</i>		486.528	465.831	429.922	258.661	256.989	249.513
	<i>b</i> ₀		13.003	12.912	48.234	11.844	11.813	12.135
	<i>b</i> ₁		-2.284	-2.266	-260.973	35.455	51.568	468.873
	<i>b</i> ₂					-2.138	-2.135	-2.174

^a score in monovariate regression.

The best *monovariate* regression reveals the fact that the vapor pressure of PCBs is a function of the molecular geometry (G - four of six best descriptors - Table 5 - are of geometric model), that further control the distribution of partial charges (P) and, ultimately, the molecular polarity. Other important local properties are electronegativity (E) and atomic mass (M).

Recall that, in biphenils, the torsion angle between the two benzene rings depends on the number and nature of attached substituents. It is involved in the extend of aromatic conjugation and thereafter in the charge distribution.

$$\log PV_{25} = 13.003 - 2.284 * \ln DGfDeP_p/d2HP2 \quad (17)$$

$$n = 15; r = -0.98690; s = 0.323; F = 486.528$$

In *bivariate* regression, the model is slightly better (Table 5, columns 6-8).

We compared the models supplied by *FPIF* with those given by some graph theoretical descriptors: IP(Di) = Wiener index W, IP2(CJDi), IE2(CJDi), IP2(CJDe), IE2(CJD2) and IP2(CFDi). The values of descriptors are included in Table 8. The drop in correlation coefficient *r* of the best models is of 1.7 % (with IP2(CJDi), column 3, Table 6) and 0.4 % (with IE2(CJDi) & IE2(CJDe), column 5) in monovariate and bivariate regression, respectively. Clearly the computational cost is far more less for the graph theoretical descriptors. This result is not surprising since the rotation of the two rings around the joining bond is quite hindered in substituted biphenils (see the occurrence of atropisomerism in this class of organic compounds).

Table 6.

Polychlorinated Biphenils PCBs and Graph Theoretical Descriptors vs. logVP25.

PCBs / Index		IP(Di)	IP2(CJDi)	IE2(CJDi)	IP2(CJDe)	IE2(CJDe)
1	Biphenyl	198	1169	360	381	72
2	2-Chloro-	240	1406	426	513	100
3	3-Chloro-	246	1501	438	508	94
4	4-Chloro-	252	1545	450	489	94
5	2,2'-Dichloro-	287	1679	499	678	133
6	3,3'-Dichloro-	301	1906	527	663	119
7	4,4'-Dichloro-	315	2008	555	616	119
8	2,5'-Dichloro-	294	1792	513	670	126
9	2,3,4-Trichloro-	358	2236	618	810	155
10	2,4,6-Trichloro-	348	2031	600	750	156
11	2,2',5,5'-Tetrachloro-	412	2511	700	1003	192
12	2,2',4,5,5'-Pentachloro-	488	3038	824	1164	226
13	2,2',4,4',6,6'-Hexachloro-	555	3325	927	1335	279
14	2,2',3,3',5,5',6,6'-Octachloro-	702	4291	1152	1855	364
15	2,2',3,3',4,4',5,5',6,6'-Decachloro-	907	5706	1483	2274	459
<i>n</i> = 15		<i>mono</i>	<i>mono</i>	<i>mono</i>	<i>mono</i>	<i>mono</i>
<i>r</i>		0.9627	0.9703	0.9647	0.9470	0.9443
<i>s</i>		0.543	0.485	0.528	0.648	0.660
<i>F</i>		164.349	209.448	173.327	112.982	106.953

CORRELATING ABILITY OF CLUJ TYPE INDICES

Table 6. (continued)

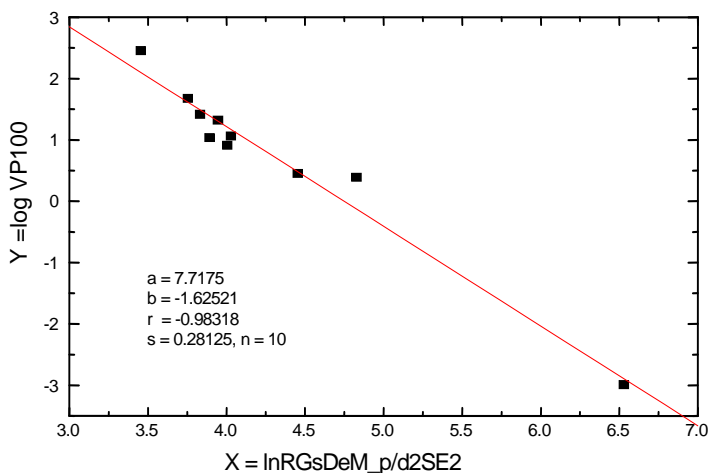
PCBs / Index	IP(Di)	IP2(CJDi)	IE2(CJDi)	IP2(CJDe)	IE2(CJDe)
b_0	1.705	1.633	2.018	1.067	0.932
b_1	-0.009	-0.002	-0.006	-0.003	-0.017
	b_i	b_i	b_i	b_i	
$n = 15$	IP(Di)	IP2(CJDi)	IP2(CJDi)	IE2(CJDi)	
	IE2(CJDe)	IP2(CJDe)	IP2(CFDi)	IE2(CJDe)	
r	0.9846	0.9822	0.9833	0.9848	
s	0.364	0.392	0.380	0.362	
F	190.879	164.390	175.340	193.354	
b_0	3.710	2.284	2.043	4.445	
b_1	-0.036	-0.004	-0.009	-0.021	
b_2	0.048	0.005	0.007	0.041	

The vapor pressure at 100 °C, as $\log VP_{100}$, is modeled using the descriptors shown in Table 6. The best monivariate model is:

$$\log PV_{100} = 7.713 - 1.625 * \ln RGSDeM_p/d2SE2 \quad (18)$$

$n = 10; r = -0.98318; s = 0.281; F = 231.873$

Looking at eq (18) reveals that: the geometry is again important in modeling the property but the local property governing VP_{100} is the atomic mass (M). It is correlated with the loss in the electrostatic interactions of molecules in liquid phase and increase of gravitational interactions (see the rare geometric model. Figure 2 shows the plot of $\ln RGSDeM_p/d2SE2$ vs $\log VP_{100}$.

**Figure 2.** The plot: $\ln RGSDeM_p/d2SE2$ vs $\log VP_{100}$.

In *bivariate* regression, the model is still better. The best model gives an additional support of the conclusion that vapor pressure of PCBs is better modeled by *FPIF* descriptors including information on geometry, partial charges and atomic mass:

$$\begin{aligned} \log VP100 = & -15.005 - 1.926 \cdot \ln RGsDeM_p/d2SE2 \\ & + 15.095 \cdot \ln RGjDeP_1/d_HE2 \\ n = & 10; r = 0.9956; s = 0.155; F = 390.790 \end{aligned} \quad (19)$$

By using the classical descriptors (Table 6), other two excellent correlations were found:

$$\begin{aligned} \log VP100 = & 2.8123 + 0.0137 IE2(CjDi) - 0.0045 IP2(CjDi) \\ n = & 10; r = 0.9934; s = 0.188; F = 265.920 \end{aligned} \quad (20)$$

$$\begin{aligned} \log VP100 = & 3.5364 - 0.0044 IP2(CjDi) + 0.0207 IP2(Di) \\ n = & 10; r = 0.9941; s = 0.179; F = 291.910 \end{aligned} \quad (21)$$

The best reported data in literature are as follows: Rouvray,⁴⁶ W ($r = 0.9632/VP25$; $r = -0.8863/VP100$) and Khadikar,⁴⁷ SZ ($0.9843/VP25$ - in error with the reported data!; corrected result: $r = 0.9647$, see Table 6, column 4; $r = -0.8921/VP100$). The fragmental property indices take into account the chemical nature of atoms (mass, electronegativity and partial charge), various kinds of interactions between the fragments of molecules as generated by Cluj and Szeged criteria and the 3D geometry of molecular structures as well.

Biological activity

Pirazolidin-3,5-diones

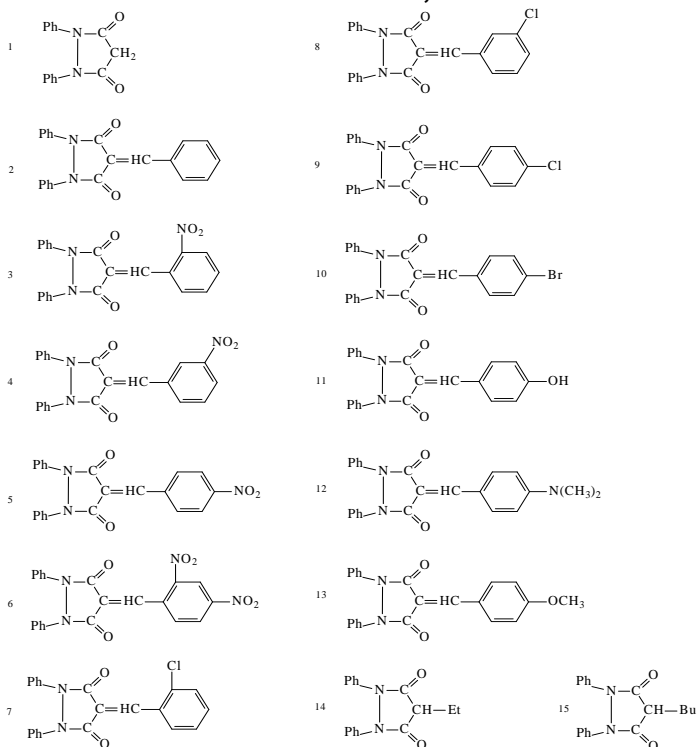


Figure 3. The set of Pirazolidin-3,5-diones.

CORRELATING ABILITY OF CLUJ TYPE INDICES

The molecules presented in Figure 2 were synthesized in our laboratory⁵⁰. The molecular structures were input and optimized by HyperChem (HyperCube Inc.) package. Partial charges were calculated by AM1 semiempirical approach.

Modeling Biological Activity

Pirazolidin-3,5-diones are known having antiinflammatory activity⁵⁰. They also show some antimicrobial and antifungal activity (on *Staphylococcus aureus*, *Bacillus subtilis*, *Escherichia coli*, *Pseudomonas aeruginosa*, *Candida albicans*, etc.). Table 7 shows the biological activity, in mm inhibition zone.

Table 7.

Antimicrobial Activity; Inhibition Zone (mm).

Compound	Gram-positives			Gram-negatives			Fungi
	Staphyl. aureus	Staphyl epider	Bacill subtilis	Esc coli	Prot. vulg.	Pseu. aerug.	Cand. albicans
1	0	0	0	0	0	0	0
2	10	10	10	0	0	0	0
3	14	10	13	0	0	10	0
4	12	17	14	0	0	10	10
5	0	0	10	0	0	10	10
6	0	0	10	0	0	10	10
7	12	0	10	0	0	10	0
8	12	0	10	0	0	10	0
9	12	0	10	0	0	10	0
10	12	10	10	0	0	0	10
11	12	13	13	0	0	10	12
12	0	0	12	0	0	10	13
13	0	0	0	0	0	10	12
14	0	0	0	0	0	0	0
15	0	0	0	0	0	0	0

In the following, only two activities are considered for modeling: BA vs *Bacillus subtilis* and BA vs *Candida albicans*.

The activity vs. *Bacillus subtilis*, was estimated, in monovariate regression. The best three regression equations are given below:

$$BA_{\text{calc}} = -147,1950 + 35,4337 * \ln \text{RGjDeE_p/d_HP2} \quad (22)$$

n = 15; r = 0.8320

$$BA_{\text{calc}} = -147,3113 + 35,4626 * \ln \text{RGfDeE_p/d_HP2} \quad (23)$$

n = 15; r = 0.8319

$$BA_{\text{calc}} = -75,9515 + 35,6724 * \ln \text{RGjDeC_p/d_HP2} \quad (24)$$

n = 15; r = 0.8316

In *bivariate* regression the model is still improved:

$$BA_{\text{calc}} = 21.0809 - 306.3117 \cdot 1/RGfDeC_p/d_HP2 + 4.4915 \cdot \ln DGjDeP_p_GE_ \\ n = 15; r = 0.9857 \quad (25)$$

$$BA_{\text{calc}} = 6.2856 - 578.8831 \cdot 1/DGjDeP_p/d2PE_ + 4.8740 \cdot \ln DGjDeP_p \cdot d_GE_ \\ n = 15; r = 0.9883 \quad (26)$$

$$BA_{\text{calc}} = 4.0166 - 191.7906 \cdot 1/RGjDeC_p/d2HE_ + 4.9157 \cdot \ln DGjDeP_p \cdot d_GE_ \\ n = 15; r = 0.9885 \quad (27)$$

Table 8 includes the observed inhibitory activity vs. *Bacillus subtilis* and calculated BA by the above equations.

Table 8.

Biological Activity BA_{obs} and BA_{calc} by eqs 25-27.

Comp. No.	BA (eq 25)	BA (eq 26)	BA (eq 27)
1	9.9993	9.9997	9.9998
2	10.2281	10.6001	10.6068
3	9.9127	10.1988	10.1479
4	10.5830	10.3631	10.4159
5	10.0743	9.4243	9.7268
6	12.2185	12.4991	12.6593
7	13.2109	12.0148	12.1553
8	11.7282	10.7701	10.9012
9	0.0143	0.6821	0.6908
10	0.7988	-0.0707	-0.0435
11	-0.4674	-0.5345	-0.5304
12	12.6072	13.3293	13.4258
13	11.2599	11.9890	11.6189
14	10.1309	10.8491	10.3785
15	-0.2987	-0.1143	-0.1529

As can be seen from eqs 25-27, the inhibiting activity of phtalazines vs *Bacillus subtilis* is controlled by the geometry (G in the symbol of indices) and electronic features of these molecules (E - electronegativity and P - partial charges).

The activity vs. *Candida albicans*, was estimated, in *monovariate* regression, as shown below:

$$BA_{\text{calc}} = - 4.3416 + 1.5663 \cdot \ln DTfDeP_p \cdot d_PP2 \quad (28) \\ n = 15; r = 0,9252$$

$$BA_{\text{calc}} = - 4.1732 + 1.5461 \cdot \ln DTjDeP_p \cdot d_PP2 \quad (29) \\ n = 15; r = 0,9235$$

$$BA_{\text{calc}} = - 2.3616 + 1.4733 \cdot \ln DTfDiP_p \cdot d_PP2 \quad (30) \\ n = 15; r = 0,8777$$

In *bivariate* regression the improvement of correlation was not so sound as in case of *Bacillus subtilis*:

CORRELATING ABILITY OF CLUJ TYPE INDICES

$$BA_{\text{calc}} = 58.0019 + 1.9258 \ln DTfDiP_p*d_PP2 - 14.1524 \ln RGSDeP2/d2GP2$$

$$n = 15; r = 0.9415 \quad (31)$$

$$BA_{\text{calc}} = 39.1986 + 1.9336 \ln DTfDiP_p*d_PP2 - 18.7211 \ln RGSDeP/d2AP2$$

$$n = 15; r = 0.9429 \quad (32)$$

$$BA_{\text{calc}} = 7.0326 + 2.3522 \ln DTjDiP_p*d_PP2 - 42.8766 \ln RGSDeP_p/d_AP2$$

$$n = 15; r = 0.9523 \quad (33)$$

From eqs 31-33, it is suggesting that the antimycotic activity of phtalazines is controlled basically by the topology (T) and geometry (G), on one hand and electronic features (P - partial charges and E - electronegativity) of molecules.

Dipeptide ACE Inhibitors

The set consists of 58 dipeptides and was taken from Cocchi's report¹⁶. The molecular structure of these peptides was input and optimized by using the MM+ and then by semiempirical AM₁ procedure of the HyperChem Program (HyperCube Inc.). Table 4 includes the dipeptide names by using the one-letter code for aminoacids, the observed ACE inhibitory activity (biological activity, **BA**, as $\log(1/IC_{50})$), the calculated BA according to the best model and the corresponding residuals. As above mentioned, **FPIF** descriptors take explicitly into account 3D-structural features of the whole molecule of dipeptides¹⁷.

Table 9 collects the statistics of monivariate and bivariate regression in modeling the ACE inhibiting potency of dipeptides by **FPIF**. Cross-validation tests (Leave-20%-out **L20%** or Leave-one-out **Loo** procedures) are given here only for bivariate regressions.

Table 9.

Statistics for ACE inhibitors set.

Index	DTfDiM_p /d2GP_	lnDGsDiE_1 /p_GE_	DTjDeM_p /d2GP_	lnDTjDeEp2 /d2AE_	DTsDeP_1 /d_GP2	lnRGSDeMp2 /d2AE_
	DTfDiM_p /d2GP_		DTjDeM_p /d2GP_		DTsDeP_1 /d_GP2	
r	0.7819	0.8870	0.7884	0.8754	0.7923	0.8717
r²	0.6114	0.7867	0.6216	0.7663	0.6277	0.7599
s	0.630	0.471	0.622	0.493	0.616	0.500
F	88.106	101.426	91.999	90.147	94.420	87.029
b₀	-0.759	35.992	0.776	21.816	0.479	3.325
b₁	0.286	-11.802	0.143	-6.681	0.268	-3.194
b₂		0.822		0.529		0.571

Table 9. (continued)

Cross-validated			
	L20%o ^a	L20%o	L20%o
<i>r</i>	0.8715	0.8592	0.8552
<i>r</i> ²	0.7595	0.7382	0.7314
<i>s</i>	0.495	0.517	0.524

^a average of twenty five 20% sets of randomly chosen objects.

The best-found model was:

$$BA_{\text{calc}} = 35.992 + 0.822 * DTfDIM_p/d2GP_ - 11.802 * \ln DGsDiE_1/p_GE_ \\ n = 58; r = 0.88696; s = 0.471; F = 101.426 \quad (34)$$

Table 10.

Comparative statistics of QSAR models of 58 ACE inhibitors and 48 sweeteners dipeptides.

	Peptide Set (Reference)	Descriptors per Residue	No. Comp.	<i>r</i> ² (fitting)	<i>r</i> ² (cross-validated)
1	ACE (Cocchi et al.) ¹⁶	7	1	0.744	nd ^a
2	ACE (Collantes et al.) ¹⁹	2	nd	0.700	nd
3	ACE (Zaliani et al. -extended) ¹⁸	3	2	0.708	0.637
4	ACE (Zaliani et al. -rotameric) ¹⁸	3	6	0.657	0.541
5	ACE (FPIF) [this work]	2	2	0.787	0.759^b
6	Sweeteners (Jonsson et al.) ²⁰	3	1	nd	0.780
7	Sweeteners (Collantes et al.) ¹⁶	2	2	0.847	nd
8	Sweeteners (Zalini et al. -extended) ¹⁸	3	3	0.754	0.710
9	Sweeteners (Zalini et al. -rotameric) ¹⁸	3	3	0.704	0.633
10	Sweeteners (FPIF) [this work]	2	2	0.851	0.833^b

^a Not determined; ^b Leave-20%-out, 25 times, of randomly chosen objects.

Both topology (**T** - in the index symbol) and geometry (**G**) contribute to the best model. As local property, the atomic mass (**M**) and electronegativity (**E**) modulate the structure-activity relationship. For the best model (see also column 3, Table 10) the L20%o cross-validation was averaged on 25 randomly chosen 20% objects. The drop in *r* is around 1.6 % that proves a good predicting ability of the models. The plot of observed **BA** vs calculated **BA** is presented in Figure 1.

The model given by **BA** equation is superior, both in estimation and prediction, to those reported in literature (see Table 11). Note that the Zaliani's results refer both to a single conformation (i.e., extended) of amino acids and to a library conformation family (i.e., rotameric).

CORRELATING ABILITY OF CLUJ TYPE INDICES

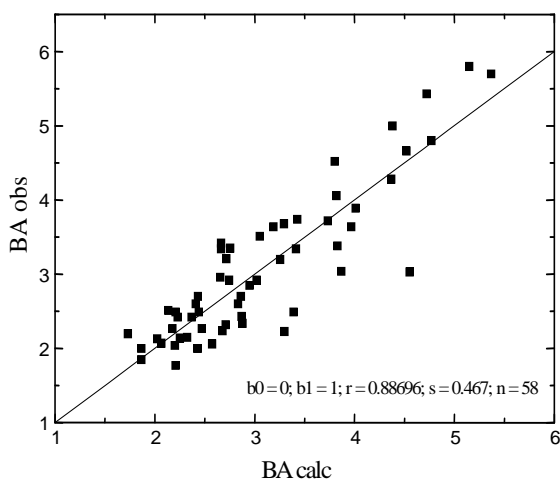


Figure 4. The plot of observed vs calculated BA.

Table 11.

The best ten bivariate regressions in ACE inhibitors test.

No.	Score 1	Score 2	Index 1	Index 2	<i>r</i>
1	89	5831	DTfDiM_p/d2GP_	lnDGsDiE_1/p_GE_	0.8870
2	54	1771	DTjDeM_p/d2GP_	lnDTjDeEp2/d2AE_	0.8754
3	29	7894	DTsDeP_1/d_GP2	lnRGsDeM2/d2AE_	0.8717
4	29	2644	DTsDeP_1/d_GP2	lnRTjDeEp2/d2HE_	0.8686
5	18	8213	DTsDeM_p/d_GP2	lnRGsDeEp2/d2AE_	0.8681
6	18	7725	DTsDeM_p/d_GP2	lnRGsDeE_p/d2AE_	0.8624
7	15	6476	DTfDeM_p/d_PP_	lnRTsDiEp2/d2AE2	0.8618
8	1	15876	RTfDeE_1/p_PP2	lnRGsDeCp2/d2HP2	0.8614
9	1	8719	RTfDeE_1/p_PP2	DGfDiP_p/d_GP_	0.8518
10	1	6485	RTfDeE_1/p_PP2	lnRTsDiEp2/d2GE2	0.8465

Table 11 shows the occurrence of descriptors in the best 10 regression equations. All indices of the first variable in bivariate regression are topological (**T** in index symbol) while only six of ten of the second variable are geometric (**G** in index symbol). In general, a model is built up by using a training set of structures (that provides a calibration equation) and further it is validated by a cross-validation procedure and also by using an external prediction set. Due to the fixed mode of selection, the **Loo** procedure strongly requires an external set for prediction. It is not the case of *averaged L20%* procedure, when the predicting sets (and implicitly the 80% training sets) can be randomly selected, thus getting enough statistical meaning for the model. A similar procedure was used in Zaliani's report¹⁸. This result correlates with the Zaliani's best result when used extended conformations (see Table 10).

As local property, the atomic mass (**M**) occurs five times in the first variable while the electronegativity (**E**) seven times in the second variable. Other occurring properties are the partial charge (**P**) and cardinality (**C**). Clearly, the chemical features play an important role in discriminating vertices (i.e., atoms or atom groups), fragments and whole molecules of dipeptides. They are strongly involved in modeling the biological activity of dipeptide ACE inhibitors.

Dipeptide Sweeteners

The set including 48 dipeptides was taken from Jonsson's paper²⁰. The molecular structures were input and optimized by using MM+ and then by semiempirical AM₁ procedure of the HyperChem Program (HyperCube Inc.).

Table 12 collects the statistics of monovariate and bivariate regression in modeling BA of dipeptide sweeteners by **FPIF**. The same remark holds for the cross-validation tests.

The best-found model was:

$$BA_{\text{calc}} = 1.142 + 0.474 * RTsDiM_1/p_SP_ - 0.043 * DGsDiE_1/p_AP_ \\ n = 48; r = 0.92272; s = 0.248; F = 128.922 \quad (35)$$

As in the previous test, both topology and geometry contribute to the best model and again the local property, was the atomic mass (**M**) and electronegativity (**E**).

In predicting tests, (see Table 12, columns 3, 5 and 7) the drop in *r* was around 1 %, proving a good stability of the models. The plot of observed BA vs calculated BA (eq 35) is presented in Figure 5. The model given by eq 35 surpasses those reported in literature (see Table 10).

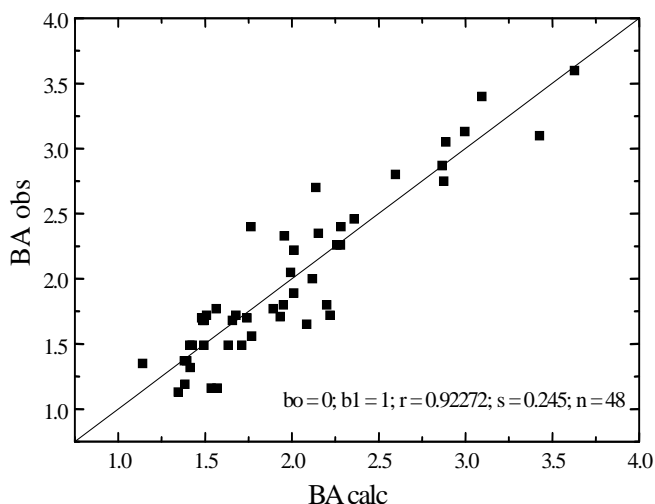


Figure 5. The plot of observed vs calculated BA (eq 35).

Table 12.

Statistics for sweeteners dipeptides.

1	2	3	4	5	6	7
Index	RTsDiE_1/ p_AE2	RTsDiEp2/ d2AE_	RTsDeE_1 /p_AE_	lnRTsDiEp2/ d2GE2	RTsDiM_1 /p_SP_	DGsDiE_1/ p_AP_
		RTsDiE_1/ p_AE2		RTsDeE_1/ p_AE_		RTsDiM_1/ p_SP_
<i>r</i>	0.81448	0.9169	0.8008	0.91525	0.7719	0.9227
<i>r</i> ²	0.66337	0.8407	0.6413	0.8377	0.5959	0.8514
<i>s</i>	0.369	0.257	0.381	0.259	0.404	0.248
<i>F</i>	90.650	118.714	82.231	116.116	67.821	128.922
<i>b</i> ₀	0.106	0.482	0.115	0.471	-0.058	1.142
<i>b</i> ₁	0.898	-0.058	0.315	-0.006	0.085	-0.043
<i>b</i> ₂		4.479		1.364		0.474
Cross-validated						
		L20%o		L20%o		L20%o (aver.) ^a
<i>r</i>		0.9067		0.9047		0.9129
<i>r</i> ²		0.8221		0.8185		0.8333
<i>s</i>		0.268		0.271		0.259

^a average of twenty five 20% sets of randomly chosen objects.

Table 13.

The best ten bivariate regressions in sweeteners dipeptides test.

No.	Score 1	Score 2	Index 1	Index 2	<i>r</i>
1	1219	7437	RTsDiM_1/p_SP_	DGsDiE_1/p_AP_	0.9227
2	6076	132	RTsDiEp2/d2AP2	DGsDeEp2/d2GE_	0.9209
3	33	6051	RTsDeE_1/p_AE_	RTsDiEp2/d2GE2	0.9153
4	1	3180	RTsDiE_1/p_AE2	RTsDiEp2/d2AE_	0.9169
5	1	3154	RTsDiE_1/p_AE2	RTfDiE_p/d2AP2	0.9076
6	1	3093	RTsDiE_1/p_AE2	RTsDiEp2/d2AP_	0.9027
7	1	3074	RTsDiE_1/p_AE2	RTjDiE_p/d_GP2	0.8846
8	1	3012	RTsDiE_1/p_AE2	RTsDeE_p/d_GP2	0.8846
9	1	2769	RTsDiE_1/p_AE2	lnDGsDeE_1/p_PP2	0.8768
10	1	2076	RTsDiE_1/p_AE2	DTsDiEp2/d2SE	0.8755

Table 13 shows the occurrence of descriptors in the best 10 regression equations. Seventeen indices in bivariate regression are topological while only three geometric. This result proves that the topology is the main feature in describing this dipeptide activity. In fact, topological indices are descriptors invariant to rototranslation, so that it is not surprising that Zaliani obtained the best correlation when used extended conformations of aminoacids.

As local property, the electronegativity (E) occurs nineteen times while the atomic mass (M) only once, in bivariate regression. It appears that the bitter tasting activity is controlled by electronic factors. The fragmental property indices take into account the chemical nature of atoms (mass, electronegativity and partial charge), various kinds of interactions between the fragments of molecules as generated by Cluj and Szeged criteria and the 3D geometry of molecular structures as well. For other **FPIF** modeling examples the reader can consult⁹.

Substituted 3-(Phthalimidoalkyl)-pyrazolin-5-ones

We tested the correlating ability of **FPIF** on a set of 17 molecular structures from the class of substituted 3-(Phthalimidoalkyl)-pyrazolin-5-ones⁹ with the sum of one-electron energy calculated at single point semi-empirical extended-Huckel and the inhibitory activity on *Lepidium sativum* L. (Cresson).

The molecular structure of the selected chemicals is given in Figures 6. It was performed by using the MM+ (for 3D-geometries) and semiempirical AM1 (for partial charge calculation) procedures of the HyperChem Program (HyperCube Inc.). The modeled properties were the sum of one-electron energy calculated at the Extended-Huckel level and the inhibitory activity (in %) of a solution of 0.05 mg/ml pyrazolin-5-one on *Lepidium sativum* L. (Cresson). The data are listed in Table 14.

Table 14.

The Sum of One-Electron Energy Calculated at Single Point Semi-Empirical Extended-Huckel and the Inhibitory Activity on *Lepidium sativum* L. (Cresson) for 17 Substituted 3-(Phthalimidoalkyl)-Pyrazolin-5-Ones*

Molecule no.	Energy (kcal/mol)	Inhibition (%)
1	50978.19	28.4
8	64751.09	65.2
7	64752.65	49.4
6	62330.33	68.3
5	38604.68	14.3
4	53416.95	27.7
3	53441.43	30.4
2	51000.36	28
17	41057.46	15.1
16	67104.64	50.6
15	64701.39	71.7
14	43473.37	18.2
13	41020.54	12.2
12	55832.12	32.6
11	55729.99	28.9
10	53424.19	29.3
9	50012.42	46.9

* Values of inhibition are taken from ref.²¹

CORRELATING ABILITY OF CLUJ TYPE INDICES

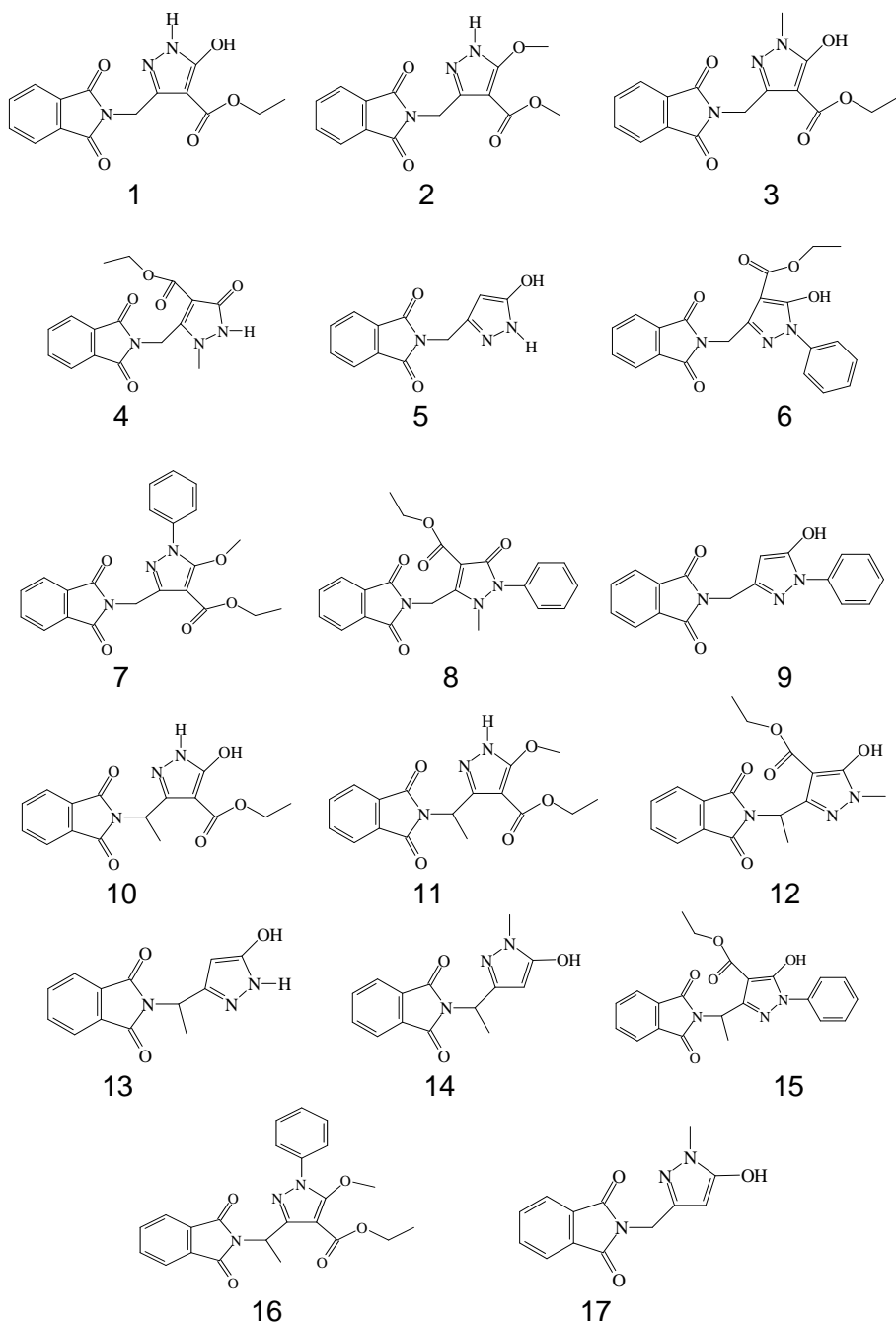


Figure 6. Structure of 17 substituted 3-(Phthalimidoalkyl)-pyrazolin-5-ones.

Monivariate Regression for Energy

The best results, in monovariate and divariable regression for energy are listed in Table 15.

Table 15.

The Bests Correlations of Energy in Monivariate and Divariate Regression.

Index No.	Index Name	R	b ₀	b ₁
1	lnDGjDeE_p/d2PE_	0.9997	5370	3760
2	DTjDeEp2/d2SE_	0.9996	8802.3	138
3	lnDGjDeE_p/d2PE2	0.9996	1289.5	3671.1
4	DTjDeMp2/d2SE_	0.9994	9188.7	922.34
4	DTjDeMp2/d2SE_	0.9999	13056	1108.8
4315	DTfDiE_p/d_AP2			-95.598
34	RTsDiM_p/d2GP2	0.99997	-1193	1674.3
5947	DTjDeEp2/d2AP_			-41.168
492	RTjDeM_p/d2SP_	0.99997	58267	46.095
1698	1/RTsDeM_p/d2AE2			-686800
492	RTjDeM_p/d2SP_	0.99998	56222	47.864
1737	1/RTsDeM_p/d2AP2			-711240

The best single variable QSPR (boldface in Table 15) was

$$\text{Predicted energy} = 5370 - 3760 * \ln DGjDeE_p/d^2PE_ \quad (36)$$

$$R = 0.99973; n = 17$$

This correlation could be satisfactory but usually a molecular property shows more than one dimension dependency. For this reason, we performed the bivariate regression.

Bivariate Regression for Energy

The first 16383 indices, labeled in decreasing order of their score in monivariate regression, are submitted for bivariate correlation. A procedure for finding subsets of optimal even number descriptors was developed. It is a simple, iterative technique that eludes the investigation of all possible descriptor combinations and reduces the time for drawing the best property model. More details will be presented in a future paper.

Here, the bivariate correlation for six pairs of indices is exemplified. The pairs are: (1, 2); (1, 10175); (4, 4315); (34, 5947); (492, 1698) and (492, 1737). The first two pairs are taken to show that the first scored index in monivariate regression does not provide the best bivariate correlation. Selection of the pairs of indices for bivariate correlation must be done by traversing the whole pool (1...16383). For additional descriptors, our procedure for optimum descriptor selection avoid the mining of all possible index combinations.

The best bivariate score was provided by the pair (492, 1737):

$$\begin{aligned} \text{Predicted energy} &= 56221.885 + 47.864 \cdot \text{RTjDeM}_p/d2\text{SP}_- \\ &711240.703 \cdot 1/\text{RTsDeM}_p/d2\text{AP2} \\ R &= 0.99998; s = 57.40; n = 17 \end{aligned} \quad (37)$$

An insight in Table 15 reveals that the best models (i.e., those showing $R > 0.9999$) show a dependency of this energy by the molecular topology (topological models) and the nature of atoms (mass and electronegativity).

Monivariate Regression for Inhibition

For the first six best indices in monivariate regression the indices and statistics are given in Table 16.

The best monivariate QSAR was:

$$\begin{aligned} \text{Predicted inhibition} &= -336.760 + 96.378 \cdot \ln\text{DGsDeC}_1/p_SE_ \\ R &= 0.9539; n = 17 \end{aligned} \quad (38)$$

which is, of course, not satisfactory, despite in ref.²¹ a value of $R = 0.92$ was reported. Thus, we performed the bivariate regression.

Table 16.

The Best Correlations of Inhibition in Monivariate and Divariate Regression.

Index No.	Index Name	R	b_0	b_1
1	$\ln\text{DGsDeC}_1/p_SE_$	0.9539	-336.76	96.378
2	$1/\text{DGsDeC}_1/p_SE_$	-0.9523	137.01	-4754.8
3	$\ln\text{DTjDeE}_p*d_HE_$	0.9517	135.80	-493.02
18	$\text{DTjDeEp2}/d2\text{AE}_-$	0.9883	121.21	1.076
16842	$\text{RGjDeP}_p/d_GP_$			-1.5194
37	$\text{DTjDeE}_p/d_AE_$	0.9906	-73.183	2.1644
11362	$\ln\text{DGjDeP}_p/d_PE2$			-4.1769
4304	$\text{DTsDiM}_p*d_HP_$	0.9927	-26.846	1.5619
7649	$\text{DGjDeE}_p/d2\text{SE2}$			-1.7043

Bivariate Regression for Inhibition

Six pairs of indices are considered here for bivariate correlation: (1, 2); (1, 1369); (2, 13227); (18, 16842); (37, 11362) and (4304, 7649).

As in the case of energy, the best scored index in monivariate correlation is not present in the pair of best bivariate correlation.

The best bivariate score was done by the pair (4304, 7649):

$$\begin{aligned} \text{Predicted inhibition} &= -26.846 + 1.562 \cdot \text{DTsDiM}_p*d_HP_ - \\ &1.704 \cdot \text{DGjDeE}_p/d2\text{SE2} \\ R &= 0.9927; s = 2.374; n = 17 \end{aligned} \quad (39)$$

Figure 7 illustrates the plot of inhibition vs predicted inhibition cf eq 39.

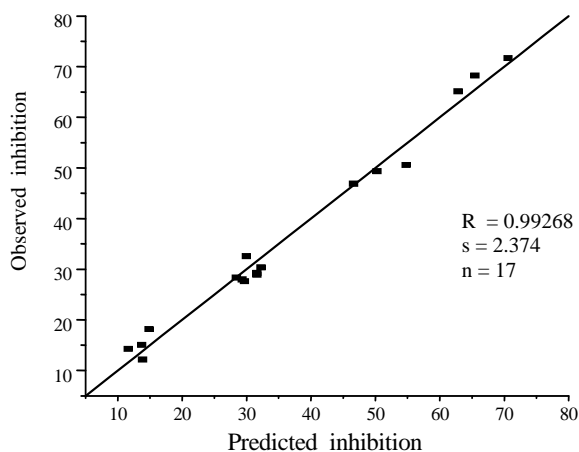


Figure 7. The plot: inhibition vs predicted inhibition of eq 32.

The constant high correlation (see Table 16) between the best indices and the mitodepressive activity on *Lepidium Savitium L. (Cresson)* demonstrate ability of this family of indices to estimate the biological activity of the considered set of chemical structures. The models with $R > 0.983$ suggest that the mitodepressive activity on *Lepidium Savitium L. (Cresson)* is dependent both on the geometric and topological features of molecules, the nature of atoms (mass and electronegativity) and the electrostatic field of atoms induced by their partial charges.

Aromatase Inhibitors

A set of substituted dichlorodiphenyls (4, 4'-dichlorodiphenyl-methanes) inhibitors of aromatase²² were considered. Enzymatic aromatization of androgens is involved in the biosynthesis of estrogens, and consequently in the estrogen-dependent diseases.

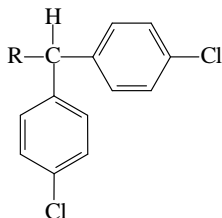
For modeling the inhibition, the authors⁴² used two dipole moment related descriptors. We modeled the inhibition in monivariate regression but no satisfactory correlation (R^2 around 0.828) was found. In divariate regression, the correlation improved.

$$\begin{aligned} \text{Predicted inhibition} = & 6.177 + 0.513 \cdot \ln \text{RTjDiP_p_HP2} - \\ & 0.071 \cdot 1/\text{DGjDeP_1/p_SP2} \\ & R^2 = 0.9716; s = 0.205; n = 10 \end{aligned} \quad (40)$$

The best reported²² correlation for this subset was: $R^2 = 0,89$; $s = 0.44$. In our model, both the topology and geometry (see the indices in eq 40) are important in modeling the aromatase inhibition by dichlorodiphenyl methanes.

Table 17.

Dichlorodiphenyl Methanes Aromatase Inhibitors.



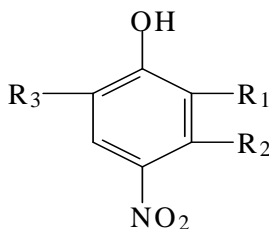
No.	R	$-\log EC_{50}$ obs
1		7.43
2		8.03
3		8.06
4		5.70
5		5.71
6		5.30
7		5.30
8		6.80
9		5.30
10		7.26

Nitrophenols

A set of 25 nitrophenols²⁷ showing herbicidal activity (Table 18) was considered for correlation with the Cluj Property indices. Nitrophenols are known to inhibit the electronic flux of photosynthesis.

Table 18.

Nitrophenols and Their Herbicidal Activity



No	R ₁	R ₂	R ₃	pl ₅₀
1	H	methyl	methyl	3.3
2	H	methyl	isopropyl	4.1
3	H	H	t-butyl	5.7
4	H	H	phenyl	4.35
5	H	H	cyclohexyl	4.85
6	Cl	methyl	methyl	4.89
7	Cl	methyl	isopropyl	6.07
8	Cl	H	t-butyl	6.88
9	Cl	H	phenyl	6.45
10	Cl	H	cyclohexyl	6.52
11	Br	methyl	methyl	5.25
12	Br	methyl	isopropyl	6.70
13	Br	H	t-butyl	6.15
14	Br	H	phenyl	6.52
15	Br	H	cyclohexyl	6.75
16	I	methyl	methyl	6.24
17	I	methyl	isopropyl	6.70
18	I	H	t-butyl	7.03
19	I	H	phenyl	6.86
20	I	H	cyclohexyl	6.65
21	NO ₂	H	H	3.00
22	NO ₂	H	methyl	3.70
23	NO ₂	H	s-butyl	5.10
24	NO ₂	H	t-butyl	5.79
25	NO ₂	H	cyclohexyl	6.05

Table 19 lists the best scores of correlation in decreasing order. From this table it can be seen that the monivariate and divariate regression are not satisfactory. Additional variables are needed for good statistics (entries 6-13).

Table 19.

Mono- and Multivariate Regression for Nitrophenols

No	X ₁	X ₂	X ₃	X ₄	X ₅	X ₆	R
1	1						0.9499
2	6	155					0.9709
3	7	174					0.9697
4	11	10620					0.9665
5	5	260					0.9662
6	13028	15806	91	15636			0.9908
7	13028	15806	12	15398			0.9901
8	12	15806	13891	15749			0.9907
9	7	13028	382	14214			0.9893
10	13028	15806	12	15398	15228	15865	0.9985
11	12	15806	13891	15749	15648	16378	0.9967
12	7	13028	382	14214	13186	16282	0.9965
13	13028	15806	91	15636	14064	14943	0.9956

The best model is given in eq 41 (see also entry 10, Table 19):

$$\begin{aligned} \text{Predicted activity} = & 8.062 - 0.003 \cdot \text{RGsDeM_p/d2PE2} + \\ & + 0.395 \cdot \text{1/DTsDiP_p*d_HE_} - 0.000008 \cdot \text{1/RTsDiPp2/d2HE2} \\ & - 229.564 \cdot \text{1/DGjDeMp2/d2PE2} + 0.003 \cdot \text{RGjDiPp2/d2HP_} \\ & + 0.004 \cdot \text{DTsDeP_p*d_HP2} \end{aligned}$$

$$R = 0.9985; s = 0.067; n = 25 \quad (41)$$

The plot of the predicted vs observed herbicidal activity, cf. eq 41, is shown in Figure 8.

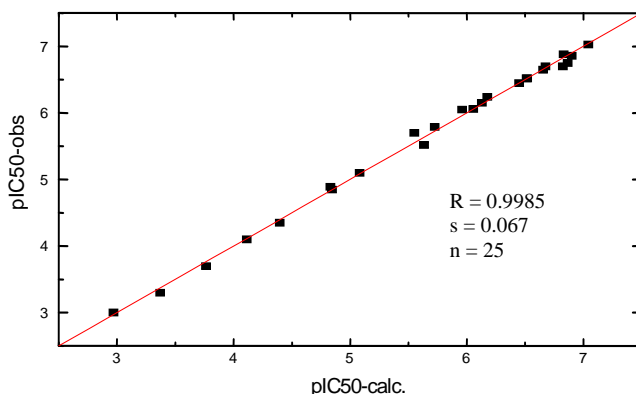


Figure 8. The plot of predicted vs. observed herbicidal activity.

The descriptors involved in eq 41 show a rather low inter-correlation (Table 20). The average absolute value of the pairwise correlation coefficients was 0.2200.

Table 20.

Intercorrelation of the indices in entry 10, Table 19.

	X ₂	X ₃	X ₄	X ₅	X ₆
X ₁	0.216489	0.6970	0.0674	0.1217	0.1710
X ₂		0.1371	0.0150	0.0609	0.2646
X ₃			0.2018	0.0397	0.2698
X ₄				0.6824	0.2219
X ₅					0.1337

The fragmental property indices take into account the chemical nature of atoms (mass and electronegativity), various kinds of interactions between the fragments of molecules and the 3D geometry of molecular structures.

Bivariate correlation with indices belonging to *FPIF* offer good quality models for quite diverse molecular properties such as the inhibition of mitodepressive activity on *Lepidium Savitium L.* ($R > 0.99$) and the aromatase inhibition as well. The same is true for the sum of one-electron energy calculated at the Extended-Hückel level ($R > 0.9999$).

Multivariate regression provided good models for the boiling points of a very diverse set of N-containing organic molecules or for the herbicidal activity.

Benzimidazole Derivatives

The correlating ability of *FPIF* was tested on a set of 15 molecular structures belonging to the class of benzimidazole²⁸. Derivatives of benzimidazole are known to show various biological activities.^{29,30}

The antiviral activity of a set of sixteen alkyl-benzimidazoles was proved by Tamm et al.³¹ This set was studied by Kier and Hall³² by using connectivity-type descriptors and recently by Estrada and Rodriguez,³³ by the aid of some sub-structural distance-based descriptors.

The first group of authors³² found the best model of the biological activity *BA* (as $\log(1/C)$) of benzimidazoles after excluding one (of sixteen structures) N-methyl- derivative:

$$BA = 1.11 + 1.40 \cdot {}^6\chi_P \quad (42)$$

$$n = 15; r = 0.950; s = 0.166; F = 120.3$$

where ${}^6\chi_P$ is the molecular connectivity index of the sixth path order.³³ The authors supposed it may act by a different mechanism.

The second group,³³ found another outlier in the remaining 15 members set: the compound no. 13 (see Table 18). They eliminated this compound by the following statistical tests: residuals, standardized residuals, studentized residuals and Cooks distance.^{35,36}

The new equation, in terms of Kier and Hall,³² is:

$$BA = 0.92 + 1.36 \chi_p \quad (43)$$

$$n = 14; r = 0.971; s = 0.125; F = 195.1$$

Estrada and Rodriguez³³ have modeled the antiviral activity of these benzimidazoles by using the number of pairs of homodistant vertices of different length in the graph. Their bivariate regression equation is:

$$BA = 0.26 + 0.0884\eta_{12} + 0.0599\eta_6 \quad (44)$$

$$n = 14; r = 0.976; s = 0.118; F = 110.7$$

where the first variable describes global molecular features and the second one is related to some specific paths in benzimidazoles.

Within this paper, we tried the modeling ability of the novel molecular descriptors *FPIF* on structures calculated by using MM+ (for 3D-geometries) and semiempirical AM₁ (for partial charge calculation) procedures of the HyperChem Program (HyperCube Inc.). The optimized geometries and partial charges thus obtained were submitted to the Cluj programmes. Topological indices and several properties are presented in ref 28. Table 21 shows the statistics of the regression analysis.

In *monovariate regression*, only the index DTjDeE_p/d2PE2 (read: Dense Topological, CJ- Detour, Electronegativity, property per squared distance, Product, Edge-calculated index) succeeded in giving a better model ($r = 0.9685$; $s = 0.132$, $n = 15$, entry 11). The *leave-one-out Loo* procedure indicated the *structure 13 as an outlier*, confirming the finding of Estrada. Table 21 clearly shows improved results for all the used indices in the set of 14 structures. Again, the index DTjDeE_p/d2PE2 was the best.

Table 21.

Statistics of Benzimidazole Regressions.

	Index	<i>n</i>	<i>a</i>	<i>b_i</i>	<i>r</i>	<i>s</i>	<i>cv %</i>	<i>F</i>
1	IP(Di)	15	1.8872	0.0069	0.9102	0.2197	7.020	62.7504
2	lnIP(Di)	15	-3.2524	1.2456	0.9428	0.1767	5.646	104.0777
		14	-3.1411	1.2174	0.9729	0.1205	3.905	212.2853
3	IP(RDe)	15	1.6298	0.1308	0.9292	0.1960	6.263	82.1537
4	ln(IP(RDe))	15	-0.2685	1.4228	0.9420	0.1780	5.689	102.3426
		14	-0.2293	1.3920	0.9735	0.1191	3.859	217.5559
5	IP2(CJDi)	15	2.0610	0.0011	0.8964	0.2351	7.511	53.1575
6	ln(IP2(CJDi))	15	-4.3584	1.1072	0.9443	0.1745	5.577	106.9970
		14	-4.2002	1.0792	0.9703	0.1260	4.084	192.9996
7	IP2(CFDi)	15	2.0286	0.0010	0.9018	0.2291	7.322	56.6254
8	ln(IP2(CFDi))	15	-4.5475	1.1155	0.9433	0.1761	5.627	104.8861
		14	-4.3974	1.0890	0.9716	0.1232	3.992	202.5371
9	IP2(SZDi)	15	2.2051	0.0006	0.8946	0.2370	7.572	52.0955
10	ln(IP2(SZDi))	15	-3.4295	0.9105	0.9390	0.1823	5.826	96.9773
		14	-3.3325	0.8922	0.9725	0.1213	3.932	209.1839

Table 21. (continued)

	Index	<i>n</i>	<i>a</i>	<i>b_i</i>	<i>r</i>	<i>s</i>	<i>cv</i> %	<i>F</i>
11	DTjDeE_p / d2PE2	15	7.3955	-0.0700	0.9685	0.1319	4.216	196.9635
		14	7.2489	-0.0680	0.9771	0.1109	3.595	252.6036
12	DTjDeE_p / d2PE2	15	9.7711	-0.0950	0.9822	0.1036	3.309	164.4465
				0.0885				
	lnDTsDiM_p / d2PE2	14	9.2202	-0.0888	0.9864	0.0893	2.896	198.4100
				0.0721				

Figure 9 shows the plot of DTjDeE_p/d2PE2 vs. **BA**, in the set of 14 benzimidazoles. This result surpasses the Estrada's results both in mono and bivariate regression.

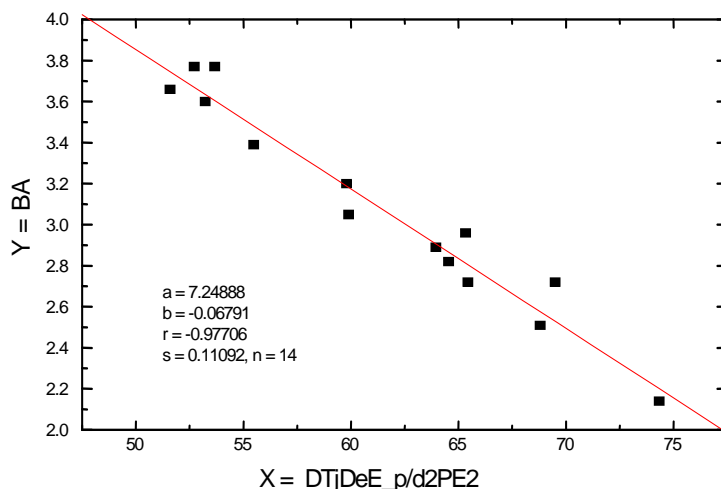


Figure 9. The best nomivariate regression model of antiviral activity of 14 Benzimidazoles

In bivariate regression, the best scored property index (above discussed) and lnDTsDiM_p/d2PE2 offered the best model (the covariance *cv* less than 3% - entry 12, Table 21) reported in literature.

$$\mathbf{BA} = 9.2202 - 0.0888 \cdot \text{DTjDeE_p / d2PE2} + 0.0721 \cdot \text{lnDTsDiM_p / d2PE2}$$

$$n = 14; r = 0.9864; s = 0.0893; cv \% = 2.896; F = 198.41 \quad (45)$$

Note that, in monivariate regression, the best four *FPIF* descriptors are of topological model (T - in the index symbol) and among the first ten descriptors only three are of geometric model (G). Similarly, in bivariate regression, the best three couples of indices are of topological model and only the fourth pair is mixed topological and geometric. It appears that the topology, reflecting the basic structure of imidazoles, is the dominant feature involved in their antiviral activity. The geometry comes as a fine tuning, that cannot, alone, decide the basic activity.

This result suggests that: the more suitable molecular description, the less outliers in modeling a chosen property of a set of compounds. The question: how large should be the drop in standard deviation (or variation in other statistical parameter) for assuming the *outlier* status for a given structure (or better, for its *measured* property) - is a matter of choice. Recall that the topological descriptors (even the Cluj *property* indices) are only mathematical properties of the molecular graphs representing chemical compounds and, therefore, no direct causal relationship can be addressed to QSAR equations.

Urea Derivatives

It is known that hydroxyureas inhibit the enzymatic conversion of ribonucleotides to deoxyribonucleotides.³⁷ The molecular mechanism of this inhibition is not known but QSAR studies³⁸ suggested that position and identity of substituents may control the ability of hydroxyureas to complex some metallo-enzymes possibly involved in.

In *monovariate regression*, the best model shows the statistics: $r = 0.96878$; $s = 9.096$; $cv\% = 10.07$ (column 4, Table 22). The best ten monovariate regressions show a variance $cv\%$ between 10 and 11.

In *bivariate regression*, the model is still improved:

$$BA = 84.905 - 13.909 \cdot \ln DGjDiP_p_GP2 + 2.035 \cdot DGsDeE_p \cdot d_PP2 \quad (46)$$

$n = 9$; $r = 0.99391$; $s = 4.367$; $cv\% = 4.834$; $F = 244.081$

The best ten monovariate regressions show a variance $cv\%$ between 5 and 6. Some best models, both in mono- and bivariate description, show a strong dependence of bioactivity by the molecular geometry (G in the symbol of indices) and electronic properties (partial charge P and electronegativity E).

Table 22.

Topological Data and Statistics for the Set of Hydroxyureas

No	Compound	BA	lnDGjDiP	lnRTsDeE_p	lnDGfDiP	DGsDeE_p	DGsDiE_p	lnDGsDeE
			_p_GP2	/d2HP2	_p_GP2	*d_PP2	*d_PP2	_p*d_PP2
1	Hydroxyurea HU	100	1.4641	0.1038	1.4641	20.0153	20.0153	2.9965
2	N-Methyl-HU	133	0.0465	0.1020	0.0465	23.8930	23.8930	3.1736
3	N-Ethyl-HU	91	3.2254	0.1148	3.2254	25.2829	25.2829	3.2301
4	N-Acetyl-HU	111	2.0073	0.1059	2.0073	25.5269	25.5269	3.2397
5	3-Phenyl-1-HU	38	4.9244	0.1729	4.6653	8.7658	14.8164	2.1709
6	Di-HU	108	1.5595	0.1087	1.5595	21.8853	21.8853	3.0858
7	N-Hydroxyurethane	92	2.2266	0.1282	2.2266	20.6392	20.6392	3.0272
8	N-Hydroxyguanidine	110	1.7146	0.1089	1.7146	20.8342	20.8342	3.0366
9	3-Phenyl-1-hydroxy -2-thiourea	30	5.2621	0.1783	4.9578	10.5093	16.7358	2.3523
			(1) ^a	(2)	(18)	(2716)	(7478)	(2021)

Table 22. (continued)

No	Compound	BA	lnDGjDiP	lnRTsDeE_p	lnDGfDiP	DGsDeE_p	DGsDiE_p	lnDGsDeE
			_p_GP2	/d2HP2	_p_GP2	*d_PP2	*d_PP2	_p*d_PP2
			monovar.			bivar.		
						lnDGjDiP	lnDGjDiP	lnDGfDiP
						_p_GP2 (1)	_p_GP2 (1)	_p_GP2 (18)
		<i>r</i>	0.9688	0.9658	0.9611	0.9939	0.9932	0.9913
		<i>s</i>	9.096	9.520	10.125	4.367	4.611	5.231
		<i>cv%</i>	10.070	10.539	11.208	4.834	5.105	5.791
		<i>F</i>	106.875	96.961	84.910	244.081	218.552	169.178
		<i>b₀</i>	139.260	229.056	140.865	84.905	71.330	20.173
		<i>b₁</i>	-19.632	-1111.106	-20.798	2.035	4.609	35.522
		<i>b₂</i>				-13.909	-12.234	-13.868

^a score in monovariate regression

CONCLUSIONS

Despite a correlational model does not involve a causal relationship between descriptors and a molecular property. However, a look upon the nature of the best scored fragmental property indices can give insight of the type of intra- and/or intermolecular interactions. The results are encouraging in case of modeling the activity vs *Bacillus subtilis* and *Candida albicans* as well as for the Rf index. They demonstrate the usefulness of our descriptors in modeling biological and physical properties of organic compounds.

FPIF offer good description for various molecular properties of this class of compounds: the antimicrobial and antifungal activity, surface tension ϵ , the antiviral activity of benzimidazoles, enzyme inhibiting activity of hydroxyureas, vapor pressure of PCBs and TLC Rf index. The fragmental property indices take into account the chemical nature of atoms (mass, electronegativity and partial charge), various kinds of interactions between the fragments of molecules as generated by Cluj criteria and the 3D geometry of molecular structures as well. As it is known, a correlational model does not involve a causal relationship between descriptors and a molecular property. However, a look upon the nature of most occurring **FIPF** indices with the best scores (and implicitly best structure description) can give insight of the type of intra- and/or intermolecular interactions. The above results demonstrate the usefulness of our descriptors in modeling biological and physical properties of organic compounds.

The original Cluj type indices demonstrated a good ability in modeling some important physico-chemical properties. In some the particular case, the recorded results surpass that reported in literature and can be used in predicting studies. It represents a promise for further **QSPR/QSAR** studies.

REFERENCES

1. S. M. Free and J. W. Wilson, *A mathematical contribution to structure-activity studies*, J. Med. Chem. **1964**, 7, 395.
2. M.V. Diudea, *Cluj matrix CJ_u : source of various graph descriptors*, Commun. Math. Comput. Chem. (MATCH), **1997**, 35, 169-183.
3. M.V. Diudea, O.M. Minailiuc, G. Katona, I. Gutman, *Szeged matrices and related numbers*, Commun. Math. Comput. Chem. (MATCH), **1997**, 35, 129-143.
4. M.V. Diudea, *Cluj matrix invariants*, J.Chem.Inf. Comput. Sci. **1997**, 37, 300-305.
5. M.V. Diudea, B. Pârv, M.I. Topan, *Derived Szeged and Cluj indices*, J. Serb. Chem. Soc. **1997**, 62, 267-276.
6. A.A. Kiss, G. Katona, M.V. Diudea, *Szeged and Cluj matrices within the matrix operator $W_{(M1,M2,M3)}$* Coll. Sci. Papers Fac. Sci. Kragujevac **1997**, 19, 95-107.
7. I. Gutman, M.V. Diudea, *Defining Cluj matrices and Cluj matrix invariants*, J. Serb. Chem. Soc. **1998**, 63, 497-504.
8. M.V. Diudea, G. Katona, I. Lukovits, N. Trinajstić, *Detour and Cluj-Detour Indices*, Croat. Chem. Acta, **1998**, 71, 459-471.
9. L. Jäntschi, G. Katona, M.V. Diudea, *Modeling molecular properties by Cluj indices*, Commun. Math. Comput. Chem. (MATCH), **2000**, 41, 151-188.
10. J.G. Topliss, R.P. Edwards, *Chance factors in studies of Quantitative Structure- Activity Relationships*, J. Med. Chem., **1979**, 22, 1238.
11. M. Randić, *On Molecular Identification Numbers*, J.Chem.Inf.Comput.Sci. **1984**, 24, 164-175.
12. F.R. Burden, *Molecular Identification Number for Substructure Search*, J. Chem. Inf. Comput. Sci. **1989**, 29, 225-227.
13. S.B. Elk, I. Gutman, *Further Properties Derivable from the Matula Numbers of an Alkane*, J.Chem.Inf.Comput.Sci. **1994**, 34, 54-57.
14. M.V. Diudea, A. Graovac, *Cyclic Graphs with Degenerate Sequences: A Study of Similarity*, Commun. Math. Comput. Chem. (MATCH), (submitted)
15. V. Pachaiyappan, S.H. Ibrahim, N.R. Kuloor, Chem. Eng. **1967**, 74, 193-196.
16. M. Cocchi, E. Johansson, *Amino Acids Characterization by GRID and Multivariate Data Analysis*. Quant. Struct.-Act. Relat., **1999**, 12, 1-8.
17. D. Opris, M.V. Diudea, *Peptide Property Modeling by Cluj Indices*, SAR/QSAR Environ.Res. **2001**, 12, 159-179
18. A. Zaliani, E.J. Gancia, *MS-WHIM Scores for amino-acids: a new 3D-description for peptide QSAR and QSPR Studies*. Chem. Inf. Comput. Sci., **1999**, 39, 525-533.
19. E.R. Collantes, W.J. Dunn III, *Amino acids side chain descriptors for Quantitative Structure-Activity relationship studies of peptide analogues*. J. Med. Chem., **1995**, 38, 2705-2713.
20. J. Jonsson, L. Eriksson, S. Hellberg, M. Sjöstroem, S. Wold, *Multivariate parametrization of 55 coded and non-coded amino acids*. Quant. Struct.-Act. Relat., **1988**, 8, 203-209.
21. S. Nikolić, M. Medić-Sarić, J. Matijević-Sosa, *A QSAR study of 3-(Phtalimidoalkyl)-pyrazolin-5-ones*, Croat. Chem. Acta, **1993**, 66, 151-160.
22. P.I. Nagy, J. Tokarski, A.J. Hopfinger, *Molecular shape and QSAR analysis of a family of substituted dichlorodiphenyl aromatase inhibitors*, J. Chem. Inf. Comput. Chem. **1994**, 34, 1190-1197.
23. M.D. Wessel, P.C. Jurs, *Prediction of normal boiling points for a diverse set of industrially important organic compounds from molecular structure*, J. Chem. Inf. Comput. Sci. **1995**, 35, 841-850.

24. D.T. Stanton, P.C. Jurs, *Development and use of charged partial surface area structural descriptors for Quantitative Structure-Property Relationships studies*. Anal. Chem. **1990**, 62, 2323.
25. E.S. Goll, P.C. Jurs, *Prediction of the Normal Boiling Points of Organic Compounds from Molecular Structures with a Computational Neural Network Model*, J. Chem. Inf. Comput. Chem. **1999**, 39, 974-983.
26. A.J. Stuper, W.E. Brugger, P.C. Jurs, *Computer-assisted studies of chemical structure and biological function*, Wiley-Interscience: New York, **1979**.
27. A. Trebst, W. Draber, Advan. Pest. Sci., Symp. Papers IV-th Int. Congress Pest. Chem., Zurich, Swiss, **1978**, pp. 223.
28. G. Katona, G. Turcu, T. Kiss, O.M. Minailiuc, M.V. Diudea, *QSAR/QSPR Studies by Cluj and Szeged Descriptors*, Rev. Roumaine Chim. **2001**, 46, 137-151.
29. A. Korolkovas, *Essentials in Molecular Pharmacology*, Wiley, New York, **1970**.
30. C. D. Nenitescu, *Organic Chemistry*, E. D. P. Bucuresti, **1986**.
31. I. Tamm; K. Folkers; C. H. Shunk; D. Hely; F. L. Horofall J. Exp. Med. **1953**, 98, 245.
32. L. H. Hall; L. B. Kier J. Pharm. Sci. **1978**, 67, 1743.
33. E. Estrada; L. Rodriguez, *Decomposition of the Wiener number into contributions coming from homodistant pairs of vertices. Definition and a QSAR application*, J. Serb. Chem. Soc. **1997**, 62, 199-205.
34. L. B. Kier; L. H. Hall *Molecular Connectivity in Chemistry and Drug Research* Acad. Press, **1976**.
35. D. A. Besley; E. Kuh; R. E. Welsch *Regression Diagnostics*, Wiley, New York, **1980**.
36. M. D. Wessel; P. C. Jurs, *Predicting of normal boiling points of hydrocarbons from molecular structure*. J. Chem. Inf. Comput. Sci. **1995**, 35, 68-76.
37. C. W. Young; H. Hodas, Science, **1964**, 146, 1172.
38. P.V. Khadikar; S. Karmarkar; S. Sharma; A. D. Seerwani; S. Joshi, *Estimation of the inhibition of DNA synthesis by the Wiener index*, J. Serb. Chem. Soc. **1997**, 62, 219-226.
39. O. Hutzinger; S. Safe; V. Zitko, *The Chemistry of PCBs*, CRC Press, Cleveland, **1974**.
40. M. D. Erickson, *Analytical Chemistry of PCBs*, Butterworth, Boston, **1968**.
41. Report of the Environmental Directorate of the Organisation for Economic Co-operation and Development, Paris, **1973**, 44.
42. R. L. Dufree; G. Contos; F. C. Whitmore; J. D. Barden; E. E. Wackman; R. A. Westin Report of the U. S. Environmental Protection Agency, Office of Toxic Substances, No. EPC 560/6-76-005 (NITS No. PB-25012), **1976**, 488.
43. S. Jensen, New Sci. **1966**, 32, 612.
44. D. J. Findly; F. H. Siff; V. J. Declaro, Report of the U. S. Environmental Protection Agency, No. EPA 5607-76-001 (N.T.I. S. No. PB - 253735) **1976**, 143.
45. J. Jatsukawa in *PCB Poisoning and pollution*, K. Higuetti, Ed., Acad. press, London, **1976**, 147.
46. D. H. Rouvray; W. Tatong, Int. J. Environ. Studies, **1989**, 33, 247.
47. S. Karmarkar; S. Karmarkar; S. Joshi; A. Das; P. V. Khadikar, *Novel application of Wiener vis-a-vis Szeged indices in predicting polychlorinated biphenils in the environment*, J. Serb. Chem. Soc. **1997**, 62, 227-234.
48. A.A. Kiss; G. Turcu; M. V. Diudea, *Correlating Studies by Cluj and Szeged Indices*, Studia Univ. Babes-Bolyai, **2001**, 45, 99-106.
49. M. Ardelean, G. Katona, I. Hopartean, M.V. Diudea, *Cluj Property Indices in Property Modeling*, Studia Univ. "Babes-Bolyai", **2001**, 45, 81-95.
50. M. Ardelean, *Master Dissertation*, Babes-Bolyai Univ., Faculty of Chemistry and Chemical Engineering, **2000**.

CURRENT ASPECTS OF THE POLYOXOMETALATE/ /METAL OXIDE-BASED CLUSTERS. I. GENERAL ASPECTS

ADRIAN PATRUT, ADRIAN NICOARA and DRAGOS MARGINEANU

*"Babes-Bolyai" University, Faculty of Chemistry and Chemical Engineering,
11 Arany Janos, 3400 Cluj-Napoca, Romania*

ABSTRACT. Current general aspects of the so-called polyoxometalate/metal oxide-based clusters are reviewed.

Anionic molecules, for which the term polyoxometalate clusters is accurate and similar neutral molecules, for which the term metal oxide-based clusters should be used are discussed.

The justification for using the term cluster in the case of polyoxometalate/metal oxide-based molecules, which contain only metal centres bonded exclusively through bridging oxygen atoms are presented.

Two generations of polyoxometalate/metal oxide-based clusters, named clusters of classic type, respectively clusters with supramolecular properties are also described and exemplified.

INTRODUCTION

Over the last ten years, the polyoxometalates have undergone a spectacular development surpassing even the most optimistic expectations of the relatively few research groups involved in investigations dedicated to this class of substances. The ceaseless diversification of polyoxometalates through the synthesis of an impressive number of new molecules having interesting electronic structures, high symmetry and unexpected topologies has broadened the frontiers of chemistry in a meso-physical world or nano-world, to be found somewhere between the micro- and the macroscopic realms [1].

All the above justifies, in our opinion, a review of certain current aspects of these amazing substances, in the wider context of the new tendencies and trends in chemistry.

The first part is dedicated to the presentation of several general aspects.

POLYOXOMETALATE/METAL OXIDE - BASED MOLECULES

According to a widely used definition, polyoxometalates (POMs) are the polyoxoanions of the early transition elements, especially Mo, W and V, constructed of linked MO_n units [2]. The M metal centres, which may belong to one or more atomic species, are named addenda.

Under the usual definition, POMs are exclusively anionic molecules (or molecular anions). The corresponding (electroneutral) compounds are in fact salts, usually hydrated, of the POM anions. For example, the yellow precipitate that is produced when ammonium molybdate is added to phosphoric acid, already described by Berzelius in 1826, correspond to the $(\text{NH}_4)_3[\text{PMo}_{12}\text{O}_{40}] \cdot n\text{H}_2\text{O}$ compound. Its main constituent is the molecular unit, namely the $[\text{PMo}_{12}\text{O}_{40}]^{3-}$ anionic molecule, which in fact represents the POM proper. But between the POM molecular anion and the NH_4^+ external cations there are only electrostatic interactions (i.e. ionic bonds) and the crystal water is linked to the compound, more precisely to the external cations and to the molecular unit, only through noncovalent bonds (i.e. hydrogen bonds).

However, recently, the situation has undergone a change, especially through the reduction of a number of metal centres and/or the introduction of other metal centres having lower oxidation numbers than those usually associated with POMs. Thus, molecules having identical or similar structures with well-known POMs but which are however electroneutral and not anionic, were obtained. Consequently, POM clusters with giant sphere-type structures are well-known especially through their prototype, the $[\text{Mo}_{72}^{\text{VI}}\text{Mo}_{60}^{\text{V}}\text{O}_{372}(\text{CH}_3\text{COO})_{30}(\text{H}_2\text{O})_{72}]^{42-}$ cluster, abridged as $[\text{Mo}_{132}]$ or $[\text{Mo}_{72}^{\text{VI}}\text{Mo}_{60}^{\text{V}}]$ [3]. But other molecules with similar structure containing only 102 metal centres were obtained, such as the $[\text{H}_4\text{Mo}_{72}^{\text{VI}}\text{Fe}_{30}^{\text{III}}\text{O}_{252}(\text{CH}_3\text{COO})_{12}(\text{H}_2\text{O})_{98}]$ cluster, abridged as $[\text{Mo}_{72}\text{Fe}_{30}]$ or $[\text{Mo}_{72}^{\text{VI}}\text{Fe}_{30}^{\text{III}}]$ [4], respectively the $[\text{Mo}_{72}^{\text{VI/V}}\text{Mo}_{30}^{\text{V}}\text{O}_{282}(\text{CH}_3\text{COO})_{12}(\text{H}_2\text{O})_{78}]$ cluster, abridged as $[\text{Mo}_{102}]$ or $[\text{Mo}_{72}^{\text{VI/V}}\text{Mo}_{30}^{\text{V}}]$ [5]. These cluster molecules are electroneutral. (It is to be mentioned that in the particular case of such electroneutral substances the terms compound and molecule are identical.)

It is obvious that for such neutral molecules the term POM with the ending -ate can no longer be used. They can be called simply metal oxide-based clusters, according to the term molybdenum-oxide based clusters used by Müller to designate the above mentioned molecules [4, 5].

We mention in passing that the term metal oxide-based (MOB) clusters is of a more general nature and can be applied to both electroneutral and electrically charged molecules (be they a anionic or, why not, even cationic). On the other hand, the traditional term POM clusters is valid only in the case of anionic molecules.

Possibly a hybrid term, such as polyoxometalate/metal oxide-based clusters, POM/MOB clusters for short, would be appropriate for covering completely the range of these remarkable molecules.

CLUSTERS WITHOUT DIRECT METAL-METAL BONDS

Initially the term (metal) cluster was used to designate coordination compounds which, instead of the central atom, contain a polyhedron made up of metal atoms linked by metal-metal bonds, forming a sort of cage surrounded

by ligands. Later on, the term cluster was extended to cover the compounds/molecules (the distinction compound-molecule is ignored again) also containing in the polyhedron non-metal atoms and having certain bridged by ligands (and not direct) metal-metal bonds. Currently, the term cluster is used for polymetallic compounds/molecules with direct metal-metal bond(s).

But, in the last few years, POM/MOB molecules are more and more frequently called clusters, although the bonds between metal centres are exclusively bridged by oxygen atoms. This could also be a consequence of the frequent use of the abridged formula of POM/MOB molecules, involving only heavy atoms (more precisely, the species acting as central atoms in a certain group of the molecule) which often are identical with the metal centres, e.g. $[\text{Mo}_{132}]$, $[\text{Mo}_{154}]$, $[\text{Mo}_{176}]$, $[\text{Mo}_{368}]$ etc.

Certain authors working directly in the POM field are in favour in this tendency, which extends the term cluster to cover all compounds/molecules having several metal centres, without going into any distinction as to the nature of the metal-metal bonds [6]. Other authors, especially those who have made their mark in other fields than POMs, question such an extrapolation and affirm that POMs and similar substances should be considered only cage compounds [7]. In fact, it is all a matter of option and preference.

Working in the POM chemistry, we will use the general term POM/ MOB clusters, also allowing the avoidance of the trap represented by the terms compound and molecule, frequent in the case of these substances.

TWO GENERATIONS OF POLYOXOMETALATE / /METAL OXIDE-BASED MOLECULES

As mentioned above, in the past ten years the chemistry of POM/MOB clusters brought about spectacular changes, due to the synthesis and characterization of giant molecules with new structures having high symmetry and remarkable topological and electronic properties. Consequently, we can talk about two distinct generation of POM/MOB clusters: one of classical type and another with supramolecular properties.

The classical POMs, which are exclusively anionic molecules, have the characteristics and properties of the traditional coordination compounds, more exactly of the molecules which form the so-called complex. They are obtained through simple intermolecular condensation of certain oxoanions that generates polyoxoanionic buildings. Depending on the nature of the oxoanion(s) involved in the condensation process and the pH value, a large number of POMs with various structures and properties were obtained. In an exaggeratedly simplified classification, polyoxometalates (POMs) are divided in isopolyoxometalates (IPOMs) and heteropolyoxometalates (HPOMs), while in the condensation

process are involved oxoanions from one or several atomic species. Rigorously speaking, in the case of IPOMs are present exclusively one or more atomic species with addenda role, while in the case of HPOMs are also present one or more atomic species with heteroatom role. The positions of the addenda and the heteroatom(s) are well defined for every structure.

20-30 years ago, the chemistry of IPOMs had become a closed area, with very limited perspectives of future development. The maximal number of metal centres seems to be limited to 10-12 atoms. On the other hand, the HPOM chemistry field knew a constant if not spectacular development. The presence of another atomic species having heteroatom role, which can be selected from about 70 elements of the periodic table, gives to the POMs not only more stability, a larger variety or the possibility of increasing the number of metal centres, but also new properties which allow for new applications. Practically, until quite recently, the POM chemistry was concentrated almost exclusively on the synthesis and investigation of new HPOMs, to which are added the research of new application.

Our chosen example of classical POM is a cluster synthesized and characterized by us, with the formula $[H_3Sb^{III}V^{IV}W_{17}O_{60}]^{8-}$, not published until now [8]. The corresponding neutral compound is $Na_2(NH_4)_6[H_3Sb^{III}V^{IV}W_{17}O_{60}] \cdot 16H_2O$.

Single-crystal X-ray diffraction analysis shows that the anionic HPOM molecule is made up of two halves, each of trilacunary Keggin-type, i.e. $[SbM_9O_{33}]$ and $[M_9O_{33}]$, linked by corners and edges and sharing six O atoms, see Fig. 1. Practically, the Sb^{III} heteroatom is statistically distributed between the two halves. The Sb^{III} heteroatom is tricoordinated building a trigonal SbO_3 pyramid in the $[SbM_9O_{33}]$ unit. The unshared pair of electrons of Sb^{III} which has a nonbonding character is pointed towards the other half-anion.

The 17 W atoms and the V^{IV} atom, which belong to the two atomic species having an addenda role, can occupy any of the 18 addenda position noted with M (M=W, V). Practically, all the 18 addenda atoms are delocalized and cannot be differentiated. (We dislike to consider and to call the V^{IV} centre, which occupy an addenda position, as secondary heteroatom.)

It should also be mentioned the fact that every M addendum/metal centre is located in the centre of a distorted MO_6 octahedron. The addenda occupy off-centre position towards the external edges, due to certain $\pi M \rightarrow O$ ($d\pi-p\pi$) bonds, which reinforce the coordinative covalent $M \leftarrow O$ bonds. Each M metal centre has only one terminal O atom.

All the bonds figured in the ORTEP diagram are covalent, namely the bonds between addenda/metal centres and oxygen atoms, respectively between the heteroatom and oxygen atoms, i.e. M-O and X-O. As can be noticed, the addenda/metal centres are linked between each other and with the heteroatom exclusively by oxygen bridged covalent bonds.

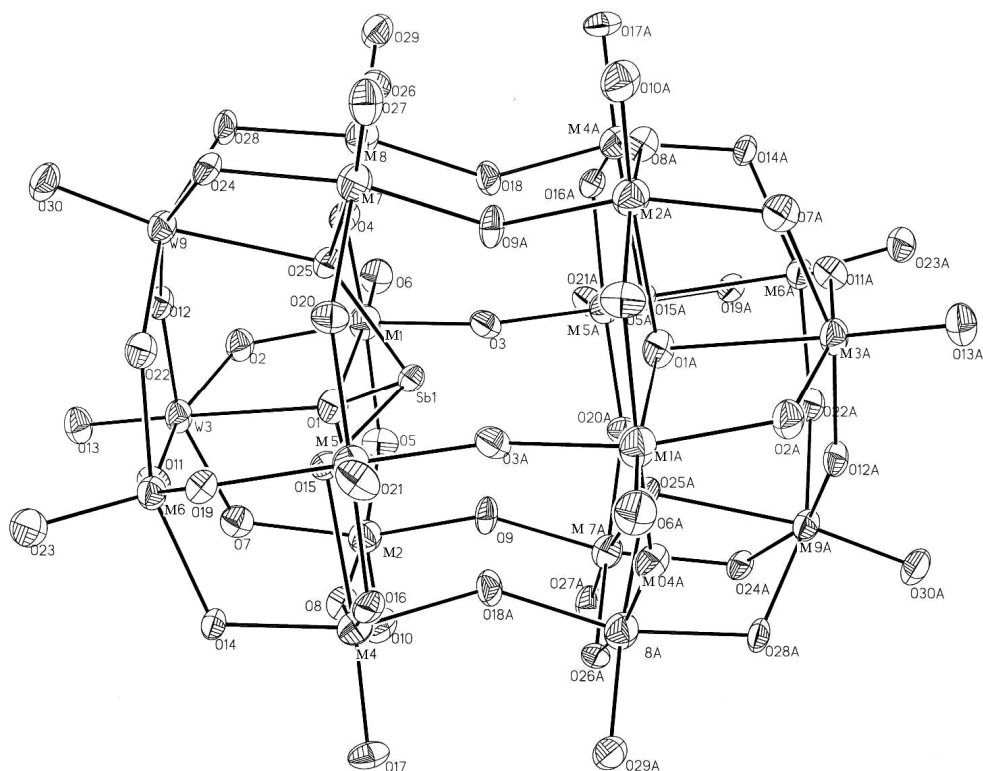


Fig. 1. ORTEP diagram of the $[\text{H}_3\text{Sb}^{\text{III}}\text{V}^{\text{IV}}\text{W}_{17}\text{O}_{60}]^{8-}$ HPOM cluster (M=W, V).

Investigations on POM clusters with the general formula $[\text{H}_n\text{XM}_{18}\text{O}_{60}]^{P-}$ have revealed that the $n\text{H}$ atoms are non-ionizable and belong to the anionic building. Evidently, the small H atoms cannot be identified by single-crystal X-ray diffraction analysis. Given that Keggin-type and Keggin-derived structures with central lacunae (in the place reserved for the heteroatom) are not known, Krebs and Klein consider that the non-ionizable H atoms are to be found inside the O_3 cavity [9]. The nature of the bonds in the unusual H_3O_3 group is not known, but it is probably the case of weak multicentre covalent bonds.

The $[\text{H}_3\text{Sb}^{\text{III}}\text{V}^{\text{IV}}\text{W}_{17}\text{O}_{60}]^{8-}$ HPOM anion has a C_3 symmetry axes and an orthogonal symmetry plane. Because it shows similarities but also differences compared to the well-known Dawson structure of the HPOMs with the formula $[\text{X}_2\text{M}_{18}\text{O}_{62}]^{9-}$, Krebs and Klein proposed the term non-Dawson for the HPOMs with a structure similar to the one studied by us, having the general formula $[\text{H}_n\text{XM}_{18}\text{O}_{60}]^{P-}$. As we have serious reservation concerning the use of the prefix non- in denominations, we prefer to name this structure pseudo-Dawson.

The new generation of POM/MOB clusters appeared only around ten years ago, but its representatives became instantly well-known worldwide and their reputation has gone beyond the realm of chemistry, mainly as a result of the Bielefeld University research team led by Achim Müller.

The new generation of very large POM/MOB molecules is based upon a novel synthesis strategy that allows, on the basis of a number of simple combinatory linkable building blocks/units at disposition, the obtaining by successive and rapid processes of self-assembly, self-organization and molecular growth of a large variety of huge molecules. The basic chemical principles for the synthesis of the new giant molecular species are: the existence of a library of linkable building blocks/units, the presence of reducing agents in the system to reduce a number of metal centres, the introduction of heteroatoms with different oxidation numbers, the introduction and/or exchange of various ligands other than oxygen (the oxide ion), which offer the possibility to tune the electron density etc. [10-13].

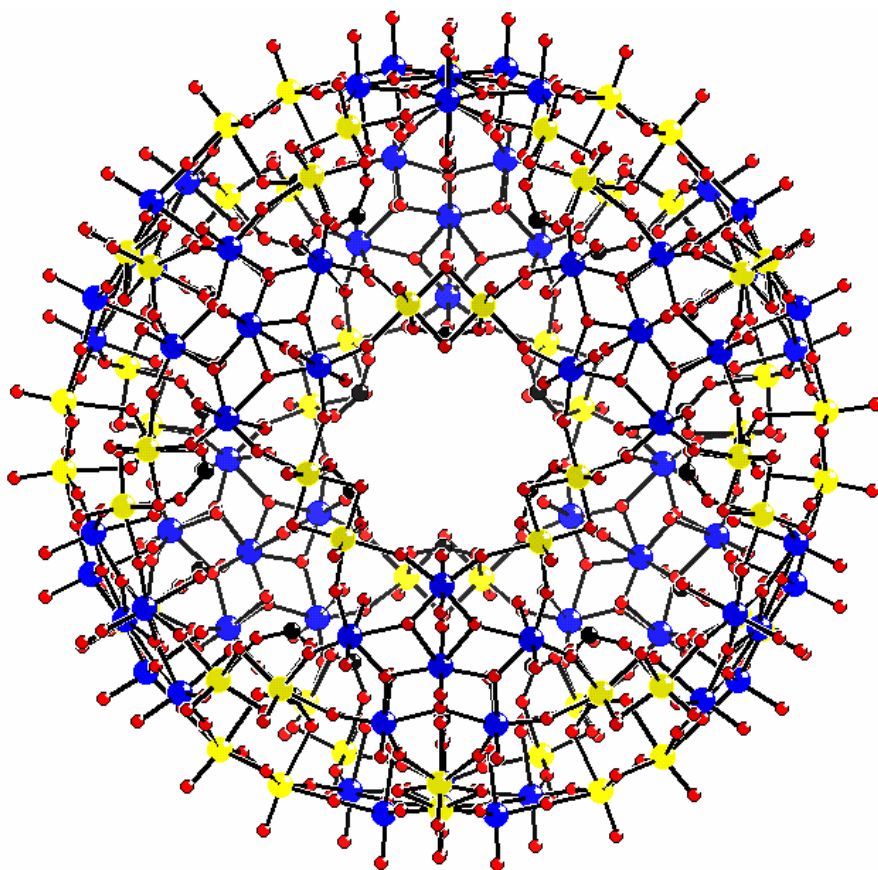


Fig. 2. The $[\text{Mo}^{\text{VI}}_{72}\text{Mo}^{\text{V}}_{60}\text{O}_{372}(\text{CH}_3\text{COO})_{30}(\text{H}_2\text{O})_{72}]^{42-} \equiv [\text{Mo}_{132}]$ POM cluster in ball-and-stick representation. Color code: Mo^{VI} blue, Mo^{V} yellow, C black, O red.

In the case of classical POM/MOB clusters, the most interesting structures belong to the HPOMs with W as addendum. Somewhat surprisingly, the new generation of POM/MOB clusters developed inside or within the IPOMs with Mo as addendum. This is due mainly to the fact that Mo can offer a much larger variety of linkable building blocks and the reduction of certain Mo^{VI} to Mo^{V} metal centres occurs more easily than in the case of W. However, for the new generation of POM/MOB clusters the distinction iso-/hetero- is surpassed. The specific positions of the (metal) centres are those of addendum and linker/spacer, which are localized in the centre of building blocks/units and linker/spacer units.

The mixed valence $[\text{Mo}^{\text{VI}}_{72}\text{Mo}^{\text{V}}_{60}\text{O}_{372}(\text{CH}_3\text{COO})_{30}(\text{H}_2\text{O})_{72}]^{42-}$ POM cluster, abridged as $[\text{Mo}_{132}]$ or $[\text{Mo}^{\text{VI}}_{72}\text{Mo}^{\text{V}}_{60}]$, obtained in 1999 by Müller and his team, is probably the most aesthetically molecule synthesized so far [3]. The spherical $[\text{Mo}_{132}]$ POM cluster is constructed of 12 $[\text{Mo}^{\text{VI/V}}_{11}]$ building blocks, which can also be decomposed in 12 $[(\text{Mo}^{\text{VI}})\text{Mo}^{\text{V}}_5\text{O}_{21}(\text{H}_2\text{O})_6]^{6-} \equiv [(\text{Mo}^{\text{VI}})\text{Mo}^{\text{V}}_5]$ and 30 $[\text{Mo}^{\text{V}}_2\text{O}_4(\text{CH}_3\text{COO})]^+ \equiv [\text{Mo}^{\text{V}}_2]$ units, the latter with linker/spacer role.

The so-called "giant sphere" structure of the $[\text{Mo}_{132}]$ cluster having an overall icosahedral symmetry is presented in Fig. 2.

All the bonds between the atoms of the $[\text{Mo}_{132}]$ POM cluster are covalent. These demonstrate that the term "the new generation of very large supramolecular POM clusters" we used in a previous review could be considered exaggerated [14]. If in the case of molecules, the mandatory characteristic is the existence of covalent bonds between the constituent atoms, to which possibly other bonds can be added, supramolecules are characterized by the mandatory presence of noncovalent bonds and by certain special properties. These special properties (the presence of a few is sufficient) are: multicomponent nature, cooperative action of the components, self-assembly and even self-organization, host-guest interactions etc.

A first observation is that usually the supramolecule is not also a discrete molecule, but rather an assembly/entity of discrete molecules linked by noncovalent bonds. Initially Lehn, one of the fathers of supramolecular chemistry, considered that the unusual properties of supramolecules, which open up new avenues in chemistry, are mainly due to the existence of noncovalent bonds. He even defined supramolecular chemistry as "the chemistry of noncovalent bonds" [15].

Perhaps it would have been better to define supramolecules exclusively by their characteristic properties, that truly bring something new to chemistry, and not through the existence of certain types of bonds. And that because it was consequently demonstrated that there exist substances, and we mean especially the POM/MOB clusters, having the properties of supramolecules but lacking noncovalent bonds. And not only that but the largest synthesized and structurally characterized molecules, which contain up to 368 metal centres, belong to these very clusters.

As a consequence, we appreciate that the new generation of the molecules under discussion could be named POM/MOB clusters with supramolecular properties or pseudosupramolecular POM/MOB clusters.

The second part of the review will be dedicated to the presentation of certain special aspects of these clusters with supramolecular properties.

Acknowledgement. The authors would like to thank Prof. Dr. Dr. h. c. mult. Achim Müller and Dr. Hartmut Bögge for providing the figures included in this paper.

REFERENCES

1. Patrut, A., Nicoara, A., Margineanu, D., Botar, A., *Acta Univ. Cibiniensis, Ser. F, Chemia*, **2002**, 5, 7.
2. Pope, M.T., Müller, A., in *Polyoxometalate Chemistry: From Topology via Self-Assembly to Applications* (eds. M.T. Pope and A. Müller), Kluwer, Dordrecht, 2001, p. 3.
3. Müller, A., Krickemeyer, E., Bögge, H., Schmidtman, M., Peters, F., *Angew. Chem. Int. Ed.*, **1998**, 37, 3360.
4. Müller, A., Sarkar, S., Shah, S.Q.N., Bögge, H., Schmidtman, M., Sarkar, S., Kögerler, P., Hauptfleisch, B., Trautwein, A.X., Schünemann, V., *Angew. Chem. Int. Ed.*, **1999**, 38, 3238.
5. Müller, A., Shah, S.Q.N., Bögge, H., Schmidtman, M., Kögerler, P., Hauptfleisch, B., Leiding, S., Wittler, K., *Angew. Chem. Int. Ed.*, **2000**, 30, 1614.
6. A. Müller, private communication, 2001.
7. I. Haiduc, private communication, 2002.
8. Patrut, A., Botar, B., Botar, A., Nicoara, A., Margineanu, D., Schmidtman, M., to be published.
9. Krebs, B., Klein, R., in *Polyoxometalates: From Platonic Solids to Anti-Retroviral Activity* (eds. M.T. Pope and A. Müller), Kluwer, Dordrecht, 1994, p. 41.
10. Müller, A., Kögerler, P., *Coord. Chem. Rev.*, **1999**, 182, 3.
11. Müller, A., Kögerler, P., Kuhlmann, C., *Chem. Commun.*, **1999**, 1347.
12. Müller, A., Kögerler, P., Bögge, H., *Struct. Bond.*, **2000**, 96, 203.
13. Müller, A., Kögerler, P., Dress, A.W.M., *Coord. Chem. Rev.*, **2001**, 222, 193.
14. Patrut, A., Nicoara, A., Margineanu, D., *Studia Univ. Babeş-Bolyai, Ser. C, Chemia*, **2002**, 47, 13.
15. Lehn, J.M., *Supramolecular Chemistry: Concepts and Perspectives*, VCH, Weinheim, 1995.

CURRENT ASPECTS OF THE POLYOXOMETALATE/ METAL OXIDE-BASED CLUSTERS. II. SPECIAL ASPECTS

ADRIAN PATRUT, ADRIAN NICOARA and DRAGOS MARGINEANU

*"Babes-Bolyai" University, Faculty of Chemistry and Chemical Engineering,
11 Arany Janos, 3400 Cluj-Napoca, Romania*

ABSTRACT. Current special aspects of the polyoxometalate/metal oxide-based clusters are presented and discussed.

Polyoxometalate/metal oxide-based clusters with infinite molecules, generated through an inflationary multiplication of a certain discrete molecule, are described and exemplified.

Supramolecular entities that consist of a guest polyoxometalate / metal oxide-based cluster incorporated in the cavity of a larger host polyoxometalate/metal oxide-based cluster are also presented and exemplified.

Eventually, a new complex system of 100 water molecules encapsulated in the internal cavity of the $[Mo_{132}]$ "giant sphere", having the surface pores closed by organic cations, is presented. The probability that this new system with amazing symmetry could open the way towards a new super-supramolecular chemistry is discussed.

The first part of the presentation of certain current aspects of the polyoxometalate/metal oxide-based (POM/MOB) clusters was dedicated to some general aspects [1]. The second part is reserved for the presentation of several special aspects concerning mostly the new generation of these clusters having supramolecular properties.

POLYOXOMETALATE/METAL OXIDE-BASED CLUSTERS WITH INFINITE MOLECULES

The great majority of POM/MOB clusters are discrete/individual molecules, generated by condensation of the corresponding oxoanions. But sometimes the condensation process may continue, resulting eventually in infinite/collective molecules. These infinite clusters are molecular assemblies, generated through an inflationary multiplication of a discrete molecule in one, two or three dimensions, with formation of chain (1D), layers (2D) or networks (3D).

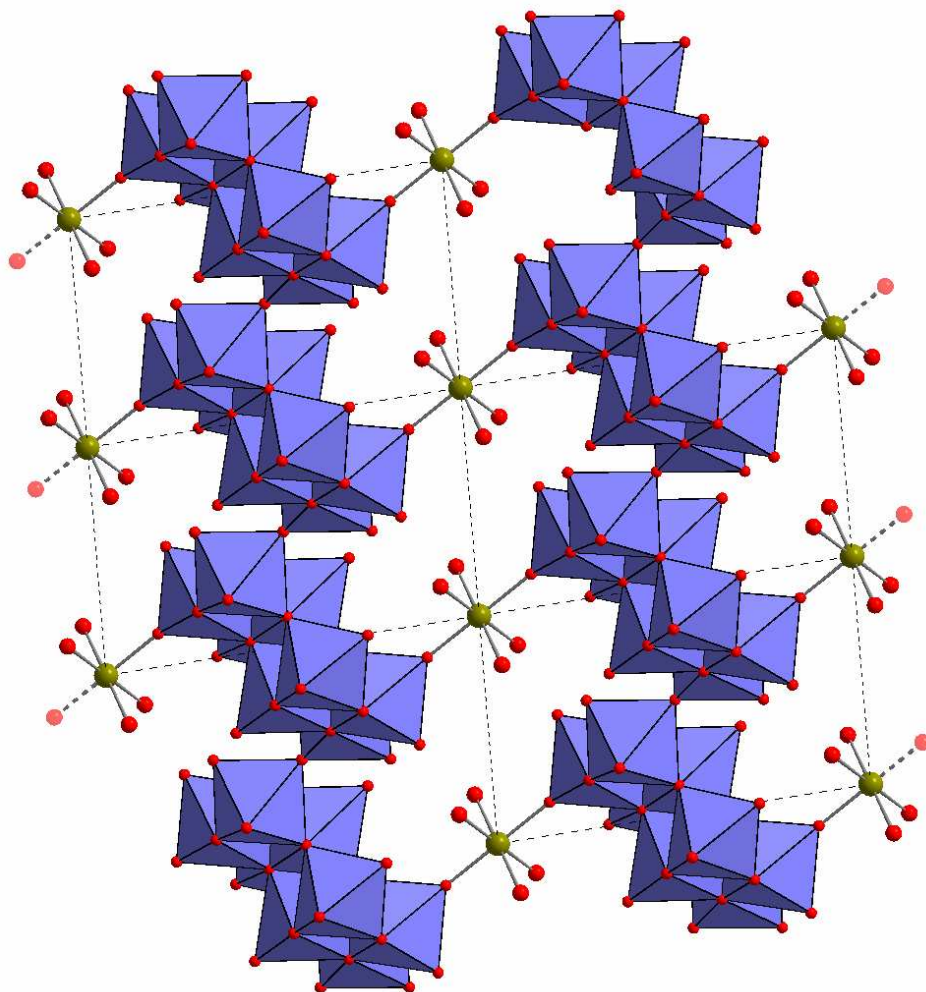


Fig. 1. Section of a $[\text{Fe}(\text{H}_2\text{O})_4\text{Mo}_8\text{O}_{27}]_\infty$ layer showing the $[\text{Mo}_8\text{O}_{27}]^{6-}$ fragments in polyhedral representation and the octahedral Fe^{II} coordination sphere in ball-and-stick representation. The Fe centres form parallelograms in the ac plane. Color code: $[\text{Mo}_8\text{O}_{27}]$ = blue; Fe = yellow; O = red.

We shall illustrate the POM/MOB clusters with infinite molecules by presenting the structure of an interesting layer cluster, not published until now [2].

Initially, the chemical analyses suggested the formula $\text{Na}_4[\text{Fe}^{\text{II}}(\text{H}_2\text{O})_4\text{Mo}_8\text{O}_{27}] \cdot 16\text{H}_2\text{O}$ for the corresponding neutral compound. But the fact that the compound is insoluble in water indicates a more complex structure. Consequently, the single-crystal X-ray diffraction analysis revealed that the compound and the corresponding POM/MOB cluster have a layer-type structure, composed of $[\text{Mo}_8\text{O}_{27}]_\infty$ chains cross-linked by partially hydrated Fe^{II} centres.

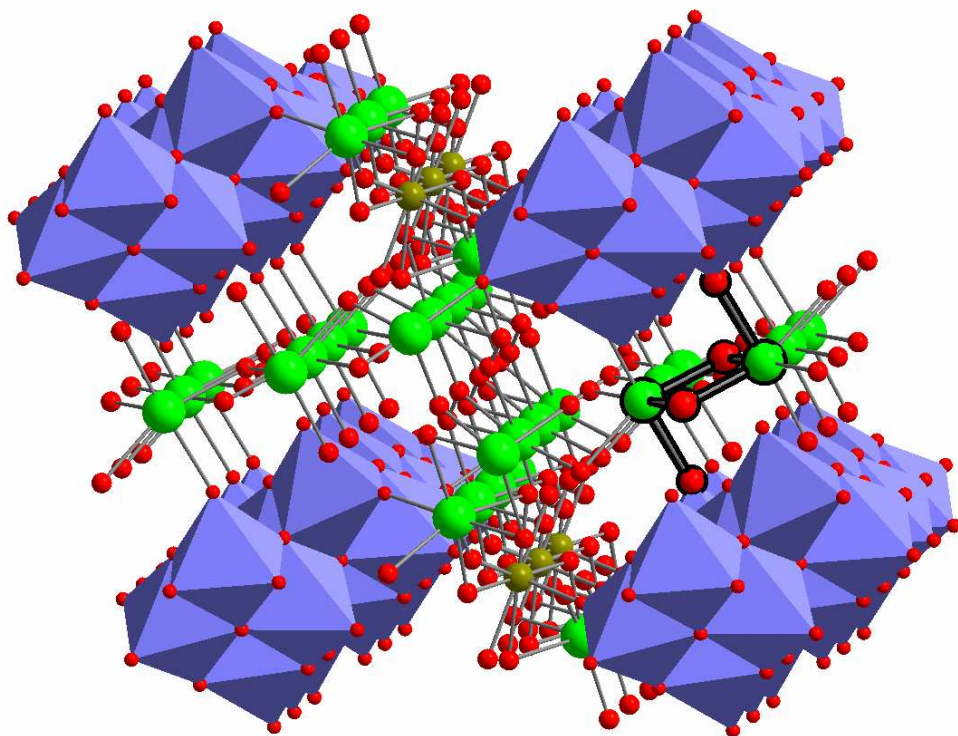


Fig. 2. Linking of two $[\text{Fe}(\text{H}_2\text{O})_4\text{Mo}_8\text{O}_{27}]_\infty$ layers (shown as section of each 2×3 connected $[\text{Mo}_8\text{O}_{27}]^{6-}$ fragments) by stacked Na centres. One O-Na-(H₂O)₂-Na-O group is emphasized. Color code: $[\text{Mo}_8\text{O}_{27}] = \text{blue}$; Fe = yellow; Na = green; O = red.

The basic fragment $[\text{Mo}_8\text{O}_{27}]^{6-}$ is built up of eight MoO_6 edge sharing octahedra. The $[\text{Mo}_8\text{O}_{27}]^{6-}$ units are linked through bridging O atoms belonging to Mo-O-Mo groups, forming $[\text{Mo}_8\text{O}_{27}]_\infty$ chains parallel to the crystallographic *a* axis. Each chain is cross-linked to an adjacent chain through Fe-O-Mo bridges, parallel to the *c* axis, thus forming a $[\text{Fe}(\text{H}_2\text{O})_4\text{Mo}_8\text{O}_{27}]_\infty$ layer in the *ac* plane. The Fe^{II} centres form intra-layer parallelograms having identical dimensions to those of the parallelograms spanned by the crystallographic *a* and *c* axes, see Fig. 1.

It should be also noticed that chains of Na⁺ ions based on staggered groups of four Na centres extend parallel to the *c* axis between the layers. Five H₂O ligands and one O atom from a $[\text{Mo}_8\text{O}_{27}]^{6-}$ unit are linked to each Na centre, which is also connected to an adjacent Na centre through two Na-H₂O-Na bridges and to one $[\text{Mo}_8\text{O}_{27}]^{6-}$ unit through a Na-O-Mo bridge. This determines additional cross-linking within and between the $[\text{Fe}(\text{H}_2\text{O})_4\text{Mo}_8\text{O}_{27}]_\infty$ layers through formal Mo-O-Na-(H₂O)₂-Na-O-Mo linkages, see Fig. 2.

The structure of the presented layer cluster with $[\text{Fe}^{\text{II}}(\text{H}_2\text{O})_4\text{Mo}_8\text{O}_{27}]_{\infty}$ chains is similar to that of another layer cluster having $[\text{Mn}^{\text{II}}(\text{H}_2\text{O})_4\text{Mo}_8\text{O}_{27}]_{\infty}$ chains [3].

PURE SUPRAMOLECULAR POLYOXOMETALATE/METAL OXIDE-BASED CLUSTER ENTITIES

In the first part of the study we underlined that the new generation of the substances under discussion, having only covalent bonds between atoms, can be named POM/MOB clusters with supramolecular properties or pseudo-supramolecular clusters.

On the other hand, the fact that POM clusters have internal cavities which can incorporate/enclose small atoms or molecules (neutral, cationic or anionic), thus building supramolecular entities was well known. For instance, the cage of certain polyoxovanadates acting as host can encapsulate simultaneously cations and anions, such as $[(2\text{NH}_4^+, 2\text{Cl}^-) \subset \text{V}_{14}\text{O}_{22}(\text{OH})_4(\text{H}_2\text{O})(\text{C}_6\text{H}_5\text{PO}_3)_8]^{6-}$ [4, 5]. The cage of the POM cluster consists of two half-shells formed from isopolyoxovanadate and phenylphosphonate units. The central guest $(2\text{NH}_4^+, 2\text{Cl}^-)$ system is a cation/anion aggregate encapsulated within the cavity of the host POM cluster, which is formally separated into two segments by two H_2O molecules bound to V^{IV} centres. The two H_2O molecules stabilize the guest $(2\text{NH}_4^+, 2\text{Cl}^-)$ system by hydrogen bonds.

But very recent research which started in 2000, led to the synthesis of certain pure POM/MOB clusters which are truly supramolecular, having all the characteristics and properties nominalized for these substances/entities. Thus, several supramolecular entities which consist of a POM/MOB cluster (guest, nucleus) incorporated in the cavity of a larger POM/MOB cluster (host, capsule) have been synthesized.

The first such example is the

$[\text{H}_x\text{PMo}_{12}\text{O}_{40} \subset \text{H}_4\text{Mo}^{\text{VI}}_{72}\text{Fe}^{\text{III}}_{30}\text{CH}_3\text{COO}]_{15}\text{O}_{254}(\text{H}_2\text{O})_{98}$ ca. 60 H_2O supramolecular entity, abridged as $[\text{PMo}_{12} \subset \text{Mo}^{\text{VI}}_{72}\text{Fe}^{\text{III}}_{30}] \cdot \text{ca. 60 H}_2\text{O}$. The supramolecular MOB entity consists of two POM/MOB clusters [6, 7]:

- an oxidized icosahedral capsule as host, corresponding to the $[\text{Mo}^{\text{VI}}_{72}\text{Fe}^{\text{III}}_{30}]$ cluster (internal cavity diameter $\approx 16 \text{ \AA}$);
- a Keggin molecule as nucleus or guest, corresponding to the reduced $[\text{H}_x\text{PMo}_{12}\text{O}_{40}]^{3-}$ ($x=1-2$) POM cluster (diameter $\approx 12 \text{ \AA}$).

The novel pure POM/MOB supramolecular entity is presented in Fig. 3.

The noncovalent host-guest interaction indicates that the reduced Keggin cluster fits exactly into the capsule cavity. The shortest $\text{O}_{\text{host}} \cdots \text{O}_{\text{guest}}$ bond lengths of $\approx 2.6 \text{ \AA}$ are typical for hydrogen bonding. The new absorption band observed in visible at $\approx 550 \text{ nm}$, which contributes to the dark green colour of the compound, was temporarily assigned to a new electronic transition of the type reduced nucleus \leftrightarrow oxidized capsule, but this assumption need to be confirmed [6].

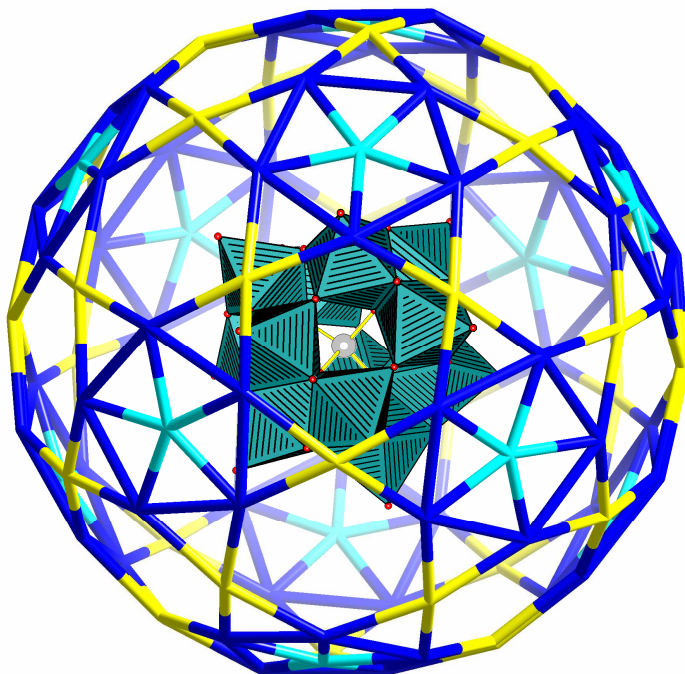


Fig. 3. Structure of the supramolecular $[\text{PMo}_{12} \subset \text{Mo}^{\text{VI}}_{72}\text{Fe}^{\text{III}}_{30}]$ entity. The $[\text{Mo}_{72}\text{Fe}_{30}]$ capsule (host) is figured in wire frame representation with the 30 Fe^{III} centres (highlighted as yellow wires) linking the 12 $[(\text{Mo})\text{Mo}_5]$ pentagons (figured in blue and turquoise). The reduced $[\text{PMo}_{12}]$ nucleus (guest) is shown in polyhedral representation (with the P heteroatom as gray large sphere and the O atoms as small red spheres).

THROUGH POLYOXOMETALATE/METAL OXIDE-BASED CLUSTERS TOWARDS A NEW SUPER-SUPRAMOLECULAR CHEMISTRY?

The huge spherical POM/MOB clusters with giant sphere-type structure having overall icosahedral symmetry can also be formulated, according to a building block principle, as $(\text{pentagon})_{12}(\text{linker})_{30}$. The prototype is the very large $[\text{Mo}^{\text{VI}}_{72}\text{Mo}^{\text{V}}_{60}\text{O}_{372}(\text{CH}_3\text{COO})_{30}(\text{H}_2\text{O})_{72}]^{42-}$ POM cluster, abridged as $[\text{Mo}_{132}]$ or $[\text{Mo}^{\text{VI}}_{72}\text{Mo}^{\text{V}}_{60}]$ [8, 9]. Like all clusters with identical or similar structure, the pentagons are represented by 12 $[(\text{Mo}^{\text{VI}})\text{Mo}^{\text{VI}}_5\text{O}_{21}(\text{H}_2\text{O})_6]^{6-}$ units, abridged as $[(\text{Mo}^{\text{VI}})\text{Mo}^{\text{VI}}_5]$. In the case of the $[\text{Mo}_{132}]$ cluster, 30 $[\text{Mo}^{\text{V}}_2\text{O}_4(\text{CH}_3\text{COO})]^+$ units, abridged as $[\text{Mo}^{\text{V}}_2]$, act as linkers/spacers.

The 12 pentagonal units and the 30 linkers/spacers, out of which the $[\text{Mo}_{132}]$ giant sphere is built up, allow not only overall object sizing but also a sizing of the large number of tailor-made pores. The 20 $[\text{Mo}_9\text{O}_9]$ pores on the surface are rings with diameters between $\approx 0.6\text{-}0.8$ nm.

The $[\text{Mo}_{132}]$ POM cluster with an external diameter of ≈ 2.9 nm has a large internal cavity having a diameter of ≈ 2.0 nm. The 20 pores are large enough to allow the passage of small spheres into the internal cavity. The fact that the $[\text{Mo}_{132}]$ POM cluster normally contains 100 encapsulated H_2O molecules was known. Interacting through the open pores with the crystal water, the assembly of 100 H_2O molecules has no special organization.

But late 2002 brought an unexpected surprise [10, 11]. If the 20 surface pores/rings, having receptor properties, are filled with organic ions, such as $[(\text{NH}_2)_3\text{C}]^+$ guanidinium cations, which fit exactly into the pores, the whole giant sphere surface becomes closed, see Fig. 4.

Closing the pores decreases the high negative charge of the cluster, stabilizes it and, especially, influences the structure of the encapsulated $[\text{H}_2\text{O}]_{100}$ system. Consequently, the 100 H_2O molecules are organized in a highly symmetrical spherical structure, in which $3 \times 12 = 36$ pentagons built up of H_2O molecules can be identified, see Fig. 5.

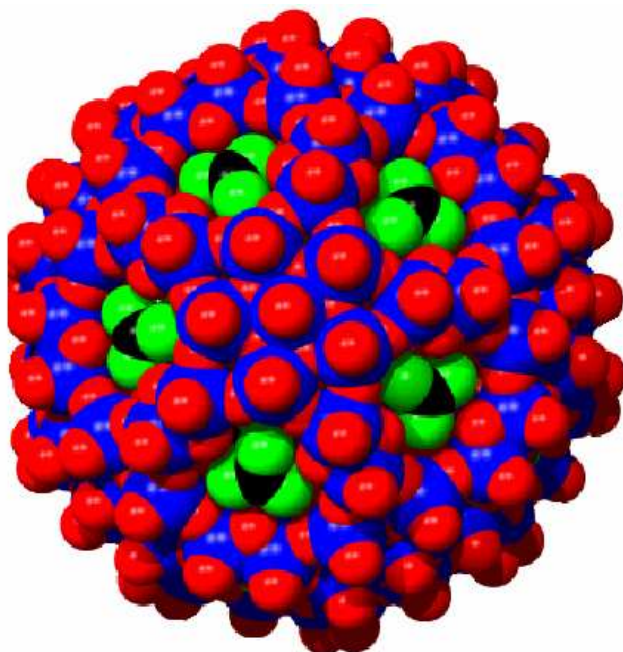


Fig. 4. Space filling representation of the $[\text{Mo}_{132}]$ POM cluster with the 20 pores closed with $[(\text{NH}_2)_3\text{C}]^+$ guanidinium cations. Color code: Mo=blue, O=red, C=black, N=green.

The amazing $[\text{H}_2\text{O}]_{100}$ aggregate/system consists of two Platonic solids, namely two dodecahedrons having each 20 pentagons as faces, and a very complex Archimedean solid, namely a rhombicosidodecahedron with 12 decagons, 20 hexagons and 30 tetragons as faces. Thus, the $[\text{H}_2\text{O}]_{100}$ system

has in its centre a $[\text{H}_2\text{O}]_{20}$ dodecahedron, which is inside another larger $[\text{H}_2\text{O}]_{20}$ dodecahedron, surrounded in its turn by a $[\text{H}_2\text{O}]_{60}$ a rhombicosidodecahedron, see Fig. 6. The 100 H_2O molecules are thus linked that they form altogether a novel icosahedral cluster with tetrahedrally coordinated O atoms. (Each H_2O molecule is tetrahedrally surrounded by other four H_2O molecules.)

Such an auto-organization leading to structures never before met in chemistry is unprecedented. That is why, Müller considers that this could open the way towards a new super-supramolecular chemistry. He states that "we could now cross the frontier (of supramolecular chemistry) to a rather large multitude of receptor sites positioned on a stable nanoobject". While it became evident that a receptor-substrate supramolecule is characterized by its geometric, thermodynamic and kinetic features, new categories of receptor-substrate types appear in the present super-supramolecule and offer the chance to study a variety of relevant cooperative effects [10].

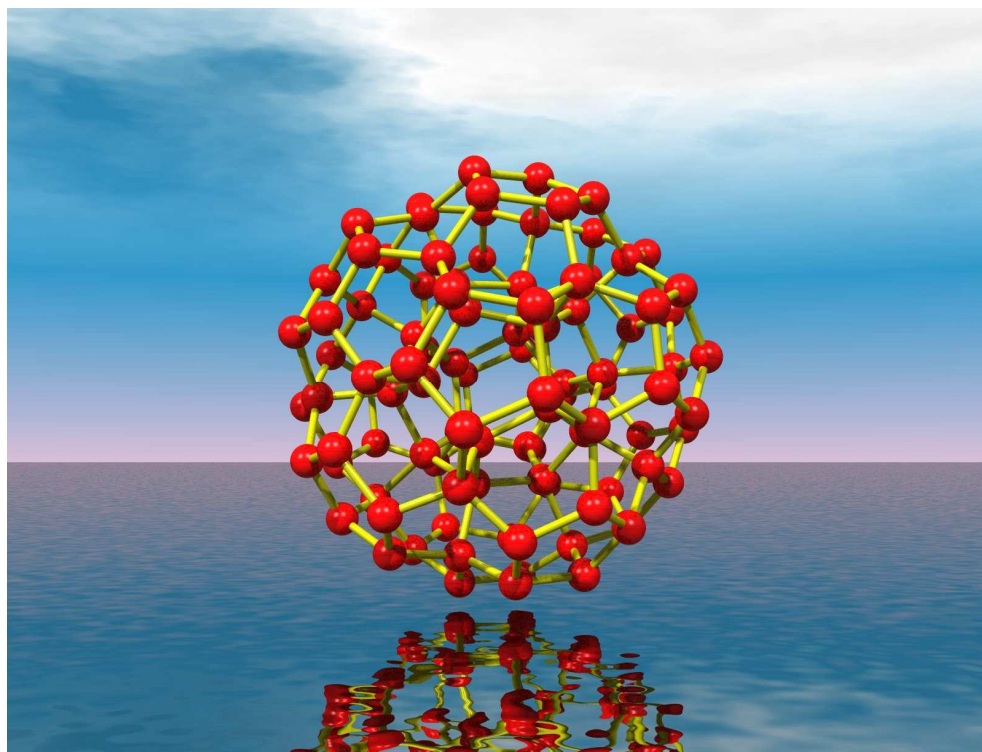


Fig. 5. Ball-and-stick representation of the organized $[\text{H}_2\text{O}]_{100}$ system (encapsulated in the $[\text{Mo}_{132}]$ POM cluster with closed pores).

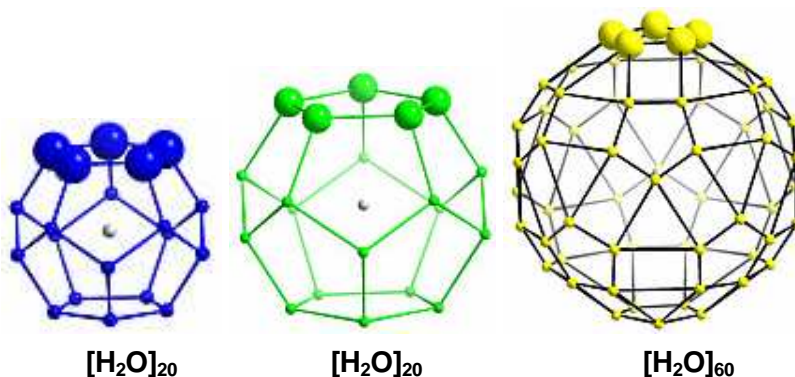


Fig. 6. Mixed wire frame and ball-and-stick representation of the first $[\text{H}_2\text{O}]_{20}$ dodecahedron (left), the second $[\text{H}_2\text{O}]_{20}$ dodecahedron (centre) and the $[\text{H}_2\text{O}]_{60}$ rhombicosidodecahedron (right), out of which the $[\text{H}_2\text{O}]_{100}$ system is built up.

Only the future will show whether Müller's suppositions were correct. The future will also reveal what other surprises are in store for us concerning these amazing substances which are the POM/MOB clusters.

Acknowledgement: The authors would like to thank Prof. Dr. Dr. h. c. mult. Achim Müller and Dr. Hartmut Bögge for providing the figures included in this paper.

REFERENCES

1. Patrut, A., Nicoara, A., Margineanu, D., *Studia Univ. Babeş-Bolyai, Ser. C, Chimia*, **2003**, 48, 3.
2. Müller, A., Koop, M., Patrut, A., Nicoara, A., Margineanu, D., Kögerler, P., Bögge, H., Schmidtman, M., to be published.
3. Müller, A., Koop, M., Bögge, H., Patrut, A., Nicoara, A., Botar, A., Kögerler, P., Schmidtman, M., *Rev. Roum. Chim.*, in press.
4. Müller, A., Hovermeyer, K., Rohlfing, K., *Angew. Chem. Int. Ed. Engl.*, **1992**, 31, 1192.
5. Müller, A., Reuter, H., Dillinger, S., *Angew. Chem. Int. Ed. Engl.*, **1995**, 34, 2328.
6. Müller, A., Das, S.K., Kögerler, P., Bögge, H., Schmidtman, M., Trautwein, A.X., Schünemann, V., Krickemeyer, E., Preetz, W., *Angew. Chem. Int. Ed.*, **2000**, 39, 3414.
7. Müller, A., Das, S.K., Bögge, H., Schmidtman, M., Botar, A., Patrut, A., *Chem. Commun.*, **2001**, 657.
8. Müller, A., Kögerler, P., *Coord. Chem. Rev.*, **1999**, 182, 3.
9. Müller, A., Kögerler, P., Bögge, H., *Struct. Bond.*, **2000**, 96, 203.
10. Müller, A., Krickemeyer, E., Bögge, H., Schmidtman, M., Roy, S., Berkle, A., *Angew. Chem. Int. Ed.*, **2002**, 41, 3604.
11. Müller, A., *Forschung an der Universität Bielefeld*, **2002**, 24, 1.

KINETIC STUDY ON HYDROLYSIS REACTION OF DIOXIMES

G. SZABÓ, J. ZSAKÓ, I. BÂLDEA and CS. BOLLA

*Babeș-Bolyai University, Faculty of Chemistry and Chemical Engineering
Department of Physical Chemistry*

ABSTRACT. The hydrolysis of 1,2,3-cyclohexanetrione-1,3-dioxime (CTD) and 1,2,3-cyclohexanetrione-2-imine-1,3-dioxime (CTDI) was studied polarographically at different concentrations of perchloric acid. It was followed the time course of diffusion current intensity of the polarographic wave. First order rate constants were derived and the influence of perchloric acid concentration was studied. A mechanism of hydrolysis reaction consisting of a protolytic pre-equilibrium, followed by a slow competitive water addition onto both the protonated and non-protonated forms of the dioxime has been suggested. The final step is presumed to be a fast elimination of hydroxylamine. On the basis of this mechanism it was derived a relationship among the rate constants, acidity constant and the hydrogen ion concentration. Acidity constants were calculated for the protonated oximes.

Introduction

Both aliphatic and alicyclic α -dioximes are stable in neutral and basic aqueous solutions. The spectrophotometric investigations showed that the dioximes are not stable in acidic solutions, they undergo hydrolysis with liberation of hydroxylamine and the corresponding diketone [1-3]. In presence of mineral acids protonation of a nitrogen atom occurs.

The hydrolysis of the oximes can be studied by means of polarography as well. Polarographic measurements are suitable also for kinetic studies.

It has been observed that hydrolysis of the alicyclic α -dioximes, namely the 1,2-cycloheptanedione-dioxime [4] and 1,2-cyclohexanedione-dioxime [5] and the alicyclic trioximes as 1,2,3-cyclohexanetrione-trioxime [6] are apparently first-order reactions. It has been observed that the increasing acidity causes the increase of rate constants, without existing of a direct proportionality between them. This indicates that protolytic pre-equilibrium is established. In order to explain the experimental results, it was presumed that a water addition onto the protonated form is the rate-determining step, followed by a fast elimination of hydroxylamine.

The aim of the present paper was to study the hydrolysis reaction of the 1,2,3-cyclohexanetrione-1,3-dioxime (CTD) and 1,2,3-cyclohexanetrione-2-imine-1,3-dioxime (CTDI) at 20 °C, to suggest a mechanism for hydrolysis reaction, to derive a mathematical relation among rate constants, acidity constant and hydrogen ion concentration and to calculate acidity constant for the protonated oximes. The influence of the group in position 2 was studied on the value of acidity constant of protonated oximes and rate constants.

Experimental

Experiments were performed in a 25-ml double-walled, water-jacketed, temperature controlled by a circulating water bath (VEB-MLW type thermostat) glass cell. A dropping mercury electrode was used by applying the forced dropping method (RADELKIS OH-991 type "Fast rapid adapter") and the reference electrode was a saturated calomel electrode (SCE). Polarograms were recorded on a Radelkis OH-120 type polarograph.

The CTD and CTDI were dissolved in distilled water to obtain a 10^{-2} M stock solution. It has been prepared before each set of measurements. Samples were prepared with perchloric acid solutions in order to ensure a final concentration of CTD and CTDI equal to $2.5 \cdot 10^{-3}$ M and the perchloric acid concentrations: 0.05, 0.1, 0.2, 0.5 M. Sodium perchlorate was added to ensure a constant ionic strength. The oxygen was eliminated from the solutions with purified methane gas.

From our previous paper [7] we can conclude that it is not necessary the chemical freezing of the reaction and addition of buffer solution. The reaction is sufficiently slow and can be investigated by the simple registration of the polarograms at different time steps.

Results and Discussion

In Table 1 the diffusion current intensities (i_d) are given as a function of the perchloric acid concentration and of the time elapse for the hydrolysis of CTD to occur.

Table 1.

Time dependence of the diffusion current intensity of the wave; $c_{\text{CTD}} = 2.5 \cdot 10^{-3}$ M.

T(K)	[H ⁺] (M)	t(s)	i_d (μA)	lg i_d	k_{app} (s ⁻¹)
293	0.05	50	9.76	0.989	$0.92 \cdot 10^{-4}$
		185	9.48	0.977	
		535	9.20	0.964	
		963	8.90	0.949	
		1260	8.78	0.943	
		1560	8.42	0.925	
		1860	8.14	0.911	

A plot of $\lg i_d$ vs. time indicates a good linearity, pleading for an apparent first order reaction. It allows determination of apparent rate constants by means of linear regression. The apparent rate constants for the hydrolysis of CTD are presented in Table 2 and for the CTDI in Table 3.

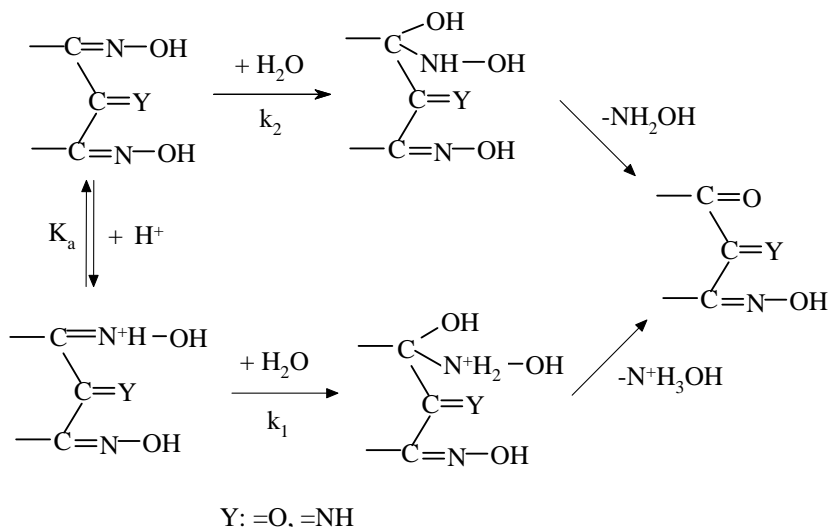
Table 2.
Apparent rate constants of the hydrolysis at 20°C; $c_{\text{CTD}}=2.5 \cdot 10^{-3}\text{M}$.

$[\text{H}^+]$ (M)	$k_{\text{app}} \cdot 10^4$ (s ⁻¹)
0.05	0.92
0.1	1.41
0.2	2.10
0.5	3.15

Table 3.
Apparent rate constants of the hydrolysis at 20°C; $c_{\text{CTDI}}=2.5 \cdot 10^{-3}\text{M}$.

$[\text{H}^+]$ (M)	$k_{\text{app}} \cdot 10^4$ (s ⁻¹)
0.05	1.42
0.1	2.08
0.2	2.88
0.5	3.88

As it can be observed in these tables, apparent rate constant increases with increasing perchloric acid concentration, but very slowly, suggesting a protolytic pre-equilibrium, implying very fast protonation and deprotonation processes. Protonation entails the polarization of the π -bond, facilitating water addition. Nevertheless the water addition onto the non-protonated form cannot be excluded either. The proposed mechanism contains two competing paths: the hydrolysis of protonated oxime and the non-protonated one.



On the basis of the above mechanism the apparent first-order rate constant can be described well by the following equation:

$$k_{\text{app}} = k_1 \cdot \frac{[\text{H}^+]}{[\text{H}^+] + K_a} + k_2 \cdot \frac{K_a}{K_a + [\text{H}^+]} \quad (1)$$

Table 4.

The hydrolysis rate constants and acidity constant of CTD at 20°C.

[H ⁺] (M)	10 ⁴ ·k _{app} (s ⁻¹)	10 ⁴ ·k ₁ (s ⁻¹)	10 ⁵ ·k ₂ (s ⁻¹)	K _a
0.05	0.92	4.93	2.73	0.310
0.1	1.41			
0.2	2.10			
0.5	3.15			

By determining four values for four H⁺ concentrations, we obtained a system of equations, which can be easily solved. The results for the CTD are presented in Table 4.

In case of CTDI, the Table 5 presents the rate constants and acidity constant.

Table 5.

The hydrolysis rate constants and acidity constant of CTDI at 20°C.

[H ⁺] (M)	10 ⁴ ·k _{app} (s ⁻¹)	10 ⁴ ·k ₁ (s ⁻¹)	10 ⁵ ·k ₂ (s ⁻¹)	K _a
0.05	1.42	5.16	4.04	0.183
0.1	2.08			
0.2	2.88			
0.5	3.88			

It is worth mentioning that k₁ and k₂ are pseudo first-order rate constants since water addition is a bimolecular reaction, but the water is the solvent and its concentration practically does not vary.

It can be observed that in both cases the value of rate constant k₂ represents approximately 10 % of value of k₁. This fact is in a good agreement with the presumption that the water addition onto the non-protonated form cannot be neglected. For the hydrolysis of CTDI both rate constants have a greater value than in case of CTD, reactions are carried out easier.

It is interesting to compare the value of acidity constants of protonated forms with other data obtained in a similar way (see Table 6).

If one compares the values of acidity constants in Table 6 it is obvious that α -dioximes are the weakest acids. The strongest acid is 1,2,3-cyclohexanetrione-trioxime, in case of which protonation occurs in position 2 and the effects of the oxime groups in both positions 1 and 3 are cumulated [4].

The CTD and CTDI are stronger acids than α -dioximes. The electron withdrawing effect of groups situated in position 2 can explain this. Since the electron withdrawing effect of =O group is larger than that of =NH, protonation of CTDI occurs much easier and acidity constant of protonated form is smaller.

Table 6.

Acidity constants of the protonated forms derived from hydrolysis kinetics' data, at 20°C.

Oxime	K_a
1,2-cycloheptanedione-1,2-dioxime	0,110
1,2-cyclohexanedione-1,2-dioxime	0,133
1,2,3-cyclohexanetrione-2-imine-1,3-dioxime	0,183
1,2,3-cyclohexanetrione-1,3-dioxime	0,310
1,2,3-cyclohexanetrione-trioxime	1,340

Value of acidity constant of protonated oximes calculated on the basis of hydrolysis reaction kinetics is used for determination of the recombination reactions rate constant.

REFERENCES

1. P.R. Elefson, I. Gordon: *Talanta*, 1967, p. 409.
2. A.N. Alibina, V.M. Peshkova: *Vestnik Moskovsk Univ.Ser.II, Khim*, 1970, p. 260.
3. V.I. Shlenskaya, T.I. Tikhvinskaya: *Vestnik Moskovsk Univ.Ser.II, Khim*, 1970, p. 337.
4. F. Mánok, E. Kőszegi, Cs. Várhely: *Acta Chim.Hung.* 1984, p. 51.
5. F. Mánok, G. Dénezsi, Cs. Várhelyi, A. Benkő: *Studia Univ. Babeş-Bolyai*, 1986, p. 3.
6. F. Mánok, Cs. Várhelyi, A. Benkő, M. Tarsoly-Magyari: *Monatsh. Chem.*, 1978, p. 1329.
7. J. Zsakó, G. Szabó: *Periodica Polytechnica ser. Chem. Eng.*, 1999, p. 35

TEMPERATURE DEPENDENCE OF THE DIOXIMES HYDROLYSIS REACTION RATE

G.SZABÓ, J. ZSAKÓ and CS. BOLLA

*Babeș-Bolyai University, Faculty of Chemistry and Chemical Engineering
Department of Physical Chemistry*

ABSTRACT. Hydrolysis reaction of 1,2,3-cyclohexanetrione-1,3-dioxime and 1,2,3-cyclohexanetrione-2-imine-1,3-dioxime was studied in presence of different concentrations of perchloric acid and at different temperatures. The hydrolysis reaction was studied polarographically. Time course of diffusion current intensity was followed. Apparent rate constants were determined at different temperatures and activation parameters were calculated.

Introduction

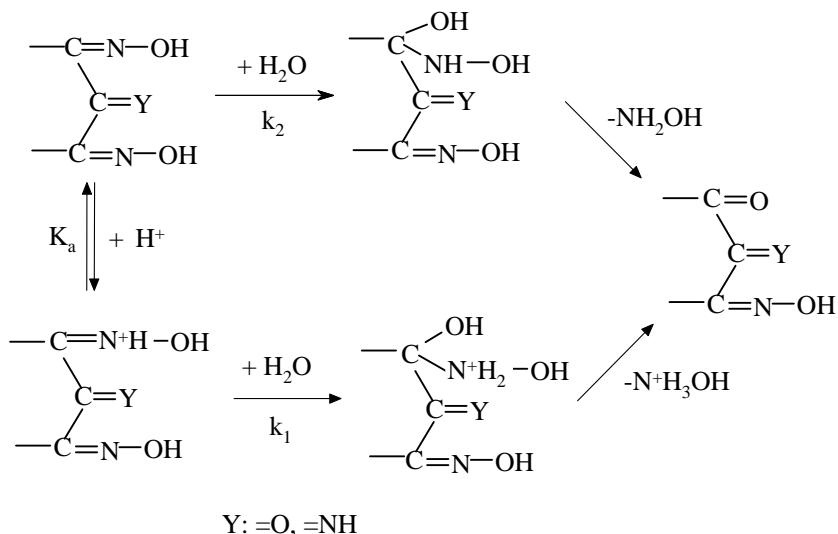
Spectrophotometric investigations demonstrated that dioximes are not stable in acidic solutions [1-3], they undergo hydrolysis with liberation of hydroxylamine and the corresponding diketone.

Hydrolysis reaction of oximes can be studied polarographically. In case of 1,2-cyclohexanedione-dioxime [4], 1,2-cycloheptanedione-dioxime [5] and 1,2,3-cyclohexanetrione-trioxime [6] rate constants were determined. The hydrolysis of 1,2,3-cyclohexanetrione-1,3-dioxime (CTD) and 1,2,3-cyclohexanetrione-2-imine-1,3-dioxime (CTDI) was studied at 20°C at different perchloric acid concentration [7].

In presence of acids protonation of nitrogen atom occurs [8], causing the polarization of the π -bond and facilitating water addition. It cannot be excluded the addition of the water onto the non-protonated oxime either. The proposed mechanism contains two competing paths: the hydrolysis of protonated oxime and the non-protonated one. On the basis of the proposed mechanism for the apparent first-order rate constant the following equation can be derived:

$$k_{\text{app}} = k_1 \cdot \frac{[\text{H}^+]}{[\text{H}^+] + K_a} + k_2 \cdot \frac{K_a}{K_a + [\text{H}^+]} \quad (1)$$

The hydrolysis reaction mechanism can be expressed by the following steps for both CTD and CTDI:



Apparent rate constants can be determined at different concentration of acid and using equation (1) values of k_1 and k_2 rate constants as well as acidity constant K_a can be calculated.

The aim of the present paper was to determine apparent rate constants as a function of hydrogen ion concentration and at different temperatures and to calculate activation parameters. From the values of activation parameters can be drawn some conclusion concerning the proposed mechanism.

Experimental

Polarographic measurements were carried out in a 25 ml double walled, water jacketed, temperature controlled with a circulating water bath (VEB-MLW type thermostat), glass cell. A dropping mercury electrode was used. By connecting the capillary to the RADELKIS OH-991 type "Fast rapid adapter" the mercury dropping was forced. The reference electrode was a saturated calomel electrode. Polarograms were recorded on a Radelkis OH-120 type polarograph.

Stock solutions of CTD and CTDI were prepared before each set of measurements. Perchloric acid was added to the oxime solutions in such a way that the final concentrations for oximes to be equal to $2.5 \cdot 10^{-3}$ M and for perchloric acid 0.05, 0.1, 0.2, 0.5 M. In order to ensure the constant ionic strength sodium perchlorate was added to the mixtures. Dissolved oxygen was eliminated with inert gas.

Polarograms were recorded at different time steps. Time course of diffusion current intensity was followed.

Results and Discussion

The hydrolysis of CTD and CTDI was performed at different temperatures. In Table 1 are presented the apparent rate constants obtained at different acidity's and at different temperatures for CTD.

Table 1.

Hydrolysis rate constants and acidity constant of the protonated CTD, at different temperatures

T(K)	[H ⁺] (M)	10 ⁴ ·k _{app} (s ⁻¹)	10 ⁴ ·k ₁ (s ⁻¹)	10 ⁵ ·k ₂ (s ⁻¹)	K _a
298	0.05	1.09	5.63	3.80	0.320
	0.1	1.63			
	0.2	2.40			
	0.5	3.58			
303	0.05	1.43	6.30	6.81	0.326
	0.1	2.00			
	0.2	2.82			
	0.5	4.08			
308	0.05	1.94	7.07	11.90	0.342
	0.1	2.52			
	0.2	3.36			
	0.5	4.68			

In the proposed mechanism the rate-determining step is the water addition onto the protonated and non-protonated form of dioximes. The k₁ and k₂ rate constants are pseudo-first order rate constants. The water addition is a bimolecular reaction, but because the water is the solvent its concentration practically does not vary.

Comparing the obtained values for the rate constants it is obvious that k₂ cannot be neglected beside k₁. By this mean the presumption referring the water addition onto the non-protonated oxime is quite realistic.

For the CTDI these values of rate and acidity constants are presented in Table 2.

Table 2.

Hydrolysis rate constants and acidity constant of the protonated CTDI at different temperatures

T (K)	[H ⁺] (M)	10 ⁴ ·k _{app} (s ⁻¹)	10 ⁴ ·k ₁ (s ⁻¹)	10 ⁵ ·k ₂ (s ⁻¹)	K _a
298	0.05	1.48	5.76	4.45	0.206
	0.1	2.18			
	0.2	3.06			
	0.5	4.21			
303	0.05	1.93	6.41	8.23	0.2029
	0.1	2.67			
	0.2	3.60			
	0.5	4.80			
308	0.05	2.54	7.25	14.60	0.218
	0.1	3.28			
	0.2	4.23			
	0.5	5.49			

The rate constants have been worked up by means of Eyring-Polányi-Evans equation:

$$k = \frac{\kappa \cdot T}{h} \cdot \exp\left[\frac{\Delta S^*}{R} - \frac{\Delta H^*}{RT}\right] \quad (2)$$

The activation parameters calculated by performing linear regression are presented in Table 3 for the water addition onto the protonated oximes.

Table 3.

Activation parameters for the water addition onto the protonated oximes

Oxime	ΔH^* (kJ/mol)	ΔS^* (J/mol·K)
CTD	15.46	-255
CTDI	14.46	-258

Activation parameters for the non-protonated oximes are presented in Table 4.

Table 4.

Activation parameters for the water addition onto the non-protonated oximes

Oxime	ΔH^* (kJ/mol)	ΔS^* (J/mol·K)
CTD	72.41	-85.6
CTDI	64.35	-110.7

The activation enthalpy values of the water addition in the case of the protonated form are lower than for the non-protonated forms.

The relatively important negative activation entropy are in agreement with the presumption that the rate determining step in an addition reaction.

REFERENCES

1. P.R. Elefson, I. Gordon: *Talanta*, 1967, p. 409.
2. A.N. Alibina, V.M. Peshkova: *Vestnik Moskovsk Univ. Ser.II, Khim*, 1970, p. 260.
3. V.I. Shlenskaya, T.I. Tikhvinskaya: *Vestnik Moskovsk Univ. Ser.II, Khim*, 1970, p. 337.
4. F. Mánok, G. Dénezsi, Cs. Várhelyi, A. Benkő: *Studia Univ. Babeş-Bolyai, ser. Chem.* 1986, p. 3.
5. F. Mánok, E. Kőszegi, Cs. Várhelyi: *Acta Chim.Hung.* 1984, p. 51
6. F. Mánok, Cs. Várhelyi, A. Benkő, M. Tarsoly-Magyari: *Monatsh. Chem.*, 1978, p. 1329.
7. G. Szabó, J. Zsakó, I. Bâldea, Cs. Bolla: submitted to *Studia Univ. Babeş-Bolyai, ser. Chem.*
8. J. Zsakó, G. Szabó: *Periodica Polytechnica ser. Chem. Eng.*, 1999, p. 35.

INFLUENCE OF IODATE ION CONCENTRATION ON OSCILLATIONS IN THE BRIGGS-RAUSCHER REACTION

E. SZABÓ, G. SZABÓ*, CS. BOLLA*

*Central Chemical Research Institute, Budapest
*Babeș-Bolyai University of Cluj Napoca,
Department of Physical Chemistry*

ABSTRACT. The Briggs-Rauscher oscillating reaction was studied in a batch mode. Mixtures were prepared in such a way that reactant concentrations were at the limit of that concentration interval in which oscillations happen. Iodate-ion concentration was varied and its influence on the oscillations was investigated. Time course of redox potential and iodide-ion concentration were recorded. At low iodate-ion concentration oscillating break was founded.

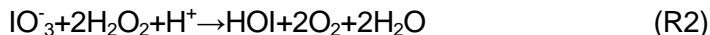
Introduction

A chemical reaction is oscillatory if two or more intermediate's concentration have extreme values. Briggs-Rauscher (BR) is an oscillatory reaction and is representing the oxidation of malonic acid by hydrogen peroxide and iodate with manganese (II) ion as a catalyst, in acidic medium. The formation velocity of oxygen and carbon dioxide as well as iodine and iodide-ion concentration presents oscillation in this system.

Several scientists investigated the mechanism of BR, namely Cook [1], Furrow and Noyes [2, 4], De Kepper and Epstein [7], Fujieda and Ogata [8] and others [3, 5, 6]. According to their proposal, the global reaction is symbolized with the following equation:

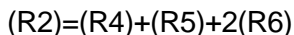


This represents the sum of the following two steps:

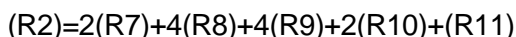
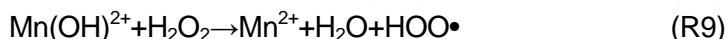
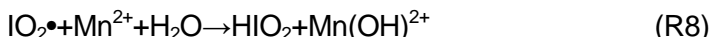


Reaction (R2) takes place in two different ways. The way in which the system develops is a function of iodide-ion concentration. If the iodide-ion concentration is high, the mechanism will obey the following non-radical steps:





If the iodide-ion concentration is smaller than the critical value, the reaction (R₂) will follow the radical path:



In BR reaction the non-radical way will change into the radical one if the iodide-ion concentration decreases below the critical value. The reaction oscillates between these two processes. The mechanism presented above is only a skeleton of what happens during the reaction. It explains the origin of oscillations in the concentration of iodine and iodide-ion, but not elucidates the path of carbon dioxide's formation, nor identifies the final organic product. That is why BR is still under research.

In most of the cases BR was investigated in continuous-flow stirred tank reactor (CSTR). Nevertheless in some papers batch mode experiments are related.

The system exhibits oscillatory behavior only if the initial concentrations of the reactants fit in a concentration interval. These intervals for the different reactants are: $[\text{H}_2\text{O}_2] = 0.3\text{-}3.5 \text{ M}$, $[\text{IO}_3^-] = 2 \cdot 10^{-2}\text{-}1 \cdot 10^{-1} \text{ M}$, $[\text{H}^+] = 5 \cdot 10^{-2}\text{-}2 \cdot 10^{-1} \text{ M}$, $[\text{Mn}(\text{II})] = 3 \cdot 10^{-3}\text{-}3 \cdot 10^{-2} \text{ M}$, $[\text{malonic acid}] = 2 \cdot 10^{-2}\text{-}1 \cdot 10^{-1} \text{ M}$ [9].

The aim of the present paper is to notice about the system's behavior in case in which the initial mixture is a non-classical one and the iodate-ion concentration is smaller than the inferior limit.

Experimental

Batch experiments were carried out in a 40 ml double walled, water-jacketed cylindrical-shaped glass reactor. Its temperature was controlled by a circulating water bath (VEB-MLW type thermostat). A magnetic stirrer was used to ensure uniform mixing. Time course of redox potential and iodide-ion concentration was followed. Platinum electrode and double-junction saturated calomel electrode was used. Iodide-ion concentration was determined by using an ion selective electrode EMIS-I. The time course of the redox potential was monitored with a "Metrohm E 478" recorder, or stored on a PC. Data acquisition was accomplished with a PCI-6023E board (National Instruments) and the Digix program was used.

The reactants sodium iodate (Chemapol, c.p.), manganese (II) sulfate (Reactivul, c.p.), hydrogen peroxide (Merck p.a.), sulfuric acid (Riedel De Haen, p.a.), malonic acid (Reachim, p.a.), potassium iodide (Reactivul, p.a.), potassium nitrate (Reactivul, p.a.) were used without further purification. Parent solutions were made. The first solution was obtained by mixing the sulfuric acid and the sodium iodate. The acid's concentration was kept 0.1 M and the iodate's concentration was varied. 0.2 M malonic acid and $2.6 \cdot 10^{-2}$ M manganese (II) sulfate composed the second solution. The third solution was the hydrogen peroxide. These solutions were mixed in such a way that $[H^+] = 2.5 \cdot 10^{-2}$ M; $[\text{malonic acid}] = 5 \cdot 10^{-2}$ M; $[\text{Mn(II)}] = 6.5 \cdot 10^{-3}$ M $[\text{H}_2\text{O}_2] = 2.2 \cdot 10^{-1}$ M and variable iodate concentrations were ensured.

Results and Discussion

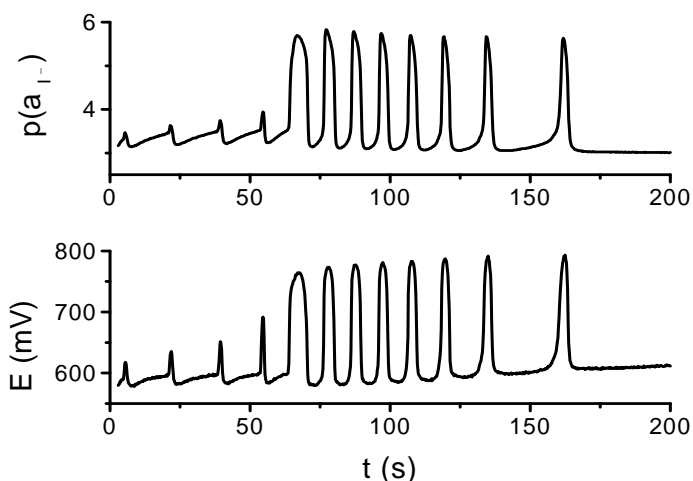


Figure 1. Time course of iodide-ion activity and redox potential for iodate-ion initial concentration $[\text{IO}_3^-] = 8,5 \cdot 10^{-2}$ M

BR was investigated in closed reactor. It is to be mentioned that batch experiments can be used only for a few oscillating reactions, but BR is one of them.

As it was revealed above, non-classical initial mixtures were prepared with variable iodate-ion concentration.

These initial concentrations for the iodate-ion had different values between: $8.5 \cdot 10^{-2}$ - $1,25 \cdot 10^{-2}$ M. It has been distinguished three different behaviors of the system.

At high iodate-ion concentration the reaction started with a few, large period and small amplitude oscillation. These were followed by the classical oscillations, with smaller period and larger amplitude. The above-described

behavior is represented in Figure 1. The oscillations had classical shape when iodate-ion's concentration value was included in $2,5 \cdot 10^{-2}$ - $6,5 \cdot 10^{-2}$ M interval. Such an oscillation is represented in Figure 2. In this case the system contained $6 \cdot 10^{-2}$ M iodate-ion.

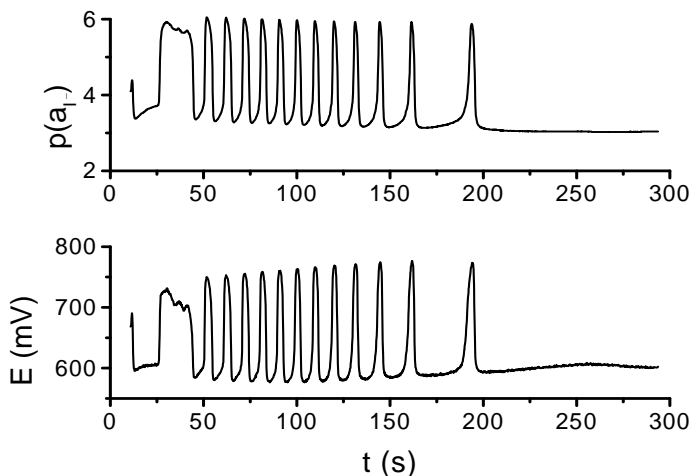


Figure 2. Time course of iodide-ion activity and redox potential for iodate-ion initial concentration $[IO_3^-] = 6 \cdot 10^{-2}$ M

With decreasing iodate-ion concentration the increases of amplitude and decreases of period was observed.

At low iodate-ion concentration the system acted in a peculiar way. The cessation of the oscillatory regime and subsequent regeneration of oscillations followed the starting few normal oscillations. This behavior is presented in Figure 3.

The shapes of the oscillations before and after the break are quite different. This can be caused by the different parametrical condition of the oscillation before and after the break.

Oscillation break was described referred to Belousov-Zhabotinsky reaction. In the case of BR was also described an oscillation break, but this was caused by an antioxidant added to the system which scavenged the free radicals [10, 11, 12].

We can conclude that even the non-classical initial mixture exhibits so called normal oscillations. The low iodate-ion concentration causes an oscillating break. The appearance of the break can be explained with the low rate of one of the steps trough which the reaction is developing. It can be caused by the too low concentration of one intermediate species, like the iodide-ion.

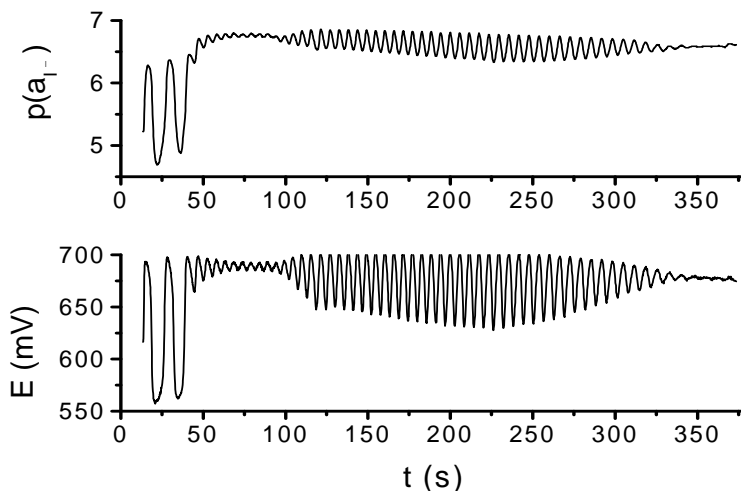


Figure 3. Time course of iodide-ion activity and redox potential for iodate-ion initial concentration $[IO_3^-]=1,38 \cdot 10^{-2}$ M

The following step will be the modeling of the described oscillation. The comparison of the computational behavior and the real one will elucidate some issues of this nonlinear phenomenon.

REFERENCES

1. D. O. Cooke, *J. Chem. Soc., Chem. Commun.*, 1984, p. 314
2. S. D. Furrow, R. M. Noyes, *J. Am. Chem. Soc.* 1982, **104**, p. 38, p.42
3. V. Vukojevic, P. Graae Sorensen, F. Hynne, *J. Phys. Chem.*, 1996, **100**, p. 17175
4. S. D. Furrow, *J. Phys. Chem.*, 1989, **93**, p. 2817
5. V. K. Vanag, M. V. Alfimov, *J. Phys. Chem.*, 1993, **97**, p. 1884
6. J. Happel, P. H. Sellers, *J. Phys. Chem.*, 1991, **95**, p. 7740
7. P. De Kepper, I. R. Epstein, *J. Am. Chem. Soc.*, 1982, **104** p. 49
8. S. Fujieda, H. Ogata, *Talanta*, 1996, p. 1989
9. Gy. Bazsa, *Nemlineáris dinamika és exotikus kinetikai jelenségek kémiai rendszerekben*, Debrecen, 1992, p.210.

10. R. Cervellati, N. Crespi-Perellino, S. Furrow, A. Minghetti, *Helv. Chim. Acta.* 2000, **83**, p. 3179
11. R. Cervellati, K. Höner, S. Furrow, C. Neddens, S. Costa, *Helv. Chim. Acta*, 2001, **84**, p. 3533
12. K. Höner, R. Cervellati, C. Neddens *Eur. Food Res. Technol.*, 2002, **214**. p. 356

FLOW GRAPHS IN CHEMICAL KINETICS (I)

MARIUS SOCOL and IOAN BALDEA

*Faculty of Chemistry and Chemical Engineering, Babes-Bolyai University of Cluj,
11 Arany Janos Str. Cluj-Napoca 3400 Romania. E-mail: m_socol2000@yahoo.com*

ABSTRACT. Flow graphs used in physics and electronics have been applied to chemical kinetics. Rate laws and expressions of various concentrations of species involved in the mechanisms have been described for several simple systems. Flow graphs were constructed in agreement with the mechanism and differential equations that characterize the time evolution of molecules or radicals involved, and the characteristic determinants for the system. A short introduction of basic principles of flow graphs, their properties and algebra are also presented. The same results were straightly obtained as those resulted from classical integration or by applying quasi-steady-state approximation.

Introduction

Graphs and diagrams of various types have been used to depict reaction mechanisms in chemistry as chain processes, catalyzed processes, and enzyme-catalyzed processes¹⁻². Temkin³⁻⁵ has proposed a convenient version of cyclic graphs. These graphs incorporate only intermediate species as vertices. They were used to deduce - in a quite simple way - the concentration of reactive intermediates and the overall reaction rate⁶⁻⁸. Numerous chemical chain reactions, photochemical reactions involving propagation of chain as elementary steps, enzyme-catalyzed reactions or even heterogeneous reactions were approached this way. Temkin and Bonchev and their co-workers⁹⁻¹² have classified various types of complex mechanisms on the ground of graphs associated with these mechanisms.

Inspired by the flow graphs used in electronics, physics and engineering¹³⁻¹⁵, we show in this work how to use flow graphs to associate them with reaction mechanisms in order to obtain some kinetic characteristics of any reaction scheme. Besides the intermediates, these graphs incorporate also the starting chemical species, the main and secondary products. At the same time, we associated determinants to chemical change and construct graphs on this base. Our approach has the advantage of offering the opportunity to calculate the concentration of any species involved either being in a quasi-steady-state or a transient concentration. These flow graphs can be used for various types of mechanisms with linear sequence, opposing processes, single route chain reactions, homogeneous and heterogeneous catalyzed reactions.

Some basic principles of flow graphs

A flow graph is a diagram that represents a set of simultaneous linear algebraic situations (linear differential equations)¹³. It is used to represent a system and to obtain the relationships among the system variables. By using the Cramer method¹⁶ with determinants one could solve the system.

A flow graph consists of a network in which nodes (or vertices) are connected by directed edges (or branches). Each node (vertex) represents a system variable, and each edge connected between two vertices acts as a signal multiplier. An arrow placed on the edge indicates the direction of a signal flow and the multiplication factor is indicated along the edge. This multiplication factor is named transmittance and it can be obtained from the coefficients of the equations. The signal flow graph depicts the flow of signals from one point of the system to another and gives the relationships among the signals and it describes the determinant of the system¹³.

Definitions related to flow graphs. Before discussing flow graphs certain terms should be defined:

Node (Vertex) is a point representing a variable or a signal. In chemistry it represents a chemical species undergoing some transformation.

Edge (branch) is a directed line segment joining two nodes. The gain of a branch is the transmittance.

Weighting of an edge (transmittance) is a real or complex gain between nodes. Such gains can be expressed in terms of transfer function between two nodes. In chemical kinetics it represents a pseudo-first- or a true first-order rate constant measuring the frequency with which chemical event takes place. By multiplying it with the actual concentration of the species in the vertex of outgoing branch and the volume of the system, the chemical flux, in the indicated direction, is obtained.

Input node or source is a node that has only outgoing edges. This corresponds to an independent variable. In chemical kinetics it represent the reactant species.

Output node or sink is a node that has only incoming edges. This corresponds to a dependent variable. In chemical kinetics, it corresponds to a reaction product.

Mixed (internal) node is one that has both outgoing and incoming edges.

Path or way is a traversal of connected branches in the direction of the branch arrows.

Forward path (way) is a path from an input node (source) or from a mixed node, if the source is missing, to an output node (sink). The way should not visit any node more than once.

Forward path gain is the product of the branch transmittances of a forward path. A flow graph example is presented in figure 1.

Properties of flow graphs. A few important proprieties of flow graphs are as follows:

A branch indicates the functional dependence of one signal on another.

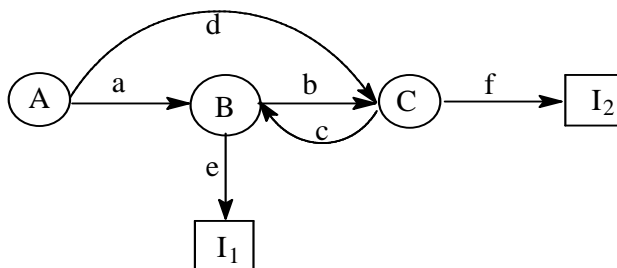


Fig.1. An example of a flow graph. A is an input node (source); I_1 I_2 are output nodes (sinks); a, b, c, d, e, and f are weighting of the edges; B, C are the internal nodes.

A signal passes trough only in the direction specified by the arrow of the branch.

A node adds the signals of all incoming branches and transmits their sum to all outgoing branches.

An interval node, which has both incoming and outgoing branches, may be viewed as an output node by ignoring its outgoing branches. Note, however, that a mixed node never can be a source (input node) in this approach.

For a given system a flow graph is not unique. More than one flow graphs can be drawn for a given system by writing the system equations or the corresponding determinants in a different way¹³⁻¹⁵.

Flow graphs algebra. A flow graph of a linear system can be drawn using the above definitions. The independent and dependent variables of the equations become the input nodes and the other nodes respectively. To determine these variables, the system is solved by using the Cramer method. Each value is a ratio of two determinants. From the reaction mechanism, the system of equations and corresponding determinants can be written. On the determinants base the flow graph can be constructed by following some rules. A simple example related to figure 1 is given bellow:

$$\begin{cases} (b + e)[B] - c[C] = a \\ -b[B] + (c + f)[C] = d \end{cases} \quad (1)$$

and $[I_1]=e[B]$, $[I_2]=f[C]$

Laplacian matrix of the system is defined by the formula (2)¹⁷:

$$La(G) = Deg(G) - A(G) \quad (2)$$

To form the flow graph for this determinant, which characterizes the system, the rules are¹⁸:

1. The above determinant can be written as:

$$\Delta = \begin{vmatrix} b + e & -c \\ -b & c + f \end{vmatrix} \quad (3)$$

2. The variables become nodes in the graph: the variables from the system (B and C) become the mixed nodes and I_1 and I_2 turn into output nodes.

3. The branch transmittance can be obtained from the coefficients of the system as follows:

- The element of line 1, column 1 represents all the transmittances of the edges, which are outgoing from the node B with the sign plus.

- The element of line 1, column 2 represents transmittance of edge outgoing from C and incoming to B with the sign minus in front of it, because it means a decrease of C variable.

The line 2 is obtained in the same way. The flow graph is presented in figure 2:

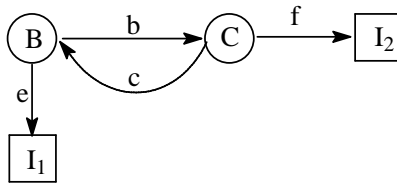


Fig. 2. The flow graph of the main determinant

The reciprocal of the above discussion is also valid. The main determinant of the system can be derived from this flow graph.

By tacking into account this flow graph and by using its properties given above, the global gain of the flow graph, which is the value of the main determinant, can be computed¹⁸. The global gain of the flow graph is the sum of the forward path gain, considering every possible way, and is represented in figure 3:

The global gain of the flow graph, which is the value of the determinant, is the sum of the all-possible forward path gain:

$$\Delta = \Delta_1 + \Delta_2 + \Delta_3 \quad (4)$$

In accordance with the definition concerning the visit of a node, the paths presented in the figure 4 cannot be considered because, in these cases, the nodes B and C have two output branches respectively. They were already considered as separate ways in figure 3. Also, the cyclic form (figure 5) cannot be considered because it disagrees with the mass conservation and has not any flux to an output node.

FLOW GRAPHS IN CHEMICAL KINETICS (I)

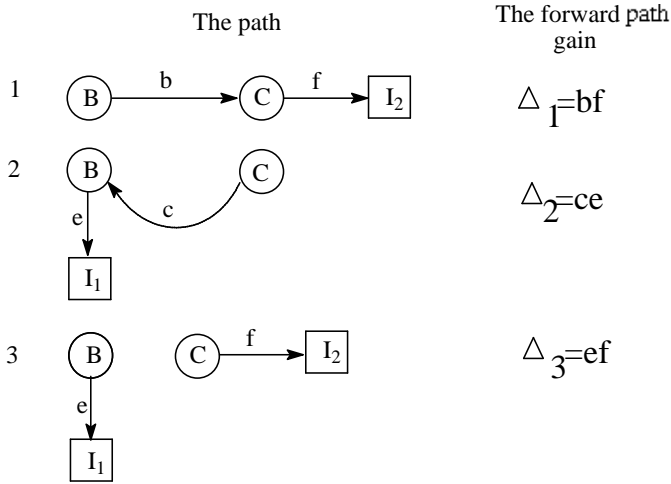


Fig. 3. The global gain of the flow graph.

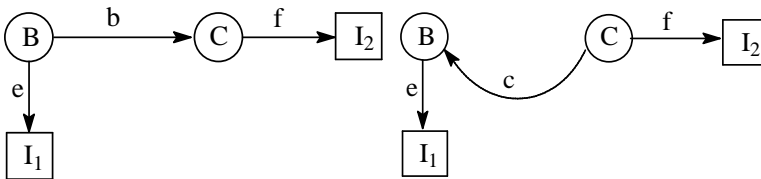


Fig. 4. Nodes with two output branches

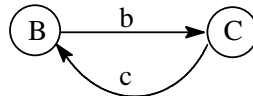


Fig. 5. Cyclic branches

As stated above, in order to calculate the dependent variables of the system, the species are considered target species or output nodes. The corresponding determinant for their formation are:

$$\Delta_B = \begin{vmatrix} A & C \\ B & a - c \\ C & d + f \end{vmatrix} \quad \text{and} \quad \Delta_C = \begin{vmatrix} B & A \\ B & b + e \\ C & -b \end{vmatrix} \quad \text{where} \quad \begin{pmatrix} a \\ d \end{pmatrix} \quad (5)$$

is the matrix of the free coefficients. They are the transmittances of the independent variable (the input node A). The sign plus is attributed to a and d in the determinant because positive gains of B and C occur from the input node A.

The flow graph for the determinant Δ_B , where B becomes an output node (figure 6):

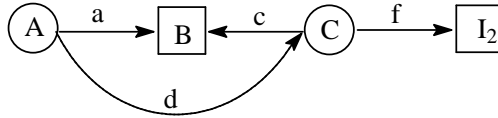


Fig. 6. The flow graph for Δ_B

and his value calculated from the above rules is :

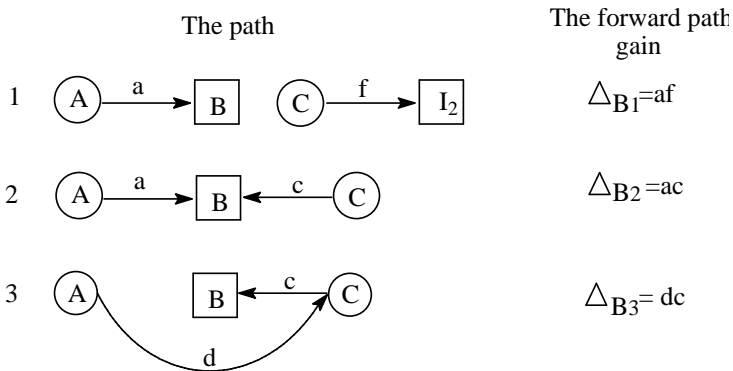


Fig. 7. Schematic ways to compute Δ_B .

The way through d and f , $\Delta_{B4}= df$, is not considered because the target species B is not visited. The value of the determinant corresponding to B species is:

$$\Delta_B = \Delta_{B1} + \Delta_{B2} + \Delta_{B3} = af + ac + dc \quad (6)$$

In the same way, when C is the output node Δ_C is obtained as $\Delta_C = ab+bd+ed$ following the same rules as shown in figure 8.

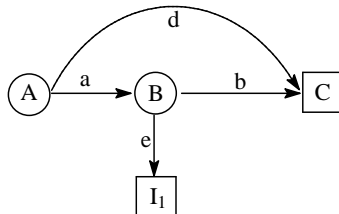


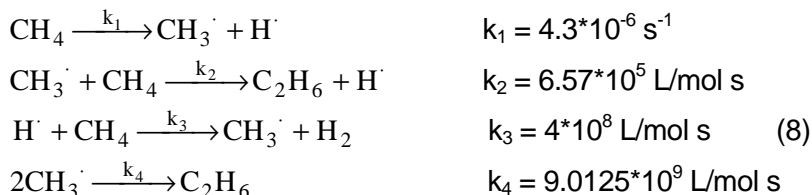
Fig. 8. The flow graph for Δ_C

If all three graphs are combined, the global graph can be constructed. It represents the flow graph for the system (eq. 7) as a whole^{14,15,18}, as presented in figure 1.

$$\begin{array}{l}
 \text{B} \\
 \text{C}
 \end{array}
 \left\{
 \begin{array}{l}
 \text{B} \quad \text{C} \quad \text{A} \\
 (b+e)[B] \quad -c[C] = a \\
 -b[B] \quad +(c+f)[C] = d
 \end{array}
 \right.
 \quad
 \begin{array}{l}
 \text{B} \\
 \text{C}
 \end{array}
 \left(
 \begin{array}{l}
 \text{B} \quad \text{C} \quad \text{A} \\
 b+e \quad -c \quad -a \\
 -b \quad c+f \quad -d
 \end{array}
 \right)
 \quad (7)$$

Application to methane pyrolysis.

The first example to be discussed is the methane pyrolysis. The following elementary processes represent the simple mechanism¹⁹, when the reverse reactions are not considered:



The accepted values of the rate constants are also given. The stoichiometry is represented by the equation:



In this case, the quasi steady state approximation (QSSA) can be applied for the active radicals. Their steady state concentrations are:

$$[\text{CH}_3 \cdot] = \sqrt{\frac{k_1}{k_4} [\text{CH}_4]} \quad [\text{H} \cdot] = \frac{k_2}{k_3} \sqrt{\frac{k_1}{k_4} [\text{CH}_4]^2} \quad (10)$$

According to the mechanism (8), the rate law is obtained as the summation of the two steps yielding ethane:

$$r = \frac{d[\text{C}_2\text{H}_6]}{dt} = k_2 [\text{CH}_3 \cdot] [\text{CH}_4] + k_4 [\text{CH}_3 \cdot]^2 \quad (11)$$

and therefore

$$r = k_2 \sqrt{\frac{k_1}{k_4} [\text{CH}_4]^3} + k_1 [\text{CH}_4] \quad (12)$$

By taking into account the values of the rate coefficients it simplifies to the form:

$$r = k_2 \sqrt{\frac{k_1}{k_4} [\text{CH}_4]^3} \quad (13)$$

An alternative way of dealing with the system is to use the flow graph method. The differential equations for the reaction system are:

$$\begin{cases} \frac{d[\text{CH}_3^\bullet]}{dt} = 0 = (k_2a + 2k_4x)[\text{CH}_3^\bullet] - k_3a[\text{H}^\bullet] - k_1[\text{CH}_4] \\ \frac{d[\text{H}^\bullet]}{dt} = 0 = -k_2a[\text{CH}_3^\bullet] + k_3a[\text{H}^\bullet] - k_1[\text{CH}_4] \end{cases} \quad (14)$$

The following notations are used further on: $[\text{CH}_4] = a$ and $[\text{CH}_3^\bullet] = x$. With these the following equations can be written:

$$\begin{cases} k_1a = (k_2a + 2k_4x)[\text{CH}_3^\bullet] - k_3a[\text{H}^\bullet] \\ k_1a = -k_2a[\text{CH}_3^\bullet] + k_3a[\text{H}^\bullet] \end{cases} \quad (15)$$

Here the matrix of the free coefficients represents the matrix of the transmittances of branches outgoing from the input node

$$\begin{matrix} & \text{CH}_3^\bullet & \text{H}^\bullet & & \text{CH}_4 \\ \text{CH}_3^\bullet & \left(k_2a + 2k_4x \right. & \left. -k_3a \right) & \begin{pmatrix} \text{CH}_3^\bullet \\ \text{H}^\bullet \end{pmatrix} & = \begin{pmatrix} k_1a \\ k_1a \end{pmatrix} \\ \text{H}^\bullet & \left(-k_2a \right. & \left. k_3a \right) & & \\ & \text{A} & \cdot & \text{B} & \text{C} \end{matrix} \quad (16)$$

The flow graph is the one in which we can transpose the extended determinant (16), as has been shown above, *obtaining a perfect image of the mechanism* (figure 9)

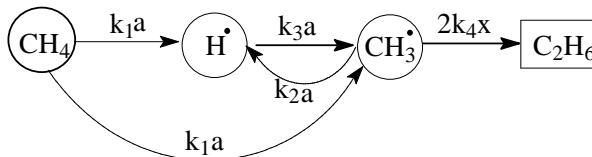


Fig. 9. Flow graph for methane pyrolysis

where C_2H_6 is the final product of termination step (the output node) and CH_4 is the main reactant (the input node). The starting species CH_4 , the radical species CH_3^\bullet and H^\bullet and the final product C_2H_6 represent the nodes and the pseudo-first order rate constants k_1 , k_2a , k_3a , and $2k_4[\text{CH}_3^\bullet]$ represent the branch transmittance, obtained from the coefficients of the system.

The main determinant, or *the global consumption of the radicals' determinant*, is that one of matrix A denoted here by Δ :

$$\det. A = \Delta = \begin{vmatrix} k_2a + 2k_4x & -k_3a \\ -k_2a & k_3a \end{vmatrix} = 2k_4x k_3a \quad (17)$$

The value of *main determinant* is also equal with the *global gain of the flow graph, without considering the reactant (the input node)*. Therefore it can be obtained straight from the graph by multiplying the branch transmittances which are outgoing from radicals to the final product, taking into account every possible ways and every radical involved in the mechanism.

The determinant for $\text{CH}_3\cdot$, *the formation determinant* is:

$$\Delta_x = \begin{vmatrix} k_1 a & -k_3 a \\ k_1 a & k_3 a \end{vmatrix} = 2k_1 a k_3 a \quad (18)$$

The value of the formation determinant *is also equal with the gain of flow graph considering the radical species an output node*. It is obtained by adding the product of transmittance of the branches, which are outgoing from the reactant CH_4 to the target radical on every possible ways, using the rules of the flow graphs.

The radical concentration $\text{CH}_3\cdot$, can be obtained by applying the Cramer rules in the same way as King and Altman did for enzyme catalyzed reactions²:

$$x = [\text{CH}_3\cdot] = \frac{\Delta_x}{\Delta} = \frac{2ak_1k_3a}{2k_4xk_3a} \quad ; \quad x = \sqrt{\frac{k_1}{k_4}} a \quad (19)$$

Thus, the determinant for $\text{H}\cdot$ (the formation determinant for $\text{H}\cdot$ species) is:

$$\Delta_{\text{H}\cdot} = \begin{vmatrix} k_2 a + 2k_4 x & k_1 a \\ -k_2 a & k_1 a \end{vmatrix} = 2k_1 a k_2 a + 2k_4 x k_1 a \quad (20)$$

$$[\text{H}\cdot] = \frac{2ak_1k_2a + 2ak_4xk_1}{2k_4k_3a\sqrt{\frac{k_1}{k_4}}a} \cong \frac{2ak_1k_2a}{2k_4k_3a\sqrt{\frac{k_1}{k_4}}a} = \sqrt{\frac{k_1}{k_4}} \cdot \frac{k_2}{k_3} a^{1/2} \quad (21)$$

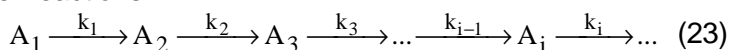
Finally, the rate law,

$$r = k_2 \sqrt{\frac{k_1}{k_4}} [\text{CH}_4]^{3/2} \quad (22)$$

is identical with the one obtained by the quasi-steady-state approximation.

Application to a series of first-order reactions

The next goal of the present work is to analyze an infinite series of consecutive first-order reactions:



The concentration of the first term in the series is calculated by solving the simple differential equation: $-d[A]/dt = k_1[A]$ yielding the solution $[A] = [A]_0 e^{-k_1 t}$. The last term concentration in the series, which is the final product, can be calculated from the mass balance. It is obvious that the concentration of any species depends on the concentrations of all previous species, starting from the reactant A_1 . By using the Cramer method, the linear system of the differential equations can be solved. It follows that:

$$[A_i] = f([A_j])_{j=1,i}; \quad [A_i] = \sum_{j=1}^i B_j e^{-\gamma_j t} = \sum_{j=1}^i B_j e^{-k_j t} \quad \text{for } i = 2, n-1; \quad B_j = \frac{\Delta_i}{\Delta_{B_j}} \quad (24)$$

where γ_j is the exponential factor and, in this case, the factors are equal with the rate constants [20] and B_j is an irreducible ratio found after simplifications of common terms. For the determination of $[A_i]$ one has to calculate "i" coefficients: $B_1, B_2, B_3, \dots, B_i$; therefore there is a number of i determinants Δ_{B_j} . The term $B_j e^{-k_j t}$ represents the contribution of species j at the formation of species i as part of the ensemble formed by all the species: i and the precursors.

Δ_i is the determinant which indicate *the formation of species A_i* and it is calculated directly from the principal flow graph, representing the mechanism, following the rules already given. The value of the determinant is equal to the flow graph gain: product of the branch transmittance of a forward path that goes to the formation of species i from the reactant A_1 as indicated in figure 10.

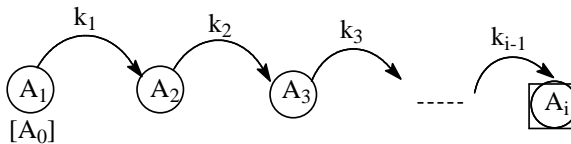


Fig. 10. The formation flow graph of A_i species.

Therefore

$$\Delta_i = [A_0] k_1 k_2 \dots k_{i-1} = [A]_0 \prod_{j=1}^{i-1} k_j \quad (25)$$

We have shown, in the case of chain reaction, that the main determinant (in the denominator) suggests a flow graph without the input node, the reactant that provides the formation of the specie involved. It is named *the global consumption determinant* because it indicates the consumption of all species in the favor of products.

Δ_{B_j} - the global consumption determinant -, being part of the term $(B_j e^{-k_j t})$, which refers to the contribution of "j" species to the formation of "i" species, it is obtained as a sub-graph that result from the principal flow graph, representing the mechanism, by eliminating the species "j", with his corresponding rate constant. Then one has to subtract k_j from every rate constant on the branches and eliminate A_j : It is shown in the figure 11.

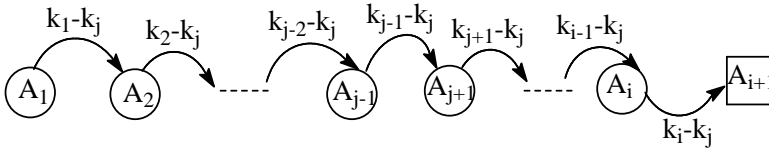


Fig. 11. The consumption flow graph of the term $B_j e^{-k_j t}$

The phenomenological explanation consists in the fact that *consumption of any intermediate species concentration involved could not occur before this species is formed. (the rate of consumption cannot exceed the rate of its formation).*

$$\begin{aligned} \Delta_{B_j} &= (k_1 - k_j)(k_2 - k_j) \dots (k_{j-2} - k_j)(k_{j-1} - k_j)(k_{j+1} - k_j) \dots (k_{i-1} - k_j)(k_i - k_j) \\ &= \prod_{l=1; l \neq j}^i (k_l - k_j) = \prod_{l=1; l \neq j}^i (\gamma_l - \gamma_j) \end{aligned} \quad (26)$$

By tacking into account the graph in figure 10, the formation determinant for the i species is:

$$\Delta_i = \begin{vmatrix} k_1 & 0 & 0 & 0 & 0 & 0 \\ -k_1 & k_2 & 0 & \dots & \dots & \dots \\ \dots & \dots & \dots & \dots & \dots & \dots \\ 0 & \dots & k_{j-1} & k_j & \dots & 0 \\ \dots & \dots & \dots & \dots & \dots & \dots \\ 0 & \dots & \dots & 0 & k_{i-1} & \dots \end{vmatrix} = \prod_{j=1}^{i-1} k_j \quad (27)$$

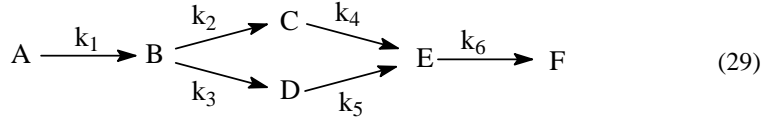
and the consumption determinant, in accordance with figure 11 is²⁰:

$$\Delta_{B_1} = \begin{vmatrix} (k_2 - k_1) & 0 & 0 & 0 & 0 & 0 \\ -(k_2 - k_1) & (k_3 - k_1) & \dots & \dots & \dots & \dots \\ 0 & \dots & \dots & \dots & \dots & 0 \\ \dots & \dots & (k_{j-1} - k_1) & (k_j - k_1) & \dots & 0 \\ \dots & \dots & \dots & \dots & \dots & \dots \\ 0 & \dots & \dots & \dots & k_{i-1} & \dots \end{vmatrix} = \prod_{j=2}^i (k_j - k_1) = \prod_{j=2}^i (\gamma_j - \gamma_1) \quad (28)$$

By using these determinants the concentration of each species in the mechanism is obtained and it is the same as obtained by classical integration of the system²¹.

Application to a mixed series and parallel reactions.

Another relevant example, encountered in the case of radioactive series, more complex in the sense it contains parallel processes, is:



It starts from $[A]_0$ in the absence of any intermediate or final product. The starting species concentration decays exponentially. To calculate $[B]$ a new flow graph should be constructed. It is a basic flow graph, for global consumption of B species, as presented in figure 12:

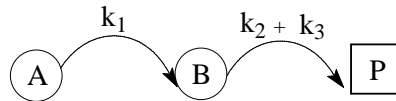


Fig. 12. For the consumption of B scheme

P stands for the products coming from B species when it reacts.

$$[B] = \sum_{j=1}^2 B_j e^{-\gamma_j t} \text{ with the coefficients }^{20}$$

$$B_j = \frac{\Delta_i}{\Delta_{B_j}}; \quad \gamma_{j=1} = k_1; \quad \gamma_{j=2} = k_2 + k_3 = k_2'$$
(30)

Δ_i is the formation determinant and it can be calculated directly from mechanism (29) starting from A to the specie (B); Δ_{B_j} is the consumption determinant and it is obtaining eliminating the species one after another from the basic flow graph for the consumption(fig.12):

$$\Delta_i = [A]_0 k_1; \quad \Delta_{B_1} = k_2' - k_1; \quad \Delta_{B_2} = k_1 - k_2'; \quad [B] = \frac{k_1 [A]_0}{k_2' - k_1} (e^{-k_1 t} - e^{-k_2' t}) \tag{31}$$

In order to calculate $[C]$ one has to construct a new basic flow graph, the one for global consumption:

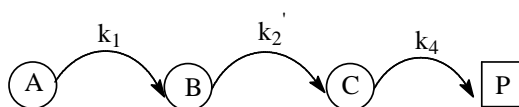


Fig. 13. The consumption flow graph for determining $[C]$.

FLOW GRAPHS IN CHEMICAL KINETICS (I)

$$\Delta_i = [A]_0 k_1 k_2; \quad \Delta_{B_1} = (k_2' - k_1)(k_4 - k_1) \quad (32)$$

$$\Delta_{B_2} = (k_1 - k_2')(k_4 - k_2'); \quad \Delta_{B_3} = (k_1 - k_4)(k_2' - k_4) \quad (33)$$

$$[C] = \frac{[A]_0 k_1 k_2 e^{-k_1 t}}{(k_2' - k_1)(k_4 - k_1)} + \frac{[A]_0 k_1 k_2 e^{-k_2' t}}{(k_1 - k_2')(k_4 - k_2')} + \frac{[A]_0 k_1 k_2 e^{-k_4 t}}{(k_1 - k_4)(k_2' - k_4)} \quad (34)$$

Similar for determination [D]:

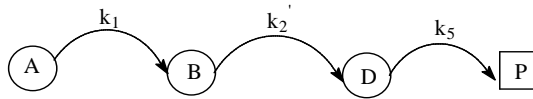


Fig. 14. The consumption flow graph for determining [D].

$$[D] = \frac{[A]_0 k_1 k_3 e^{-k_1 t}}{(k_2' - k_1)(k_5 - k_1)} + \frac{[A]_0 k_1 k_3 e^{-k_2' t}}{(k_1 - k_2')(k_5 - k_2')} + \frac{[A]_0 k_1 k_3 e^{-k_5 t}}{(k_1 - k_5)(k_2' - k_5)} \quad (35)$$

The global consumption determinants for [E] results from the two basic flows graph (figure 15) because there are two different ways to obtain it.

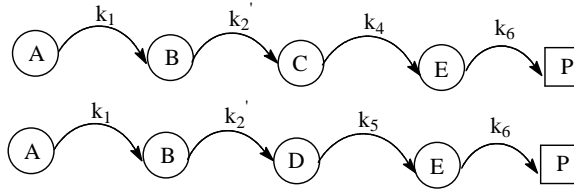


Fig. 15. The two ways of consumption of E species

$$\begin{aligned} \frac{[E]}{[A]_0} = & \frac{k_1 k_2 k_4 e^{-k_1 t}}{(k_2' - k_1)(k_4 - k_1)(k_6 - k_1)} + \frac{k_1 k_2 k_4 e^{-k_2' t}}{(k_1 - k_2')(k_4 - k_2')(k_6 - k_2')} + \\ & + \frac{k_1 k_2 k_4 e^{-k_4 t}}{(k_1 - k_4)(k_2' - k_4)(k_6 - k_4)} + \frac{k_1 k_2 k_4 e^{-k_6 t}}{(k_1 - k_6)(k_2' - k_6)(k_4 - k_6)} + \\ & + \frac{k_1 k_3 k_5 e^{-k_1 t}}{(k_2' - k_1)(k_5 - k_1)(k_6 - k_1)} + \frac{k_1 k_3 k_5 e^{-k_2' t}}{(k_1 - k_2')(k_5 - k_2')(k_6 - k_2')} + \\ & + \frac{k_1 k_3 k_5 e^{-k_5 t}}{(k_1 - k_5)(k_2' - k_5)(k_6 - k_5)} + \frac{k_1 k_3 k_5 e^{-k_6 t}}{(k_1 - k_6)(k_2' - k_6)(k_5 - k_6)} \end{aligned} \quad (36)$$

The final species concentration is obtained from the mass balance:

$$[A]_0 - [A] - [B] - [C] - [D] - [E] = [F] \quad (37)$$

A new approach of methane pyrolysis

The same way of treatment can be applied to the methane pyrolysis in its simple mechanism presented above, considered as an open sequence. If QSSA is not taken into consideration, from the flow graph depicted in figure 9, the global determinant, which provides the exponential factor, is^{20,22}:

$$\Delta_{\gamma} = \begin{vmatrix} k_2 a + 2k_4 x - \gamma & -k_3 a & -k_1 \\ -k_2 a & k_3 a - \gamma & -k_1 \\ 0 & 0 & 2k_1 - \gamma \end{vmatrix} = 0 \quad (38)$$

$$\Delta_{\gamma} = (2k_1 - \gamma)[\gamma^2 - \gamma(k_2 a + k_3 a + 2k_4 x) + 2k_4 x k_3 a] = 0 \quad (39)$$

where $[\text{CH}_3\cdot] = x$, $\gamma_1 = 2k_1$, $\gamma_2 \approx k_3 a$ and $\gamma_3 \approx 2k_4 x$. Because the transformation of the intermediate species is considered now as consecutive steps, the methyl radical concentration is:

$$x = \frac{2ak_1 k_3 a}{(\gamma_2 - \gamma_1)(\gamma_3 - \gamma_1)} e^{-\gamma_1 t} + \frac{2ak_1 k_3 a}{(\gamma_1 - \gamma_2)(\gamma_3 - \gamma_2)} e^{-\gamma_2 t} + \frac{2ak_1 k_3 a}{(\gamma_1 - \gamma_3)(\gamma_2 - \gamma_3)} e^{-\gamma_3 t} \quad (40)$$

$$x = \frac{2ak_1 k_3 a}{(k_3 a - 2k_1)(2k_4 x - 2k_1)} e^{-2k_1 t} + \frac{2ak_1 k_3 a}{(2k_1 - k_3 a)(2k_4 x - k_3 a)} e^{-k_3 a t} + \frac{2ak_1 k_3 a}{(2k_1 - 2k_4 x)(k_3 a - 2k_4 x)} e^{-2k_4 x t} \quad (41)$$

Now, considering that the terms two and three in the summation are much smaller than the first, a simpler expression is obtained:

$$x \approx \frac{2ak_1 k_3 a}{(k_3 a - 2k_1)(2k_4 x - 2k_1)} e^{-2k_1 t} \quad (42)$$

Because the first step rate coefficient is very small as compared to the others, the exponential is close to unity at least at the short reaction period $e^{-2k_1 t} \approx 1$. Consequently $2k_1 \ll 2k_4 x$ and $2k_1 \ll k_3 a$. It results that:

$$x \approx \frac{2ak_1 k_3 a}{k_3 a 2k_4 x} = \frac{ak_1}{k_4 x} \quad \text{or} \quad x = \sqrt{\frac{ak_1}{k_4}} \quad (43)$$

which is the same result as the one obtained by applying QSSA method (see eq.10). The rate of the final product formation is $k_2 a x + k_4 x^2 \approx k_2 a x$, the same as obtained by QSSA.

Various other complex mechanisms as the homogeneous catalyzed reactions, enzyme catalyzed reactions, single route chain reactions and multiple route chain reactions in the classification of Zeigarnik and Tenkin¹¹, will be

treated by using flow graph in the future papers of the series. They will involve situations where QSSA is used as well as opposing reactions, mixed series with opposing reactions, where QSSA is not appropriate.

Conclusions

The main conclusion concerning the flow graph employment in chemical kinetics is that a straight way to calculate the concentration of any species either for reactive intermediates or for transient intermediate, accumulating and decaying during the reaction.

In the case of the systems where QSSA is applicable, the flow graph is unique and the image of the reaction mechanism. In the case of open sequences, when the concentration of the intermediate species is not in a steady state, more than one graph should be considered. They can be constructed from the mechanism by taking into consideration several simple rules to form the formation and consumption determinants.

REFERENCES

1. J. A. Christiansen, *Adv. Catalysis*, **1953**, 5, 311-353.
2. E. L. King, C. Altman, *Phys. Chem.*, **1956**, 60, 1375
3. M. I. Temkin, *Dokl. Akad. Nauk SSSR*, **1963**, 152, 156-159.
4. M. I. Temkin, *Dokl. Akad. Nauk SSSR*, **1965**, 165, 615-618.
5. M. I. Temkin, *Mechanism and Kinetics of Complicated Reactions*, S. Z. Roginski, Moscow, **1970**, p. 57.
6. E. Segal, *Ann. Univ. Bucuresti* (**2002**).
7. E. Segal, *Progress in Catalysis*, **1997**, 6, 135-141.
8. E. Segal, *Progress in Catalysis*, **1998**, 7, 1-4.
9. O. N. Temkin, D. G. Bonchev, *J. Chem. Ed.*, **1992**, 69, 544-550.
10. A. V. Zeigarnik, O. N. Temkin, D. G. Bonchev, A. V. Zeigarnik, *J. Chem. Inf. Comput. Sci.*, **1995**, 35, 729-737.
11. A. V. Zeigarnik, O. N. Temkin, D. G. Bonchev, *J. Chem. Inf. Comput. Sci.*, **1996**, 36, 973-981.
12. A. V. Zeigarnik, *Kinet. Katal.*, **1996**, 37, 372-385.
13. K. Ogata, *Modern Control Engineering*, Prentice Hall International, New Jersey, **1995**.
14. N. S. Niece, *Control System Engineering*, Addison-Westley Publishing Company, **1995**, p. 240-260, 268-275.
15. R. C. Dorf, R. H. Bishop, *Modern Control System*, Prentice Hall International, New Jersey, **2001**, p. 66-80, 118-158.

16. A. C. A i t k e n, *Determinants and Matrices*, Oliver and Boyd, Edinburgh, **1939**, Chap. 2.
17. M. V. D i u d e a, O. I v a n c i u c, *Topologie Moleculara*, Ed. Complex, Cluj, **1995**, p. 37.
18. T. I o n e s c u, *Grafuri. Aplicatii. Vol 1*. Ed. Didactica si Pedagogica, Bucuresti, **1973**, p. 198- 207.
19. K. H. E b e r t, H, J. E d e r e r, G. I s b a r n, *Int. J. of Chem. Kinet.*, **1983**, 15(5), 486-493..
20. P. J u e r g e n, *Reaktionskinetische Auswertung Spektroskopischer Hessdaten*, Braunschweig, **1995**, p. 160-183.
- 21 C. C a p e l l o s, B. H. J. B i e l s k i, *Kinetic System*, Wiley-Interscience., New-York, **1972**, p. 52-56; J. A l - K a ' b i, P. H. G o r e, E. F S a a d, D. N. W a t e r s, G. F. Moxon, *Int. J. of Chem. Kinet.*, **1983**, 15, 697-703.
22. M. N. B e r b e r a n - S a n t o s, J. M. G. M a r t i n h o, *J. Chem. Ed.*, **1990**, 67, 375-379.

KINETICS AND MECHANISM OF *O*-XYLENE OXIDATION BY Ce(IV) IN AQUEOUS ACIDIC MEDIUM

GABRIELA-CRISTINA BUCȘA*, CLAUDIA GEMMA MUREȘANU
and IOAN BÂLDEA

*Department of Physical Chemistry, Faculty of Chemistry and Chemical Engineering of "Babeș-Bolyai" University, 11 Arany Janos, 3400, Cluj-Napoca, Romania (*e-mail: gbucsa@chem.ubbcluj.ro)*

ABSTRACT. The oxidation of *o*-xylene in aqueous acidic media, using perchloric acid, has been followed spectrophotometrically. A first-order dependence on Ce(IV) concentration and a complex dependence on *o*-xylene and hydrogen ion concentrations have been established. The effect of ionic strength on the reaction rate has been studied and activation parameters were calculated. The global reaction rate is consistent with a mechanism involving the rapid formation of a complex, suffering an intramolecular electron transfer.

Keywords: cerium, *o*-xylene, kinetics and oxidation

INTRODUCTION

In acidic media, Ce(IV) is a strong oxidizing agent and is widely used in analytical and inorganic chemistry. The oxidation of different types of organic compounds is mentioned in literature and the kinetics of such reactions has been studied¹⁻²⁸. The rate laws and mechanisms for the oxidation of toluene and some substituted toluene in aqueous sulphuric acid media were reported²⁹⁻³¹, and in the case of *p*-xylene oxidation with Ce(IV), the activation energy has been determined³⁰. In order to get more details concerning the kinetic and the mechanism of *o*-xylene oxidation, we have investigated this reaction by using perchloric acid as a hydrogen ion source, where no complex formation between Ce(IV) and ClO₄⁻ is to be expected.

EXPERIMENTAL

The chemicals used in this study were of reagent grade purity, purchased from commercial sources (Reactivul Bucharest, Merck and Fluka) and employed without further purification.

Kinetic measurements were performed by means of an Able Jasco V-530 spectrophotometer, provided with a temperature jacket surrounding the cell holder.

The cuvette jacket was connected to a Lauda M-20 recirculatory water bath. Reaction mixtures were prepared directly in the quartz cell of the spectrophotometer with 5cm-path length. A rapid adding of a measured amount of cerium (IV) stock solution over the reaction mixture containing HClO_4 , NaClO_4 , *o*-xylene in twice-distilled water at desired concentration, started the reaction. The reaction progress was followed by monitoring the decrease of absorbance at 315 nm, where the UV/VIS spectrum of Ce(IV) exhibits an absorption band.

RESULTS AND DISCUSSIONS

Preliminary investigations

Check of Lambert-Beer law. The validity of Lambert-Beer law has been verified over the concentration range used, because the kinetic study consists in absorbance measurements. Figure 1 presents the linear dependence of absorbance upon Ce(IV) concentration in the absence and the presence of *o*-xylene.

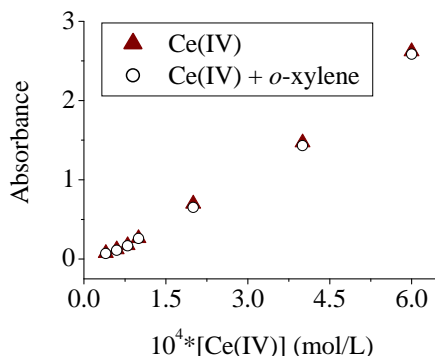


Fig. 1. Dependence prescribed by Lambert-Beer law at 315 nm
 $[\text{H}^+] = 1 \text{ mol/L}$; $\mu = 1 \text{ mol/L}$; $[\text{o-xilen}]_0 = 4 \cdot 10^{-4} \text{ mol/L}$; $t = 20^\circ\text{C}$

As it can be seen, only a slight decrease of molar absorption coefficient occurs when the mixture contains also *o*-xylene, but the linearity is maintained. Table 1 contains the values for the molar absorption coefficients for the experimental conditions. These facts suggest that a new absorbing species is formed, either in a small concentration, or it absorbs similarly to Ce(IV).

Table 1

Molar absorptivities in the absence and the presence of *o*-xylene

Reaction mixture	$[\text{H}^+] = 1 \text{ mol.L}^{-1}$; $[\text{ClO}_4] = 1 \text{ mol.L}^{-1}$; $\mu = 2 \text{ mol.L}^{-1}$; $t = 20^\circ\text{C}$			
	Ce(IV)		Ce(IV) + <i>o</i> -xylene $4 \cdot 10^{-4} \text{ mol.L}^{-1}$	
λ , nm	315	320	315	320
$\epsilon \text{ L.mol}^{-1}\text{cm}^{-1}$	4039 ± 198	4047 ± 207	3958 ± 209	3898 ± 201

Check for an intermediate species formation. By recording the spectra of reaction mixture immediately after mixing at 20°C and various increasing concentration of organic hydrocarbon, a small but systematic decrease of the intensity of Ce(IV) absorption band and the occurrence of an isosbestic point located at 375 nm have been noticed (fig. 2). This is brought about by the presence of a new absorbing species besides Ce(IV). It can be a complex involving Ce(IV) and the substrate.

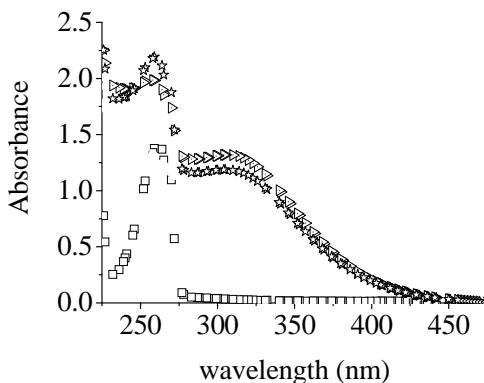


Fig. 2. Some spectra recorded immediately after mixing of Ce(IV) and *o*-xylene at various concentration (8.0×10^{-5} to 1.0×10^{-3}) of *o*-xylene

Stoichiometry determination. The stoichiometry of the reaction has been determined by a spectrophotometrical titration. Various mixtures having increasing ratios of [*o*-xylene]:[Ce(IV)] were allowed to react to completion at constant acidity. The absorbance values of the unreacted Ce(IV) were determined. Part of the Ce(IV) was consumed by the water molecule oxidation. Nevertheless, the mixture reacted the same period of time, and comparison has been done to the blank probe. The plot of absorbance difference between blank probe and those with *o*-xylene shows a turning point at the ratio 0.5, as can be seen in fig. 3. It predicts a ratio of 2 Ce(IV) ions to a molecule of *o*-xylene, indicating the oxidation yields *o*-methylbenzylic alcohol as the main oxidation product.

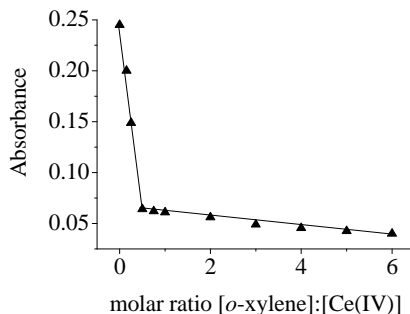
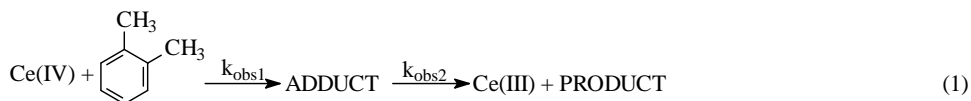


Fig. 3. Remainder absorbance difference at various molar ratios.

Kinetics

Experimental measurement consists in absorbance readings against time.

According to the shape of the experimental curve absorbance versus time, which looks like a biphasic plot, the oxidation of *o*-xylene by Ce(IV) consists in two consecutive stages of the type:



The first stage, perceptible at low degrees of transformation, could be attributed to the formation of an adduct between Ce(IV) and *o*-xylene. The second stage, perceptible at higher degrees of transformation, may be associated with the redox process consisting of an inner electron transfer within the complex, yielding the products of the reaction.

The reaction order with respect to Ce(IV) was determined from the dependence $\lg(r) = f(\lg[\text{Ce(IV)}])$. As can be seen in the figure 4, first-order with respect to cerium has been found for both stages of the reaction.

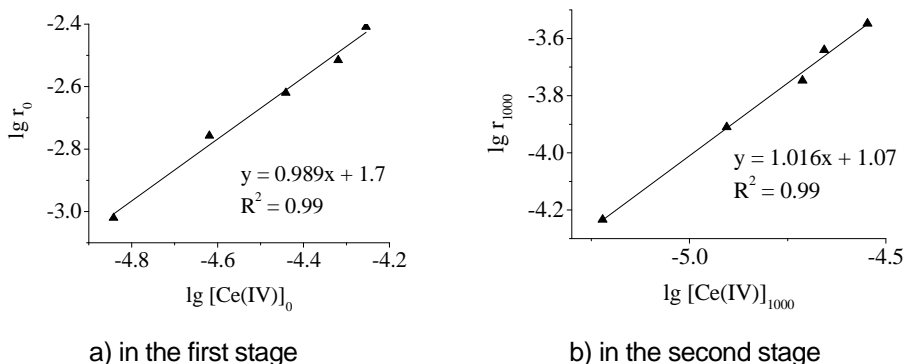


Fig. 4. Determination of reaction order with respect to cerium (IV) in the two stages of the reaction described above

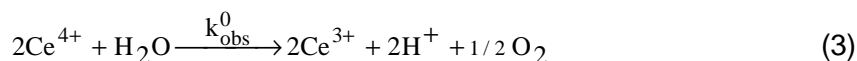
The experimental curves, $A = f(t)$, were the subject of derivation, at the initial moment and at $t = 1000\text{s}$, while the reaction rates and the corresponding concentrations of cerium were calculated by taking $\epsilon = 4039 \text{ M}^{-1} \text{ cm}^{-1}$.

Once it has been established, we preferred to determine the rate constants by a non-linear fitting of the experimental $A = f(t)$ curves, with the bi-exponential equation:

$$A - A_\infty = C_1 \exp(-k_{\text{obs1}}^0 \cdot t) + C_2 \exp(-k_{\text{obs2}}^0 \cdot t) \quad (2)$$

which describes the decay of the absorbance of the limiting component in a first order follow up reaction. A and A_{∞} stand for the absorbance at actual time and at the end of the reaction respectively. The parameters C_1 and C_2 are constants including the molar absorbance coefficients and Ce(IV) initial concentration. k_{obs1}^0 and k_{obs2}^0 are apparent rate constants of the two reaction steps.

Parallel to the oxidation of *o*-xylene, oxidation of water by Ce(IV) takes place, according to the stoichiometry:



The kinetics was of a first-order. We determined the influence of different parameters over the oxidation of water. Because in the literature³² we found that Ce(III) (which is a product of the reaction) diminishes the rate of the water oxidation reaction we put it in the reaction mixture in equal concentration to Ce(IV). The experimental curves for the water oxidation reaction were determined by a fitting method with the equation:

$$A - A_{\infty} = C_3 \exp(-k_{\text{obs}}^0 \cdot t) \quad (4)$$

Once we had all the rate constants, we subtract the rate constants for the oxidation of water from the rate constants of the overall reaction as follows:

$$k_{\text{obs1}} = k_{\text{obs1}}^0 - k_{\text{obs}}^0 \quad (5)$$

$$k_{\text{obs2}} = k_{\text{obs2}}^0 - k_{\text{obs}}^0 \quad (6)$$

where: k_{obs1} and k_{obs2} are the observed first-order rate constants of the xylene reaction for the first and the second step and k_{obs}^0 is the observed first-order rate constant for the water oxidation reaction.

The effect of *o*-xylene excess concentration upon the apparent rate coefficient, at constant hydrogen ion concentration and ionic strength, is presented in Table 2. Observed rate constants were obtained using equation (5) and (6).

In order to find the reaction order with respect to the *ortho*-xylene concentration, the logarithm of the apparent rate constants were plotted against the logarithm of *ortho*-xylene concentration excess.

Table 2

Effect of *o*-xylene concentration on the apparent rate constants.
 $[\text{Ce(IV)}] = [\text{Ce(III)}] = 8 \cdot 10^{-5} \text{ mol.L}^{-1}$; $[\text{H}^+] = 1 \text{ mol.L}^{-1}$; $\mu = 1 \text{ mol.L}^{-1}$; $t = 40^\circ\text{C}$

$10^4 \cdot [\text{o-xylene}]$ (mol/L)	$10^3 \cdot k_{\text{obs1}}$ (s ⁻¹)	$10^4 \cdot k_{\text{obs2}}$ (s ⁻¹)
4	1.13	0.86
6	1.73	1.06
7	1.94	1.14
8	2.22	1.23
9	2.58	1.31
10	2.9	1.39

For the first stage of reaction, we found first-order dependence with respect to *o*-xylene and sub-unit fraction order for the second stage. The best fit, we could find for the data from table 1 was obtained by using the equations:

$$k_{\text{obs1}} = (-3 \cdot 10^{-5} \pm 6 \cdot 10^{-5}) + (2.89 \pm 0.08)[\text{o-xylene}]_0 \quad (7)$$

$$k_{\text{obs2}} = \frac{(0.32 \pm 0.06)[\text{o-xylene}]_0}{1 + (1308 \pm 484)[\text{o-xylene}]_0} \quad (8)$$

It is easy to recognize in the dependence of the second stage a Michaelis – Menten pattern, suggesting also the involvement of an intermediate.

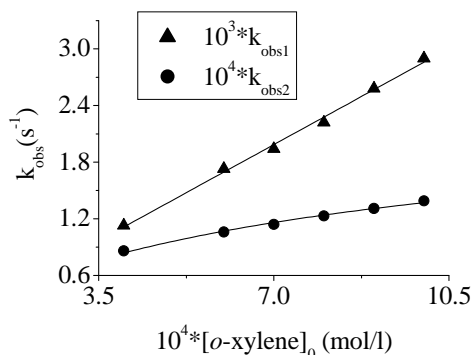


Fig. 5. The effect of *o*-xylene for the first and the second stage of the reaction;
 $[\text{Ce(IV)}] = [\text{Ce(III)}] = 8 \cdot 10^{-5} \text{ mol/L}$; $[\text{H}^+] = 1 \text{ mol/L}$; $\mu = 2 \text{ mol/L}$; $t = 40^\circ\text{C}$

Even under high acid concentration, the hydrolysis of Ce(IV) ion, and the formation of polynuclear ions complicate the kinetics of Ce(IV) reaction. It is revealed from the influence of hydrogen ion concentration on the rate constant that it is quite complex, investigated in the limits presented in the Table 3.

Table 3

Effect of hydrogen ion concentration on the apparent rate constant; $[Ce(IV)]=8 \cdot 10^{-5} \text{ mol.L}^{-1}$; $[Ce(III)]=8 \cdot 10^{-5} \text{ mol.L}^{-1}$; $[o\text{-xylene}]=4 \cdot 10^{-4} \text{ mol/L}$; $\mu = 3 \text{ mol.L}^{-1}$; $t = 40^{\circ}\text{C}$

$[H^+]$ (mol.L ⁻¹)	$10^3 \cdot k_{obs1}$ (s ⁻¹)	$10^4 \cdot k_{obs2}$ (s ⁻¹)
0.5	11.39	0.99
1	8.37	2.25
1.5	6.9	3.09
2	5.87	4.22
2.5	5.12	5.34

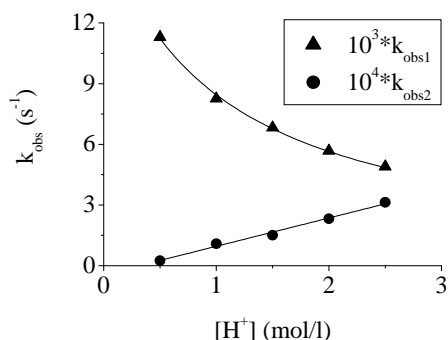


Fig. 6. Dependence of rate constant upon the hydrogen ion concentration; $[Ce(IV)]=[Ce(III)]=8 \cdot 10^{-5} \text{ mol.L}^{-1}$; $[o\text{-xilen}]=4 \cdot 10^{-4} \text{ mol.L}^{-1}$; $\mu = 3 \text{ mol/L}$; $t = 40^{\circ}\text{C}$.

As it can be seen the concentration of hydrogen ion has an opposite effect on the two stages of the reaction (fig. 6). It diminishes the rate constants of the first step, according to equation above, and revealing the loss of the proton:

$$k_{obs1} = \frac{(0.016 \pm 1.24 \cdot 10^{-3})}{1 + (0.9 \pm 0.14)[H^+]} \quad (9)$$

and causes a linear increase of the rate constant on the hydrogen ion concentration of the form:

$$k_{obs2} = (2.1 \cdot 10^{-4} \pm 1 \cdot 10^{-5}) [H^+] \quad (10)$$

The influence of ionic strength on the reaction rate was also studied. As can be seen from table 4, ionic strength has a positive effect on both the first and the second stages of the reaction. Although Debye – Hückel relation for activity coefficients could be applied only at lower ionic strengths ($\approx 10^2 \text{ mol/L}$) we have plotted equation of the form:

$$\ln k_{\mu} = \ln k_{\mu=0} + \frac{2Az_A z_B \sqrt{\mu}}{1 + Ba\sqrt{\mu}} \quad (11)$$

Table 4

Influence of ionic strength on the rate constants for both processes
 $[Ce(IV)] = [Ce(III)] = 8.0 \times 10^{-5} \text{ mol.L}^{-1}$; $[o\text{-xylene}] = 4.0 \times 10^{-4} \text{ mol.L}^{-1}$; $t = 40^{\circ}\text{C}$

$\mu \text{ (mol.L}^{-1}\text{)}$	$10^3 k_{\text{obs1}} \text{ (s}^{-1}\text{)}$	$10^4 k_{\text{obs2}} \text{ (s}^{-1}\text{)}$
0.5	1.39	0.28
1	2.19	0.56
1.5	2.88	0.77
2	4.08	1.03
2.5	5.28	1.25
3	6.17	1.43

which can be seen in the figure 7.

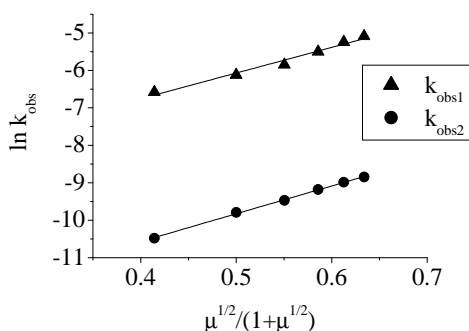


Fig. 7. Dependence of rate constant upon ionic strength. Debye – Huckel representation;
 $[Ce(IV)] = [Ce(III)] = 8.0 \times 10^{-5} \text{ mol.L}^{-1}$; $[o\text{-xylene}] = 4.0 \times 10^{-4} \text{ mol.L}^{-1}$;
 $[H^+] = 0.5 \text{ mol.L}^{-1}$ and $t = 40^{\circ}\text{C}$

The relation (11) lead to the following expressions with our data:

$$\ln k_{\text{obs1}} = (-9.49 \pm 0.2) + (6.83 \pm 0.36) \frac{\sqrt{\mu}}{1 + \sqrt{\mu}} \quad R^2 = 0.960, \chi^2 = 0.013, N = 18$$

$$\ln k_{\text{ap2}} = (-13.52 \pm 0.1) + (7.4 \pm 0.19) \frac{\sqrt{\mu}}{1 + \sqrt{\mu}} \quad R^2 = 0.991, \chi^2 = 0.0026, N = 18$$

As can be seen in the figure 6, the plots are linear for both stages. Even so, we can only say that the influence of ionic strength has a contribution of primary salt effect as well as secondary salt effect and involves ions of like charges.

Activation parameters were determined for both stages of the reaction from the Arrhenius and from the Eyring plot. The effect of the temperature is presented in table 5. The plots of the linear form of Arrhenius and Eyring equations were linear with quite good correlation coefficients. The results are presented in table 6.

Table 5

Temperature effect on the first-order rate constants. $[H^+] = 1.5 \text{ mol.L}^{-1}$; $\mu = 3 \text{ mol.L}^{-1}$; $[Ce(IV)] = [Ce(III)] = 8.0 \times 10^{-5} \text{ mol.L}^{-1}$; $[o\text{-xylene}] = 4.0 \times 10^{-4} \text{ mol.L}^{-1}$

Temp. (K)	308	313	318	323	328	333
$10^2 k_{\text{obs1}} (\text{s}^{-1})$	0.46	0.56	0.66	0.93	1.81	2.64
$10^{4*} k_{\text{obs2}} (\text{s}^{-1})$	0.46	0.54	1.13	1.39	2.69	3.4

The relatively small values of activation energy and activation enthalpy could be explained by the involvement of an adduct formation pre-equilibrium, and intramolecular electron transfer. Concerning the rate determining step the rate law is, depending on the concentrations of organic compound, of hydrogen ion and of oxidizing agent, of the form:

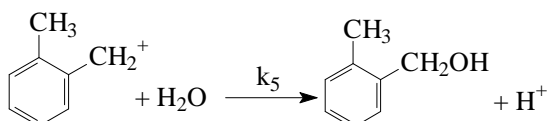
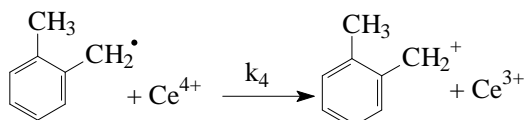
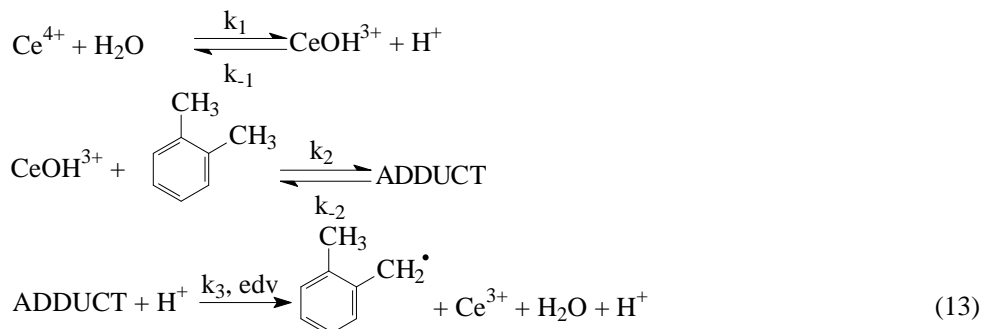
$$r = k_2 \frac{a [o\text{-xylene}]_0 [H^+] [Ce(IV)]}{1 + b [o\text{-xylene}]_0} \quad (12)$$

Table 6

Activation parameters for the two stages of oxidation of o-xylene.

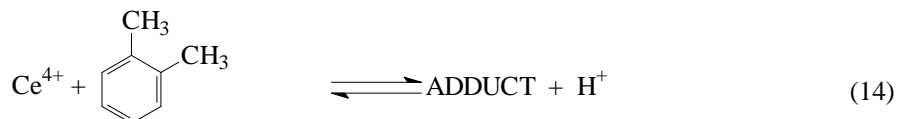
Stage	E_a (kJ/mol)	ΔH^\ddagger (kJ/mol)	ΔS^\ddagger (J/K)
1	61.1 ± 7.8	58.5 ± 7.7	-101.6 ± 0.02
2	87 ± 4.9	84.4 ± 4.9	-55.6 ± 0.2

A reaction mechanism (13) can be suggested, based on spectral measurements, the stoichiometry, the rate law and literature data. It involves the formation of an adduct between o-xylene and the hydrocomplex of Ce(IV),



followed by the inner electron transfer. This step is the rate determining. The subsequent steps are very rapid leading finally to the major oxidation product, which is *o*-methylbenzylic alcohol.

If the first two pre-equilibria from the mechanism are combined as follows:



than the rate equation determined from the mechanism suggested by us will have the form:

$$r = k_3 K_h K_2 \frac{[\text{Ce(IV)}][\text{H}^+][\text{o-xylene}]_0}{1 + K_h[\text{H}^+] + K_2[\text{o-xylene}]_0} \quad (15)$$

in accordance with the kinetic and extra-kinetic data. The complex between Ce(IV) named here adduct is formed at the interaction of Ce(OH)³⁺ and xylene, when a hydrogen ion coming from a methyl group bonds to hydroxyl ion and carbon anion bonds to Ce(IV) entering its coordination sphere. In the rate-determining step the supplementary proton seems to be necessary to stabilize the methylbenzyl free radical formed.

REFERENCES

1. Das A. K., Das M., *J. Chem. Soc. Dalton Trans.*, **1994**, 589.
2. Willard H. H., Young P., *J. Am. Chem. Soc.*, **1930**, 52, 132.
3. Pondit A. K., Das A. K., Banerjea D., *Transitionmet. Chem.*, **1991**, 16, 324.
4. Hintz H. L., Johnson D. C., *J. Org. Chem.*, **1967**, 32, 556.
5. Duke F. R., Bremer R. F., *J. Am. Chem. Soc.*, **1951**, 73, 5179.
6. Waters W. A., Jones J. R., Litter J. S., *J. Chem. Soc.*, **1961**, 240.
7. Muhammad S. S., Rao K. V., *Bull. Chem. Soc. Jpn.*, **1963**, 36, 943.
8. Ardon M., *J. Chem. Soc.*, **1957**, 1811.
9. Hargreaves G., Sutcliffe L. H., *Trans. Faraday Soc.*, **1955**, 51, 1105.
10. Sankhla P. S., Mehrotra R. N., *J. Inorg. Nucl. Chem.*, **1972**, 34, 3781.

11. Rangaswamy M., Santappa M., *Acta Chim. Acad. Sci. Hung.*, **1968**, 56, 413.
12. Grover V.K., Gupta Y.K., *J. Inorg. Nucl. Chem.*, **1969**, 31, 1403.
13. Wells C.F., Husain M., *Trans. Faraday Soc.*, **1970**, 66, 679.
14. Balasubramanian T.R., Venkatasubramanian N., *Indian J. Chem.*, **1970**, 8, 305.
15. Dayal R., Bakore G.V., *Indian J. Chem.*, **1972**, 10, 1165.
16. Rao G.N., *Indian J. Chem.*, **1970**, 8, 328.
17. Krishna B., Tewari K. C., *J. Chem. Soc.*, **1961**, 3077.
18. Gopal Rao G., Madhava Rao B., *Anal. Chim. Acta*, **1972**, 59(3), 461.
19. Trahanovsky W.S., Young L.B., *J. Org. Chem.*, **1966**, 31, 2033.
20. Syper L., *Tetrahedron Letters*, **1966**, 37, 4493.
21. Ignaczak M., Dziegiec J., Markiewicz M., *Pol. J. Chem.*, **1980**, 54, 1121.
22. Sethuram B., Muhammad S.S., *Acta Chim. Acad. Sci. Hung.*, **1965**, 46, 115.
23. Sethuram B., Muhammad S.S., *Acta Chim. Acad. Sci. Hung.*, **1965**, 46, 125.
24. Trahanovsky W.S., Young L.B., Brown G.L., *J. Org. Chem.*, **1967**, 32, 3865.
25. Paquette D., Zador M., *Can. J. Chem.*, **1968**, 46, 3507.
26. Melicherik M., Treindl L., *Chem. Zvesti*, **1981**, 35, 153.
27. Wiberg K.B., Ford P.C., *J. Am. Chem. Soc.*, **1969**, 91, 124.
28. Ignaczak M., Deka M., *Pol. J. Chem.*, **1980**, 54, 259.
29. Baciocchi E., Rol C., Sebastiani G.V., *J. Chem. Research(Synopsis)*, **1983**, 9, 232.
30. Ramaswamy M.S., Venkatachalapathy M.S., Udupa H.V.K., *Bull. Chem. Soc. Jpn.*, **1962**, 35, 214.
31. Radhakrishna P.S., Pati S.C., *Chem. Ind.*, **1967**, 17, 702.
32. D.Kolp, H.C.Thomas, *J. Am. Chem. Soc.*, **1949**, 71, 3047.

SAMPLE HANDLING. CHROMATOGRAPHIC ANALYSIS OF TRIFLURALIN FROM ENVIRONMENTAL SAMPLE. I. WATER SAMPLE

I.HAIDUC¹, S.COBZAC¹, A.MOCANU², M.C.BACIU¹

¹Faculty of Chemistry and Chemical Engineering, Babes-Bolyai University,
11 Arany Janos Street, Cluj-Napoca

²Institute for Public Health, 6 Pasteur Street, Cluj-Napoca

ABSTRACT. Trifluralin is a preemergent herbicide with little postemer-gent activity. When incorporated in the soil it is effective for the control of annual grasses and broad-leaved weeds in beans, soyabeans, sugar beet, sunflower, and tomatoes. That is why trifluralin can be found in small quantities in the soil and accidentally, in greater concentrations in soil and water as a consequence of other human activities in the field.

In the analytical chain, sample handling is very important for the accuracy and the precision of the analysis. this pesticide is extracted from environmental water sample using liquid-liquid extraction and solid phase extraction.

The present paper deals with solid phase extraction (SPE) of trifluralin on C18 cartridge. The efficiency of the sample treatment was evaluated by the recovery degree of the pesticide from spiked water samples.

When methanol was used as a conditioning and elution solvent, the recovery was higher than 90% and the reproductibility was better.

Keyword: trifluraline, SPE, GC, HPLC, water.

I. Introduction

Trifluralin or 2,6- dinitro-N,N-dipropyl-4-trifluoromethylaniline (fig. 1) is an orange crystalline solid, have the melting point at 48,5 – 49°C, small solubility in water 1mg/mL and maximum solubility in xilen 580g/mL.

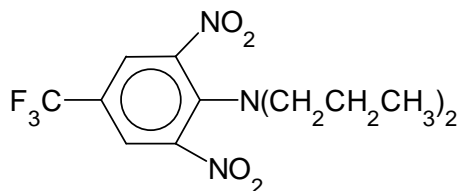


Figure 1. Trifluralin structure.

Trifluralin is a preemergent herbicide with little postemergent activity. When incorporated in the soil it is effective for the control of annual grasses and broad-leaved weeds in beans, soyabeans, sugar beet, sunflower, and tomatoes. That is why trifluralin can be found in small quantities in the soil and accidentally, in greater concentrations in soil and water as a consequence of other human activities in the field.

In the analytical chain, sample handling is very important for the accuracy and the precision of the analysis. This pesticide is extracted from environmental water sample using liquid-liquid extraction or solid phase extraction.

The present paper deals with solid phase extraction (SPE) of trifluralin on C18 cartridge. The efficiency of the sample treatment was evaluated by the recovery degree of the pesticide from spiked water samples.

In a study [1] for the determination of trifluralin from water, Colina used the solid phase extraction on C18 cartridge. The sorbent conditioning was achieved with 5 mL isooctane, ethyl acetate, methanol and water passed successively through the cartridge. After analyt retention achieved at a flow rate 10-15 mL/min the sorbent was washed with water and dried with air. The elution was perform with a solvent mixture consisting in ethyl acetate – isooctane (1:1, v/v). The elution solvent was evaporated and the residuum was dissolved in 1 mL methanol. This procedure provides a 96% recovery. The same procedure applied on river water provides a 85% recovery. When Empore C18 discs and ethyl acetate as elution solvent were used the recovery for trifluralin from water samples was 72,3% [2]. Other solvents like ethyl ether [3] or a dichlormethan-acetone (1:1, v/v) mixture [4] were also used, the recovery ranging between 65%-96%.

In last period sample preparation for trifluralin involved solid phase microextraction (SPME), a new technique that do not need solvents [5].

Generaly gas chromatography is used for trifluralin identification and quantification [6-8].

II. Experimental

Because of the high volatility of these solvents and because they are not mixable with water, in this paper we try to use methanol either as conditioning and elution solvent.

For the extraction of trifluralin three types of home made Sil C18 was used. The chemicaly modified surface was achived using three different procedure, obtaining three sorbent with different properties (Sil C18 I, Sil C18 II, Sil C18 III) [9]. It was also used a comercial SepPack C18 cartridge from Merck.

Also we try to use liquid-chromatography instead of gas chromatography.

Chemicals and standard solution

Solvents from Chimopar (Bucuresti, Romania), trifluralin – technical grade from CIG –Turda (Romania), solid phase cartridge SepPack C18, Merck (Darmstadt, Germany) were used and a methanol solution containing 10,85 µg trifluralin / mL for gas-chromatography and another one containing 100µg trifluralin / mL for liquid chromatography analysis were prepared.

Procedure

Sample preparation using SPE

1. Water Sample Preparation for Liquid-Chromatography

The extraction cartridge containing 300 mg sorbent was prepared. The sorbent conditioning was achieved in two ways:

- a) 5 mL methanol
- b) 5 mL acetone followed by 5 mL methanol.

The solvent excess was removed with 5-mL water. The trifluralin retention from the synthetic sample (100mL water spiked with 1 mL stock solution - 100µg trifluralin / mL) was achieved by passing it through the cartridge at a flow rate 10 mL/min. The cartridge was then washed with 5-mL water, air- dried and the analyt eluted in two ways:

- a) 3 mL methanol
- b) 3 mL acetone.

The organic solvent was evaporated and the solid residuum was dissolved into 1 mL methanol. The symbols for this sample are given in Table 1.

Table 1.

The symbol for each sample obtained after the SPE procedure.

Sorbent	Conditioning and elution type	Nr. of extraction	Symbol
Sil C 18 I	A	1 ; 2 ; 3	Ia ₁ ; Ia ₂ ; Ia ₃
	B	1 ; 2 ; 3	Ib ₁ ; Ib ₂ ; Ib ₃
Sil C 18 II	A	1 ; 2 ; 3	IIa ₁ ; IIa ₂ ; IIa ₃
	B	1 ; 2 ; 3	IIb ₁ ; IIb ₂ ; IIb ₃
Sil C 18 III	A	1 ; 2 ; 3	IIIa ₁ ; IIIa ₂ ; IIIa ₃
	B	1 ; 2 ; 3	IIIb ₁ ; IIIb ₂ ; IIIb ₃
Sil C18 IV (Sep Pack C18)	A	1 ; 2 ; 3	IVa ₁ ; IVa ₂ ; IVa ₃
	B	1 ; 2 ; 3	IVb ₁ ; IVb ₂ ; IVb ₃

2. Water Sample Preparation for Gas-Chromatography

After cartridge preparation the sorbent was conditioned in two ways:

- a) 5 ml methanol
- b) 5 ml ethyl acetate followed by 5 mL methanol.

The conditioning solvent was then removed with 5 mL water. The trifluralin retention from the synthetic sample (100 mL water spiked with 1 mL stock solution 10,85µg/mL) was achieved at a 10 mL/min flow rate. After the sorbent was dried, trifluralin was eluted in two ways:

- a) 1 mL methanol
- b) 1 mL ethyl acetate.

The volume of the sample was then adjusted to 1 mL with methanol, respectively with ethyl acetate.

Chromatographic analysis

1. HPLC Analysis

The determination was achieved on a Hewlett Packard 1100 liquid-chromatograph, with manual injection (20 μ m microcolumn), operated at 25°C. A Lichrosphere RP 60 Select B, 250mmx4mm column was used. The mobile phase was an acetonitrile – water (85:15, v/v) mixture, at a 1 mL/min flow rate. The detection was achieved in UV at 275nm, where the trifluralin has a maximum absorbance spectrum (fig.2).

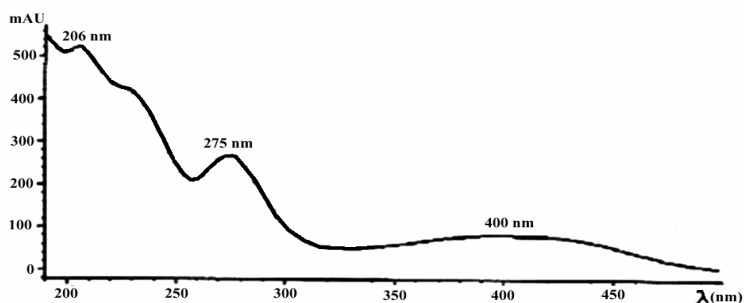


Figure 2. Absorbance spectrum.

2. Gas-Chromatography Analysis

The determination was achieved on a Fractovap 2450, Karlo Erba gas chromatograph equipped with capture electron detector. The stainless steel column filed with OV 17 (methylfenil silicon), 3% on a Gas-Chrom support, was operated at 170°C. Nitrogen at 15mL/min flow rate was used as eluent.

III. Results and discussion

1. Water Sample Analysis by Liquid-Chromatography

In Figure 3 the chromatogram for trifluralin in stock solution is presented. The chromatographic peak of trifluralin was observed at 3.89 min retention time. The recovery was calculated by dividing the peak area of trifluralin from the processed sample by the peak area of trifluralin from the stock solution. Table 2 presents the recoveries after the SPE procedures presented above.

The small recovery values can be explained only by analyt losses in the evaporation phase, when variable quantities of trifluralin also evaporated. A slightly increasing of recovery was observed in case of methanol elution.

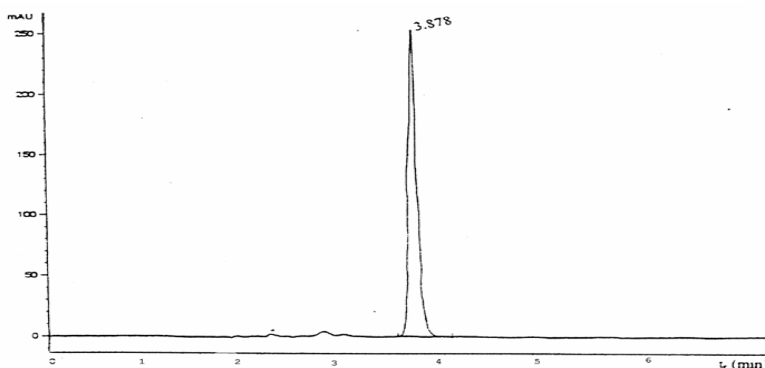


Figure 3. The trifluralin chromatogram ($\lambda=275$).

Table 2.

The recoveries of trifluralin when using different sorbents and elution solvents.

Sample	Recovery (GR%)			Average GR% \pm RSD%
	Extr. 1	Extr. 2	Extr. 3	
Ia	52,51	54,75	53,29	53,52 \pm 2,124
Ib	45,50	43,25	44,45	44,4 \pm 2,536
IIa	52,62	48,43	48,26	49,77 \pm 5,00
IIb	49,92	43,52	45,92	46,45 \pm 6,96
IIIa	60,80	54,60	58,54	57,98 \pm 1,961
IIIb	51,66	54,74	53,49	53,30 \pm 2,908
IVa	54,77	57,55	56,39	56,24 \pm 2,489
IVb	41,96	45,93	40,88	42,92 \pm 6,198

2. Water Sample Analysis by Gas-Chromatography

In these condition the peak of trifluraline was observe at 7.4 min. retention time. In Table 3 are given the recoveries calculated in the same manner like presented before.

In this experiment, it can be observe that the recovery values are higher as first attempt. These can be explained by avoiding the looses from evaporation step. So, the recovery increased from 50% at 90%.

Table 3.

The recoveries of trifluralin when using different sorbents and elution solvents.

Sorbent	Recovery (%)						Average GR \pm RSD (%)
	Solvent						
	Ethyl Acetate	Methanol					
Era. 1		E 2	Ext 3	Ex. 4	E. 5		
Sil C18 I	107,5	98,35	103,75	107,25	81,75	81,00	94,42 \pm 12,33
Sil C18 II	83,14	107,25	99,38	99,14	78,87	80,62	93,05 \pm 12,59
Sil C18 III	87,43	99,00	105,00	102,00	86,25	80,25	94,50 \pm 10,7
Sil C18 IV	92,57	95,14	96,75	94,50	99,75	96,00	96,43 \pm 2,04

IV. Conclusions

It is clear that the preparation step is very important in obtaining accurate results. So, when evaporation step is eliminated the recovery increased from 50% to 90%. For different C18 phases, better reproductibility were achieved when a polar organic solvent, like methanol, mixable with water was used.

BIBLIOGRAPHY

- [1]. De la Colina C.; Rosero F.S.; Cancela G.D.; Taboada E.R.; Pena A., *Analyst*, **120** (1995), 1723.
- [2]. Senseman S.A.; Lavy T.L.; Matice J.D.; *Anal.Chem.*, **67** (1995), 3064.
- [3]. Cabras P.; Melis M.; Spaneda L.; Tuberosa C.; *J.Chromatogr.*, **585** (1991), 164.
- [4]. Triska J., *Chromatographia*, **40** (1995), 712.
- [5] A.B.Boland, S.Magdic, J.B.Pawliszyn, *Analyst*, **121** (1996), 929.
- [6]. Cesena A.J.; Kerr L.A.; Patey E.; Zhu T.; Desjardins R.L.; *J.Chromatogr.*, **710** (1995), 251.
- [7]. Liu Z.; Sirimane S.R.; Patterson D.G.; Needham L.L.; Phillips J.B., *Anal.Chem.*, **66** (1994), 3086.
- [8]. Worthing R.C; Phil D., *The Pesticide Manual*, The Lavenham Press Limited, Suffol, 1987.
- [9]. Cobzac Simona, *Studiul extracției pe fază solidă C18 a unor pesticide din apă precum și a unor componente active din maceratele glicerice din plante medicinale*, Teză de doctorat, 2000, 34 - 67.

CATHODIC ELECTRODEPOSITION OF TITANIUM DIOXIDE FILMS

ANCA PETER¹, VIRGINIA DANCIU², VERONICA COSOVEANU²

¹ *Department of Chemistry, North University of Baia Mare, 4800 Baia Mare, Romania*

² *Electrochemical Research Laboratory, Babes-Bolyai University, 3400 Cluj-Napoca, Romania*

ABSTRACT. A galvanostatic technique for deposition of nanocrystalline titanium dioxide thin films on titanium sheet was developed. This techniques is a two-stage process: 1) cathodic electrodeposition of titanium oxyhydroxide gel film from aqueous solution containing a Ti precursor and 2) subsequent heat-treatment of this gel film results in the formation of titanium dioxide film. The deposition current density and the pH of the electrolyte have a considerable effect on the formation of nanocrystalline film.

1. Introduction

Semiconductor photocatalytic reaction has been investigated extensively, with applications focussing on solar energy conversion and storage [1,2], reductive fixation of CO₂ [3-5], organic synthesis [6,7] or mineralization and/or detoxification of organic compounds [8-10]. Among semiconductors, titanium dioxide is one of the most popular and promising materials as a photocatalyst because it is stable in various solvents under photoirradiation, nontoxic, available commercially, and easy to prepare in the laboratory and has potent ability to induce various types of redox reactions.

In a series of studies on TiO₂ photocatalytic reactions [11-14] it has shown that the overall kinetics depend on both amount of substrate adsorbed on the surface to be reduced or oxidized by photoexcited electron (e⁻) or positive hole (h⁺), respectively, and rate of geminate recombination of e⁻ or h⁺. To obtain highly active TiO₂ photocatalyst, therefore, it is necessary to give it, simultaneously, a couple of properties: large surface area to adsorb substrates and high crystallinity to diminish the e⁻ - h⁺ recombination. When the semiconductor is a powder suspended in the wastewater, many pollutants, even at low concentrations (ppm), can be completely mineralized [15]. This method, however, cannot work continuously because, after the degradation process, the photocatalyst must be removed from the suspension, either by filtering or sedimentation, which can leave traces of particulate in the treated fluid. In this context, fixed bed photoreactors are more practical because they can work continuously. Moreover, when the support is a conducting one, the process efficiency can be improved by applying a suitable potential [16].

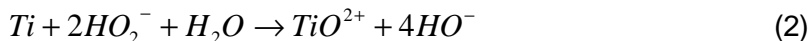
A TiO₂ photoanod can be obtained by sol-gel method (SGM) [17-22], chemical vapor deposition (CVD) [23], cathodic electrodeposition (CE) [24], electrochemical oxidation of titanium metal [25], anodic dissolution of titanium metal followed by cathodic photodeposition [26] or anodic oxidation of hydrolyzed TiCl₃ [27].

Our research focused on preparation of TiO₂ films by cathodic electrodeposition in galvanostatic conditions and study of its electrochemical behavior.

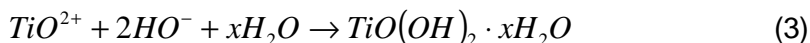
2. Experimental Section

Materials. Powder titanium (>98,5%) and plate titanium (99,99%) were supplied from Fluka AG. Ammonia (25%) was purchased from Reactivul - Romania and hydrogen peroxide (30%) from Chimopar- Romania. Sulfuric acid (97-98%) and potassium nitrate were supplied from Primexchim-Romania and Reactivul- Romania, respectively. Doubly distilled water was used to make the aqueous solutions throughout this study.

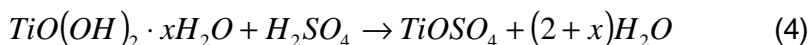
Preparation of titanium (IV) oxide precursor. In order to prepare the aqueous titanium oxysulfate solution, titanium powder was dissolved in H₂O₂ and ammonia (1:2 v/v) mixture.



The excess H₂O₂ and ammonia was decomposed by heating the solution on a hot plate until a yellow colored gel was obtained. This yellow gel may be in monomeric or oligomeric form [28]. But, for simplicity, it was considered that this Ti (IV) species exists in monomeric form as mentioned in reaction 3.



By dissolving the yellow gel in 2 M H₂SO₄ a red colored solution was obtained.



This red solution was used as the stock solution for further deposition. The concentration of titanium oxysulfate solution was determinate by spectrophotometric method [29].

Cathodic electrodeposition of TiO₂ thin films. For electrochemical experiments a potentiostat/galvanostat (PS3 Meinsberg, Germany) and a three electrodes cell were used. A Pt-foil as the counterelectrode and a saturated calomel electrode (SCE) as reference electrode were used. The substrate for

TiO₂ thin film was a 10x10-mm titanium sheet. Before electrodeposition, the titanium plates were introduced in HCl (37%) : H₂O (1:1 v/v) solution, for 30 min. and then, washed by water and ethanol. The deposition electrolyte contained both Ti precursor and KNO₃. The concentration of nitrate ions was at least equal with TiO²⁺ concentration. Due to the reduction of nitrate ions at potentials more negative than – 0,9 V, the hydroxyl ions were generated as shown in reaction (5):



The generation of OH⁻ ions increased the local pH at the electrode surface resulting in the TiO(OH)₂ · xH₂O gel film formation on the electrode, reaction 3 [24]. The gel films were prepared in galvanostatic conditions, at 10, 15, 20 and 25 mA/cm² and different pH values (0,5; 2).

Thermal treatment of the obtained gel film. The gel films obtained in the preceding step was heat-treated at 400^o C, for 30 min, to form TiO₂ film (reaction 6):



Measurement techniques. Cyclovoltammetric measurements were performed with a PGSTAT 10 AUTOLAB computer-controlled potentiostat driven by Model GPES 4.4 electrochemical analysis software. A single – compartment cell with a working electrode, consisting of approximately 19 mm² of a TiO₂/Ti and a Pt-plate as counter-electrode was used. A Pt-wire served as a quasi-reference electrode. The measurements were carried out in the 1M LiClO₄ / acetonitrile.

X-ray diffraction measurements were made using a DRON 3M X-ray diffractometer using a Co (Co K_α λ = 1,7902Å) anode.

The morphology and thickness of TiO₂ films were observed using scanning electron microscopy (type Leica Cambridge Instruments S 360) with an accelerating voltage of 5 kV.

3. Results and Discussion

In the figure 1, cyclic voltammograms on the TiO₂/Ti electrode in LiClO₄/acetonitrile solution with different lithium ion concentrations are shown. The potential scan was carried out in the potential range 0 to –3 V with scan rate of 10 mV/s. On the cathodic scan, when the potential was scanned till –3V, two broad peaks are seen and on the anodic scan two humps are seen. This shows that two redox reactions are involved. One must be reaction 7 and the other is probably lithium reduction/oxidation (reaction 8).



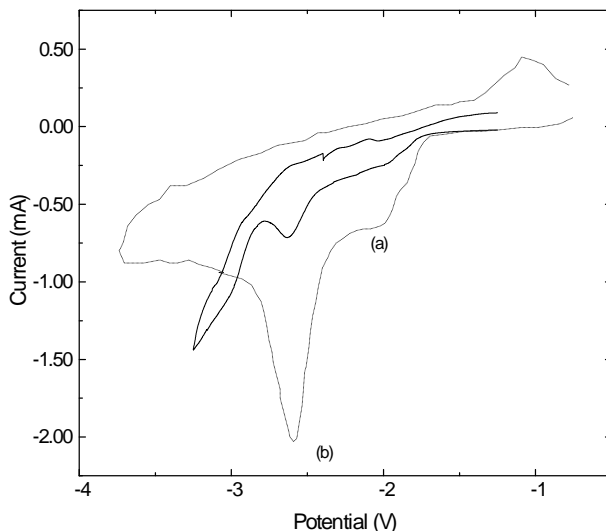


Figure 1. Voltammograms of TiO_2 films (deposited at 20 mA/cm^2 , $\text{pH}=0,5$ and 25°C) in $\text{LiClO}_4/\text{acetonitrile}$ at different lithium ion concentrations

Using an electrolyte solution with 0.5M lithium ion concentration, a twice decreasing of the cathodic peak intensity to -1.9V was observed; this confirm that this peak (b) corresponds to Li reduction.

Table 1 shows that the optimal current intensity for the electrodeposition of the TiO_2 films is 15 mA/cm^2 , the cathodic peak being at least twice higher than of those deposited at others current densities.

Table 1.

Ti^{4+} reduction peak intensities measured in 1M LiClO_4 (sweep rate 10 mV/s) of TiO_2 electrodes obtained at different current densities, in $1.25 \text{ M TiO}(\text{SO}_4)$ solution, $\text{pH}=0,5$ at 25°C

Current density [mA/cm^2]	Cathodic peak intensity [mA]
10	0.38
15	3.56
20	0.64
25	1.25

The voltammograms of TiO_2 films obtained at two different pH values of $\text{TiO}(\text{SO}_4)$ solution (fig. 2) show that the cathodic peak of titanium ions (IV) deposited in aqueous titanium oxysulfate solution with $\text{pH}=0,5$ is three times higher than that obtained in electrolyte with $\text{pH}=1,95$. It means that the more acidic solution favours the preparation of a thicker film.

CATHODIC ELECTRODEPOSITION OF TITANIUM DIOXIDE FILMS

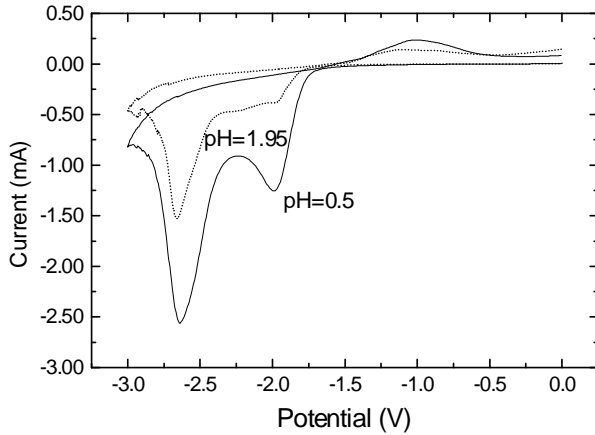


Figure 2. Voltammograms of TiO₂ films (obtained at two pH values of TiO(SO₄) solution, 25mA), in 1M LiClO₄ / acetonitrile, at 25° C ($v=10$ mV/s)

Fig. 3 shows a linear relationship between the TiO₂ film thickness and the number of coating cycles. The line does not go through the origin due to the fact that the films from the second and subsequent coatings formed on previously formed material, while the first coating formed on the titanium substrate. The thickness of the first coating is about 0.15 μ m, while the average film thickness per coating cycle from the second coating onward is estimated to be about 0.08 μ m. The thickness was measured using scanning electron microscopy and the weight method.

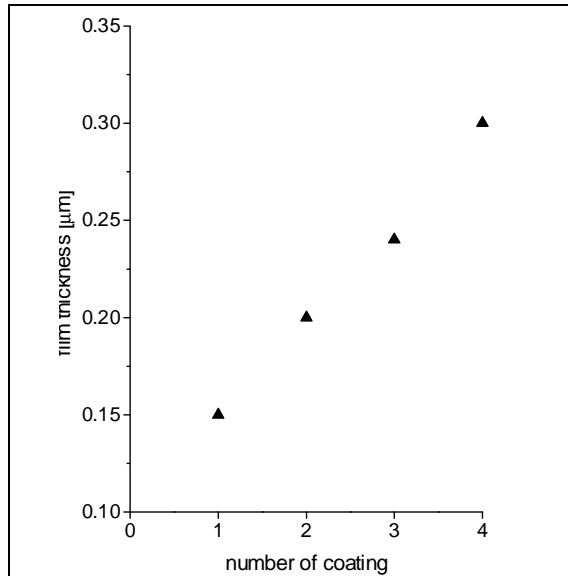


Figure 3. Relationship between film thickness and number of coating cycles (pH=0.5; $i=15$ mA/cm²; 25° C)

X-ray diffraction of the films deposited at 15 mA/cm^2 showed the formation of TiO_2 - anatase films (fig.4).

Fig. 5 presents the scanning electron microscopy of the surface of TiO_2 film deposited on titanium by 4 coating cycles. It is observed that the TiO_2 film has a nanocrystalline structure.

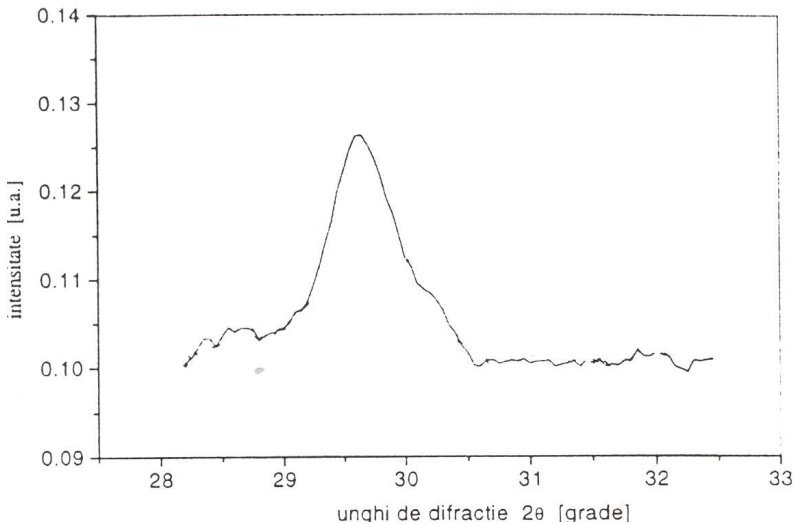


Figure 4. X-ray diffraction of the films deposited at 15 mA/cm^2 ($\text{pH}=0.5$; $i=15\text{mA/cm}^2$; 25° C)

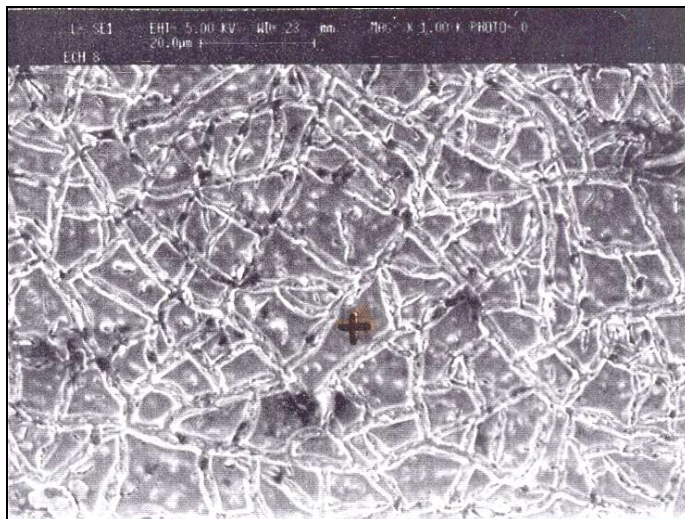


Figure 5. Scanning electron microscopy of the surface of TiO_2 film deposited on titanium by 4 coating cycles ($\text{pH}=0.5$; $i=15\text{mA/cm}^2$; 25° C)

Conclusions

The results showed that by cathodic electrodeposition of titanium oxyhydroxide gel film from aqueous solution containing a Ti precursor, followed by heat-treatment of the gel film, nanocrystalline titanium dioxide-anatase thin films are obtained.

The optimal current density for electrodeposition of TiO₂ films is 15 mA/cm².

The better pH value of aqueous titanium oxysulfate solution used to electrodeposition of TiO₂ films is 0,5.

REFERENCES

1. A.J. Bard, *Science*, 1980, **207**, 139
2. A.J. Bard, *J. Phys. Chem.*, 1982, **86**, 172
3. T. Inoue, A. Fujishima, S. Konishi, H. Honda, *Nature*, 1979, **277**, 633
4. A. Henglein, A. Gutierrez, C.-H. Fisher, *Ber. Bunsenges. Phys. Chem.*, 1984, **88**, 170
5. R.L. Cook, R.C. MacDuff, A. F. Sammells, *J. Electrochem. Soc.*, 1988, **135**, 3069
6. M. A. Fox, M.T. Dulay, *Chem. Rev.*, 1993, **93**, 341
7. H. Kisch, *J. Prakt. Chem.*, 1994, **336**, 635
8. A. Mills, R. H. Davies, D. Worsley, *Chem. Soc. Rev.*, 1993, **417**
9. P. V. Kamat, *Chem. Rev.* 1993, **93**, 267
10. M. R. Hoffmann, S.T. Martin, W. Choi, D. W. Bahnemann, *Chem. Rev.* 1995, **95**, 69
11. B. Ohtani, Y. Okugawa, S.-I. Nishimoto, T. Kagiya, *J. Photochem. Photobiol. A: Chem.*, 1992, **64**, 223
12. B. Ohtani, S. -W. Zhang, S.-I. Nishimoto, T. Kagiya, *J. Pys. Chem.*, 1987, **91**, 3550
13. B. Ohtani, S.-I. Nishimoto, *J. Pys. Chem.*, 1993, **97**, 920
14. B. Ohtani, K. Tennou, S.-I. Nishimoto, T. Inui, *J. Photosci.*, 1995, **2**, 7
15. N.Serpone, E. Pelizzetti, *Photocatalysis. Fundamentals and Applications*, Wiley Ed., New York, 1989, 261
16. P. A. Mandelbaum, A. E. Regazzoni, M. A. Blesa, S.A. Bilmes, *J. Pys. Chem.*, 1999, **B 103**, 5505
17. J. Sabate, M. Anderson, M. Aguado, J.Gimenez, S. Cervera-March, March, *J. Mol. Catal.*, 1992,**71**, 57
18. W. A. Zeltner, *Chemtech.*, 1993, 21
19. J. Sabate, M. A. Anderson, H. Kikkawa, Q. Xu, S. Cervera-March, C. G. Hill Jr., *J. Catal.*, 1992,**134**, 36
20. M. Anderson, M. J. Gieselmann, Q. Xu, *J. Membram. Sci.*, 1988, **39**, 243

21. S. Tunesi, M. Anderson, *J. Phys. Chem.*, 1991, **95**, 3399
22. M. Anderson, S. Tunesi, Q. Xu, US Patent No. 5035784, 1991
23. M. Anpo, N. Aikawa, Y. Kubokawa, M. Che, C. Louise, E. Giamello, *J. Phys. Chem.* 1985, **89**, 5689
24. C. Natarajan, G. Nogami, *J. Electrochem. Soc.*, 1996, **143** (5) , 1547
25. M. L. Hitchman, *J. Chem. Soc., Faraday Trans.*, 1996, **92** (20), 4049-4052
26. G. Zotti, G. Schiavon, S. Zecchin, *J. Electrochem. Soc.*, 1999, **146** (2), 637-641
27. L. Kavan, B. O'Regan, Kay, M. Gratzel, *J. Electroanal. Chem.*, 1993, **348**, 291-307.
28. P. Comba, A. Merbach, *Inorg. Chem.*, 1987, **26**, 1315
29. J. D. Ellis, A. G. Sykes, *J. C. S. Dalton*, 1973, 537

AN INVESTIGATION INTO THE Cu, Pb AND Zn POLLUTION OF THE SOMES AND LAPUS RIVERS OF BAIJA-MARE AREA, ROMANIA

MICHAELA PONTA¹, TIBERIU FRENTIU¹, CHRISTOPHER McCORMICK², ABRAHAM BELA³, CECILIA ROMAN³, EMIL CORDOS¹

¹ Babes-Bolyai University, Department of Analytical Chemistry, Str. Arany Janos 11, 3400 Cluj-Napoca, Romania

² IC Consultants Ltd, Imperial College, London, Great Britain

³ Research Institute for Analytical Instrumentation, Str. Donath 67, 3400 Cluj-Napoca, Romania

ABSTRACT. An evaluation of Cu, Pb and Zn in sediment and water collected in the catchment of the Somes river one year and a half after the cyanide spill accident in January 2000 is presented. The sediments show a high content of heavy metals in the range (mg Kg^{-1}): 8.9 – 339 (Cu); 59 – 465 (Pb) and 56 – 2060 (Zn) that demonstrate their potential toxicity for the ecosystem. As compared to data recorded after the accident, the content of heavy metals decreased at the station near the place of cyanide spill and increased downstream. Copper exceeds the admissible level in water near the place of cyanide spill (0.070 mg L^{-1}), while Pb is below the admissible level. The high concentration of Zn up to 1.038 mg L^{-1} in water can not be attributed exclusively to the pollution but is also due to natural background. The situation in the investigated period is better than that after the accident, when Cu and Zn exceeded up to 10 and 68 times, respectively the permissible limits.

INTRODUCTION

Baia-Mare area, situated in the nord-west of Romania, is one of the "environmental hot spot". The town is the site of two major plants and a flotation station for Pb, Cu and Zn ore processing, which caused in time a significant pollution with heavy metals. These phenomena were investigated in previous studies concerning the speciation of Pb, Zn and Cu in sedimented dust and soil [1] and the determination of Cd in sedimented dust [2]. The speciation indicated that in the sedimented dust Pb and Zn occurred mainly as sulfides and sulfates, while Cu as sulfides and oxides. The analysis of soil revealed a residual pollution with sulfides. Besides plants to process Cu, Pb and Zn ores, a company for gold extraction exists in the area of Baia-Mare. The technological process involves extracting gold and silver by cyanide leaching from older tailings in an existing dam situated near the town. Gold

and silver are extracted by carbon-in-pulp technology, since the resulting slurry is transported by pipeline on a distance of 6 km to be deposited in a decantation pond. The resulting slurry contains about 400 mg L⁻¹ cyanide, half of which as free cyanide, and the rest as complexed cyanide. After decantation the resulted water containing cyanide is fed back to the plant.

In January 2000 a major cyanide spill took place following a breach in the decantation pond as a result of improper structural elements and operational conditions. It caused the release of a huge volume of liquid mine tailings containing a high quantity of cyanide and heavy metals. The pollution spread across the local fields and entered the river system through the Lapus and Somes rivers. The spill was recognized as having long-term consequences for the ecosystem that has determined periodical evaluation of the river system.

The aim of this paper is to present an evaluation of Cu, Pb and Zn in sediment and water collected from the Somes and Lapus rivers one year and a half after the cyanide spill and to compare data with those recorded after the accident. These elements were selected for the study as they are the main products of the mining and nonferrous metallurgical industry in the area and are more likely to be found in the tailings and in the wastewater in a significant amount.

EXPERIMENTAL

Sample collection and digestion procedure. Sediment and water samples were collected during June 2001 from 10 sites upstream (20 km) and downstream (30 km) from the Somes and Lapus rivers confluence. Sampling stations were divided on equal split number between upstream and downstream. In addition, two more stations were included in the study, namely Bozanta Mare, the first village downstream from the dam and a station further upstream from the dam in the mountainous area of Codru Butesii. The last station was selected to act as a control one since it is high up in the low population area of the mountains, free from any industrial or agricultural activities. The twelve collection sites are shown on the map in Fig. 1. In order to get an overall picture of the distribution of heavy metals in the Somes river in the vicinity of the confluence with the Lapus river, sediments for the deposited particulate phases as well as water samples for the dissolved and suspended phases were collected.

Reagents. Single element stock solutions of 1000 μg mL⁻¹ were prepared by dissolution of the high-purity metal (Merck, Darmstadt, Germany) in the minimum volume of HNO₃ (Cu, Pb) or HCl (Zn) and diluting to 1 L. Starting from these, multielement standards were prepared. The reagents used for the digestion of sediment and water samples and for standards preparation were HNO₃ puriss 65%, HCl puriss p.a.>36.5% (Flucka, Riedle-de Haen) and H₂O₂ puriss 30% (Merck, Darmstadt, Germany). The blank sample contained only the reagents used for the digestion. All solutions were stored in plastic vials cleaned with acid solution and rinsed with distilled water.

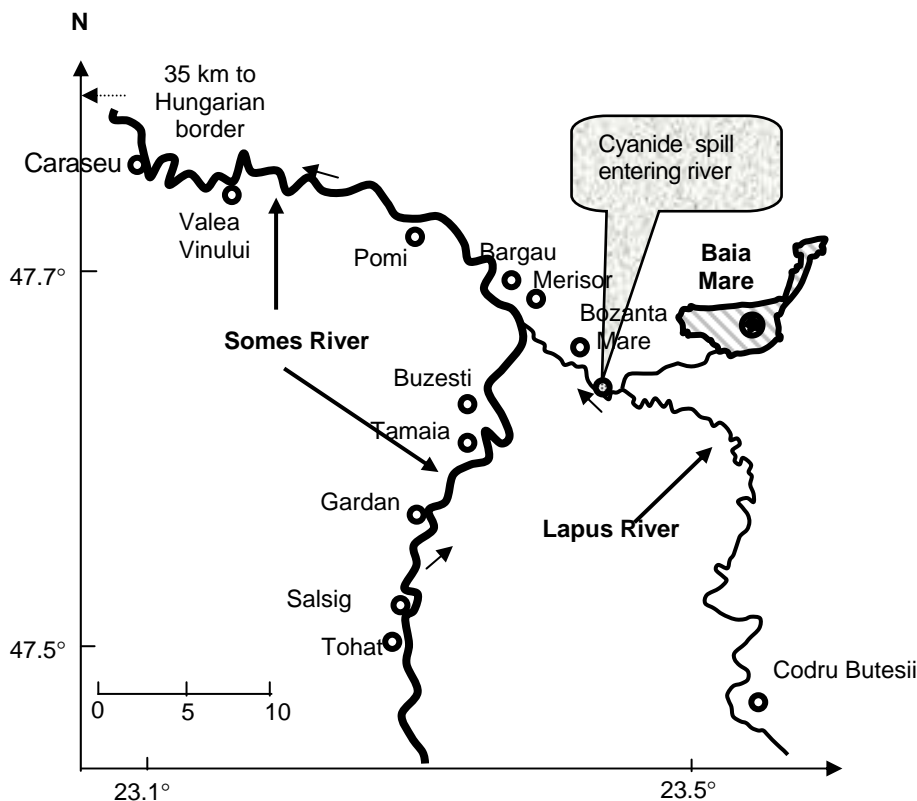


Fig. 1. Sampling sites for sediments and water

Sediment. At each station two sediment samples were collected from the surface of the riverbeds in order to obtain samples from the same surface layer and to ensure the same environmental conditions for all samples. Samples were transferred into polyethylene bags and closed. The samples were first dried at 105 °C to constant weight, homogenized and sieved through a 2 mm sieve, then through a 125 μm sieve. Five g of precise weight aliquot of dried sample were refluxed with 20 mL concentrated (65%) HNO_3 for 15 min. The mixture was cooled and again refluxed with 10 mL 30% H_2O_2 . After cooling the resulting solution was quantitatively filtrated through a precleaned G4 glass filter and diluted to 250 mL.

Water. At each station, three water samples were collected in nitric acid (65%) clean polyethylene bottles, acidified to $\text{pH} \leq 2$ and stored at 4°C. Before analysis, a 50 mL sample was digested with HNO_3 (0.5 mL) and HCl (1.5 mL) by heating on a sand bath for 15 min. After cooling, the filtrate was diluted to 50 mL.

Copper, Pb and Zn in sediment and water samples were determined by ICP-AES.

Instrumentation. The determination by ICP-AES was performed using a SPECTROFLAME (SPECTRO, Kleve, Germany). The main characteristics and the operating conditions are presented in Table 1.

Table 1

Instrumental conditions used for measurements by ICP-AES

Plasma frequency	27.12 MHz		
RF power / W	1200		
Torch Ar flow	cooling 12 L min ⁻¹ ; nebulizer 1 L min ⁻¹		
Auxiliary Ar flow	1 L min ⁻¹		
Observation height	15 mm		
Nebulizer	Concentric, Meinhardt type		
Pump rate for analysis	2 mL min ⁻¹		
Flush time	20 s		
Calibration	4 – point linear		
Data acquisition	Smart Analyzer Soft, Pentium III CPU 450 MHz		
	Cu	Pb	Zn
Wavelength / nm	324.76	283.31	213.86
Standard range / mgL ⁻¹	0 - 10	0 - 10	0 - 50

RESULTS AND DISCUSSIONS

Distribution study of Cu, Pb and Zn in sediment and water. The concentration range for Cu, Pb and Zn in sediment and water collected from the stations in Fig.1 are summarized in Table 2, while their distribution in the sampling points along the rivers is presented in Fig. 2. Data corresponding to a site represent the average of 2 independent sediment samples and 3 independent water samples, respectively.

Table 2

Concentration range for Cu, Pb and Zn in sediment and water in the Somes river

	Cu	Pb	Zn
Water / mg L ⁻¹	< 0.007 – 0.070	< 0.030 – 0.045	< 0.005 – 1.038
Control sample / mg L ⁻¹	< 0.007	< 0.030	0.055
Sediment / mg Kg ⁻¹	8.9 - 339	59 - 465	56 - 2060
Control sample/ mg Kg ⁻¹	59	120	315
Maximum admissible concentration in water ^a /mg L ⁻¹	0.050	0.050	0.030

^a Romanian Standard 4706/88

For the content of heavy metals in sediment, values in order of hundreds of mg Kg^{-1} were recorded. The maximum level of Cu, Pb and Zn occurred at Bozanta Mare station. From data in Fig. 2, curves 1, it is evident that there is a marked difference between the ranges of heavy metals concentrations in sediments upstream and downstream from the inflow of Lapus in Somes river. Data are related to both natural background of the river and water quality. Other characteristics, like flow, velocity and turbulence are decisive factors for the sediment quality and composition.

A comparison of the mean contents of heavy metals in the Somes river, upstream and downstream from the inflow of the Lapus river, revealed different situations for Cu and Zn on one side and Pb on the other side. Thus, for Cu the means were 17.1 and 109.1 mg Kg^{-1} and their ratio, expressing a concentration factor, was 6.4. The corresponding data for Zn were 104.5 and 854.5 mg Kg^{-1} , respectively and the concentration factor was 8.2. In the case of Pb, the two means were closer, 100.2 and 176 mg Kg^{-1} and the concentration factor was only 1.8. The fact could be explained on the basis of the history of Pb pollution in the area resulting from its industrial past. This generated a widespread dispersal of Pb in the area, reflected in a more uniform Pb content in sediments upstream and downstream from the confluence.

On the other side, a comparison with data recorded after the cyanide spill in 2000 [3] revealed that the Cu content in sediment from Bozanta Mare station decreased in time, since that of Pb and Zn remained almost constant. Downstream from the confluence with the Lapus river the content of all three elements has increased during the period after the accident.

The possible toxic potential of heavy metals in the sediment is difficult to evaluate since there are no Romanian Standards regarding the maximum admissible level of heavy metals in sediment. The toxic potential could be estimated either by assimilating the sediment with soil and the application of the Romanian Standards [4] and /or by using Canadian sediment quality guideline, which gives the Probable Effect Levels (PEL) [3,5]. In fact, there is a relation between these values, as PELs for Cu and Pb are similar with Romanian intervention level for soil in sensitive area (mg Kg^{-1} : Cu-200; Pb-90) and PEL for Zn with Romanian alert level for soil in sensitive area (300 mg Kg^{-1}). These limits are exceeded many times at most of the stations downstream from the inflow of Lapus river, which demonstrates the potential toxicity of the sediments on ecosystem.

In the case of water (Fig. 2, curves 2), the Cu content was below the limit of detection throughout the collection sites excepting Bozanta Mare, where it reached 0.070 mg L^{-1} and exceeded the admissible limit. The situation was better than in 2000 after the accident [3], when the recorded levels were 0.491 and 0.120 mg L^{-1} Cu at Bozanta Mare and in the Somes river immediately after the

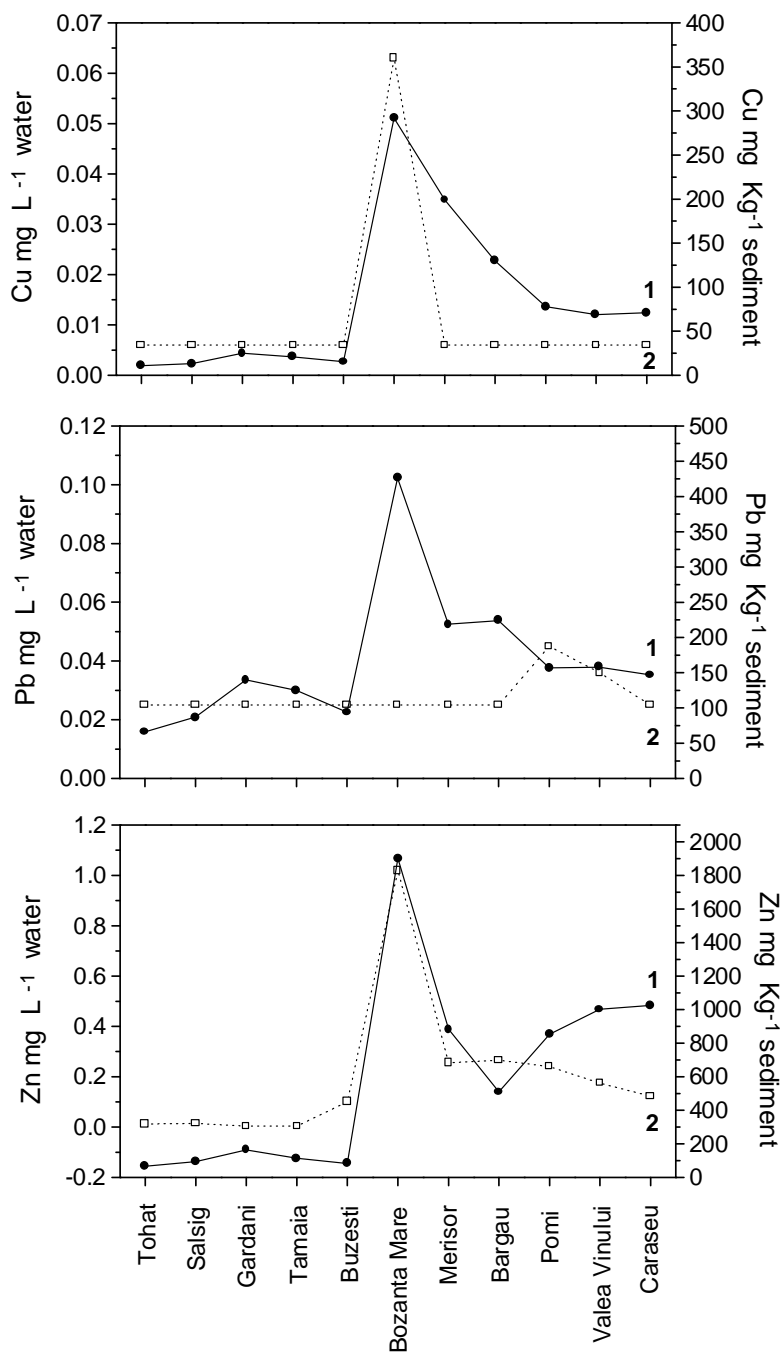


Fig. 2. Graphical sketch of Cu, Pb and Zn concentrations in sediment (1) and water (2)

confluence with Lapus, namely 10 and 2.5 times the permissible limits. For Pb, the present study revealed concentrations that scarcely exceeded the limit of detection in two sites and, unlike Cu and Zn, there was no maximum corresponding to Bozanta Mare station. In fact, Pb did not exceed the admissible level even after the cyanide spill in 2000. The case of Zn is different. The present study indicated that Zn exceeded the admissible level in 10 out of 12 collection sites. However, compared to results recorded in 2000 after the accident, the Zn concentration in Bozanta Mare station decreased to half, but remained almost constant in the Somes river after the confluence with the Lapus river. An interesting case is that of the station taken as control. Codru Butesii is a small village situated in the Lapus Gorges, far from the units with mining profile and close to its springs. However, the found Zn concentration in water exceeded the admissible level. This proves that the high content of Zn in the Lapus river is due to the natural background. The chemistry of rivers is often greatly affected by the physical surroundings that characterize the water [6].

The concentrations of Cu, Pb and Zn were determined also in several filtered water samples and were generally lower than in unfiltered water. Thus, Pb level was throughout below the limit of detection, while Cu content was above the limit of detection only at Bozanta Mare. The concentration of Zn in filtered water was below the limit of detection upstream from the confluence, up to 0.928 mgL^{-1} at Bozanta Mare, and did not decrease below 0.037 mg L^{-1} downstream from the inflow of Lapus in Somes river, exceeding 3-30 times the admissible concentration.

The concentration of heavy metals in surface water depends on sampling date, because the pollution level is strongly influenced by the river flow and temperature. Our samples were collected during summer, period of minimum velocity flow of water. Consequently, it is expected that the majority of the suspended matter most associated with the river transport of pollution [7,8] will be in the deposited side of the equilibrium between re-suspension and deposition.

Summarizing, the water quality does not represent an alarming problem, even though several critical values were recorded. In the case of Zn they can not be attributed exclusively to the pollution. The water quality strongly depends on the discharge of the used waters from the ore processing units in the area.

Analytical merits of chemical analysis

Limit of detection (LD). The limits of detection for Cu, Pb and Zn were calculated as three times the standard deviation of replicate background readings. For sediment they were related to dry mass taking into account the weight of the sample and the dilution (Table 3).

For sediments the use of ICP-AES as analytical method was the best one as its dynamic range cover several orders of magnitude. For Cu and Zn the admissible levels in water are seven and six times respectively, the detection limit and there is no difficulty in establishing them. The limit of detection for Pb was not low enough in comparison with the admissible level, but it raised no problem, as in most of water samples Pb was below the limit of detection.

Internal precision (Relative Standard Deviation, RSD). The internal precision was evaluated on the basis of three subsequent readings taken during the measurements of each of the samples.

Table 3

Analytical merits of Cu, Pb and Zn determination by ICP-AES using SPECTROFLAME (SPECTRO, Kleve, Germany)

Matrix		Units	Cu	Pb	Zn
Sediment	Precision (n=24)	%	0.3 – 2.3	0.4 – 3.3	0.2 – 6.6
	Concentration range	mg Kg ⁻¹	8.9 - 339	59 - 465	56 - 2060
	Reproducibility (n=3)	%	1.8 – 3.6	0.5 - 2	5 – 6
	Concentration range	mg Kg ⁻¹	34 - 130	190 - 219	218 - 1099
	Limit of detection	mg Kg ⁻¹	0.35	1.5	0.25
Water	Precision (n=36)	%	-	48.9 – 61.1	0.5 – 3.7
	Reproducibility (n=3)	%	-	-	0.8 – 37.6
	Concentration range	mg L ⁻¹	-	0.036 – 0.045	0.038 – 0.240
	Limit of detection	mg L ⁻¹	0.007	0.030	0.005

Reproducibility. To evaluate the reproducibility selected sediment samples (3) were chosen and 4 sub-samples were subject to the same chemical sample preparation step and subsequent measurements. The samples chosen were encompassing low and high concentrations. With respect to the water samples, three aliquots were measured from each sample.

As seen in Table 3, the internal precision was good for all the sediment data and in general below 3% except slightly higher errors for Zn in the low concentration ranges (RSD between 3 and 6.6% for concentrations below 200 mg Kg⁻¹). This good internal precision is due to the fact that measured concentrations are relatively high compared to the limit of detection. The lowest concentration was at least 10 times above the limit of detection (for Pb) but in general well above 50 fold. The water samples show good internal precision (RSD<3%) for Zn, where concentrations are well above the limit of detection. In the determinations of Pb just above the detection limit, the RSD was higher than 50%.

The reproducibility of the analysis in sediments indicated similar trends like the internal precision. Different concentration ranges had similar errors (RSD<5%) for all three elements.

Conclusions

In the investigated period the water quality of the Somes river was within the range of Romanian standards in respect of Cu and Pb. Critical values were found in a few sites, but they did not represent a major problem. The situation was found to be better than after the cyanide spill accident when the concentrations of Cu and Zn exceeded many times the admissible values. The high content of Zn in water can not be attributed exclusively to the pollution, but also to natural background.

The sediment situation is different, as the contents of the investigated heavy metals are exceeding manifolds the critical limits for soil in Romania or Canadian Possible Effect Limits (Canada) and demonstrates the potential toxicity of sediments for the ecosystem.

The cyanide spill accident that occurred close to Baia-Mare, Romania, in 2000, was recognized as having long-term consequences for the ecosystem, which impose further periodical evaluation of the river system status.

Acknowledgements. The work has been carried out under financial support of the European Commission under Contract Number ICA2-CT-2000-10036.

REFERENCES

1. E.A. Cordos, T. Frentiu, A.M. Rusu, G. Vatca, *Analyst*, 1995, **120**, 725.
2. T. Frentiu, M. Ponta, A. Rusu, S.D. Anghel, A. Simon, E.A. Cordos, *Anal. Lett.*, 2000, **33**, 323.
3. UNEP / OCHA, Report of the UNEP / OCHA Assessment Mission on the "Cyanide Spill at Baia-Mare Romania", 23 February – 6 March 2000. Geneva, March, 2000.
4. Romanian Ministry of the Forest, Water and Environment, Order No. 756/1997, Monitorul Oficial, 1997, No. 303 bis /06.11.1997
5. Canadian Councils of the Environment, 1999.
6. K.S. Whiting and R.L. Olsen, Identification of sources of metals in stream sediments using Electron Microprobe techniques. Tailings and Mine waste 1997 Conference, pp. 519-528, Balkema publishing.
7. P. Szefer, *Applied Geochemistry*, 1998, 13, 287.
8. M. Abrameto, M.I. Gil, R.H. Freiji, J. Marcovecchio, Int. Conference on Heavy Metals in the Environmental, Michigan, 2000.

VOLTAMPEROMETRIC METHODS FOR THE COPPER IONS DETERMINATION

MARIA JITARU*, RAMONA IACOB, AND MARIA POPA**

* "Babeș-Bolyai" University, Faculty of Chemistry and Chemical Engineering
Associated Francophone Laboratory 11, Arany Janos street, 3400 Cluj-Napoca
mjitaru@chem.ubbcluj.ro

** "1 Decembrie" University of Alba-Iulia, Faculty of Sciences 11-13, N. Iorga street
2500 Alba-Iulia, mpopa@Imm.uab.ro

ABSTRACT. We have evaluated procedures to improve the reproducibility and sensitivity of the voltamperometric methods for the copper ions determinations in wastewaters. The influence of the analytical parameters (pH, electrolyte composition, deposition time and potential) on the performances of the method has been investigated. The optimal analytical conditions were found. Using these methods the copper concentration in the wastewaters after the electrochemical synthesis of the m-amino sulphonic acid on copper electrode and after the copper recovery by electrochemical methods, was determined. In these conditions, the limit of detection was 0.05 – 1.5 ppm copper, with standard deviation 2 - 10%, depending of the concentration range and method.

Key words: *copper ions determinations, stripping and voltammetry methods*

Introduction

Continuing our interest in the field of the electroanalytical determination of the heavy metal ions [1], this contribution compares the performances of different electrochemical methods, applied for copper ions determinations.

The data published in the field of environmental pollution and related effects of the heavy metals on the flower cultivation [2] have been reported the negative influence of the high concentration of copper and other ions on the bottom and flower system of the plant.

One important property of the cyclic voltamograms (CV) or of the polarograms corresponding to the reduction of the ions is the proportionality of the peak current with the solution concentration. The detection limit of cyclic voltammetry (CV) is relatively high (10^{-2} – 10^{-5} M), but the method could be used for the quantitative control of the composition of the wastewater in the specified concentration range. The quantitative use of CV has been limited by

the fact that the dependence of the i/E curves on electrochemical and chemical (concentration) parameters in general is very complicated. [3]. Stripping analysis is an analytical method that uses a bulk electrolysis step (preelectrolysis) to preconcentrate the electroactive species from solution into a small volume of a mercury drop, on mercury film or on the surface of other electrodes (e.g. glassy carbon electrode - GCE) followed by the oxidation step. The major advantage of the stripping method, as compared to direct voltammetric analysis is the high surface concentration responsible for a high peak current, so the answer is less perturbed by the small currents due to the impurities oxidation. The technique is useful for the analysis of trace concentration (ppm and ppb). There are a few stripping methods valuable for the Cu (II) and other ions determination, from anodic stripping voltammetry (ASV) to adsorptive stripping methods. Adsorptive stripping voltammetry (AdSV) has been known to give excellent sensitivity for a variety of trace (ppb) metals at the mercury electrode [4]. This method involves complexation of the metal ion with different ligands and adsorption of the resulting complex onto the mercury drop or mercury film surface. The adsorbed complex is removed by scanning the electrode potential, usually in a reductive direction – cathodic stripping analysis (CSA). The metal ions are reduced and simultaneously amalgamated. Due to the peak separation the mixture of different metals could be analysed. Other variants, such as stripping by a current or potential step or different combined procedures have been also proposed [5, 6].

The electrochemical techniques like the stripping methods ensure the determination of the traces –ppb- metals ions [1]. There are two main stages in the stripping analysis:

- Preconcentration (plating) consists in the application of a constant reductive potential for a period of time, when takes place the adsorptive accumulation of metal on Hg surface: $Me^{n+} + ne^{-} \Rightarrow Me(Hg)$
- Stripping, when the metal ions or metal-complex accumulated on Hg surface is oxidised and the oxidation current, proportional with the metal concentration, is determined.

Copper could be determined by the anodic stripping voltammetry directly in organic solvents [1]. There are two conditions for that: solubility of the copper (II) complex species in the given solvent and the possibility to assure the conductivity of the supporting organic electrolyte [6].

The most common pre-treatment of GCE is pre-anodisation and pre-cathodisation. The effect of treatment procedure on electrochemical response depends on the applied voltage, pH value of the electrolyte solution and the duration of the treatment. The treated GCE usually behaves as a metal film-coated electrode (MFCE) [7].

The aim of this paper is to compare the performances of copper ions determination by different voltamperometric methods.

Experimental

Instrumentation and software

The computer aided instruments used for potential control was BAS 100W equipped with Controlled Growth Mercury Electrode (CGME) West Lafayette, USA and the Portable Trace Element Analyser, PTEA –WAGTECH equipped with glassy carbon electrode, GCE. The classical three electrodes cell has been used for the cyclic voltammetry determinations (WE- GCE; CE- Pt wire and RE - Ag/AgCl). Reference (Ag/AgCl) and Pt wire auxiliary electrodes used to this work, were from BAS Co. The UNICAN Helios β UV-VIS spectrometer has been used to control the results of the electrochemical methods.

Reagents

All solution were prepared with MiliQ purified water and analytical grade chemicals (Merck).

Procedure

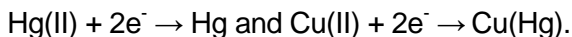
PTEA is equipped with a classical three electrodes cell, all built into the unit. The sample volume is 20 cm³.

The glassy carbon electrode (GCE) has been activated according to literature data [8], before the copper determination. The reactivation procedure has been according to the PTEA producer [9]. All the measurements have been made in the appropriate supporting electrolyte (ASE), containing :17g NaCl, 35.5g ascorbic acid, 7.7 g NaOH in 500 mL MiliQ purified water.

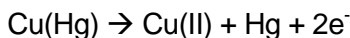
Results and discussions

We compared the results obtained by different electrochemical techniques:

- Direct voltammetric and polarographic measurements on mercury electrode;
 - Stripping voltammetric analysis (SVA) on the CGME
- Prior the Cu (II) determination with CGME, Hg (II) has been added into the sample, when the following reactions take place:



The reduced species Cu (Hg) is then re-oxidized:



Influence of the Cu (II) concentration

The electrochemical answer depending on Cu (II) concentration has been investigated by polarography, cyclic voltammetry and stripping techniques. The reversible one electron reduction of Cu (II) in (ASE) supporting electrolyte, demonstrated the proportionality of peak current with the concentration – figure 1.

The effect of Cu (II) concentration on peak current, (Figure 1) and on polarographic limiting current (Figure 2) is demonstrated by the linear increasing of the current with increasing concentration.

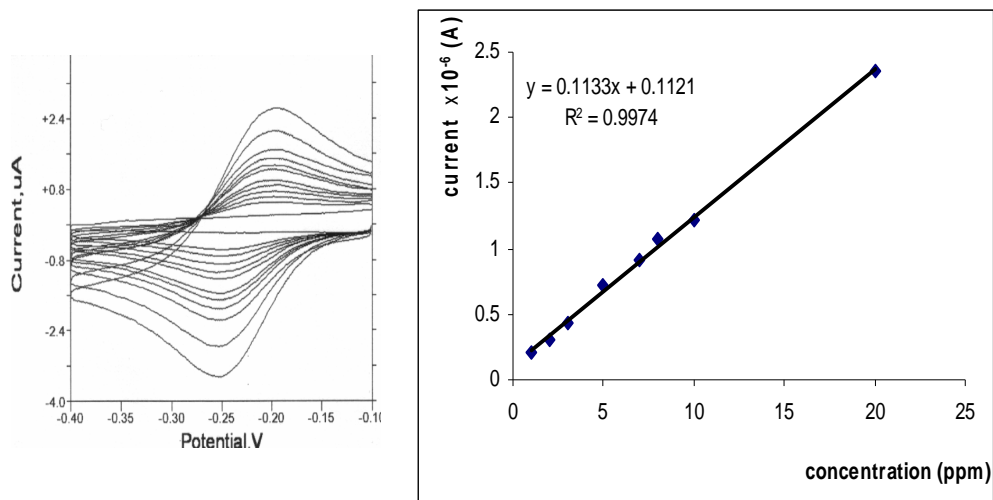


Figure 1. Cyclic voltammograms (CV) of Cu(II) with increasing concentration from 0-25 $\mu\text{g mL}^{-1}$ along with the resulting calibration plots.

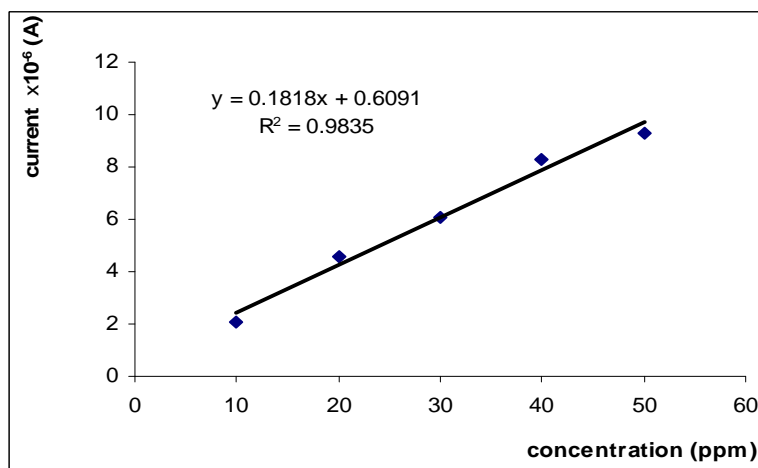


Figure 2. Calibration curve obtained from polarographic data; drop size: 6 μm ; v : 10 mVsec^{-1} .

In the concentration range from 1–25 ppm, figure 1 and 10–60 ppm, figure 2, the slope is 0.1133, respectively 0.1818 $\mu\text{A/ppm}$. The detection limit is higher for cyclic voltammetry.

The reproducibility of the CV response is good, with $R^2 = 0,99$. A 4.5% relative standard deviation of peak currents was obtained under 6 measurements of $20.0 \mu\text{g mL}^{-1}$.

Influence of mercury drop size

In order to find the optimal conditions for the Cu (II) determination we investigated the influence of Hg drop size on the peak current – Figure 3.

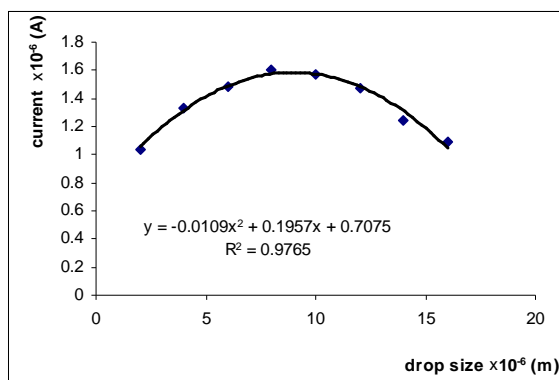


Figure 3. Influence of drop size on the polarographic current.

The dependence follows the equation of $y = -0.0109x^2 + 0.1957x + 0.7075$ and the drop size of 8-10 μm gives higher currents.

Stripping analysis

The best results have been obtained on CGME, by stripping techniques (Figure 4), when the calibration curve is described by the equation $y = 3.2566x + 3.012$, for the smaller concentration (1-12 ppm).

The peak area for Cu oxidation can be used to estimate the adsorbed amount of ions at the CGME. From the equation $\Gamma = Q/nFA$, the surface coverage Γ of the adsorbed species can be calculated from the values of the charge Q (the area of the peak) and electron transfer number n - the value 2 is taken into account for the oxidation of Cu to Cu(II).

The voltammogram of $20.0 \mu\text{g mL}^{-1}$ adsorbed at CGME gives a peak area of $7.3 \mu\text{C}$ and the surface coverage Γ of $3.01 \times 10^{-10} \text{ mol cm}^{-2}$ can be obtained.

Obviously, the surface coverage of adsorbed species is close to the theoretical value of a monolayer.

The slope indicates that the electrode process is simultaneously controlled by surface adsorption and heterogeneous electron transfer rate.

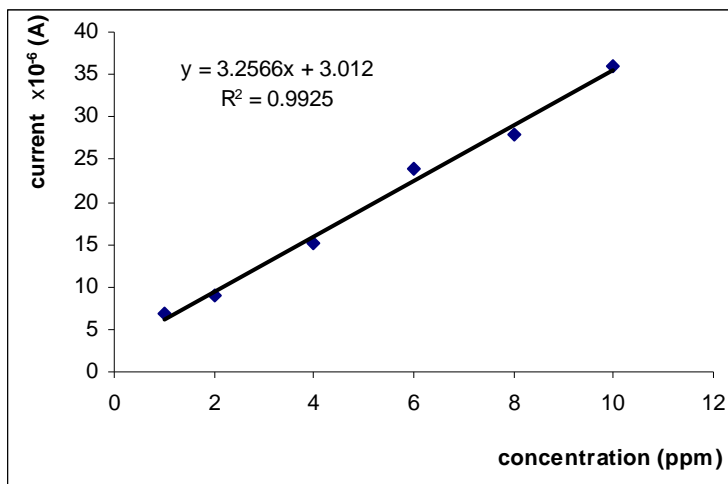


Figure 4. Plots of i_p – concentration for the oxidation of accumulated copper on CGME.

Influence of the Accumulation Time

With increasing accumulation time, the peak current initially increases and then trends to saturation value after 500 s, as illustrated in Figure 5.

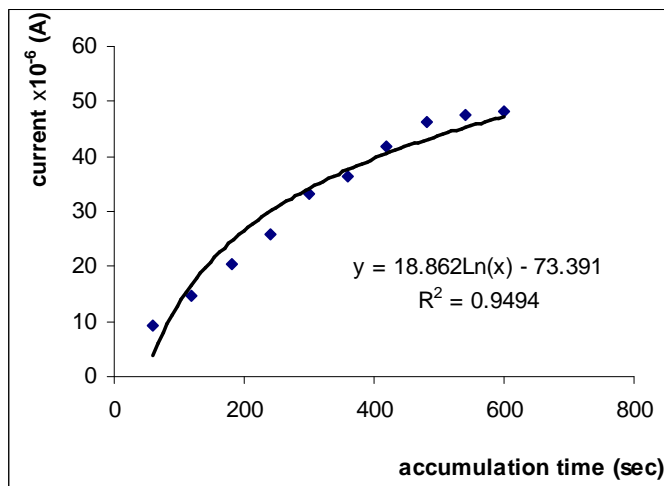


Figure 5. Effect of accumulation time on peak current. (500s was chosen as the accumulation time for all experiments).

The detection limit for stripping method is about 0.05 ppm, with a R^2 of 0.9992 and it is lower comparing to other electrochemical investigated methods. The stripping techniques seem to give the best results, comparing to other analytical methods – table 1.

Table 1.

Performance of the applied methods (* for 4 ppm)

Method	Detection limit [ppm]	Concentration range [ppm]	R ²	Standard deviation [%]
Spectrophotometry*	>10	50-100	0.9600	3-6.8
Polarography	9	9-50	0.9752	4.2-4.5
Cyclic voltammetry	1	1-10	0.9928	2.25-3.23
Stripping (on CGME)	0.05	0.05-10	0.9992	1.37-1.91
Stripping (on MFGC)		0.05-10	0.9880	7-10.33*

* comparing method

Conclusion

The proposed stripping method on CGME is selective and enough sensitive for the determination of low concentration of Cu (II), up to 0.05 ppm. Using the Wagtech PTEA (Portable Trace Element Analyser) equipped with thin mercury film on glassy carbon electrode (MFGC), the detection limit and the standard deviation are lower than those obtained using other electrochemical methods – Table 1. The obtained results were compared with the simple voltamperometric (detection limite 1 ppm) and spectrophotometric methods (detection limite >10 ppm).

For the future, we propose to continue the research by using different complexing agents (azodyes) for the determination of other polluting ions; the preliminary data concerning the adsorptive stripping voltammetry using azodyes like ligands are promising. The stripping method on CGME will be used to control the depollution of wastewaters using PRIAM reactor.

Acknowledgements. This work was financially supported by the Roumanian Ministry of Education & Research and AUF project (2001/PAS/24).

REFERENCES

1. M.Jitaru, M.Popa & I.Etves Presented at "A 10-a Conferinta de chimie-fizica", IASI, 26-29 Sept. **2000**
2. D.Alandjiiski, O. Tafradjiiski, I.Ivanova, J.Environm. Protection and Ecology, **2001**, 2 (1), 157.
3. B.Speiser, Anal.Chem., **1985**, 57, 1390.
4. A. Miropi Paneli, A. Voulgaropoulos, Electroanalysis, **1993**, 5, 355
5. E. Sahlin, D. Jagner, R. Ratana-Ohpas, Anal. Chim. Acta, **1997**, 346, 157.

6. M.H.Pournaghi-Azar & Co, *Anal.Chim.Acta*, **2001**, 63, 975
7. C.Barbero, J.J. Silber, L.Sereno, *J.Electroanal. Chem.*, **1998**, 248, 321.
8. B.B. Radcliff, J.W.Klancke M.D.Koppang, R.C. Engstrom, *Anal. Chem.*, **1996**, 68, 2001.
9. Wagtech Int. Ltd PTEA, Operating Instructions.

THE DETERMINATION OF THE KINETIC PARAMETERS TO SULFUR DIOXIDE CHEMOSORPTION IN AMMONIA SULFITE

**AURORA BĂȚINAȘ, ALEXANDRU POP,
CAMELIA GHERMAN, ȘERBAN AGACHI**

*"Babes-Bolyai" University of Cluj-Napoca, Faculty of Chemistry and Chemical Engineering, Arany Janos street No. 11, 3400 Cluj-Napoca, Romania
Tel.: 0040-264-193833, Fax: 0040-264-190818
E-mail: abatinas@chem.ubbcluj.ro*

ABSTRACT. The main experimental results regarding the SO₂ absorption kinetics in ammonia sulfite are shown in this paper. The working conditions in which the mass transfer through the gaseous and liquid phase does not influence the chemical reaction speed have been determinate. The paper describes the temperature and concentration of influence on the reaction rate. The activation energy of the reaction and the reaction order for the ammonia sulfite was determined. The obtained kinetic data can be used for calculation of process acceleration factor taken into consideration in the design calculation of the absorption devices.

1. Introduction

The gas emissions desulphurisations containing sulfur dioxide is of great importance nowadays, given its ecological impact. For the elimination of SO₂ from waste gases were proposed many processes: the Battersa process which uses as absorbent a very diluted alkaline solution, the process of eliminating SO₂ by absorption in xylidine uses as an absorbent a mixture of xylidine and water, etc [1]. These processes allow the SO₂ recovery, but from resulting compounds don't recovery of the absorbents.

In comparison with these processes were developments processes, which allow the recovery of the absorbents, and producing the pure SO₂, which is an important source of sulfur by reduction. Thus processes are:

a) the Wellman-Lord (WL) process [2, 3] is currently the leading SO₂ recovery process, where SO₂ is absorbed in an aqueous solution of sodium sulfite, producing sodium bisulfite.

The loaded solution is termally regenerated by evaporation of H₂O+SO₂. After condensing the water vapor, nearly pure gaseous SO₂ is obtained as an overhead product, ready for further processing. Solid Na₂SO₃, which is precipitated in the evaporator, is redissolved in condense/water to the appropriate concentration for a new absorption cycle.

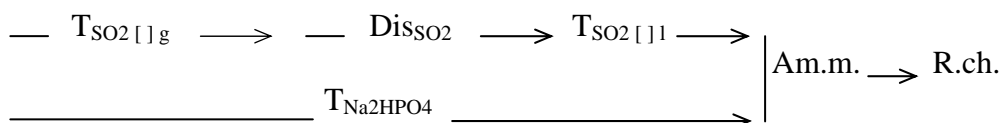
b) the citrate absorption – steam-stripping process is best known as the Flakt-Boliden process. In this process absorption and regeneration take place in packed towers with small pressure losses, no solids formation and very small oxidation losses. The most serious limitation of this process concerns its application to gases with very low SO₂ contents, such as are often found in thermal power plants, since the specific steam requirement will then be too high. The citrate absorption process is considered to be very competitive for SO₂ recovery from relatively rich gas [4].

c) the adipate absorption – steam-stripping process offers the same advantages as the citrate process and, in addition, a system specific possibility of reducing the specific steam requirement. The adipate process is therefore suitable for much lower feed gas SO₂-partial pressures than the citrate process. However, both these processes require relatively high the specific steam requirement values for very lean gases, and problems may arise when extremely low emission limits have to be met [4].

Such procedures present a great disadvantage: their economic efficiency is satisfactory only when the concentration of SO₂ in the gases is relatively high. To the same category of processes belongs the separation of SO₂ by absorption into buffer solution of mono- and disodic phosphates. This process is characterized by in the desorption phase the steam consumed is very low, a relatively high capacity of absorption and a reduced oxidizability of the SO₂ to SO₄²⁻. The study upon the absorption within the buffer solutions made by Erga [4] reveals the fact that one can obtain relatively easy concentrations of SO₂ in the purified gases at low values of 10 ppm even when the temperature is between 50 – 60 degrees Celsius; this denotes that such a solution is an excellent absorbant which can be used with weak, diluted gases; consequently this method will have good perspectives in the future. The literature in the field does not come up with studies referring to the kinetic of the chemisorption process. This paper presents a part of the possible kinetic models as well as the experimental data obtained in order to determine the kinetic parameters determination (constant rate of the chemical reaction, the reaction order, and activation energy) of the chemisorption of the SO₂ within phosphate buffer. The paper also draws a comparison between the rate of absorption within the disodic phosphate solutions and that within the buffer phosphate solutions.

2. The possible macrokinetics models

The absorption process of SO₂ into phosphate solution is a gas-liquid process [5, 6, 7], which has the following scheme:



This scheme shows that SO₂ gas is first transferred through gas phase (T_{SO₂[g]}), until the gas-liquid interface, then SO₂ is dissolved into the liquid phase (Dis_{SO₂}), then dissolving SO₂ is transferred through liquid phase (T_{SO₂[l]}). The Na₂HPO₄ is transferred through into liquid phase (T_{Na₂HPO₄}) too, then chemical reaction (R) between SO₂ and Na₂HPO₄ is taking place in the liquid phase.

The comparing the chemical reaction rate between SO₂ and Na₂HPO₄ (v_r) with transfer process rate (v_{tr}) carries at the following models:

- v_r << v_{tr}, when the chemical reaction is very slow and global process rate is equal with chemical reaction rate, and the kinetics equation for this case is given by:

$$-r_{SO_2} = k_1 \cdot C_{SO_2}^n \cdot C_{Na_2HPO_4}^m \quad (1)$$

- v_r >> v_{tr}, when the chemical reaction is practically instantaneous and this has been placed at the gas-liquid interface. The SO₂ transfer process is slower than the SO₂ dissolving process, and the kinetics equation is given by:

$$-r_{SO_2} = -\frac{dn_{SO_2}}{S \cdot d\tau} = k_{g,SO_2} \cdot C_{SO_2} \quad (2)$$

- v_{tr} ≈ v_r, chemical reaction rate is equal with transfer process rate and in this case the global process is described by the equation for diffusion with chemical reaction in the stationary system:

$$D_{SO_2} \frac{\partial^2 C_{SO_2}}{\partial x^2} + k \cdot C_{SO_2} = 0 \quad (3)$$

If n=1, for an irreversible reaction, equation (3) can be write:

$$D_{SO_2} \frac{\partial^2 C_{SO_2}}{\partial x^2} + k \cdot C_{SO_2} = 0 \quad (4)$$

The solution of equation (4) is:

$$C_{SO_2}(x) = \beta_1 \cdot e^{Ax} + \beta_2 \cdot e^{-Ax} \quad (5)$$

where $A = \sqrt{k/D_{SO_2}}$

At the gas-liquid interface (x = 0) the rate of gas absorption at any time is given by equation:

$$r = D_{SO_2} \left(\frac{dC_{SO_2}}{dx} \right)_{x=0} = A \cdot D_{SO_2} \frac{ch(A \cdot x_0)}{sh(A \cdot x_0)} \left[C_{SO_2}^* - \frac{C_{SO_2}}{ch(A \cdot x_0)} \right] \quad (6)$$

when is equal to the Hatta number (Ha) and x_0 is equal to D_{SO_2}/k_{SO_2} and the global process rate is given by equation:

$$r = k_{SO_2} \frac{Ha}{thHa} \left(C_{SO_2}^* - \frac{C_{SO_2}}{chHa} \right) \quad (7)$$

The SO_2 transfer process rate without chemical reaction is given by equation:

$$r_{tr} = k_{l,SO_2} (C_{SO_2}^* - C_{SO_2}) \quad (8)$$

The enhancement factor, E, is the ratio of the process rate with chemical reaction and without chemical reaction is given by equation:

$$E = \frac{r}{r_{tr}} = \frac{Ha}{tgHa} \left(\frac{1 - \frac{\phi}{chHa}}{1 - \phi} \right) \quad (9)$$

where $\phi = C_{SO_2} / C_{SO_2}^*$. In general ϕ has low value and $C_{SO_2} \rightarrow 1$ and the enhancement factor in this case is:

$$E = \frac{Ha}{tgHa} \quad (10)$$

$$r = E \cdot r_{tr} = E \cdot k_{l,SO_2} \cdot (C_{SO_2}^* - C_{SO_2}) \quad (11)$$

The equation (11) shows that the chemical reaction speeds the absorption process rate and the influence of the chemical reaction about global process rate is given by enhancement factor, which depends, from number of Hatta.

To agreement with these theoretical studies is necessary experimental determination of kinetic parameters as the constant rate of the process, k, activation energy, E_a , and reaction order.

3. Experimental

In order to determine the kinetic parameters that we have discussed above, we must establish if the conditions of the transfer phenomena during the liquid and gaseous phases do not influence the process. To avoid the influence of the transfer during the gaseous phase, pure SO_2 has been used. To eliminate the influence of the transfer during liquid phase, kinetic

studies upon different rotation speeds of the agitator proved necessary. In a previous paper it has been determined that at an agitator speed higher than 80 rotations/minute the speed of the process remains constant - as a consequence, the transfer of the mass through the liquid phase is not a factor of influence. The SO_2 used has the 99% concentration and flow was measured using a flow meter. The SO_2 that was not absorbed at first was transferred in a bubbling container and absorbed in NaOH (sodium hydroxide). The conditions were temperatures = 15° , 33° , and 50°C , and the concentration variation of ammonia sulphite.

The process evolution in time was determined noting the SO_2 concentration from the phosphate solution. The determination of SO_2 concentration was made on iodometric means, titration with $\text{Na}_2\text{S}_2\text{O}_3$ 0.1N the excess of iodine.

4. Results

The first experimental determination draws out the influence of the absorbent nature on the rate and capacity of absorption. In this scope we worked at three different concentration of ammonia sulfite and different temperatures.

The kinetic results were processed for the reaction rate estimation, for which the $\ln C = f(t)$ curves were traced, from the straight lines slopes obtained the k constants rate. Fig 1 shows the variation of SO_2 absorption rate at different concentration of ammonia sulfite at rotation speed of stirrer $n=70$ rot/min. Fig. 2 shows the variations of the absorbed SO_2 concentrations in time and that the absorbed SO_2 ratio increases at temperatures. The activation energy was determined, having as a purpose the drawing of the diagrams $\ln k = f(1/T)$ on the basis of the Arrhenius equation.

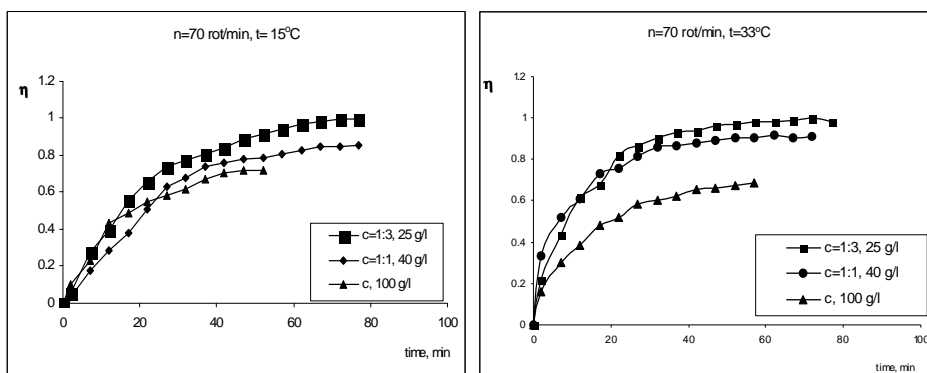


Fig. 1. SO_2 absorption rate versus time at different concentration of ammonia sulphite, at the rotation speeds of the stirrer 70 rot/min

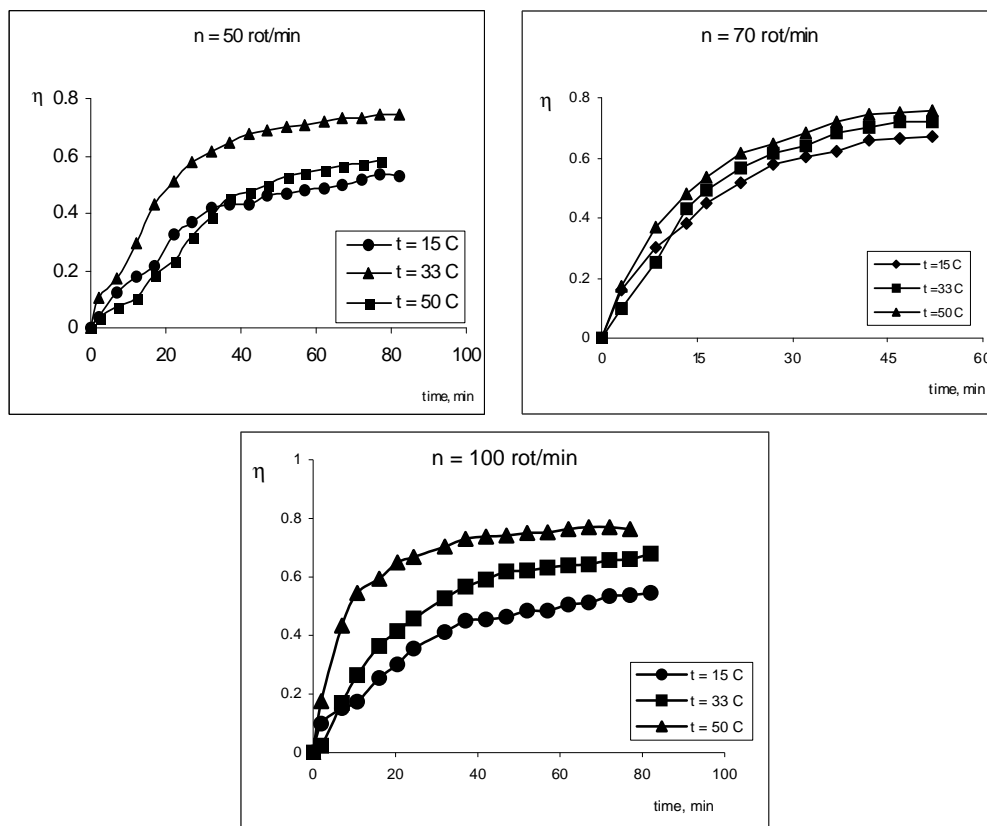


Fig. 2. SO_2 absorption rate versus time at different temperatures and the different rotation speeds of stirrer.

5. Conclusions

1. It was established the constants rate, k , and activation energies, E_a of the SO_2 absorption into ammonia sulfite. The high values of the activation energies show that the chemical reaction is the limitative step of the absorption process in the experimental conditions.

2. It was determined the reaction order of SO_2 absorption into ammonia sulfite, and the obtained results show that the order of the reaction between SO_2 and ammonia sulfite is equal to one.

3. The determined kinetic parameters can be used for determination the enhancement factor of the absorption process from the mathematics model of the SO_2 chemisorption process into ammonia sulfite.

Symbol used

$C_{SO_2}^*$	[mol/l]	SO ₂ concentration at gas-liquid interface
C_{SO_2}	[mol/l]	SO ₂ concentration into bulk liquid
D_{SO_2}	cm ² /s	diffusivity of SO ₂ in liquid
E	-	enhancement factor
E_0	cal/mol.K	activation energy
k_{l,SO_2}	cm/s	liquid-film mass transfer coefficient
k	s ⁻¹	constant of reaction rate
r	mole/m ² min	absorption process rate
S	cm ²	surface
v_r	mole/m ² min	reaction rate
v_{tr}	mole/m ² min	SO ₂ transfer process rate in liquid phase
τ	s	time
η		transformation rate

REFERENCES

- [1] Stratula, C., *Gases purification*, Scientifically and Encyclopedia Editure, Bucharest, 1984, 358.
- [2] Pedroso, R.I., Press, K.M., *Sulphur Recovered from in Large Coal Fired Power Plants*, in: *The Control of Sulphur and Other Gaseous Emissions* (I. Chem. E. Symposium Series No. 57), The Institution Of Chemical Engineers, London, 1979, F1.
- [3] Torstrick, R.L., et. al., *NATO-CCMS Flue Gas Desulphuration Pilot Study: Phase II Applicability Study*, U.S. EPA-600/7-80-142, NTIS No. PB 81-136475, 1980.
- [4] Erga, O., *Chem. Eng. Technol.*, **11**, 1988, 407.
- [5] Calistru, C., *Inorganic Compounds Technology*, Science and Technique Editure, Bucharest, 1979.
- [6] Hector Lopez-Arjona, et. al., A film-penetration model for non-isothermal absorption with chemical reaction, *Chemical Engineering Science*, **55** (2000) 5897-5906.
- [7] Charlotte Brogren and Hans T. Karlsson, Modeling the absorption of SO₂ in a spray scrubber the penetration theory, *Chemical Engineering Science*, **52** (18), (1997) 3085-3099.

HORSERADISH PEROXIDASE - CATALYZED OXIDATION OF SOME BENZYL-TYPE ALCOHOLS

R. SILAGHI-DUMITRESCU, F.D. IRIMIE, C. PAIZS, CORNELIA MAJDIK, MONICA TOSA, PAULA MOLDOVAN, ANGELA SAS, L. TAMAS

Department of Chemistry and Chemical Engineering, "Babes-Bolyai" University, RO-3400 Cluj-Napoca, Romania

ABSTRACT. Horseradish peroxidase catalyzed the selective oxidation of some hydroxymethyl-furan derivatives to the corresponding aldehydes only in the presence of a thiol, manganous ions, sodium malonate and a co-solvent.

INTRODUCTION

Horseradish peroxidase (HRP) is a haemoprotein known to catalyze the oxidation of a wide range of compounds. Its normal catalytic cycle involves the oxidation by hydrogen peroxide of the native state of the enzyme (ferric) to an intermediate two oxidation equivalents above (termed Compound I), which contains a porphyrin radical cation and a ferryl group. Compound I then interacts with the substrate, yielding Compound II (one oxidation equivalent above the native state) and substrate radical cation. Compound II similarly reacts with another substrate molecule to yield the ferric state of the enzyme and a substrate radical cation [1].

While the oxidation of typical substrates (phenols and aromatic amines) presents low selectivity and often proceeds towards rather complex reaction mixtures, a few more selective reactions are also performed by HRP [1]. Among these is the oxidation of benzyl-type alcohols to the respective aldehydes. The earliest example in that respect was provided by Saunders [2], while oxidizing mesitol with HRP and H_2O_2 (Fig. 1).

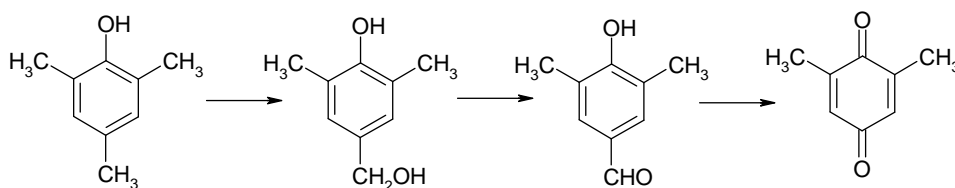


Fig. 1. Mesitol oxidation as performed by HRP/ H_2O_2 . All of the above compounds were recovered from the reaction mixture [1].

However, this has remained for a long time an isolated observation, although other peroxidases are known to perform the same reaction on a larger number of substrates.

Soybean peroxidase (SBP) has been shown to oxidize benzyl-type alcohols at extremely acid pH's [3]. Although the SBP reactivity is rather similar to that of HRP, SBP is characterized by stronger resistance to external factors (either temperature or pH). Thus, although HRP was eventually shown to oxidize the hydroxymethyl group, the enzyme was rapidly inactivated at the respective pH [3].

Lignin peroxidase and manganese peroxidase have veratryl alcohol as a natural substrate (while employing manganous ions as cofactors). Although the veratryl alcohol redox potential is outside the range of HRP substrates, the selective oxidation of veratryl and benzyl alcohols (mediated by thiols and Mn^{2+}) to the respective aldehydes has been surprisingly reported [4]. O_2 is consumed and H_2O_2 is not required in the process. An organic chelator (such as malonate) was also required. Aerobically generated thiyl radicals were found to have a key role both in initiating the reaction and in providing a complex with the manganous ion that would eventually interact with the substrate and generate substrate radical cations. Only two substrates were tested (veratryl alcohol and benzyl alcohol) [4].

While the influence of all components of the reaction mixture has been examined in the previous study [4], little attention was paid to the possibility of using non water-soluble substrates. However, performing the reaction in organic media would greatly enhance the range of prospective substrates.

Our interest in the chemistry of heterocycles has recently led to the synthesis of some hydroxymethyl-substituted furan derivatives as well as of the respective aldehydes [5-8]. In order to perform the HRP-catalyzed oxidation of the former to the latter, the problem of substrate insolubility in water had to be overcome.

RESULTS AND DISCUSSION

The oxidation of the hydroxymethyl substituted furan derivatives 1A-8A to the corresponding aldehydes 1B-8B (Fig. 2) was performed in conditions

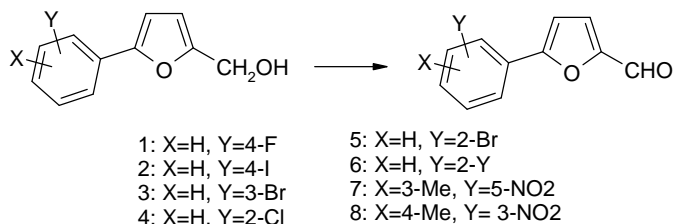


Fig. 2. The selective oxidation of some furan derivatives.

identical to those already reported, with the significant exception of the presence of a large quantity of co-solvent (its concentration was chosen in the range of 40-70% in order to provide a homogenous reaction mixture). Of the co-solvents tested, the better yields were obtained with methanol. Although no side reactions were observed (significantly, no carboxylic acid could be detected), the yields were not very high (20-60%, depending mainly on the co-solvent used).

Control experiments were run with the furan derivative 1 (see EXPERIMENTAL) using HRP and hydrogen peroxide as oxidizing agents in water/methanol mixtures, in the pH range 2-8. No aldehyde could be detected over a 24h period. Longer exposure brought about non-enzymatic degradation of the substrate. On the other hand furfural was easily oxidized to furoic acid under the same conditions. Control experiments with the aldehyde counterpart of 1 as substrate showed that on exposure to either HRP/H₂O₂ or HRP/ thiol/Mn²⁺ over more than 24 hrs gradual consumption of the aldehyde occurred. This was expected since carbonyl derivatives (especially isobutyraldehyde and acetophenone) are known peroxidase substrates [1].

The reaction mechanism suggested for this oxidation is illustrated in Fig. 3.

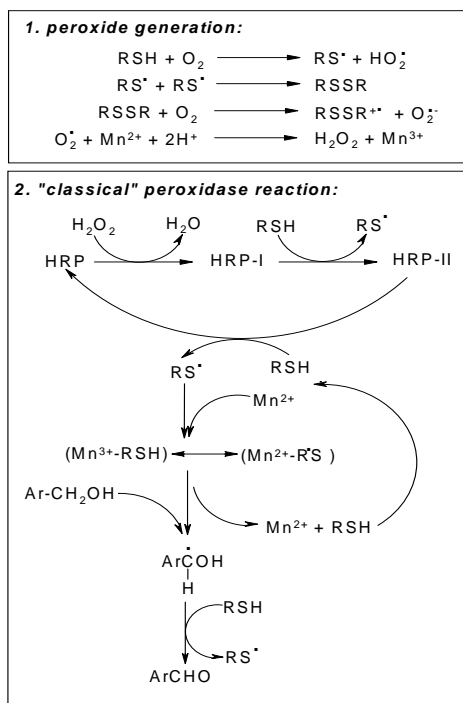


Fig. 3. The proposed mechanism for the oxidation of benzyl-type alcohols [4]. HRP-I and HRP-II are the peroxidase Compounds I and II, respectively. The mechanism implies two distinct steps: (1) peroxide generation from molecular oxygen (initiated by thiols), and (2), a peroxidasic reaction sustained by peroxide generated in (1).

Thus, the method described proves to be an interesting synthetic route towards aldehydes, and is of use for both water soluble and non-water soluble substrates.

EXPERIMENTAL

Horseradish peroxidase was an aqueous preparation [9]. A single stock solution was used and the enzyme concentration ($\epsilon = 98000$ at 408 nm), as well as its RZ and activity [10] were routinely checked by known procedures. All other reagents were of analytical grade. 1A-8A were prepared as previously described [6,7].

A typical reaction mixture included a thiol (glutathion or cysteine, 16 mM), MnCl_2 (1 mM), sodium malonate (10 mM) and the substrate (1 mM) in acetate buffer (0,1M, pH=4)/organic solvent (methanol, DMSO or dioxane). The reaction was started by adding the enzyme (1 μM). After stirring for 60-90 min the mixture was extracted with ether; the organic solvent was evaporated and the residue recrystallized from petroleum ether, thus providing the aldehyde (yields 20-60%; the best yield was obtained with 1 using methanol as a co-solvent).

The $^1\text{H-NMR}$ spectra were recorded on a Varian Gemini 300 Spectrometer operating at 300MHz, in CDCl_3 solution and TMS as internal standard. IR spectra were obtained in KBr pellets on a Nicolet FT205 spectrometer and are reported in wavenumbers (cm^{-1}). The mass spectra were recorded on Double focusing Varian Matt 311 Spectrometer, with an electronic impact source at 70eV and 300mA.

The melting points and the spectral data of 1B-8B have identical values with those previously described [8,9] confirming the reaction products.

1B: 5-(4-fluorophenyl)-furan-2-carboxaldehyde: white crystals, mp: 69;

IR (KBr) 1650 (CHO);

$^1\text{H-NMR}$ (CDCl_3) δ 6.8(d,1H) 7.34 (d,1H) 7.80 (d,2H) 7.82 (d,2H) 9.64 (s,1H);

MS m/e: 190(92)M, 171(5), 162(21), 144(2), 133(100).

2B: 5-(4-iodophenyl)-furan-2-carboxaldehyde: white crystals, mp: 144 $^\circ\text{C}$;

IR (KBr) 1680(CHO);

$^1\text{H-NMR}$ (CDCl_3) δ 6.87(d,1H) 7.34(d,1H) 7.55(d,2H) 7.90(d,2H) 9.65(s,1H);

MS m/e: 298(100)M, 270(13), 241(28), 171(3).

3B: 5-(3-bromophenyl)-furan-2-carboxaldehyde: white crystals, mp: 107 $^\circ\text{C}$;

IR (KBr) 1700(CHO);

$^1\text{H-NMR}$ (CDCl_3) δ 6.87(d,1H) 7.34(d,1H) 7.33(d,1H) 7.53(d,1H) 7.75(d,1H) 7.98(s,1H) 9.67(s,1H);

MS m/e: 250, 252 (100)M, 222, 224(8), 193, 195(33).

4B: 5-(2-chlorophenyl)-furan-2-carboxaldehyde: white crystals, mp: 77 $^\circ\text{C}$;

IR (KBr) 1673(CHO);

¹H-NMR (CDCl₃) δ 7.30-8.05(m,6H) 9.69(s,1H);

5B: **5-(2-bromophenyl)-furan-2-carboxaldehyde**: white crystals, mp: 57^oC;

IR (KBr) 1683(CHO);

¹H-NMR (CDCl₃) δ 7.37-7.97(m, 6H) 9.69(s,1H);

MS m/e: 250, 252(100)M, 222, 224(10), 193, 195(33).

6B: **5-(2-iodophenyl)-furan-2-carboxaldehyde**: white crystals, mp: 64^oC;

IR (KBr) 1675(CHO);

¹H-NMR (CDCl₃) δ 6.87(d,1H) 7.34(d,1H) 7.55-7.93(m,4H) 9.65(s,1H);

MS m/e: 298(100)M, 270(13), 241(32), 171(2).

7B: **5-(3-methyl-5-nitrophenyl)-furan-2-carboxaldehyde**: white crystals, mp: 113^oC;

IR (KBr) 1680(CHO);

¹H-NMR (CDCl₃) δ 2.68(s,3H) 6.96(d,1H) 7.41(d,1H) 8.03 (d,2H) 8,14(d,2H) 8.18(s,1H) 9.75(s,1H),

MS m/e: 231(100)M, 205(3)M-28, 201(13)M-30, 185(7), 128(43)

8B: **5-(4-methyl-3-nitrophenyl)-furan-2-carboxaldehyde**: white crystals, mp: 143^oC;

IR (KBr) 1675(CHO);

¹H-NMR (CDCl₃) δ 2.65(s,3H) 6.95(d,1H) 7.37(d,1H) 7.45 (d,1H) 7.95(d,1H) 9.39(s,1H) 9.69 (s,1H);

MS m/e: 231(100)M, 205(3)M-28, 201(13)M-30, 185(7), 128(43).

ACKNOWLEDGEMENT. We are grateful to Mr. R. Dumitru for his help on the enzyme preparations.

REFERENCES

1. J. Everse, K. Everse, B.M. Grisham, "Peroxidases in Chemistry and Biology", CRC Press, Boca Raton, 1991.
2. B.C. Saunders, in G.L. Eichhorn, "Inorganic Biochemistry", Elsevier, Amsterdam, 1973, pp 955-1024.
3. J.P. Mc Eldoon, A.R. Pokora, J.S. Dordrick, *Enzyme Microb. Technol.*, 1995, **17(4)**, 359.
4. J.P. McEldoon and J.S. Dordrick, *J. Biol. Chem.* 1991, **266(22)**, 14288.
5. F.D. Irimie, Cs. Paizs, Fr. Joo, R. Silaghi-Dumitrescu, M. Tosa, C. Majdik, *Roum. Biotechnol. Lett.*, 1999, **4(1)**, 71.
6. F.D. Irimie, Cs. Paizs, M. Tosa, C. Majdik, P. Moldovan, R. Misca, M. Caprioara, M. Neacsu, *Studia Universitas Babes-Bolyai,Chemia*, 2000, **XLV**, 23.

R. SILAGHI-DUMITRESCU, F.D. IRIMIE, C. PAIZS, C. MAJDIK, M. TOSA, P. MOLDOVAN, A. SAS, L. TAMAS

7. M. Tosa, Cs. Paizs, C. Majdik, P. Moldovan, R. Misca, F.D. Irimie, *Roum. Biotechnol. Lett.*, 2001, **6(3)**, 273.
8. F.D. Irimie, Cs. Paizs, R. Silaghi-Dumitrescu, G. Damian, C. Majdik, M. Tosa, *Studia Universitas Babes-Bolyai, Chemia*, 1998, **XLIII**, 173.
9. M.M. Baluta, Rom RO 90105 (CI A61K17/48), 30 aug 1986, Appl 02 nov 1984.
10. R.P.F. Gregory, *Biochem J.*, 1966, **101**, 582.

SEDIMENTATION. KOAGULATION. FLOCCULATION. I. SEDIMENTATIONSANAYSE EINER GEFLOCKTEN KAOLINSUSPENSION

ADINA GHIRISAN^{*}, ALEXANDRU POP^{*} und VASILE MICLAUȘ^{*}

^{}Fakultät für Chemie und Chemieingenieurwesen
Universität "Babeș-Bolyai" Cluj-Napoca*

ABSTRACT. The separation of flocculated caolin-water-suspensions on the sedimentation process was examined using a simple test laboratory device. The sedimentation behaviour, the optimal conditions of the flocculation, the settling rate of the flocculated network or the bulk and the kinetic evolution of flocculated caolin-water-suspension during the sedimentation prosses were determined by representative methods. The measurements were based on the determination of the temporal variation of the local position of the interface particle free fluid/flocculated suspension in tubes with constant cross section.

EINLEITUNG

Eine der Hauptaufgaben der Trink-, Abwasseraufbereitung und Reinigung von Abwässern aus der chemischen, pharmazeutischen, mineralischen und keramischen Industrie ist das Entfernen von Schwebestoffen. Diese bestehen aus organischen oder anorganischen Partikeln und enthalten feinste bis kolloidale Partikel.

In der Verfahrenstechnik wird Sedimentation als kostengünstiges Verfahren zur Auftrennung von dispersen Gemischen aus Feststoff und Flüssigkeit in den einzelnen Phasen eingesetzt.

Bei den meisten mechanischen Verfahren zur Trennung von Suspensionen in Feststoff und Flüssigkeit ist es erwünscht, dass der Feststoff aus möglichst grossen Partikeln besteht.

Bei der Sedimentation sinken grosse Partikel schneller als kleine Partikel, wie an der Stokesschen Gleichung (1) für die Sinkgeschwindigkeit w_{St} eines Partikels im laminaren Bereich zu erkennen ist.

$$w_{St} = \frac{1}{18} \cdot \frac{\rho_p - \rho_f}{\eta_f} \cdot d^2 \cdot g \quad (1)$$

mit ρ_p – Dichte des Partikels; ρ_f – Dichte des Fluids; η_f – dynamische Viskosität des Fluids; d – Partikeldurchmesser und g – Erdbeschleunigung.

Für die Abschätzung des Einflusses der gegenseitigen Behinderung der Teilchen während des Absetzens und Berücksichtigung der Flockenbildung hat sich die Beziehung von Richardson und Zaki [1] als besonders geeignet erwiesen:

$$\frac{w}{w_{St}} = (1 - c_v)^{4.65} \quad (2)$$

wobei: w ist die Geschwindigkeit der Flocken und c_v – Flockenkonzentration (Volumen %).

Bei den Partikeln, die so klein sind, dass sie im Gravitationsfeld der Erde gar nicht oder nur langsam sedimentieren, um diese Partikel dennoch vom Wasser zu trennen, gibt man Flockungsmittel mit langkettigen Molekülen oder Flockungshilfsmittel zu, damit sich aus den Partikeln Agglomerate bilden. Die Partikelagglomerate können weiter durch Sedimentation oder Filtration aus der Flüssigkeit entfernt werden.

Eine Agglomeration von suspendierten Feinstpartikeln zu Flocken verfolgt im wesentlichen zwei Ziele: a) Verbesserung der Sedimentationsgeschwindigkeit und somit eine Beschleunigung der Absetzgeschwindigkeit des Feststoffes und b) eine günstige Beeinflussung der Porenstruktur des Haufwerkes mit verbesserten Kuchenbildungs- und Entwässerungseigenschaften bei Filtrationspressen.

Die Agglomeration setzt sich prinzipiell aus zwei Vorgängen zusammen. Sie ist das Ergebnis eines Entstabilisierungsvorganges und eines Transportvorganges [2]. Der erste bewirkt durch Koagulation und Flocculation eine hinreichende Haufwahrscheinlichkeit pro Stoß zwischen Partikel-Partikel, Partikel-Agglomerate oder Agglomerat-Agglomerate.

Der zweite Vorgang bestimmt durch Trägheit (bei den Partikeln, die grösser als $1 \mu\text{m}$ sind) und Diffusion (bei den Teilchen, die kleiner als $1 \mu\text{m}$ sind) die Stoßwahrscheinlichkeit zwischen den agglomerierenden Feststoffteilchen. Man spricht entsprechend von orthokinetischem und perikinetischem Teilchentransport.

Die Entstabilisierung lässt sich in dem Koagulationsmechanismus und dem Flocculationsmechanismus unterteilen. Beide Mechanismen können sich dabei in ihrer Wirkung überlagern [3,4]. Bei der Koagulation lagern sich Teilchen infolge interpartikulärer Kräfte zusammen. Dabei wirken auf der einen Seite elektrostatische Abstoßungskräfte und auf der anderen van-der-Waalssche Anziehungskräfte. Vom Kräfteverhältnis hängt es ab, ob eine Agglomeration der Feststoffpartikel erfolgt, oder ob die Suspension stabil bleibt. Durch Variation von Menge und Ladung der zugesetzten Ionen können die Potenzialverhältnisse verändert werden und somit wird eine Koagulation ermöglicht.

In den Praktischen Anwendungen werden die Ionen hauptsächlich in Form von Aluminium- und Eisensalze verwendet. Bei einer Koagulation, bei der sich das Oberflächenpotential auf null reduziert, spricht man von einer isoelektrischen Flockung.

Bei der Flocculation werden die Partikel mit Hilfe von synthetischen und polymeren Flockungsmittel durch die Bildung permanenter Brücken aus makromolekularen Substanzen, miteinander vernetzt. Es handelt sich bei diesen Flockungsmitteln in der Regel um wasserlösliche Kohlenwasserstoff Verbindungen mit unterschiedlichem Molekulargewicht und reaktiven Gruppen. Es gibt zwei Typen zwischen natürliche organische Flockungsmittel (wie z.B. Stärke oder Glucose) und synthetische hergestellte Polymere.

Man unterscheidet sie nach ihrem Polymerisationsgrad, sowie nach ihrer Ladung. Die Ladung wird durch reaktive chemische Gruppen erzeugt, die in den Polymerketten eingefügt sind.

Die Anlagerung der Polymermoleküle an der Oberfläche der Feststoffteilchen kann nach der Art des Flockungsmittels über einen oder mehrere der folgenden vier Mechanismen erfolgen: a) Wasserstoffbrückenbildungen zur Hydrathülle des Teilchens; b) elektrostatische Wechselwirkungskräfte; c) Bildung von Ionenbrücken zwischen den gleichsinnig geladenen Feststoffoberflächen und den reaktiven Gruppen des geladenen Polymermoleküls und d) Bildung von höherer Ionenkonzentration in Feststoffnähe.

Für diese Mechanismen gibt es zwei Modellvorstellungen. Bei dem Brückenbildungsmodell haften Polymermoleküle (mit hochmolekularen oder langkettigen Molekülen) nur mit wenigen reaktiven Gruppen an der Feststoffoberfläche und verbinden die Partikeln über eine Entfernung, die grösser sein kann als die Reichweite der interpartikulären Kräfte. Für kurzkettige Polymermoleküle lagern sich diese vollständig an der Feststoffoberfläche an und beeinflussen dort die Ladung des Partikels. Die Adsorption von Polymermolekülen mit einer der Feststoffoberflächenladung entgegengesetzten Ladung kann an der Partikeloberfläche eine partielle Ladungsumkehr bewirken. Dadurch kann es an der Feststoffoberfläche zu negativ und positiv geladenen Oberflächenbereichen kommen. Eine Zusammenlagerung der Partikeln zu Flocken erfolgt in diesem Fall über die elektrischen Wechselwirkungskräfte zwischen den unterschiedlich geladenen Zonen der Partikel.

Die Flocculation der kolloidalen Teilchen einer Suspension hat eine zunehmende Bedeutung in der Abwasseraufbereitung [4,5]. Im Rahmen dieser Arbeit wurden die Sedimentationsprozesse einer geflockten Kaolin-Wasser-Suspension mit verschiedenen Flockungsmittelskonzentrationen im Vergleich mit einer reinen Kaolin-Wasser-Suspension untersucht. Die Eigenschaften der geflockten Suspensionen wurden im Verlauf der Sedimentation analysiert und das kinetische Modell der Flocculation wurde bei den Kompressionszonen festgesetzt.

VERSUCHSDURCHFÜHRUNG

Die Trennung einer Kaolin-Wasser-Suspension ($d_{50\%} < 20 \mu\text{m}$) wurde durch reine Sedimentation und Flocculation in einem Schüttelapparat (mit vier Standzylindern; diskontinuierlicher Absetzversuch) durchgeführt.

Der Standzylinder (Durchmesser $\phi = 50 \text{ mm}$ und Höhe $H = 300 \text{ mm}$) des Schüttelapparats wurde mit einer 10 % konzentrierten Kaolin-Wasser-Suspension gefüllt. Dazu gab man 40 g Kaolin der Qualität **KO1** (die Dichte des trockenen Feststoffs $\rho_p = 2500 \text{ kg/m}^3$) und 400 ml Wasser. Der Zylinder wurde mit dem Stöpsel verschlossen und im Schüttelapparat kräftig geschüttelt, so dass eine homogene Suspension entstand. Die Höhe der Suspension (h_0) wurde dann in jedem Fall gemessen.

Polyacrylamid und die Copolymeren des Polyacrylamids sind Flockungsmittel, die oft im Flockungsvorgang zu empfehlen sind [6, 7]. Die Synthese der hier vorgeschlagenen Flockungsmittel beruht wie auf Abbildung 1 durch Copolymerisierung in organischen Lösungsmitteln (t-Butanol) aus Acrylamid, Acrylsäure und N-iso-Propylacrylamid in gewissen Mol Verhältnissen in Anwesenheit von Azo-bis-isobutyronitril (AIBN) nach einem modifizierten Verfahren [8] von F.M. Winnik [9]. Das Molekulargewicht der hergestellten Polymere liegt im Bereich von 150-200000. Diese Werte wurden durch HPLC über eine PIGel GP-MXB Säule im Vergleich mit Standard - Polymermustern überprüft [8].

In diesem Artikel werden die Ergebnisse der Flocculation der Kaolin-Wasser-Suspensionen mit nichtionischem Polyacrylamid (**PAA**) von unterschiedlichen Flockungsmittelskonzentrationen vorgelegt.

Das Flockungsmittel wurde von 0.5 g nichtionisches Polyacrylamid und 500 ml Leitungswasser nach einer starken magnetischen Vermischung hergestellt.

Es wurde bei jedem neuen Versuch verschiedene Volumen des Flockungsmittels PAA 0.1 % zugegeben und zwar folgende Mengen: 1.0 ml; 2.0 ml; 4.0 ml; 5.0 ml; 10.0 ml; 15.0 ml und 20.0 ml. So wurden flockulate Suspensionen unterschiedlicher Konzentration erhalten und zwar 2.25 ppm; 4.5 ppm; 9.0 ppm; 11,2 ppm; 22.5 ppm; 35.0 ppm und 43.4 ppm. Die pH-Werte liegen in dem Bereich 6.3 - 6.5 in jedem Fall.

Die Zylinder wurden danach im Apparat 10 mal geschüttelt. Weil der Flockungsvorgang mit der Art der Dosierung des Flockungsmittels und dessen Vermischung mit der Suspension beginnt, wurden alle Versuche in denselben Bedingungen mehrmals durchgeführt. Danach wurden die Mittelwerte vorgestellt.

Der Sedimentationsvorgang wurde beobachtet und analysiert. Dazu wurde die Bewegung des Trennspiegels (die Grenze zwischen den sedimentierenden Partikeln/sedimentierenden geflocketen Suspensionen und der geklärten Flüssigkeit) im Laufe der Zeit (alle 30 Sekunden) aufgenommen.

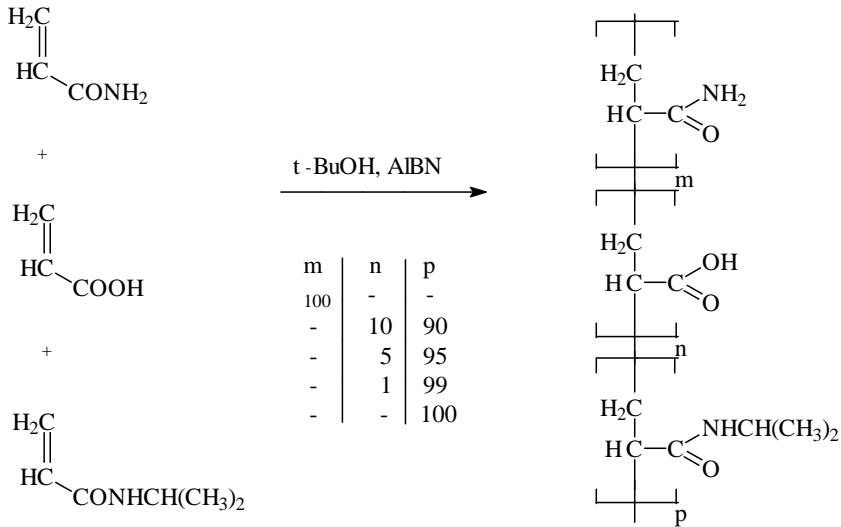


Abb. 1. Synthetische Flockungsmittel.

ERGEBNISSE UND DISKUSSION

Die Durchführung dieser Versuche erfolgt nach mehreren standardisierten Testmethoden in Zusammenhang mit den theoretischen Grundlagen [7, 10].

Für alle Versuche wurde die genannte Höhe des Trennspiegels h in Abhängigkeit von der Zeit in der Abbildung 2 dargestellt.

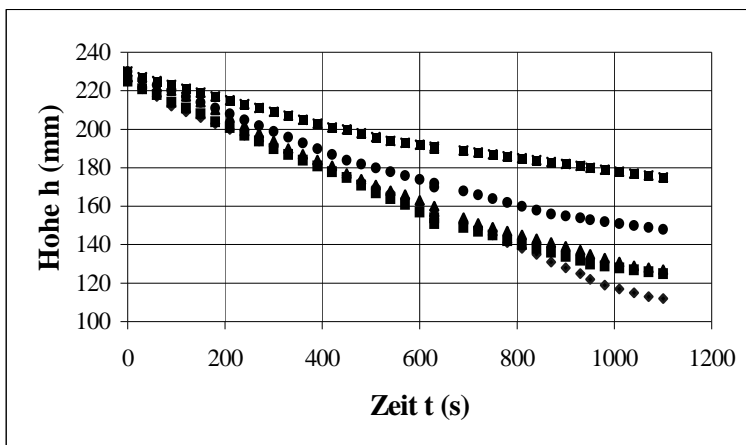


Abb. 2. Höhe der Gränzfläche Wasser/geflockte Suspension in Abhängigkeit von der Zeit.

◆ 4.5 ppm PAA; ■ 9.0 ppm PAA; ▲ 11.2 ppm PAA; * 22.5 ppm PAA und ■ 35.0 ppm PAA.

Die Analyse des Sedimentationsverhaltens zeigt, dass die charakteristischen Eigenschaften der geflockten Suspensionen sich mit dem Grad der Flockenbildung (Flockungsmittelskonzentration) ändern, obwohl alle $h(t)$ – Kurven des Trennspiegels im Bereich der Sedimentations- und Kompressionszonen verläuft.

Mit zunehmender Flockungsmittelskonzentration wurden die nächsten Absetzverhalten verfolgt.

Bei kleiner Flockungsmittelskonzentration $C_{FM} = 2.25$ ppm wurde die Sedimentation sehr schwach und unvollständig. Die meisten Feststoffteilchen des Kaolins setzen sich mehr in Form einzelner Partikeln ab und nur wenige Teilchen bewegen sich als Einzelflocken. Beim diskontinuierlichen Absetzversuch zeigen die Suspensionen keine Grenzlinie zwischen den absetzenden Feststoffteilchen und Flüssigkeit.

Die Suspension ist noch eine Trübe, mit einem kolloidalen Aspekt, die sehr langsam sedimentiert. Das bedeutet, dass nicht alle Kaolinteilchen der Suspension geflockt wurden und nur die grossen Kaolinteilchen sich als geflockte Suspension lagern. Auf Grund der niedrigen Konzentration des Flockungsmittels wurden nur Mikro-Flocken ausgebaut, die noch nicht alle feinsten Teilchen zusammenballen konnten.

Mit zunehmender Flockungsmittelskonzentration (4.5 ppm; 9.0 ppm und 11.2 ppm PAA) tritt ein Trennspiegel auf, obwohl die Flüssigkeit über der geflockten Suspension noch nicht klar ist (Abb. 2). In diesen Fällen bewegt sich der Trennspiegel nicht gleichförmig nach unten. Wesentlich ist, ob und wie stark die Einzelteilchen der Suspension zu den aufgetreten Flocken, mit zunehmender Flockungsmittelkonzentration, sich zusammenballen. Nicht alle Einzelteilchen der Suspension lagern sich mit den Flocken, die durch Adsorption an den Feststoffoberflächen zu einer Agglomeration führen. Nicht flockende Feststoffteilchen sind langsamer als die geflockte Suspension gelagert.

Man bemerkt, dass die charakteristischen Eigenschaften der Suspension sich ändern und die Absetzgeschwindigkeit grösser wird. Die geflockten Feststoffteilchen sedimentieren mit einer einheitlichen Struktur. Mit zunehmender Konzentration und wachsender Ausbildung von Flocken geht der Absetzvorgang in der Sedimentationszone über. Die Absetzgeschwindigkeit des Trennspiegels wurde in diesem Bereich zwischen 0.1 – 0.15 mm/s berechnet. Von der Abbildung 2 wurde der Übergang zwischen Sedimentations- und Kompressionszone bei etwa 630 Sekunden bestimmt.

Zwischen Klarwasser und geflockte Suspension ist bei der Flockungsmittelskonzentration ab 22.5 ppm PAA ein deutlicher Trennspiegel erschienen. Einzelne feine und feinste Feststoffteilchen bewegen sich zur Gesamtstruktur. In diesem Fall wurde die Flockungsmittelkonzentration so hoch, dass die gebildeten Flocken eine zueinander banden und sich so, wie ein kompaktes Netz nach unten bewegt haben.

Bei höherer Konzentration verläuft die $h(t)$ - Kurve in den Kompressionszonen von Anfang an gekrümmt. In diesem Fall können die Flocken aufgrund dichter Lagerung mechanische Kräfte übertragen und aufnehmen, die zu einer Verdichtung der Struktur führen.

Höhere Konzentration des Flockungsmittels in der Suspension bedeutet aber auch kleinere Absetzgeschwindigkeit des Trennspiegels ($w < 0.03$ mm/s).

Die Durchführung dieser Versuche bestimmt die optimale Flockungsmittelmenge bei einer Flockungsmittelskonzentration $C_{FM} = 33.0$ ppm PAA. Alle feine und feinsten Feststoffteilchen der Suspension sind in dem kompakten Netz gebunden und man erhält klares Wasser als Flüssigkeit. Das Flockungsergebnis war in diesem Fall sehr gut.

Eine Überdosierung von Flockungsmittel ($C_{FM} = 45.0$ ppm PAA) führt zum gegenteiligen Effekt, zu einer Stabilisierung der Flockungsmittel-Partikel und zu einer schwächeren Separation.

Im Vergleich wurde die Kaolin-Wasser-Suspension ohne Flockungsmittel gar nicht sedimentiert. Für die Kaolinpartikel ($d_{50\%} < 20$ μ m) muss man Flockungsmittel mit langkettigen Molekülen zugeben, damit sich aus den Partikeln Agglomerate bilden.

Im Rahmen dieser Arbeit wurde auch der Einfluss des Flockungsmittels auf die Kinetik der Sedimentation in der Kompressionszone untersucht. Wie in der Abbildung 2 (Trennspiegelhöhe durch Zeit) dargestellt ist, ändert sich die Flockenbildung mit der Flockungsmittelskonzentration und der Absetzgeschwindigkeit.

Im allgemeinen kann die Absetzgeschwindigkeit des Trennspiegels, die aus der Steigung der $h(t)$ - Kurve berechnet ist, als Trennspiegelhöhe (dh/dt) definiert werden. Sie hängt von der Zeit durch die Gleichung (3) ab [4]:

$$\frac{dh}{dt} = -kh \quad (3)$$

Hierbei ist k die Geschwindigkeitskonstante (s^{-1}) in Abhängigkeit mit den Suspensionseigenschaften. Das negative Gleichungszeichen zeigt, dass die Absetzgeschwindigkeit kleiner mit der Zeit wird. Durch die Integrierung der Gleichung (3) und aus den Grenzbedingungen erhält man die kinetische Gleichung (4):

$$\frac{h}{h_0} = e^{-kt} \quad \text{oder} \quad \frac{h_0}{h} = e^{kt} \quad (4)$$

Die Gleichung (4) beschreibt die liniare Sedimentationkinetik, die eine akzeptable Approximation für bestimmte Zeitspannen ist. Für die komplexen Fälle kann man die Gleichung (5) benutzen:

$$\frac{h_0}{h} = e^{-kt^m} \quad (5)$$

Die kinetischen Koeffizienten k und m wurden von experimentälen Daten graphisch festgesetzt. Im doppeltlogarithmischen Massstab ergibt die Gleichung (5) eine Gerade mit der Steigung m und dem Ordinatenabschnitt k (Abbildung 3). Weil die bestimmte Steigung $m = 0.91$ ist, kann man die Sedimentation als kinetischen Versuch erster Ordnung betrachten.

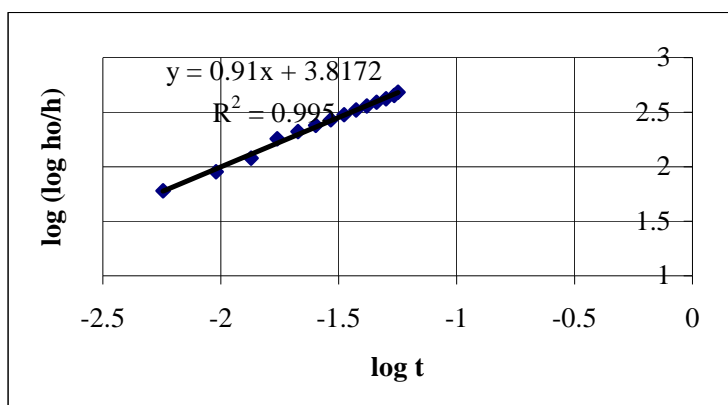


Abb. 3. Doppeltlogarithmische Darstellung der Gleichung (5) in dem Fall einer geflockten Suspension 33.0 ppm PAA im Kompressionsbereich.

LITERATURVERZEICHNIS

1. R. Freidinger, Maschinenmarkt 1982, **88**, 1855
2. H. Hahn, Jahrbuch "Vom Wasser", 1976, **333**, 176
3. B. Koglin, Chem. Ing. Tech., 1984, **56(2)**, 111
4. J. Florea und D. Robescu, Hidrodinamica instalatiilor de transport hidropneumatic și de depoluare a apei și a aerului, **EDP**, 1982
5. D. H. Belhateche, Chem.Eng.Prog., 1995, **91(8)**, 32
6. Kirk-Othmer, *Encyclopedia of Chemical technology*, 1968, Vol. **16**
7. L. Henning-Schlosser, F. Nan und D. Tivadar, *Revista de Chimie*, 1984, **35(10)**, 901
8. V. Miclăuș, nicht veröffentlichte Ergebnisse
9. F. M. Winnik, *Macromolecules*, 1990, **23(1)**, 231; F. M. Winnik, M. F. Ottavianni, S. H. Bossmann, W. Pan, M. Garcya-Garibay, N. Turro . *J. Phys. Chem.*, 1993, **97**, 12998
10. Unterlagen zum Kurs Fest-Flüssig-Trennung, Institut MVM der Universität Karlsruhe (TH), 1999, Deutschland

THE SOLUBILITY OF DRUGS IN SUPERCRITICAL CO₂ AND THE EFFECT OF ENTRAINERS

SIMION DRAGAN¹, MIHAELA DRAGAN²

¹ Faculty of Chemistry and Chemical Engineering "Babes-Bolyai" University Cluj-Napoca

² Faculty of Economics, "Babes-Bolyai" University Cluj-Napoca

ABSTRACT. In this work the solubility of two drugs in supercritical carbon dioxide are being measured. There were investigated the solubility of terfenadine and griseofulvin in s.c. carbon dioxide at pressures in the range of 140 – 180 bar and two temperatures 313,2 K and 343,2 K.

To evaluate the solubility of the two drugs we are using an equation of Chrastil type and obtained the values for the association number k , and for the two constants a , b which take into account the enthalpy of solvation and vapourization of the solute and the molecular weight of the species. This chemicals have relatively low solubilities with values ranging from $3,092 \times 10^{-7}$ to $1,8550 \times 10^{-6}$ mole fraction. The solubilities exhibit a clear dependence on the solvent density and this has been used to provide a simple and precise correlation of the data.

The effect of ethanol added to CO₂ as an entrainer was investigated, varying its concentration in CO₂ from 1wt % to 5wt. %.

1. INTRODUCTION

In recent years there has been an increasing level of interest in utilizing supercritical fluid (SF) technology for processing pharmaceutical and nutraceutical materials. The unique feature of the supercritical state is that the solvating power strongly depends on the fluid density and can be adjusted, without changing chemical composition, by controlling the pressure and temperature. This property opens up a wide range of possibilities for selective extraction, purification and precipitation processes [1]. Extraction processes with supercritical fluids are established even in industrial scale and become again more interesting for industry.

Supercritical fluid extraction of active molecules from medicinal plants, extraction from dilute media for metabolite recovery, enzymatic reactions, precipitation, micronization and impregnation are some of the areas of application under investigation and development [2]. Purification of pharmaceuticals and detoxification of hazardous wastes are a few of the many applications in which conventional organic solvents are being replaced by environmentally benign supercritical fluids such as carbon dioxide [3].

The experimental determination of drugs solubility in supercritical fluid system is important owing to the increasing applications of the dense gases.

Carbon dioxide is by far the most important processing medium because of its relatively low critical temperature and pressure (31,3°C and 72,9 bar), low toxicity and low cost. In the compressed state, supercritical CO₂ can be described as a hydrophobic solvent with a polarity comparable to that of hexane or pentane.

In this work, the solubilities of two Anti-Inflammatory Drugs- Terfenadine and Griseofulvin – have been measured in supercritical carbon dioxide.

The experimental data were correlated by a semiempirical method proposed by Chrastil [4] which is based on the hypothesis that one molecule of solute associates with k molecules of supercritical fluid forming a complex in a state of chemical equilibrium.

It is well known that the addition of a cosolvent to a supercritical fluid often leads to an enhancement in the solubility of a solute [5]. In this work, we have used ethanol as a cosolvent, varying its concentration in CO₂ from 1 wt% to 5 wt%.

2. EXPERIMENTAL

The supercritical fluid – carbon dioxide – was available with purity of 99,99% from AGA Gas GmbH Hamburg.

Terfenadine and Griseofulvin were purchased from Merck Co. with purity greater than 99,9%.

The structures of the two drugs are shown in Figure 1.

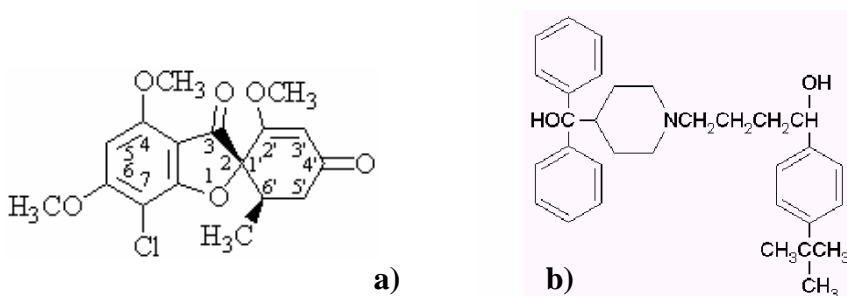


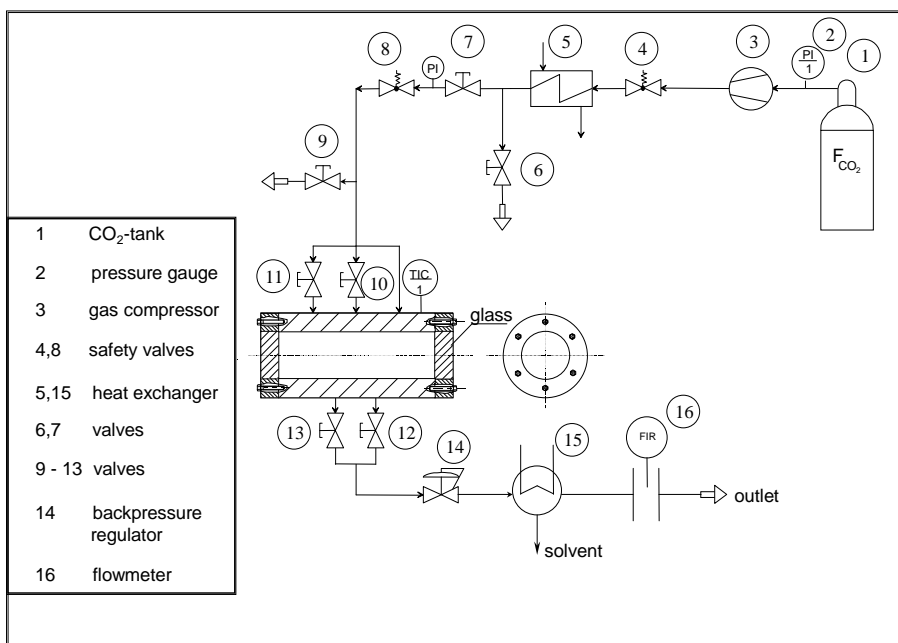
Figure1. Structure of the studied drugs: a). Grieofulvin; b). Terfenadine

Some of the available physical and chemical property data for the compounds used in this study are listed in Table 1.

Table 1.Molar Mass M , Melting Point T_m , and Solubility S in water for the Drugs

Compound	M [g. mol ⁻¹]	T_m [K]	S [mg/ml H ₂ O]
Terfenadine	471,29	419,2 – 421,2	0,010 at 30 C
Griseofulvin	352,8	495,2	40,1 at 25 C

The solubility of terfenadine and griseofulvin in supercritical carbon dioxide is not available in the literature. It was determined experimentally using the experimental equipment presented in Figure 2.

**Figure 2.** Flow sheet of the apparatus

The main part of the experimental equipment is the autoclave with a volum of 249,5 ml. The diameter of each inlet and outlet is 1 mm. For a better mixing in the liquid phase, the autoclave can be rocked with constant velocity. The temperature is maintained by means of a heating jacket and temperature controller with an accuracy of $\pm 1^\circ$ C. The temperature was measured with a Pt 100 thermocouple calibrated by two points measurements. In order to determine the solubility of the two drugs in supercritical CO₂, a specific amount of the substance was filled in a metal cage, weighed and placed on the bottom of the autoclave. The autoclave was closed and heated up to a fixed temperature (40 and 70° C).

The CO₂ gas, comes from the tank (1), is compressed in the gas pump (3) (membrane compressor, Whitey Model LC-10) and heated up to the desired temperature in the heat exchanger (5). Then CO₂, preheated to the same temperature was pumped into the autoclave up to the desired pressure (140; 160; and 180 bar) was reached. The system was stored under stirring for 24 h. The temperature could be kept constant with an accuracy of $\pm 1^\circ\text{C}$ and the pressure varied within 5 bar.

After the equilibrium was reached, CO₂ was vented out with a constant flow rate (~ 20 NL/hour) and then the autoclave was cooled to room temperature.

The metal cage with the rest of the substance was weighed and the amount of the dissolved substance calculated.

The amount of CO₂ in the autoclave was calculated from the known volume and corresponding CO₂ density. The values of CO₂ density were taken from NIST data base [NIST].

3. RESULTS AND DISCUSSIONS

The solubilities of the two drugs along with the temperature, pressure and density of CO₂ that corresponds to each measurement are listed in Table 2.

Table 2.

Experimental solubility for the Drugs in Supercritical CO₂

T [K]	P [bar]	D _{CO₂} [g/l]	10 ⁶ x Solubility as molar fraction	
			Terfenadine	Griseofulvin
313,2	140	763,27	0,9985	3,6006
	160	794,9	1,2939	6,2735
	180	819,51	1,5344	6,9466
343,2	140	456,62	0,33376	0,445876
	160	547,75	1,0435	1,7656
	180	612,24	1,9914	6,5678

For the description of the solubility behavior of substances in compressed gases different equations were developed including the density of the fluid [6], [7] In this work, the solubilities were correlated using the density-based equation proposed by Chrastil [4]:

$$\ln c = k \ln d + \frac{a}{T} + b \quad (1)$$

where c is the concentration of the solute in the supercritical fluid (g/L), d is the density of the fluid (g/L), k is the number of fluid molecules associating with one molecule of solute to form a solvatocomplex. The constants a , b take into account the enthalpy of solvation and vapourization of the solute and the molecular weight of the species.

The parameters k, and a,b have to be fitted to experimental data and are presented in Figures 3 and 4, and summarized in Table 3.

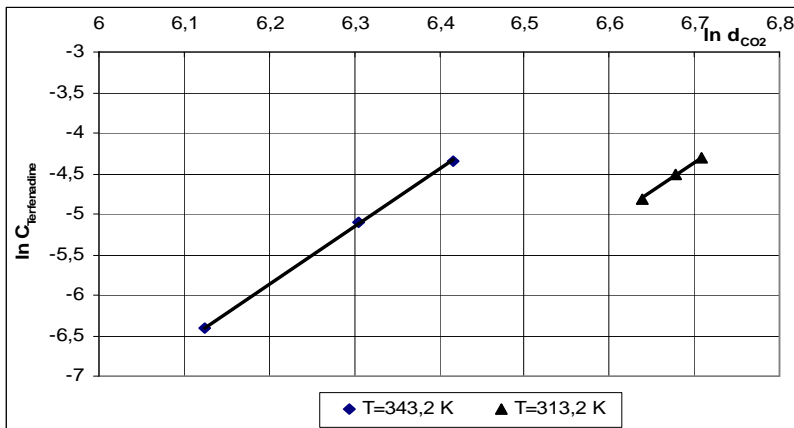


Figure 3. Solubility of terfenadine in CO₂. Determination of the solubility constants k and a, b.

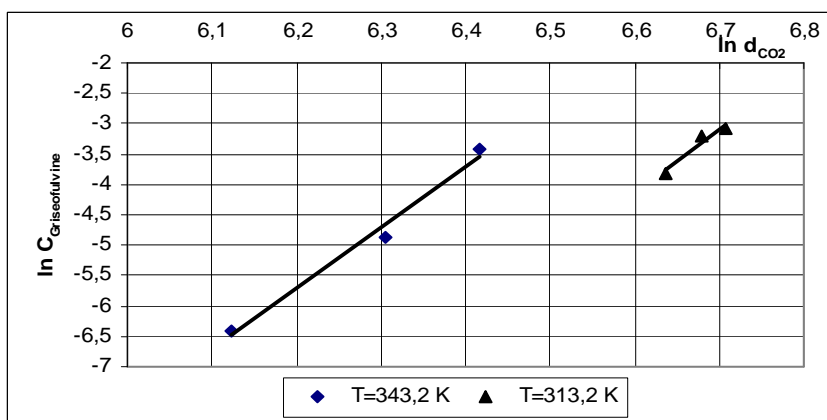


Figure 4. Solubility of Griseofulvin in CO₂. Determination of the solubility constants k and a,b

Table 3.

Solubility constants in Carbon Dioxide

Compound	k	a	b
Terfenadine	7,108	-5894,0091	-32,8513
Griseofulvin	10,152	-20480,518	-8,112

As a result, the solubility of terfenadine and griseofulvin in CO₂ can be expressed as follows:

$$\ln c = 7,108 \ln d - \frac{5894,0091}{T} - 32,8513 \quad (2)$$

$$\ln c = 10,152 \ln d - \frac{20480,518}{T} - 8,112 \quad (3)$$

The solubilities for the two systems as a function of pressure and CO₂ density comparative with the predicted solubilities with the Chrastil-equation [4] are presented in Figures 5 – 8 and summerized in Table 4.

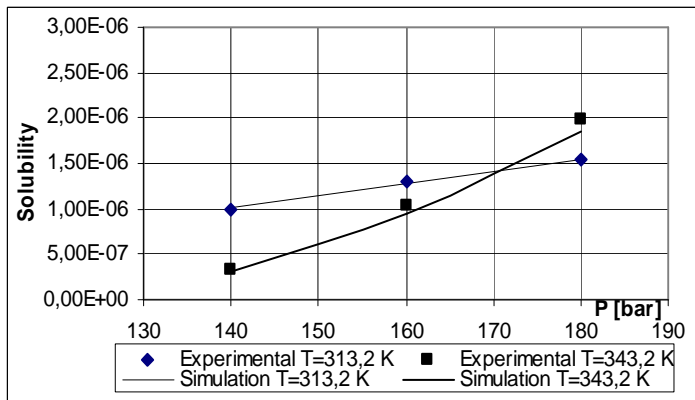


Figure 5. Mole fraction solubility of terfenadine as a function of pressure P in supercritical carbon dioxide

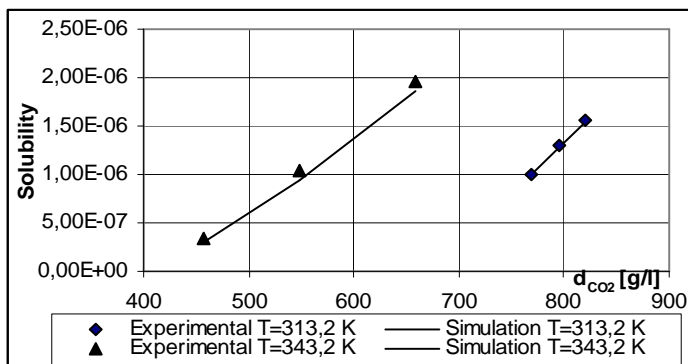


Figure 6. Mole fraction solubility of terfenadine as a function of the carbon dioxide density

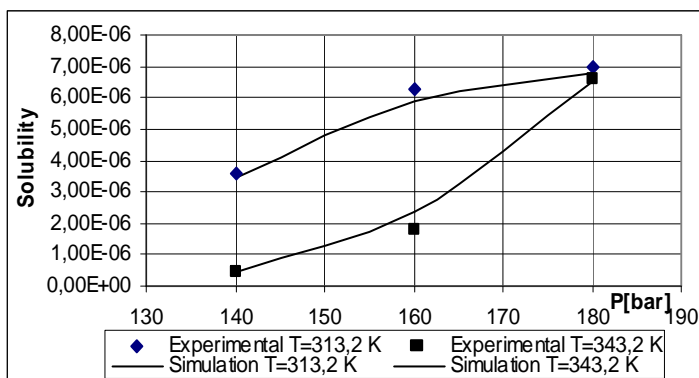


Figure 7. Mole fraction solubility of griseofulvin as a function of pressure P in supercritical carbon dioxide

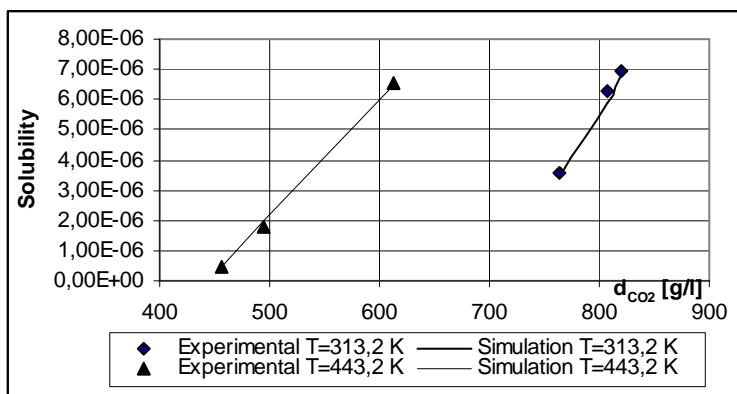


Figure 8. Mole fraction solubility of griseofulvin as a function of the carbon dioxide density

The results from Figures 5 and 7 show an increase of the terfenadine and griseofulvin solubility with the experimental pressure while the temperature was kept constant.

For terfenadine has been obtained a higher solubility at 313,2 K at a pressure of 170 bar. Over this value of pressure, the solubility is higher at 343,2 K.

In the case of griseofulvin we have noticed that in the whole range there have been obtained a higher solubility at the temperature of 313,2 K.

Figures 6 and 8 have show an increase of the terfenadine and griseofulvin solubility, with the solvent density.

The predicted solubilities values presented in Table 4 are in a good agreement with the experimental data for the two drugs.

Table 4.

Prediction of terfenadine and griseofulvin solubilities at three density values of CO₂ according to the Chrastil equation

Compound	T [K]	P [bar]	10 ⁶ x Mole fraction solubility		AAD [%]
			experimental	calculated	
Terfenadine	313,2	140	0,9985	1,004	0,55
		160	1,2939	1,2840	0,76
		180	1,5344	1,545	0,69
	343,2	140	0,3376	1,3092	7,35
		160	1,0435	0,94	7,21
		180	1,9914	1,8550	6,85
Griseofulvin	313,2	140	3,6006	3,454	4,07
		160	6,2735	5,88	6,27
		180	6,9466	6,786	2,31
	343,2	140	0,44586	0,4594	3,03
		160	1,7656	1,977	11,9
		180	6,5678	6,4962	1,09

The absolute average percentage deviation of calculated from experimental values (AAD) are for terfenadine in the range: 0,55% - 7,35% and for griseofulvin these are ranging from 1,09% to 11,9%.

In order to enhance the dissolution of the two drugs with pharmaceutical applications – terfenadine and griseofulvin – it had been used as entrainer, ethanol. The experiments were performed with ethanol concentration in CO₂ varying from 0 to 5 wt. %. The influence of the entrainer concentrations on the terfenadine and griseofulvin solubilities are presented in Figure 9.

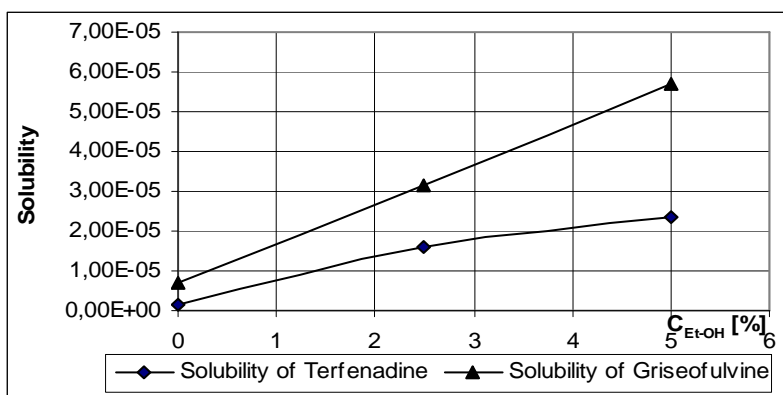


Figure 9. Influence of Et-OH concentration on the terfenadine and griseofulvin Mole Fraction Solubilities at T=313,2 K and P=180 bar

The results from Figure 9 show that the solubility of both active compounds increases significantly in presence of the entrainer.

An empirical relation which described the influence of the ethanol concentration has the following form [8]:

$$y = y_0 + n(y_0 w_e)^m \quad (4)$$

where y is the solubility of the two drugs in CO₂ with entrainer (mol/mol), y_0 is the solubility of the two drugs in pure CO₂ (mol/mol) and w_e is the concentration of ethanol in CO₂ (g/g).

From our experimental data, we deduced the following relations which described the influence of ethanol added to CO₂ as an entrainer on the terfenadine and griseofulvin:

$$y = y_0 + 0,0745 \cdot (y_0 w_e)^{0,5} \quad (5)$$

$$y = y_0 + 137,04 \cdot (y_0 w_e) \quad (6)$$

The experimental solubility of the two drugs in the presence of the entrainer and the predicted solubility with the equations (5) and (6) are presented in Table 5.

Table 5.

Experimental and predicted solubility of terfenadine and griseofulvin in supercritical CO₂ with Ethanol at T=313,2K and P=180 bar.

Et-OH [%]		0	2,5	5,0
Compound				
Terfenadine	y_{exp}	$1,5344 \times 10^{-6}$	$1,5873 \times 10^{-5}$	$2,3343 \times 10^{-5}$
	$y_{calc.}$	$1,5344 \times 10^{-6}$	$1,6311 \times 10^{-5}$	$2,2705 \times 10^{-5}$
	A.A.D. [%]	0	2,76	2,73
Griseofulvin	y_{exp}	$6,9466 \times 10^{-6}$	$3,1310 \times 10^{-5}$	$5,7143 \times 10^{-5}$
	$y_{calc.}$	$6,9466 \times 10^{-6}$	$3,1350 \times 10^{-5}$	$5,7048 \times 10^{-5}$
	A.A.D. [%]	0	0,14	0,17

4. CONCLUSIONS

The solubilities of two drugs have been measured in supercritical CO₂ at pressures between 140 – 180 bar and at temperatures of 313,2 K and 343,2 K. The experimental error is estimated for terfenadine to be in the range of 0,55% - 7,35% and for griseofulvin these are ranging from 1,09% to 11,9%.

The parameters required by the predictive method for the evaluating the solubilities of solid in supercritical carbon dioxide are the molecular weight, structure and the melting temperature.

It was shown that the addition of a small amount of ethanol as entrainer to the supercritical carbon dioxide can increase selectively the solubilities of the two drugs.

Acknowledgment: We greatly appreciate the support for our experimental work to the Institute of Thermodynamic and Chemical Engineering of the Technical University of Berlin and for the discussions with Prof.Dr-Ing.W. Arlt.

LITERATURE

1. S. Bristow, B. Shekunov, P. York, *Ind. Eng. Chem. Res.*, 2001, **40**, 1732 – 1739.
2. S. Macnaughton, I. Kikik, N. Foster, P.Alessi, *J.Chem. Eng. Data*, 1996, **41**, 1083 – 1086.
3. J.M. Santiago, A.S. Teja, *Fluid Phase Equilibria*, 1999, **158-160**, 501-510.
4. J. Chrastil, *J. Phys. Chem.*, 1982, **86**, 3016 – 3021.
5. C.D. Saquing, F.P. Lucien, N.R. Foster, *Ind. Eng. Chem. Res.*, 1998, **37**, 4190 – 4197.
6. R. Marr, T. Gamse, *Chemical Engineering and Processing*, 2000, **39**, 19 – 28.
7. S. Mitra, N.K.Wilson, *J. Chrom. Sci.*, 1991, **29**, 305 – 319.
8. H. Sovova, *Journal of Supercritical Fluids*, 2001, **21**, 195 – 203.

ADSORPTION KINETICS OF DIBUCAINE AND TETRACAINE AT THE BENZENE/WATER INTERFACE STUDIED BY PENDANT DROP METHOD

MARIA TOMOAI-COTIȘEL, JÁNOS ZSAKÓ[#], AURORA MOCANU,
MARIUS SĂLĂJAN, CSABA RACZ, SIMONA BRAN and EMIL CHIFU[#]

"Babeș-Bolyai" University, Department of Physical Chemistry, 3400
Cluj-Napoca, Romania

[#] Deceased

ABSTRACT. Dynamic interfacial tensions have been measured at the benzene/water interface in order to study the adsorption behavior of some local anesthetics, *namely* dibucaine and tetracaine, from the aqueous bulk solutions at the interface with pure benzene. For this purpose the pendant drop method was used. To describe the adsorption kinetics of these anesthetics at liquid interface, *a new theoretical approach* has been developed for the diffusion controlled adsorption of surfactants at the benzene/water interface. Therefore, various kinetic equations are tested and *a new diffusion controlled kinetic equation* is proposed, based on the Ward and Tordai diffusion equation associated with the two dimensional van der Waals state equation. This analysis provides a better understanding of the interfacial properties of adsorbed anesthetics layers at liquid interfaces. Diffusion coefficients, subsurface concentrations and molecular interaction parameters are derived from the experimental data and discussed in terms of the local anesthetics molecular structure.

Key words: adsorption kinetics at liquid interfaces; local anesthetics; dibucaine; tetracaine; diffusion coefficient; intermolecular interaction parameters

INTRODUCTION

The adsorption kinetics of various surfactants at liquid interfaces frequently plays a major role in many diverse processes, with a substantial scientific and technological impact, such as interfacial turbulence, foaming and wetting, as well as in biological processes [1-3]. Thus, the modeling [1-13] of the adsorption kinetics represents a key step to understand and improve processes which involve the stabilization of interfaces, such as the production of emulsions, drug delivery systems, pharmaceuticals and cosmetics, lubrication and oil recovery. Moreover, for basic research, the kinetics and mechanisms of the surfactant adsorption are also powerful tools to investigate the structure of adsorbed layers of surfactants [14-21] and the molecular interactions at the liquid interfaces [18-20].

If an interface is generated between a bulk aqueous solution, containing a surfactant, and a pure non-polar solvent, the adsorption of the surfactant at the interface occurs. This adsorption is not instantaneous since it implies the diffusion of surfactant molecules from the bulk solution towards the interface and at the interface the adsorption itself takes place by traversing a potential adsorption barrier. The time dependence of surfactant adsorption is complicated also by desorption processes.

If the rate of adsorption and desorption processes is high as compared to the diffusion, the adsorption may be considered as being diffusion-controlled. On the other hand, if the diffusion is assumed to be fast as compared to the transfer between the subsurface and interface, the process will be kinetic-controlled or barrier-controlled [1-3]. Both steps are taken into account in mixed kinetic controlled models.

Local anesthetics are widely used in the anesthesia processes and the molecular mechanism of their action is not fully understood. However, the anesthesia mechanism has been generally based on the anesthetics interactions with biological membranes. Several properties of plasma membranes seem to be modulated by anesthetics, such as, the lipid membrane structure [18-25], where the adsorption of anesthetics molecules at liquid interfaces is an essential step.

One of the goals of this study is to develop a kinetic model and to apply it to the adsorption of the two local anesthetics, namely dibucaine and tetracaine, from aqueous bulk solutions to the interface with pure benzene. The interest for this type of studies is recently increased because the oil/water interface (e.g., benzene/water) is generally considered as a model for biological membranes.

THEORETICAL MODELS FOR ADSORPTION

Diffusion Controlled Adsorption Kinetics

The quantitative model for the adsorption kinetics controlled by diffusion of surfactants from the bulk solution to the freshly formed liquid interface was proposed first by the Ward and Tordai [4]:

$$\Gamma(t) = 2 \left(\frac{D}{\pi} \right)^{1/2} \left\{ c_0 t^{1/2} - \int_0^{t^{1/2}} c_s(t-\tau) d\tau^{1/2} \right\} \quad (1)$$

where $\Gamma(t)$ represents the surfactant adsorption at the time t , D is the diffusion coefficient, π is 3,1415..., c_0 is the bulk solution concentration far from the liquid interface, c_s represents the subsurface concentration and τ is a dummy variable ranging from 0 to t .

The direct application of this theory is rather complicated. However, some *asymptotic approximations* were derived and commonly used [5], namely:

for $t \rightarrow 0$, a *short time approximation* results:

$$\Gamma(t) = 2 c_0 \left(\frac{D}{\pi} \right)^{1/2} t^{1/2} \quad (2)$$

and for $t \rightarrow \infty$, a *long time approximation* [5 - 9] was derived, called also the *Joos relationship*:

$$\Delta\sigma(t)_{t \rightarrow \infty} = \sigma(t) - \sigma_e = \frac{RT\Gamma^2}{2c_0} \left(\frac{\pi}{Dt} \right)^{1/2} \quad (3)$$

Joos equation can be also written as:

$$\left[\frac{d\sigma(t)}{d(1/\sqrt{t})} \right]_{t \rightarrow \infty} = \frac{RT\Gamma^2}{2c_0} \sqrt{\frac{\pi}{D}} \quad (4)$$

where R is the gas law constant, T is the temperature, $\sigma(t)$ and σ_e are the dynamic and the equilibrium surface tensions, respectively. The Eq. (3) is the theoretical basis for the extrapolation $\sigma_e = \sigma(t^{-1/2})_{t \rightarrow \infty}$ and the intersection

with the ordinate is frequently used as the equilibrium interfacial tension value. The linear relationship between $\sigma(t)$ and $1/\sqrt{t}$ remains valid only for a restricted period of time and it indicates that the adsorption process is controlled by diffusion.

Eq. (1) takes into account only the diffusion process and as boundary condition the conservation of mass at the interface. Since the subsurface concentration c_s is unknown, Eq. (1) is not alone suitable to predict the surfactant adsorption with time. Frequently, one assumes a local equilibrium between the liquid interface and the *subsurface* (i.e., the *adjacent layer* only a few angstroms away from the interface and still belonging to the bulk phase).

Usually, it has been assumed that the relation between the experimental interfacial pressure and the surfactant adsorption curves is better described by the *Frumkin isotherm* than by the *Langmuir isotherm*. It is argued that the *Langmuir isotherm* does not consider mutual interactions [9] among the adsorbed molecules, and therefore, the *Frumkin isotherm* might be better to describe the experimental curves because it introduces such intermolecular interactions [12].

On the other hand, it is well known that the surfactant adsorption can be transformed into the mean molecular area of the surfactant. Keeping this in mind, we can conclude that the experimental curves of the interfacial pressure as a function of the mean molecular area can be quite well described by the surface state equations because they introduce the intermolecular interactions within the adsorbed layers at liquid interface as an adjustable parameter [26-31].

Langmuir Adsorption Kinetics

In some cases it is found that experimental data cannot be understood by a simple diffusion and one must drop the boundary condition of the local equilibrium and replace it by the *Langmuir kinetic equation* [10, 11]:

$$\frac{d\Gamma}{dt} = k_1 c_s \left(1 - \frac{\Gamma}{\Gamma_\infty} \right) - k_2 \frac{\Gamma}{\Gamma_\infty} \quad (5)$$

where, k_1 is the adsorption rate constant, k_2 is the desorption rate constant, and Γ_∞ represents the maximum adsorption or the maximum surface coverage by the surfactant molecules at the liquid interface.

In Eq. (5) the adsorption rate is presumed to be directly proportional with the subsurface concentration c_s and with the free interface. Also, Eq. (5) takes into account a desorption process, with a rate directly proportional with the interface occupied by the surfactant. The kinetic Eq. (5) assumes an ideal localized layer [10].

Eq. (5) is valid also at equilibrium, when $\frac{d\Gamma}{dt} = 0$, $\Gamma = \Gamma_e$ and $c_s = c_0$.

With these equilibrium conditions Eq. (5) can then be rewritten as:

$$k_1 c_0 = \frac{k_1 c_0 + k_2}{\Gamma_\infty} \Gamma_e = k \Gamma_e \quad (5')$$

For some cases, with surfactant concentration high enough, a diffusion equilibrium can be thought to be established, involving $c_s = c_0$. In this case, the combination [11] of Eqs. (5) and (5') results in:

$$\frac{d\Gamma}{dt} = -k(\Gamma - \Gamma_e)$$

relationship and by its integration yields:

$$\Delta\Gamma = \Delta\Gamma_0 e^{-kt} \quad (6)$$

with $\Delta\Gamma = \Gamma - \Gamma_e$, $\Delta\Gamma_0 = \Gamma_0 - \Gamma_e$, where Γ_0 stands for the adsorption at $t = 0$, i.e. $\Gamma_0 = 0$.

In the situation that, the increase of adsorption is proportional to the decrease of interfacial tension, Eq. (6) may be written as:

$$\Delta\sigma = \Delta\sigma_0 e^{-kt} \quad (6')$$

or in a logarithmic form gives:

$$\ln \frac{\Delta\sigma_0}{\Delta\sigma} = \ln \frac{\sigma_0 - \sigma_e}{\sigma - \sigma_e} = kt \quad (7)$$

where σ , σ_e and σ_0 stand for the actual, for the equilibrium interfacial tension, and for the interfacial tension in the absence of the surfactant, respectively.

In the present paper two local anesthetics, viz. dibucaine and tetracaine have been studied by measuring dynamic interfacial tension values at the benzene/water interface and for the beginning Eq. (7) has been tested.

EXPERIMENTAL

The two local anesthetics used, dibucaine (2-butoxy-N-[2-(diethylamino)ethyl]-4-quinoline carboxamide hydrochloride) and tetracaine (4-butyl amino benzoic acid 2-(dimethyl amino)ethyl ester hydrochloride), both synthetic commercial products of high purity (minimum 99%) were purchased from Sigma. Benzene pro-analysis was purchased from Merck. All chemicals were used without further purification. Twice-distilled water of pH 2 was used, containing 0.01 mole dm^{-3} hydrochloric acid. Volumetric aqueous solutions of HCl pro-analysis were purchased from Reactivul Bucharest.

In order to study the anesthetic adsorption at the same liquid interface the benzene/water of pH 2 systems were chosen. At pH 2, dibucaine and tetracaine may exist in three forms: uncharged (free base) and charged ones, *i.e.*, monocation (mono-protonated) and dication (diprotonated) molecules. The calculations show at pH 2, that the dibucaine is almost in mono-protonated form, and the tetracaine is a mixture of monocation (45%, mono-protonated) and dication (55 %, di- protonated) molecular species [32]. At pH 2, the molecular species of anesthetics existing in the aqueous solutions are completely insoluble in the bulk benzene phase. Therefore, any transport across the benzene/water interface can be neglected. The pH of aqueous solutions was constant during all experiments and it was measured by an MV-84 type pH-meter by using a glass electrode.

Dynamic interfacial tensions in the time range from 1 minute up to 90 minutes for the aqueous solutions (pH 2) of various anesthetic concentrations at the interface with pure benzene were measured by pendant drop method described by us elsewhere[21, 33]. The shape of drops was recorded on a highly quality film in order to determine the characteristic drop diameters. By using a computer program in Basic language the dynamic interfacial tension values were finally determined.

Experimental data obtained by the pendant drop technique were compared with the data obtained by ring method, that was described by us previously [34-36]. The agreement between the two methods is excellent and the deviations do not exceed the error of the individual method. The accuracy of interfacial tension measurements was ± 0.1 mN/m, in agreement with literature data [1,6]. All measurements were performed at constant temperature of 20 ± 0.1 °C.

RESULTS AND DISCUSSION

Dynamic interfacial tension values, together with the equilibrium values are presented in Tab. 1

In order to test the validity of Eq. (7), the left hand side, denoted as y , has been calculated by using experimental σ values presented in Tab. 1 as well as their equilibrium values σ_e corresponding to $t = \infty$, and by taking $\sigma_0 = 34.7$ mN/m.

The plot of y vs. t exhibits a quite good linearity, although the straight lines do not pass through the origin of the coordinate system, *i.e.*, actually Eq. (7) is of the following form:

$$y = \ln \frac{\sigma_0 - \sigma_e}{\sigma - \sigma_e} = a + kt \quad (7')$$

By performing a linear regression, the parameters a and k have been determined. Results are presented, together with the correlation coefficient, in Table 2. In the last column n indicates the number of experimental points used in the linear regression.

Table 1
Dynamic interfacial tensions (mN/m) at the benzene/water interface

Anesthetics t , min	Dibucaine			Tetracaine		
	C_0 , mole dm^{-3}					
	0.001	0.005	0.010	0.001	0.005	0.010
1	31.9	28.7	26.4	32.8	31.1	29.9
2	31.1	27.1	24.25	31.85	30.53	28.95
3	30.2	25.4	22.2	31.7	29.2	27.5
4	29.7	24.6	20.8	31.3	28.75	27.0
5	29.2	23.5	20.0	31.1	28.2	26.2
6	28.8	23.1	19.2	30.8	27.72	25.9
7	28.4	22.1	18.6	30.7	27.5	25.3
8	28.1	21.85	18.15	30.5	27.2	25.1
9	27.8	21.2	17.5	30.3	27.0	24.7
10	27.5	20.9	17.3	30.1	26.7	24.5
11	27.3	20.4	16.8	30.0	26.6	24.3
12	27.0	20.1	16.6	29.9	26.4	24.0
13	26.9	19.7	16.2	29.8	26.3	23.9
14	26.6	19.4	16.0	29.6	26.1	23.8
15	26.5	19.2	15.8	29.5	26.0	23.7
∞	26.0	18.6	15.6	29.3	25.6	23.3

Table 2.
The a and k parameters of Eq. (7').

Anesthetics	C_0 mole dm^{-3}	a	k min^{-1}	r	n
Dibucaine	0.001	0.152	0.169	0.9932	15
	0.005	0.202	0.190	0.9918	15
	0.010	0.284	0.234	0.9909	14
Tetracaine	0.001	0.342	0.154	0.9966	13
	0.005	0.340	0.176	0.9974	14
	0.010	0.330	0.199	0.9984	15

As seen from Tab. 2, the a values are rather far from zero. This means that the *basic hypothesis* used at the deriving of Eq. (7) is not perfectly valid, presumably the diffusion equilibrium is not yet established and the boundary condition $c_s = c_0$ is not fulfilled. Nevertheless, from the k values reported in Tab. 2, some conclusions can be drawn. As seen, with the increasing C_0 the obtained k values are also increased. According to Eq. (5') written as follows:

$$k = \frac{k_1}{\Gamma_\infty} C_0 + \frac{k_2}{\Gamma_\infty} \quad (8)$$

it is clear that the plot of k vs. C_0 exhibits indeed an acceptable linearity. The k_1/Γ_∞ and k_2/Γ_∞ values and the corresponding correlation coefficients are presented in Table 3.

Table 3.

Relative adsorption and desorption rate constants derived from k values, given in Table 2.

Anesthetics	k_1/Γ_∞ dm ³ mole ⁻¹ min ⁻¹	k_2/Γ_∞ min ⁻¹	r
Dibucaine	7.25	0.159	0.9914
Tetracaine	4.99	0.149	0.9988

Inspection of Tab. 3 shows the quite good agreement with Eq. (8). The relative rate constant values are rather reasonable. The k_1 values are much higher than the k_2 ones, pleading for a high interfacial activity of these local anesthetics in good agreement with their behavior at liquid interfaces.

In the Ward and Tordai Eq. (1) the second term, the back diffusion integral being neglected, one obtains:

$$\Gamma = 2 \left(\frac{D}{\pi} \right)^{1/2} \cdot c_0 t^{1/2} \quad (9)$$

It is to be noted that the Eq. (9) coincides with the *short time approximation* given by the Eq. (2).

At the other hand, by performing an integration by parts of Eq. (1), and by neglecting the remaining integral, one obtains:

$$\Gamma = 2(c_0 - c_s) \left(\frac{D}{\pi} \right)^{1/2} t^{1/2} \quad (10)$$

Clearly, both Eqs. (9) and (10) suggest a proportionality of the adsorption with $t^{1/2}$.

In order to establish a correlation between the adsorption and the interfacial tension σ or the interfacial pressure Π , frequently, the surface state equation:

$$\Pi A = kT \text{ or } \Pi = \Gamma kT \quad (11)$$

is used, which is the two dimensional analog of the perfect gas state equation. A represents the molecular area ($A = 1/\Gamma$) and Γ is the surfactant adsorption expressed in molecules per unit interface.

By combining Eq. (11) with Eqs. (9) and (10), respectively, one obtains:

$$\Pi = 2kT \left(\frac{D}{\pi} \right)^{1/2} c_0 t^{1/2} \quad (12)$$

and

$$\Pi = 2kT \left(\frac{D}{\pi} \right)^{1/2} (c_0 - c_s) t^{1/2} \quad (13)$$

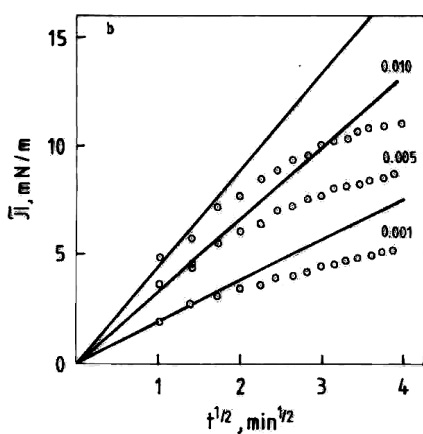


Fig. 1. Experimental dynamic interfacial pressures of dibucaine aqueous solutions as a function of $t^{1/2}$ at the interface benzene/water. Figures indicate the dibucaine bulk concentration C_0 in mole dm^{-3} .

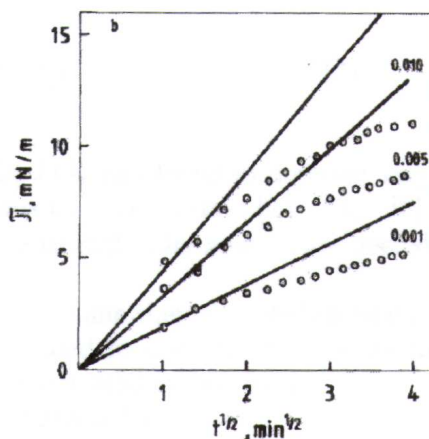


Fig. 2. Experimental dynamic interfacial pressures of tetracaine aqueous solutions as a function of $t^{1/2}$ at the benzene/water interface. Figures indicate the tetracaine bulk concentration C_0 in mole dm^{-3} .

In order to test the validity of Eqs. (12) and (13) we performed an analysis of the experimental Π vs. $t^{1/2}$ data. Experimental Π values, calculated from σ_0 and from σ values given in Tab. 1, are presented in Figs. 1-2, plotted vs. $t^{1/2}$ values, for dibucaine and tetracaine, respectively.

If the relations (12) or (13) were valid, the Π vs. $t^{1/2}$ curves would exhibit a linear portion at least at small t values. This is why the tangency to the curve for $t = 0$ was constructed in Figs. 1 and 2. It is to be noted that the experimental curves exhibit an important negative deviation from these straight lines. This means that a better approach is needed to describe the behavior of anesthetics at the oil/water interfaces.

Deriving of a New Diffusion Controlled Kinetic Equation

Eqs. (12) and (13) have been obtained by presuming the state equation (11) to be valid. But interfacial monolayers do not obey Eq. (11). One of the best state equations [21, 26-31] proposed for the surfactant monolayers at the liquid interfaces is of the following form:

$$\left(\Pi + \frac{\alpha}{A^{3/2}} \right) (A - A_0) = kT \quad (14)$$

where A stands for the mean molecular area. Eq. (14) was found to describe very well the compression isotherms of miscellaneous monolayers [21, 28, 30], especially if the interaction parameter α and the own molecular area A_0 are treated as adjustable parameters.

Because the equilibrium data for another local anesthetics, *namely* procaine [30], are well described by the Eq. (14) we decided to consider this model to describe the experimental data for the local anesthetics used in this study.

From the state equation (14), Π may be expressed as:

$$\Pi = \frac{kT}{A - A_0} - \frac{\alpha}{A^{3/2}} = \frac{kT\Gamma}{1 - \Gamma A_0} - \alpha\Gamma^{3/2} \quad (15)$$

Let us denote:

$$x = 2(c_0 - c_s) \left(\frac{D}{\pi} \right)^{1/2} \quad (16)$$

Eq. (10) may be written as $\Gamma = xt^{1/2}$. Thus, by combining Eqs. (10), (14) and (16), one obtains:

$$\Pi = \frac{kTxt^{1/2}}{1 - A_0xt^{1/2}} - \alpha x^{3/2} t^{3/4} = kTx \left[\frac{t^{1/2}}{1 - A_0xt^{1/2}} - \frac{\alpha x^{1/2}}{kT} t^{3/4} \right] \quad (17)$$

One may expect Eq. (17) to describe better the time dependence of Π , than Eq. (13) does.

In order to study the properties and possibilities of Eq. (17), let us introduce a reduced time scale. If in an experiment Π has been followed from $t = 0$ up to a maximum time t_m , a reduced time can be defined as:

$$\tau = \frac{t}{t_m} \quad (18)$$

By combining Eqs. (17) and (18) one obtains:

$$\Pi = kT \chi t_m^{1/2} \left[\frac{\tau^{1/2}}{1 - A_0 \chi t_m^{1/2} \tau^{1/2}} - \frac{\alpha \chi^{1/2}}{kT} t_m^{1/4} \tau^{3/4} \right] \quad (19)$$

This equation may be written as:

$$\Pi = a \left[\frac{\tau^{1/2}}{1 - b\tau^{1/2}} - c\tau^{3/4} \right] = a\varphi(\tau) \quad (20)$$

with:

$$a = 2kT(c_0 - c_s) \left(\frac{Dt_m}{\pi} \right)^{1/2}$$

$$b = 2A_0(c_0 - c_s) \left(\frac{Dt_m}{\pi} \right)^{1/2}$$

$$c = \frac{2^{1/2} \alpha (c_0 - c_s)^{1/2}}{kT} \left(\frac{Dt_m}{\pi} \right)^{1/4}$$

From the Eq. (20), of the parameters a , b and c , one obtains:

$$D = \left[\frac{a}{2kT(c_0 - c_s)} \right]^2 \frac{\pi}{t_m}; \quad A_0 = \frac{kTb}{a}; \quad \alpha = \frac{c}{a^{1/2}} (kT)^{3/2} \quad (21)$$

It is clear that, if $t = t_m$, one has $\tau = 1$ and Eq. (20) becomes:

$$\Pi_m = a\varphi(1) = a \left[\frac{1}{1-b} - c \right] \quad (22)$$

Let us introduce also for the interfacial pressure a reduced scale:

$$\Pi^* = \frac{\Pi}{\Pi_m} \quad (23)$$

which according to Eqs. (20) and (22) can be expressed as:

$$\Pi^* = \frac{\Pi}{\Pi_m} = \frac{\varphi(\tau)}{\varphi(1)} \quad (24)$$

Thus one obtains finally for the time dependence of the interfacial pressure:

$$\Pi = \frac{\Pi_m}{\varphi(1)} \varphi(\tau) \tag{25}$$

By comparing Eq. (25) with Eq. (20) it is obvious that:

$$a = \frac{\Pi_m}{\varphi(1)} \tag{26}$$

In order to check the possibilities of Eq. (25), we studied the influence of the parameters b and c upon the shape of the Π/a vs. τ and Π^* vs. τ curves. For this purpose theoretic curves have been constructed. Some examples are given in Fig. 3.

In Fig. 3 the influence of parameter c upon the shape of the $\Pi/a = \varphi(\tau)$ vs. τ curves is illustrated, by taking the $b = 0.1$, as a constant value. The dashed line curve is the $\tau^{1/2}$ vs. τ plot, corresponding to the validity of Eqs. (12) or (13).

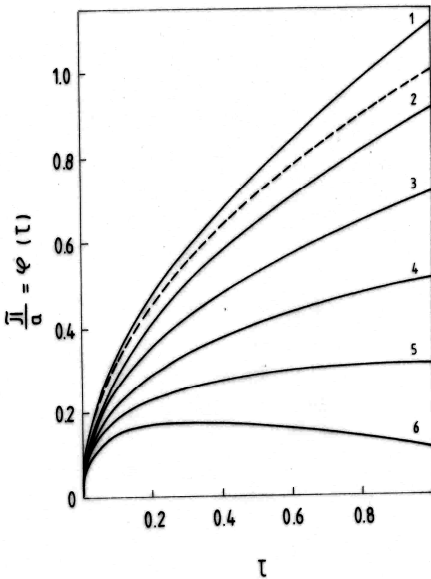


Fig. 3. Influence of the c parameter upon the theoretical $\varphi(\tau)$ vs. τ curves; $b = 0.1$; curve (1): c 0; (2) 0.2; (3) 0.4; (4) 0.6; (5) 0.8; (6) 1.0. Dashed line curve: $b = c = 0$.

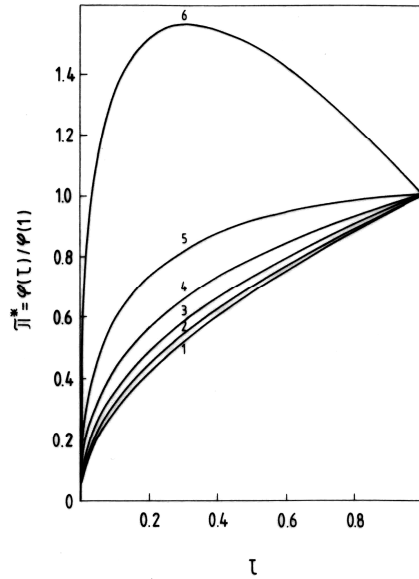


Fig. 4. Influence of the c parameter upon the theoretical Π^* vs. τ curves. b and c values as in Fig. 3

Since parameters b and c influence also the $\varphi(1)$ value, the shift of the theoretical curves makes their comparison more difficult. The influence of these parameters is more clear if the $\Pi^* = \varphi(\tau)/\varphi(1)$ vs. τ curves are constructed. This is shown in Fig. 4.

It is worth mentioning that for $b = 0.1$ and $c = 1.0$ both $\varphi(\tau)$ and Π^* exhibit a maximum for about $\tau = 0.3$. This would imply the appearance of a maximum interfacial pressure at a certain time, followed by the diminution of Π . This is of course unrealistic. It is obvious that not all $b - c$ pairs can describe real adsorption kinetics. Although not all $\varphi(\tau)$ functions correspond to real behavior of surfactants the main feature is that in the case of diffusion controlled adsorption the own molecular area A_0 and the intermolecular interactions expressed by the parameter α may account for both positive and negative deviations from the $t^{1/2}$ law.

The deviation of the reduced surface pressure from the $t^{1/2}$ law may be expressed by the function:

$$\Delta = \frac{\varphi(\tau)}{\varphi(1)} - \tau^{1/2} \tag{27}$$

The influence of the c parameter upon the theoretical Δ vs. τ curves is illustrated in Fig. 5.

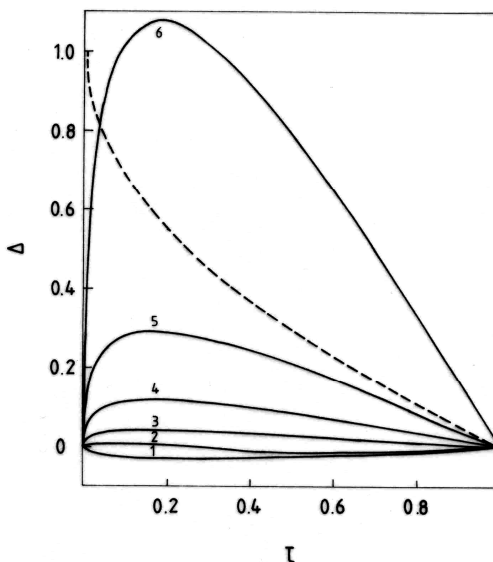


Fig. 5. Influence of the c parameter upon the theoretical Δ vs. τ curves. b and c parameters as in Fig. 3.

It is obvious that both positive and negative Δ values may appear and the deviation from the $t^{1/2}$ law may be very important.

In real systems, as seen in Figs. 1 and 2 with increasing time negative deviations from the $t^{1/2}$ law appear. In a Π^* vs. τ plot this means that the curve is more convex as compared to $\tau^{1/2}$, *i.e.* Δ has positive values. Consequently, negative Δ values indicate unrealistic theoretical curves. Even

the positive values have an upper limit, it is easy to see that the Π vs. t curve passes through a maximum if $\Delta > 1 - \tau^{1/2}$. The dashed line curve in Fig. 5 indicates this upper limit $\Delta = 1 - \tau^{1/2}$.

Adsorption Dynamics of Dibucaine and Tetracaine at the Benzene/Water Interface

In order to derive the parameters a , b and c we adopted the following procedure of working up the experimental data given in Tab. 4. We choose $t_m = 15$ min in the case of both local anesthetics and calculated for each experimental point the reduced parameters τ and Π^* . Further we calculated, for the found τ values, the theoretical Π^* values by taking certain $\underline{b} - \underline{c}$ pairs. In the *first approach* we took $b = 0$ and calculated theoretical Π^* values for different c ones. In the case of each c value the *standard deviation* (noted Δ) of the experimental Π^* values from the theoretical ones was calculated. By means of a systematic variation of c the minimum standard deviation was sought for.

Calculations were repeated, then, for other b values too. Thus, a *double minimization* of the standard deviation has been performed and the $b - c$ pair ensuring the least value for the standard deviation has been taken for the most realistic parameter values. This calculation procedure is visualized in Fig. 6, for the aqueous solution of tetracaine for C_0 of 0.001 mole dm^{-3} at the interface with pure benzene.

Curve 1 gives the minimum standard deviation obtained for different b values presumed and curve 2 indicates the corresponding c value. Let us take e.g. $b = 0.062$. Eq. (24) allows us to calculate theoretical Π^* values corresponding to $b = 0.062$ and to different c values. In each case, *i.e.* with each c value presumed, the standard deviation:

$$\Delta = \sqrt{\frac{1}{n} \sum (\Pi_t^* - \Pi_e^*)^2} \quad (28)$$

is calculated where n stands for the number of points used, Π_t^* and Π_e^* stand for the theoretical and for the experimental reduced interfacial pressure, respectively. By trying different \underline{c} values, one observes that the standard deviation will be the less for $c = 0.559$, *viz.* it will be equal to $\Delta = 0.00473$. Thus, we obtained a point on curve 1 and a point on curve 2.

By repeating these calculations for other \underline{b} values, eventually one obtains the whole curves 1 and 2. As seen, curve 1 has a minimum (indicated by a downward vertical arrow), corresponding to $b = 0.0697$; this *minimum* of the Δ value is ensured by the c value equal to 0.571 (indicated on the curve 2 by an upward vertical arrow).

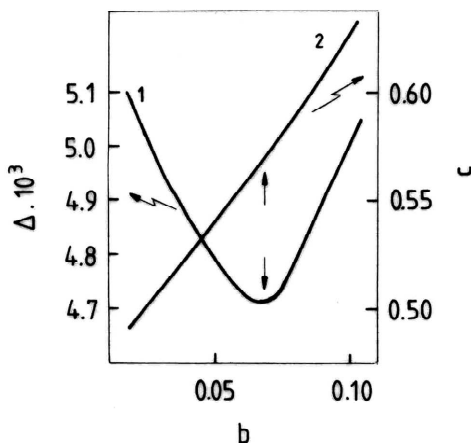


Fig. 6. Deriving of b and c parameters for tetracaine aqueous solution of $C_0=0.001$ mole dm^{-3} at the interface with pure benzene.

Table 4.
Parameters of Eq. (20) derived from our experimental data. C_0 is expressed in mole dm^{-3} .

Anesthetics	C_0	t_m min	Π_m mN/m	$\varphi(1)$	a	b	c	Δ mN/m
Dibucaine	0.001	15	8.2	0.5926	13.84	0	0.407	0.0028
	0.005	15	15.5	0.4863	31.87	0.0039	0.518	0.0029
	0.010	15	18.9	0.4096	46.14	0	0.590	0.0014
Tetracaine	0.001	15	5.2	0.5042	10.31	0.0697	0.571	0.0047
	0.005	15	8.7	0.4328	20.10	0.0465	0.616	0.0025
	0.010	15	11.0	0.4135	26.60	0	0.586	0.0028

By using the obtained b and c values, $\varphi(1)$ may be easily calculated according to Eq. (22), as well as the parameter a by means of Eq. (26). Results obtained by means of this procedure are presented in Tab. 4.

The parameter values given in Tab. 4 allow us to construct by means of Eq. (20) theoretical Π vs. t curves. These curves are given in Figs. 7 and 8 as full line curves. Thus, it is clear that Eq. (20) describes very well the experimental curves.

Inspection of Tab. 4 shows that with a given anesthetic the a parameter increases with increasing bulk concentration C_0 . The c parameter shows also a clear increasing tendency. The b parameter has very small values, frequently vanishing ones and cannot be correlated with C_0 values.

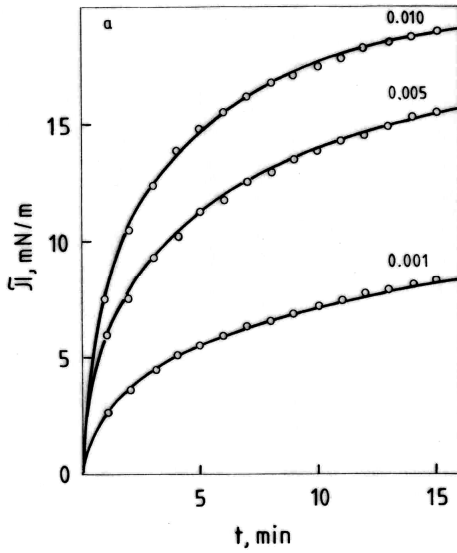


Fig. 7. Data as in Fig.1 represented function of time.

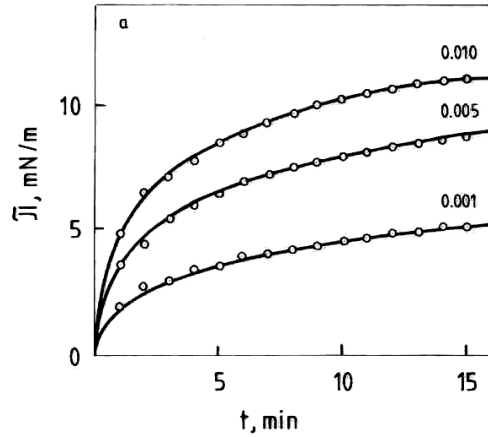


Fig. 8. Data as in Fig. 2 represented as a function of time.

With respect to the meaning of the parameter a , according to Eq. (21), it allows us to calculate the diffusion coefficient D . Let us assume as a *first approach* that $C_s = 0$ at all bulk concentrations C_0 . By taking into account that c_0 represents the bulk concentration expressed in molecules cm^{-3} , and C_0 is given in mole dm^{-3} , one has $c_0 = C_0 \cdot 10^{-3} N_A$, where N_A stands for Avogadro's constant. Thus, Eq. (21) becomes:

$$D = \left(\frac{a}{2kT \cdot 10^{-3} \cdot N_A \cdot C_0} \right)^2 \frac{\pi}{t_m} \quad (29)$$

The diffusion coefficients calculated by means of Eq. (29) and by using the a values given in Tab. 4, are presented in Tab. 5.

By inspecting the D values (Tab 5) one can see that the D values are of the same order of magnitude and show a slight decreasing tendency with increasing bulk concentration. Moreover, in the case of aqueous anesthetic solutions of the same anesthetic concentration of $0.001 \text{ mole dm}^{-3}$, the D value of dibucaine is less than two times higher than that of tetracaine.

Table 5.

Diffusion coefficients D , subsurface concentrations C_s and interaction parameters α calculated from the a and c parameters of Eq. (20).

Anesthetics	C_0 mole dm^{-3}	$D \cdot 10^{10}$ $\text{cm}^2 \cdot \text{s}^{-1}$	$D_0 \cdot 10^{10}$ $\text{cm}^2 \cdot \text{s}^{-1}$	$C_s \cdot 10^3$ mole dm^{-3}	$\alpha \cdot 10^{22}$ dyne $\cdot \text{cm}^2$
Dibucaine	0.001	2.84	2.84	0	8.90
	0.005	0.602		2.70	7.46
	0.010	0.316		6.67	7.07
Tetracaine	0.001	1.58	1.58	0	14.4
	0.005	0.240		3.05	11.2
	0.010	0.105		7.42	9.25

As a *second approach* we shall presume that this relation $C_s = 0$ is valid only in the case of anesthetic aqueous solutions of $C_0 = 0.001$ mole dm^{-3} and that the C_s value increases with increasing bulk concentration C_0 , but the diffusion coefficient remains the same D_0 as obtained from the a value for the aqueous anesthetic solution of 0.001 mole dm^{-3} . In this assumption C_s may be calculated from Eq. (21) and one obtains:

$$C_s = C_0 - \frac{\pi^{1/2} \cdot a}{2kT \cdot 10^{-3} \cdot N_A \cdot D_0^{1/2} \cdot t_m^{1/2}} \quad (30)$$

Results are presented in the same Tab. 5. The C_s values obtained seem to be quite realistic and the C_s values increase systematically with increasing C_0 values.

Eq. (21) allows also the calculation of the interaction parameter α from the parameters a and c of Eq. (20). Results are presented also in Tab. 5. As seen one does not obtain the same value in the case of differing bulk concentrations, *viz.* a decreasing tendency is observed with increasing C_0 . This might be due to experimental errors, to the interfacial active impurities, and/or to the imperfection of the model. However, by calculating the mean α values, some properties of the adsorbed monolayers of anesthetics at the benzene/water interface can be evidenced. Therefore, the mean α value is calculated; for dibucaine is $\alpha = 0.78 \cdot 10^{-21}$ dyne $\cdot \text{cm}^2$, and for tetracaine is $\alpha = 1.16 \cdot 10^{-21}$ dyne $\cdot \text{cm}^2$.

The higher α value of tetracaine as compared to that of dibucaine seems to be reasonable. Inspecting their molecular structures one can see that with dibucaine steric factors hinder the close packing of the molecules, consequently the intermolecular attraction will be weaker as compared to tetracaine. At the other hand the polar headgroup of dibucaine has a higher

polarity than that of tetracaine. This can be seen from the acidity constant of the protonated species. In the case of tetracaine one has $pK = 8.15$ but with dibucaine $pK = 10.19$ [32]. This means that the polar headgroup of dibucaine anchored into the water phase, due to its higher proton affinity will be more hydrated as compared to the tetracaine, entailing a weaker intermolecular attraction.

CONCLUSIONS

The diffusion controlled kinetics Eq. (20) proposed by us seems to describe very well the adsorption dynamics of dibucaine and tetracaine at the benzene/water interface. Because, the deviations of the experimental points from the calculated curves (Figs 7 and 8.) are within the limit of experimental accuracy, this refinement was further pursued.

Finally, the Eq. (21) allows us to obtain the diffusion coefficients, the subsurface concentrations and the interaction parameters α , for the adsorption dynamics of dibucaine and tetracaine at the benzene/water interface.

REFERENCES

1. R. Miller, P. Joos and V. B. Fainerman, *Advances in Colloid and Interface Science*, **49**, 249-302 (1994).
2. C. H. Chang and E. I. Franses, *Colloids Surfaces A: Physicochem. Eng. Aspects*, **100**, 1-45 (1995).
3. L. Liggieri, F. Ravera and A. Passerone, *Colloids Surfaces A: Physicochem. Eng. Aspects*, **114**, 351 (1996).
4. F.H. Ward and L. Tordai, *J. Chem. Phys.* **14**, 453 (1946).
5. G. Czichocki, A. V. Makievski, V. B. Fainerman and R. Miller, *Colloids Surfaces A: Physicochem. Eng. Aspects*, **122**, 189 (1997).
6. J. Li, V. B. Fainerman and R. Miller, *Langmuir*, **12**, 5138 (1996).
7. E. Rillaerts and P. Joos, *J. Phys. Chem.*, **96**, 3471 (1982).
8. R. Van den Bogaert and P. Joos, *J. Phys. Chem.*, **83**, 2244 (1979).
9. J. Li, R. Miller and H. Mohwald, *Colloids Surfaces A: Physicochem. Eng. Aspects*, **114**, 113 (1996).
10. P. Joos, G. Bleys and G. Petre, *J. Chim. Phys.*, **79**, 387 (1982).
11. P. Joos and G. Serrien, *J. Colloid Interface Sci.*, **127**, 97 (1989).
12. S. S. Dukhin, G. Kretzschmar and R. Miller, "Dynamics of Adsorption at Liquid Interfaces: Theory, Experiment, Application", in *Studies of Interface Science*, D. Mobius and R. Miller, Eds., Elsevier, Amsterdam, 1995, Vol. 1.

13. V. B. Fainerman, S. A. Zholob, R. Miller and P. Joos, *Colloids Surfaces A: Physicochem. Eng. Aspects*, **143**, 243 (1998).
14. J. F. Baret, *J. Chim. Phys.*, **65**, 895 (1968).
15. M. Tomoaia-Cotisel, E. Chifu, A. Mocanu, J. Zsako, M. Salajan and P.T. Frangopol, *Rev. Roum. Biochim.*, **25**, 227 (1988).
16. M. Tomoaia-Cotisel, J. Zsako, E. Chifu, P.T. Frangopol, W. A. P. Luck and E. Osawa, *Rev. Roum. Biochim.*, **26**, 305 (1989).
17. E. Chifu, M. Tomoaia-Cotisel, J. Zsako, I. Albu, A. Mocanu and P.T. Frangopol, *Rev. Roum. Chim.*, **35**, 879 (1990).
18. M. Tomoaia-Cotisel, *Progr. Colloid Polym. Sci.*, **83**, 155 (1990).
19. J. Zsako, M. Tomoaia-Cotisel, E. Chifu, A. Mocanu and P.T. Frangopol, *Biochim. Biophys. Acta*, **1024**, 227 (1990).
20. M. Tomoaia-Cotisel and D. A. Cadenhead, *Langmuir*, **7**, 964 (1991).
21. M. Tomoaia-Cotisel, J. Zsako, A. Mocanu, E. Chifu, M. Salajan and S. Bran, *J. Colloid Surface Chem.*, **3**, 32 (1999).
22. Asgharian, D. A. Cadenhead and M. Tomoaia-Cotisel, *Langmuir*, **9**, 228 (1993).
23. T. Hata, H. Matsuki and S. Kaneshina, *Biophys. Chem.*, **87**, 25 (2000).
24. P. T. Frangopol and D. Mihailescu, *Colloids Surfaces B: Biointerfaces*, **22**, 3 (2001).
25. I. Yun, E. S. Cho, H. O. Jang, U. K. Kim, C. H. Choi, I.K. Chung, I. S. Kim and W. G. Wood, *Biochim. Biophys. Acta*, **1564**, 123 (2002).
26. J. Guastalla, *Cahiers Phys.* **10**, 30 (1942).
27. J. Guastalla, *J. Chim. Phys.* **43**, 184 (1946).
28. L. Ter Minassian-Saraga, *J. Chim. Phys.* **52**, 80 (1955).
29. E. Chifu, J. Zsakó and M. Tomoaia-Cotișel, *J. Colloid Interface Sci.*, **95**, 346 (1983).
30. J. T. Davies and E. K. Rideal, "Interfacial Phenomena", *Second Edition*, Academic Press, New York, *Chapter 5*, pp. 217 - 281, (1963).
31. M. Tomoaia-Cotișel, J. Zsako and E. Chifu, *Stud. Univ. Babeș-Bolyai, Chem.*, **33** (2), 54 (1988).
32. J. Zsakó, M. Tomoaia-Cotișel, I. Albu, A. Mocanu, E. Chifu and P.T. Frangopol, *Rev. Roum. Biochim.* **28**, 33 (1991).
33. E. Chifu, M. Sălăjan, J. Demeter-Vodnár and M. Tomoaia-Cotișel, *Rev. Roumaine Chim.*, **32**, 683 (1987).
34. M. Tomoaia-Cotișel, *Ph. D. Thesis*, "Babeș-Bolyai" Univ., 1979.
35. E. Chifu, M. Tomoaia, E. Nicoara and A. Olteanu, *Rev. Roum. Chim.*, **23**, 1163.
36. M. Tomoaia-Cotișel, I. Albu and E. Chifu, *Stud. Univ. Babeș-Bolyai, Chem.* **24** (2), 68 (1979).

PHOTOELECTROCHEMICAL PHENOMENA ON SEMICONDUCTOR REDOX GLASS ELECTRODES

ELISABETA VERESS^a, VICTOR LITEANU^a, IULIU O. MARIAN^b,
ANDREEA OLTEAN^b

"Babeș-Bolyai" University, Faculty of Chemistry and Chemical Engineering

*^a Department of Inorganic Chemistry, ^b Department of Physical Chemistry,
11 Arany Janos Street, RO-3400 Cluj-Napoca.*

E-mail: iomar@chem.ubbcluj.ro

ABSTRACT. Photoelectrochemical properties of the $\text{SiO}_2\text{-Na}_2\text{O-B}_2\text{O}_3\text{-Fe}_2\text{O}_3\text{-FeO-Al}_2\text{O}_3$ semiconductor glass are investigated in order to evaluate the radiation contribution to the electrode potential of redox sensors. For this purpose the open circuit phototension was determined in the presence of the $\text{Fe}(\text{CN})_6^{3-} / \text{Fe}(\text{CN})_6^{4-}$ redox couple, depending on the incident radiation power and the working electrolyte pH, using 514.5 and 488.0 nm laser excitation. The nearly logarithmic shape of the $\Delta U_{\text{ph}}^{\text{oc}}\text{-P}$ function in visible domain (514.5 and 488.0 nm) corresponds to an Schottky junction.

Introduction

Partial substitution of $\text{SiO}_2\text{-Na}_2\text{O}$ or $\text{SiO}_2\text{-Li}_2\text{O}$ glasses by transition metal oxide that can exist in different redox state in glass results in the appearance of electronic conduction too. The predominance of one of the other conduction type depends on the nature and content of the substituent [1,2]. In the case of predominantly electronic conductor glasses transport mechanism is considered to be an activated electron transfer between the transition metal ions in different oxidative states. These glasses behave as n-type semi-conductors [2,5].

Semiconductors glass membranes exhibit redox sensitivity (redox potentiometric electrode function) if both the free electron activation energy (E_a) and the membrane electrical resistivity (ρ) are sufficiently low, namely, $E_a = 0,3$ eV and $\rho < 10^6$ ohmcm [2,4].

The following study evaluates the radiating contribution to the electrode response of $\text{SiO}_2\text{-Na}_2\text{O-B}_2\text{O}_3\text{-Fe}_2\text{O}_3\text{-FeO-Al}_2\text{O}_3$ glass electrodes used as potentiometric redox sensors.

Therefore, the photo response (phototension $\Delta U_{\text{ph}}^{\text{oc}}$ vs incident radiation power (P) of irradiated electrodes was determined in the presence of the $\text{Fe}(\text{CN})_6^{3-}/\text{Fe}(\text{CN})_6^{4-}$ redox couple, at different pH values of the support solution.

Experimental

Photoelectrochemical determinations were carried out using an electrochemical cell containing the redox glass working electrode and a Pt ring counter electrode.

Redox glass electrodes were constructed as follows: The 1,5-2mm thick semiconductor membranes were made from a $\text{SiO}_2\text{Na}_2\text{O-B}_2\text{O}_3\text{-Fe}_2\text{O}_3\text{-FeO-Al}_2\text{O}_3$ glass containing 8mol % of Fe_2O_3 and FeO. On the internal side of the membrane ohmic contact was assured through an Hg bridge. The external membrane surface's zonal control requirements were assured by polishing with $0,3\mu\text{ Al}_2\text{O}_3$ powder.

Working electrolytes were freshly mixed from 0.1 M $\text{K}_3[\text{Fe}(\text{CN})_6]$ and 0,1 M $\text{K}_4[\text{Fe}(\text{CN})_6]$ stock solution prepared in pH buffers of pH = 4,01 (0,05M KH phtalate); 6,86 (0,025M KH_2PO_4 + 0,025M Na_2HPO_4) and 9,18 (0,05M borax). Concentration ratios of oxidized and reduced species were fixed at [ox]:[red] = 1:100 (c_1) and 100:1 (c_2), respectively.

Determinations were made on normal light incidence. As light sources, Ar ion laser (488.0 and 514.5 nm) was utilized. Incident laser beam power (P) was varied between 20 and 120 mW for both wavelengths. The incident light power was measured with an LM-2 (Karl Zeiss) type power-meter.

Photo response ($\Delta U_{\text{ph}}^{\text{oc}}$) measurements were performed in open circuit conditions using fresh working solutions. The dark potential value (U_d) was measured at all times.

The pH response of the semiconductor glass electrode was determined between pH=1 and 12, in glycine - HCl and glycine - NaOH buffer solutions, respectively [prepared from 0.1 M glycine + 0.1M NaCl; 0.1M HCl and 0.1 NaOH stock solutions].

Electronic measurements were carried out with usual laboratory purpose digital pH meter (± 1 mV sensitivity).

All solutions were prepared from analytical grade reagents, in demineralised water.

Results and discussion

On basis of the experimental data corresponding to 514.5 and 488.0 nm (as seen below) it may be presumed that at relatively larger power values the $\Delta U_{\text{ph}}^{\text{oc}}\text{-P}$ function would become logarithmic.

Photo responses obtained at 514.5 and 488.0 nm approach the open circuit values ($\Delta U_{\text{ph}}^{\text{oc}}$) expected for an Schottky junction [6].

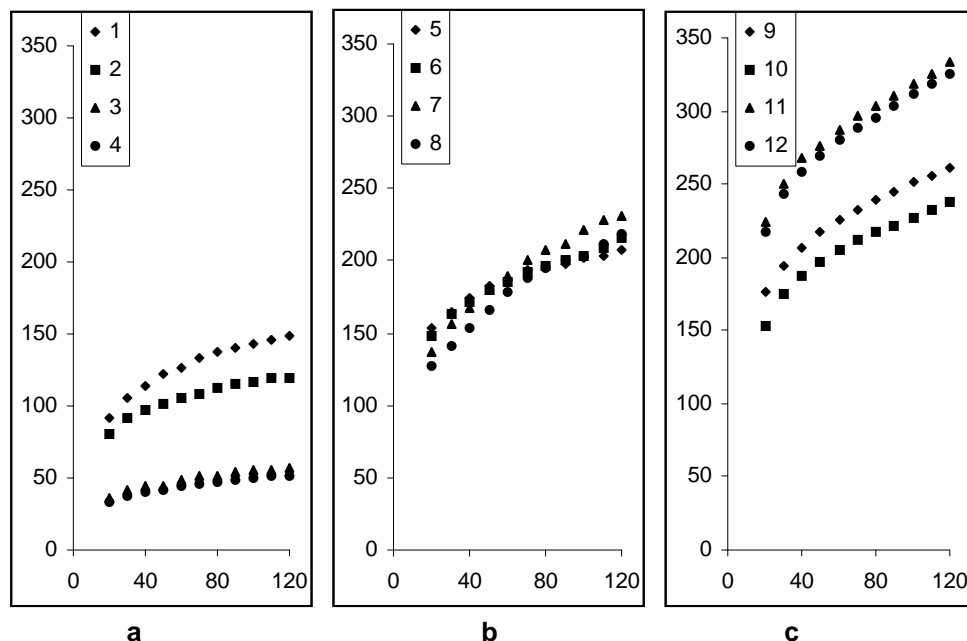


Fig. 1. Photo response ΔU_{ph}^{oc} (mV) vs P (mW) obtained at pH = 4 (a); pH = 6.9 (b); pH = 9.2 (c), using Ar ion laser excitation: c_1 solution at 488 nm (\blacklozenge); c_1 solution at 514,5 nm (\blacksquare); c_2 solution at 488 nm (\blacktriangle); c_2 solution at 514.5 nm (\bullet)

$$\Delta U_{ph}^{oc} = \beta_s k T e_0^{-1} \ln (j_L j_s^{-1} + 1) \quad (1)$$

The value of empirical coefficient β_s is determined by experimental conditions; current density j_L is proportional to the incident radiation power and j_s is the saturation current density, respectively.

The ΔU_{ph}^{oc} -P curves presented on Fig.1 have logarithmic shapes. In this powers range, experimental data fit fairly well the empirical expression:

$$\Delta U_{ph}^{oc} = K \ln (P + 1) \quad (2)$$

in accordance with eq. (1),considering that $P = const \cdot j_L$ and $K = j_s \cdot k T e_0^{-1}$

At power values larger than 100mW the shape of the ΔU_{ph}^{oc} -P curves is slightly changed, probably due to the interfering nonradiative effects occurring in the depletion region of the semiconductor surface.

The influence of the working solution's pH is considerable. The extent of the pH effect differs for solution c_1 and c_2 . Because of this, the succession of the nearly parallel curves c_1 and c_2 corresponding to the same wavelength on Fig. 1c (pH = 9.2) is inverted vs. that on Fig. 1a (pH = 4). At pH = 6.9, the very close curves intersect at about 50 mW (488.0 nm), and at about 95 mW (514.5nm), respectively (Fig.1b). From the table 1 the values of correlation coefficients r [7] are close to unit and represent a good choice of log-fits [7].

The relatively reduced differences observed between K values corresponding to the same solution at different wavelength of the incident radiation may be associated with the nonradiative effect. The pH influence acts through the modification of the empirical β_s coefficient and produces larger differences (see Table 1).

Table 1.

Values of K fitted from experimental data

Trial	Slope K / mV	Noise* / mV	$\angle r \angle$	100·r ² / %
1	30.93167	1.18	0.9979	99.57
2	25.62451	1.92	0.9881	97.63
3	11.86609	0.58	0.9963	97.27
4	10.78779	0.27	0.9990	99.80
5	45.08126	8.10	0.8830	77.97
6	45.26659	4.95	0.9709	94.26
7	46.98645	4.96	0.9869	97.40
8	43.69968	6.13	0.9789	95.82
9	54.93272	4.08	0.9883	97.68
10	49.72481	2.13	0.9967	99.33
11	69.94974	6.10	0.9833	96.68
12	68.22529	4.98	0.9890	97.80

* standard deviation of adequacy

The constancy of the potential values without laser excitation indicates that the effect of directly induced thermal modifications due to the nonradiative recombination effects with the bulk solution was negligible.

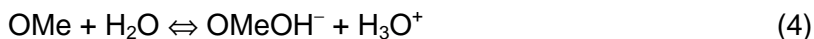
Redox potential values obtained with platinum measuring electrode in the working aqueous solutions agree with formerly published data [8]. The variation of the phototension with pH indicates that the effect observed on glass redox electrodes has other origin, correlated with the stability of electrodic surface.

In search of explanations, the $U = f(\text{pH})$ function has been determined for the studied glass electrodes in the range of 1 ÷ 12 pH (see Fig. 2). It shows a quite close resemblance with the pH dependence of the flatband potential of certain oxidic semiconductors [9], presenting a similar irregularity about pH = 7.

In case of oxidic semiconductors the flatband potential U_{fb} varies with the pH of solution in accordance with the Gerischer equation [9]:

$$-\partial U_{fb}/\partial \text{pH} = 2,3 kT e_0^{-1} / [1 + (kT e_0^{-1}) (C_H e_0^{-1}) (N_{MeOH^+} + N_{OMeOH^-})^{-1}] \quad (3)$$

C_H is the Helmholtz capacitance and N_{MeOH^+} , N_{OMeOH^-} are the concentrations of charged species on oxidic semiconductor surfaces according to the following adsorption equilibria:



MeO and OMe being the disposable (active) surface adsorption centres.

Therefore, the $U_{f,b}$ – pH dependence is determined by the changes produced in the chemical activity (a) of the charged species adsorbed on the semiconductor surface.

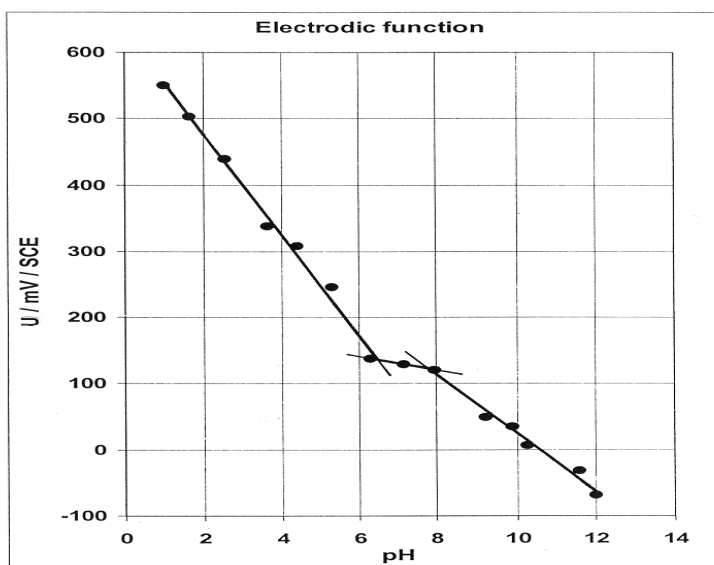


Fig. 2. The pH response of the semiconductor glass studied

It may be considered that similarly, in the case of semiconductor oxidic glasses, the modification of the potential is determined by the surface – adsorbed charged species (H_3O^+ and OH^-) concentration, which similarly, beside the pH, depends on the global composition of the working solution and the discreteness of charge effect. The electroodic function present three domain in pH units (1;6.54), (6.54;7.78) and (7.78;12). In alkaline domain because of considerable change of chemical activity with of amount of surface charge (see second term of denominator in eq. 3) the slope of potential vs pH is 43.89 mV/pH, and a good functional dependence ($R=0.992$). The great values 75.37 mV/pH in the acidic range ($R=0.996$) indicate another aspect related by the "discreteness of charge effect". This can explain too, why the pH due modifications of the potential becomes significant only if the concentrations of coexisting oxidized and reduced species in the solution differ significantly

and in same time why the electrostatic term in electrochemical potential of the adsorbed ions is the local potential at the place of the ion and not the potential at the surface of oxidic semiconductor.

Acknowledgements. We are in debt to our colleague Dr. Alexandra Rustoiu-Csavdari for the useful discussions and suggestions.

REFERENCES

1. D. W. Roe, *J. Electrochem. Soc.*, **1965**, 112(10), 1005.
2. M. J. L. Trap, J. M. Stevels, *Verres Refract.*, **1971**, 25(4/5), 176.
3. Yu. I. Nicolaev, A. M. Pisarevskii, M. M. Schultz, *Elektrokimiya*, **1986**, 20(6), 739.
4. M. M. Schultz, A. V. Andreenko, A. M. Pisarevskii, *Dokl. Acad. Nauk SSSR*, **1984**, 274(6), 1430.
5. A. M. Pisarevskii, A. V. Andreenko, V. G. Konakov, *Vestnik Leningr. Univ.*, **1986**, 4, 109.
6. C. A. Mead, *Solid State Electronics*, **1966**, 9, 1023.
7. J. Neter, M. H. Kutner, C. J. Nachtsheim and W. Wasserman, *Applied linear regression models*, Third Ed., **1996**, Irwin Inc. Chicago, p. 70-71, 80-82.
8. R. A. Vandenberghe, F. Cardon, W. P. Gomes, *Surf. Sci.*, **1973**, 39, 368.
9. H. Gerischer, *Electrochimica Acta*, **1989**, 34(8), 1005.

FLAME ATOMIC EMISSION DETERMINATION OF STRONTIUM IN FLOTATION TAILINGS USING THE METHANE-AIR FLAME AS EXCITATION SOURCE

LADISLAU KÉKEDY-NAGY, TIBERIU FRENȚIU, ANA-MARIA RUSU,
MICHAELA PONTA and EMIL Ȃ. CORDOȘ

*Universitatea "Babeș-Bolyai", Facultatea de Chimie și Inginerie Chimică
3400 Cluj-Napoca, Arany J. 11, România*

ABSTRACT. The strontium content of flotation tailings has been determined by flame atomic emission spectroscopy using the methane-air flame. It was studied and optimized the flame and instrumental parameters (flame composition, the observation height in the flame) on the emission of strontium. The best results were obtained with the strontium line of 460.7 nm at the observation height of 7 mm, with the flame composition of 1.12 (relative stoichiometric units, (RSU)). The effect of Na, K, Mg, Ca, Al, ClO_4^- , SO_4^{2-} , and PO_4^{3-} on the emission of strontium was studied too. The calibration curve was linear in the 0.1 - 10 mg L⁻¹ range, the detection limit of 0.030 ± 0.022 mg.L⁻¹ was obtained in the presence of 200 mg L⁻¹ of Cs. The strontium content of flotation tailings has been determined in the presence of 100 mg L⁻¹ HClO₄ using the calibration curve and the standard addition method. With background correction results agree between these two methods.

INTRODUCTION

Strontium is the 21st in the rank of the element-abundance in the Earth crust, having of magma origin. Its dispersion into the environment is due to the erosion of the volcanic rocks (crashing and subsequent dissolution) giving rise of the weather factors. Therefore these types of rocks (granite, andezite and others) are considered as primary strontium source in the environment, the degree of its loading is determined by the dissolution rate of the different strontium compounds. The mobility of the strontium in the environment as a water-soluble salt is high, being ensured mainly by the natural waters (ground waters, rivers, oceanic streams, etc.).

The mean Sr content of the surface waters is of 80 μg L⁻¹ and of the seawater of 80 mg L⁻¹, respectively [1]. The human technological activities as mining for metal processing contribute significantly to the release and the mobilization of strontium in the environment. Huge amounts of rocks are

displaced and processed annually, the flotation tailing wastes are stored open air as heaps for long time, usually close to the processing factories. These tailings act as long term point-pollution sources, the soil, the ground waters and the streams are primarily polluted. Strontium, among the other elements, enters the ecosystem, moves from an ecological trophic layer into the other, accumulates in living organisms, throughout the food chain, which has humans at its top. Therefore it is important to know the degree of pollution produced by the source in order to assess the environment loading and to evaluate the risk for health. Strontium is retained by soils (the mean Sr-content being of 280 mg kg^{-1}) and by the living organisms (biosorption). From biological point of view it is not considered as essential element for life, its compounds generally are non-toxic, not hazardous to health [2]. However sometimes it exhibits toxic effect for low order organisms, young humans and animals when their calcium intake is low, the Ca/Sr intake ratio is also low [3,4]. Plants accumulate more strontium, humans and animals less, 99% of the strontium being accumulated in the bones. The daily human strontium intake is attained with vegetables and drinking water.

Flame atomic emission spectrometry (FAES) is a simple method, largely used for the determination of strontium in samples of different origin, as: biological materials [5, 6, 7], aluminum alloys [8], rocks and brine [9], minerals [10]. As excitation sources the C_2H_2 -air, C_2H_2 - N_2O flames have been used. The optimal flame conditions for the quantification of strontium in these flames were established, the detection limits being of order of 10^{-3} - $10^{-4} \text{ } \mu\text{g L}^{-1}$ using the most sensitive atomic resonance line of 406.8 nm [11]. Strontium yields different refractory compounds (chemical interference) in the flame as: SrO and SrOH, spinell-type mixed oxides with Ca, Al, Mg, Si, etc. [12]. Refractory compounds are formed with the SO_4^{2-} and PO_4^{3-} ions too [13]. The depressing effect of the interferents on the emission signal could be minimized by using the hotter C_2H_2 - N_2O flame [14]; by adding either 1-5 % La or 0.1 M EDTA or 2% quinolin-8-ol (as releasing agent) [14, 15]; ascorbic acid - K citrate (as matrix modifier) to the sample [16]. The releasing agents are effective only in the hot flames. Strontium ionizes partially in the acetylene flames, this phenomenon can be suppressed by adding either K, Rb or Cs salts to the sample in excess [11]. The cooler flames, as propane-butane-air (PB-A) and the natural gas-air (NG-A) flames are seldom used, often in low performance commercial flame-photometers, designated for routine analysis. The methane-air flame (M-A) has similar properties with the PB-A and NG-A flames, exhibiting lower temperature and burning velocity than the C_2H_2 ones. To our best knowledge the behaviour of strontium in the M-A flame was not reported. The aim of this work is to study the behaviour of strontium in the M-A flame, to optimize the flame and instrumental parameters and the determination of strontium in flotation tailing wastes, respectively.

EXPERIMENTAL INSTRUMENTATION

The measurements were carried out with a HEATH-701 (Heath Co., Benton Harbor, MI, USA) spectrophotometer. The instrumentation and operation conditions are provided in Table I.

Table I

Instrumentation and operating conditions

Equipment	Characteristics
Flame	Premixed methane – air Fuel: 99 % purity methane from pipe, flow rate 44 – 56 L h ⁻¹ , depending on flame composition Oxidant: compressed air, flow rate 500 L h ⁻¹
Burner	Mecker-type, made of brass, 50 mm long, 4 x 20 holes, laboratory made
Sample introduction and desolvation system	Concentric pneumatic nebulizer, 150 mL cylindrical glass spray chamber (AAS –1, Carl Zeiss Jena, Germany) provided with a laboratory made 1 mm cylindrical impactor placed at 5 mm from the nebulizer head. Liquid aspiration mode: natural, flow rate 3,5 mL min ⁻¹ , 11% nebulization efficiency
Optics	scanning monochromator, Czerny-Turner mount, spectral range 190-1000 nm, 350 mm focal length, 1180 grooves mm ⁻¹ blazed at 250 nm, bandpass 0.2 nm at slitwidth 0.1 mm (HEATH EU-700, Heath Co., Benton Harbor, MI, USA)
Photodetection	1P28A (RCA, USA) photomultiplier supplied with -700 V from an HEATH EU - 700 - 30 (Heath Co., Benton Harbor, MI, USA) power supply
Data acquisition system	Strip chart recorder K-201 (Carl Zeiss Jena, Germany)

REAGENTS

Stock standard solutions (1000 mg L⁻¹) were prepared by dissolving the appropriate amounts of metals (Mg and Al (Specpure, Johnson Matthey Chemicals Limited, England)) and compounds (CaCO₃, SrCO₃ (Specpure, Johnson Matthey Chemicals Limited, England) in corresponding acid. KCl, NaCl (analytical grade, Reactivul, București, Romania), CsCl, HCl, H₂SO₄, HClO₄ and H₃PO₄ (analytical grade, Merck, Darmstadt, Germany)) were dissolved and diluted with double distilled water, respectively. For further dilutions double distilled water was used in all cases.

SAMPLING AND SAMPLE HANDLING

The solid samples were collected from the flotation tailings heap, situated in the city Deva area (Hunedoara county), Romania. The samples were taken with metallic hoe from different selected places and sites of the heap, at depths of 20 and 40 centimeters, respectively. After removal of the vegetable (leaves, roots etc.) and other foreign matters, the samples were air dried at room temperature, grounded, homogenized, sieved through 120-mesh sieve and stored in airtight plastic bags. The samples were digested using the method proposed by M. van Avendonk, R. Scogerboe [17], namely: ~ 2 grams of solid was weighed from each sample in 100 mL glass beaker and 20 mL of conc. HClO_4 was added at room temperature. The beakers were heated on the sand bath to dryness and the residue was treated two times with 3 mL of conc. HClO_4 and evaporated to dryness. To the final evaporation residue 20 mL of HNO_3 2% was added, the suspension was filtered in 100 mL of volumetric flask and filled with HNO_3 2% to sign.

PROCEDURE

The behaviour of strontium in the M-A flame was studied up to $h = 18$ mm over the burner head (1-mm steps), at three different flame compositions: 0.88; 1.00; 1.12 (expressed in relative stoichiometric units, RSU). Four replicate measurements were made. The mean, the standard deviation, the S/N and the signal-to-background (S/B) ratio were calculated for each h and flame composition investigated. It was tested the homogeneity of the means (at a significance level of 0.05) too. The burner was held parallel to the optical axis of the spectrophotometer. The slit width of the monochromator was of 0.1 mm, unless stated otherwise. The sensitivity of the strip chart recorder was different in different spectral domains, considering the intensity of the emission lines and the background observed. For a given set of determinations the sensitivity was kept constant.

RESULTS AND DISCUSSION THE EMISSION SPECTRUM OF STRONTIUM, DETERMINATION OF THE ANALYTICAL EMISSION LINE

The emission spectrum of strontium in the M-A flame was determined first in the 200 - 800 nm spectral domain. It was registered the flame spectrum alone and its spectrum in the presence of a strontium of 100 mg L^{-1} in the flame. Using spectral table [18] it was identified, surprisingly, ionic lines with wavelengths of 407.7 nm and 421.5 nm, taking account of the relatively low temperature of the M-A flame. In addition it was also identified the strong atomic line of 460.7 nm and the molecular bands in the 375 – 392 nm, 595 – 626 nm and 640 – 720 nm spectral domain, belonging to refractory SrO and $\text{Sr}(\text{OH})_2$. The most intensive bandhead was located at 606 nm.

OPTIMIZATION OF THE FLAME AND INSTRUMENTAL PARAMETERS

The aim is to get that value for the flame composition and observation height h for whose the S/N ratio is maximal. The composition of the flame was kept constant, at 1.12 RSU. The concentration of the working calibration solutions was different, depending on the line intensity measured. The analytical signal, intensity (I , in a.u.), was measured at 407.7 nm, 421.5 nm, 460.7 and 606 nm and the background intensity (in the presence of strontium), at the base of the atomic emission line studied, at 461.5 nm. The variation of the line intensities versus observation height over the burner head is represented in Fig.1.

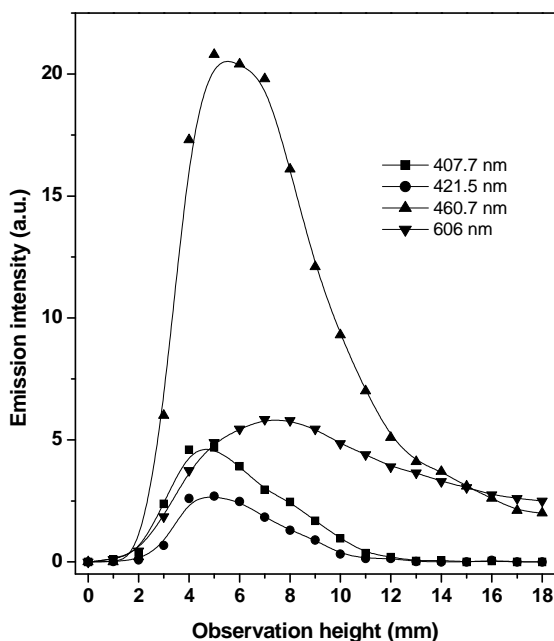


Fig. 1. The intensity of different strontium lines (not in scale) versus observation height

For the quantitative estimation of the results at different wavelengths only the maximal value of the analytical signal for each line was selected (I_{\max}). It was calculated the relative intensity for each line (I_{rel}) considering the sensitivity of the chart recorder and the concentration of the working standard used. The reference line was the weakest one. The S/B ratio was determined in the same way. The results are summarized in Table II.

The ionic lines are weak, being excited by radicals in the primary reaction zone of the flame. The most intensive line is the atomic line of 460.7 nm, being excited in the interconal reaction zone of the flame, observed at 7 mm over the burner head. The maximum of molecular emission appears at the same height, their emission are less influenced by excitation conditions in the flame. The

influence of the flame composition and of observation height on the analytical signal only for the most sensitive line was investigated further, using three flame compositions (0.88, 1.00, 1.12 RSU), at the concentration level of $10 \text{ mg L}^{-1} \text{ Sr}$. The data were processed by using the MicroCal Origin™ Software package, version 6.0 (MicroCal Software Inc., MA, USA) and plotted as 2D contour map (Fig.2).

Table II

The relative intensities of the strontium emission lines in the M-A flame

Wavelength (nm)	Emittent	h (mm)	I_{\max}	I_{rel}	S / B
407.7	Sr II	5	23.5	1.74	0.45
421.5	Sr II	5	13.5	1.00	0.24
460.7	Sr I	7	20.8	1540.74	610.00
606.0	SrOH	7 - 8	11.8	86.66	106.30

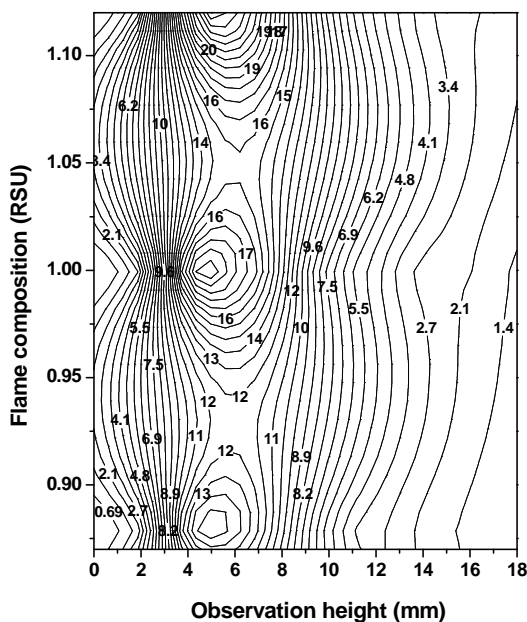


Fig. 2. The 2D contour map of the emission of the 460.7 nm strontium-line vs. observation height and flame composition relation. The data labels on the plot indicate the grid matrix values

The results show that the analytical signal depends both of observation height and flame composition and increases significantly with the increase of the methane content in the flame. The emission maxima are located at observation heights between 5-7 mm. The standard deviation of all means were homogeneous, the magnitude of the S/N ratio being decided by the magnitude of the mean. In conclusion, the optimal conditions for the quantitative determination of strontium in the M-A flame are $\lambda = 460.7 \text{ nm}$, $h = 7 \text{ mm}$, flame composition 1.12 RSU.

THE INFLUENCE OF THE SPECTRAL BANDPASS OF THE MONOCHROMATOR ON THE ANALYTICAL SIGNAL, S/N AND S/B RATIO

A possibility to enhance the analytical signal consists in the extending the radiation energy reaching the photodetector, in broaden the spectral bandpass of the monochromator, in our case. It is determined, among others, by the width of the slit (SW) of the monochromator, which influences in different manner the amplitude and the fluctuations of the emission signal. Therefore the optimal value of SW can be determined for which the S/N ratio is maximum. The influence of the slitwidth on I, the S/N and S/B ratio was studied in the 0.1 – 1.5 mm domain, in steps of 0.1 mm, using a 1 mg L⁻¹ strontium solution. The flame and instrumental parameters used were the optimal ones, determined earlier. The results show that the emission signal increases linearly with the spectral bandpass of the monochromator ($I = -0.0309 + 1.763SW$, $r^2 = 0.9883$) in the range of 0.1 – 1.1 mm. The standard deviation of the means increases slowly with the increase of SW but remains homogeneous in the entire SW domain. The maximum value of S/N was of 26 at the SW of 0.8 mm. The S/B ratio decreases continuously, its variation could be approximated best with a fifth order polinomial function. In conclusion, the slitwidth could be increased up to 0.8 mm without a significant decay of the S/N ratio.

INTERFERENCES

The effect of Na, K, Mg, Ca, Al, SO₄²⁻ and PO₄³⁻ on the emission signal of strontium of 5 mg L⁻¹ was investigated, as possible inorganic interferences in the samples. The effect of HClO₄ was tested too, used as releasing agent. The experimental conditions were the optimal ones, determined previously. The background signal was measured at 461.5 nm, in the presence of working standard in the flame. The variation of the net analytical signal versus the concentration of the interferences is represented in Fig 3.

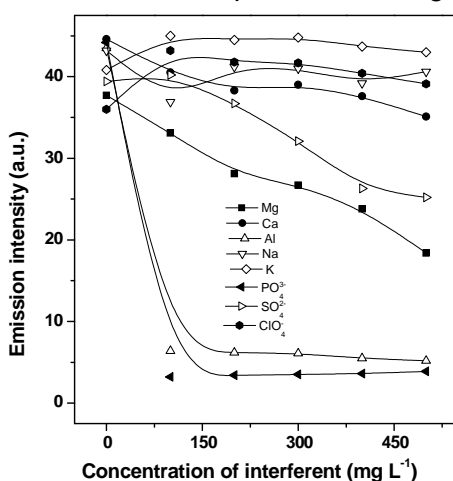


Figure 3. Influence of Na, K, Mg, Ca, Al, SO₄²⁻, PO₄³⁻ and ClO₄⁻ on the emission signal of strontium of 5 mg L⁻¹

K acts as ionization suppresser, enhancing simultaneously the analyte and the flame background signal too. The influence of Na is lower, and is mainly due to the background enhancement. Calcium enhances the analytical signal in 20-fold excess too, acting as releasing agent by binding the free O and OH radicals of the flame and hindering the formation of the strontium (SrO, SrOH) compounds. Mg and Al decrease gradually the strontium emission signal by formation the thermally stabile mixed oxides. The SO_4^{2-} and PO_4^{3-} ions decrease drastically the strontium emission signal even at low concentrations. HClO_4 as matrix modifier, enhances the strontium emission signal with 19 %, without enhancing the flame background.

CALIBRATION, DETERMINATION OF THE DETECTION LIMIT

For the determination of the detection limit the variation of the analytical signal versus concentration was studied. The calibration curves were plotted in the 0.1-100 mg L^{-1} strontium concentration range. Each calibration curve, covering only one order of magnitude of concentration, was established by using six standard solutions. Six replicate measurements were made at each concentration level. The homogeneity of the means and the linearity of the calibration curve was tested, it was calculated the equation of the regression line, the confidence limits, the coefficient of correlation (r^2), with the least squares method. The detection limit was calculated using the two step Neyman-Pearson model [19,20], for the fixed values of $(P_{10})_0 = 0.025$ and $(P_{11})_d = 0.975$. In order to extend the determination limit to lower concentrations 200 mg L^{-1} of Cs in final concentration was added to the diluted working Sr standards. The results are summarized in Table III.

Table III

The calibration data of strontium determination in the M-A flame

Nr.	Concentration range (mg/L)	Slitwidth (mm)	Equation of the calibration curve	r^2
(1)	100 – 10	0.1	$I = -1.54 + 0.66 \cdot C - 0.0023 \cdot C^2 - 7 \cdot 10^{-7} \cdot C^3$	0.9966
(2)	40 – 10	0.1	$I = 2.29 + 0.566 \cdot C$	0.9863
(3)	100 – 60	0.1	$I = 15.75 + 0.29 \cdot C$	0.9963
(4)	10 – 1	0.1	$I = 0.25 + 2.15 \cdot C$	0.9976
(5)	10 – 1	0.4	$I = -0.78 + 2.69 \cdot C$	0.9985
(6)	1 – 0.1	0.1	$I = -0.31 + 24.25 \cdot C$	0.9922
(7) [@]	1 – 0.1	0.1	$I = -1.1 + 24.95 \cdot C$	0.9972
(8) [@]	1 – 0.1	0.8	$I = -0.1 + 7.17 \cdot C$	0.9922

[@] 200 mg L^{-1} of Cs added

In the 10-100 mg L^{-1} domain the concentration-intensity relationship is not linear in the whole concentration range, it could be approximated best with a third-order polinom. (eq.(1)). Linear correlation exists only in narrower concentration domains (eq.(2) and (eq.3)), and at lower concentrations (eq.(4) - (eq.(8)). The presence of Cs enhances the sensitivity and the linearity of the calibration curve. The detection limit was calculated only in the 0.1- 1 mg L^{-1} concentration range, in the presence of Cs, being of $0.030 \pm 0.022 \text{ mg L}^{-1}$.

DETERMINATION OF STRONTIUM IN SOLID SAMPLES

The calibration and the standard addition method have carried out for the strontium quantification in the flotation tailings, the later being used as reference method (absence of certified reference material). The determinations were performed with optimal instrumental parameters, determined previously. The measurements were carried out in the presence of $100 \text{ mg L}^{-1} \text{ HClO}_4$, regardless of method used; the background signal being measured at 461.5 nm with the sample nebulized into the flame. In the case of standard addition method $100 \text{ }\mu\text{L}$ of concentrated strontium standard was added to the 25 mL of sample. Three additions of standard were made, in 1 mg L^{-1} concentration steps. It was calculated the regression line, the strontium content was determined from the intercept with the abscissa of the line. Comparing the calibration curves, the slope of calibration curves corresponding to the standard additions are significantly lower than of the calibration, fact, which suggests the existence of the chemical interference. The results of the determination of strontium content of flotation tailings are summarized in Table IV.

Table IV

Results of analysis of flotation tailings samples ($n = 4$)

Sample cod number	Heap collection site and depth (cm)	Concentration (mg kg^{-1} , calibration)	Concentration (mg kg^{-1} , standard addition)
DHS 1	TOP, 40	7.0 ± 1.6	7.1 ± 1.9
DHS 2	TOP, 20	7.1 ± 1.6	8.9 ± 1.9
DHS 3	TOP, 40	6.2 ± 1.6	7.5 ± 1.9
DHS 4	BASE, 20	7.4 ± 1.6	6.9 ± 1.9
DHS 5	BASE, 20	8.3 ± 1.6	9.5 ± 1.9
DHS 6	BASE, 40	5.0 ± 1.6	5.5 ± 1.9

The results of the two methods agree, they are within the errors of the determinations. With the standard addition method the results are generally higher probably due to the chemical interference, but the means obtained with the two methods do not differ significantly ($t_{\text{calc.}} = 0.8292 < t_{\text{tab}} = 2.97$, for fixed value of $(P_{10})_0 = 0.025$). We can consider that both methods give acceptable results, the standard addition method offering better results, closer to the real strontium content. The strontium content of the tailing is low, lower than that admitted for soils (20 mg kg^{-1}), uniformly dispersed in different sites of the heap. The loading of the environment with strontium erasing from the heap is also low, it is not hazardous to health from this point of view.

In conclusion the strontium content of flotation tailings can be determined with acceptable precision in the presence of 0.01 N HClO_4 , with the background correction, using the M-A flame. Due to the existence of chemical interference the standard addition method is recommended.

CONCLUSIONS

Strontium exhibits ionic, atomic and molecular spectrum in the M-A flame. The most intensive is the atomic line of 460.7 nm. The intensity of this line varies with the composition of the flame and observation height, the optimal observation height over the burner head is 7 mm, in fuel rich flame (RSU = 1.12). The presence of Mg, Al, SO_4^{2-} , and PO_4^{3-} decreases the emission of strontium. 0.01 N HClO_4 exhibits a good releasing effect. The intensity-concentration relationship is linear in the 0.1-10 mg L^{-1} range, the detection limit in the presence of 200 mg L^{-1} Cs is of $0.050 \pm 0.022 \text{ mg L}^{-1}$. The strontium content of flotation tailings can be determined precisely in the presence of 0.01 N HClO_4 using background correction with the calibration or the standard addition method. Due to chemical interference the standard addition method is recommended. The strontium content of the heap is low, uniformly distributed, being not hazardous to health.

In final conclusion, M-A flame is a suitable excitation source with acceptable precision determination of strontium in flotation tailings using the calibration method and the standard addition method with the background correction.

REFERENCES

1. M. Anke, L. Angelow, Proc. VI. Internat. Tr.El.Symp., (Ed.I.Pais), Budapest, (1994)
2. S.C. Skoryna, *Tr.El.Med.*, 1986, **3**, 153
3. F.J. Dwyer, *Environ.Toxicol.Chem.*, 1992, **11**, 513
4. C.W. Weber, et al, *Poultry Sci.*, 1972, **47**, 1318
5. A. Sanz-Medel, R. Rodriguez Roza, C. Perez Conde, *Analyst* (London), 1983, **108**, 204
6. H. Matusiewicz, *Anal.Chim.Acta*, 1982, 136215, 223
7. B.B. Razmilic, *At.Spectrosc.*, 1986, **7**, 43
8. M. Brill, *Aluminium* (Duesseldorf), 1982, **58**, E189
9. H. Matusiewicz, *Spectroscopy*, 1986, **1**, 32
10. G. Schwedt, *LaborPraxis*, 1990, **14**, 620
11. E. Cordoș T. Frențiu, M. Ponta, A. Rusu, A. Fodor, *Analiza prin spectrometria atomică* Institutul Național de Optoelectronică București, 1989
12. W.W. Harrison, W.H. Wadlin, *Anal.Chem.*, 1969, **41**, 374.
13. C.B. Boss, G.M. Hieftje, *Anal.Chem.*, 1979, **51**, 1897
14. W. Luecke, *J.Anal.At.Spectrom.*, 1994, **9**, 105
15. J. Liang, Y. Ruan, *Guangpu-Shiyanshi*, 1993, **10**, 24
16. D.S.R. Murty, B.N. Tikoo, *At.Spectrosc.*, 1987, **8**, 79
17. M. van Avendonk, R. Scogerboe, *Anal.Chem.*, 1981, **53**, 2349
18. R. Mavrodineanu, H. Boiteux, *Flame spectroscopy*, Wiley Interscience, New York, 1965.
19. C. Liteanu, I. Rică, *Statistical Theory and Methodology of Trace Analysis*, John Wiley, New York, 1980.
20. D.L. Massart, B.G.M. Vandeginste, S.N. Deming, Y. Michotte, L. Kaufman, *Chemometrics: a textbook*, Elsevier, New York, 1988.